

University of Warwick institutional repository: <http://go.warwick.ac.uk/wrap>

**A Thesis Submitted for the Degree of PhD at the University of Warwick**

<http://go.warwick.ac.uk/wrap/57427>

This thesis is made available online and is protected by original copyright.

Please scroll down to view the document itself.

Please refer to the repository record for this item for information to help you to cite it. Our policy information is available from the repository home page.

## Library Declaration and Deposit Agreement

### 1. STUDENT DETAILS

*Please complete the following:*

Full name: .....

University ID number: .....

### 2. THESIS DEPOSIT

2.1 I understand that under my registration at the University, I am required to deposit my thesis with the University in BOTH hard copy and in digital format. The digital version should normally be saved as a single pdf file.

2.2 The hard copy will be housed in the University Library. The digital version will be deposited in the University's Institutional Repository (WRAP). Unless otherwise indicated (see 2.3 below) this will be made openly accessible on the Internet and will be supplied to the British Library to be made available online via its Electronic Theses Online Service (EThOS) service.

[At present, theses submitted for a Master's degree by Research (MA, MSc, LLM, MS or MMedSci) are not being deposited in WRAP and not being made available via EThOS. This may change in future.]

2.3 In exceptional circumstances, the Chair of the Board of Graduate Studies may grant permission for an embargo to be placed on public access to the hard copy thesis for a limited period. It is also possible to apply separately for an embargo on the digital version. (Further information is available in the *Guide to Examinations for Higher Degrees by Research*.)

2.4 *If you are depositing a thesis for a Master's degree by Research, please complete section (a) below. For all other research degrees, please complete both sections (a) and (b) below:*

#### (a) Hard Copy

I hereby deposit a hard copy of my thesis in the University Library to be made publicly available to readers (please delete as appropriate) EITHER immediately OR after an embargo period of ..... months/years as agreed by the Chair of the Board of Graduate Studies.

I agree that my thesis may be photocopied.

YES / NO (*Please delete as appropriate*)

#### (b) Digital Copy

I hereby deposit a digital copy of my thesis to be held in WRAP and made available via EThOS.

Please choose one of the following options:

EITHER My thesis can be made publicly available online. YES / NO (*Please delete as appropriate*)

OR My thesis can be made publicly available only after.....[date] (*Please give date*)

YES / NO (*Please delete as appropriate*)

OR My full thesis cannot be made publicly available online but I am submitting a separately identified additional, abridged version that can be made available online.

YES / NO (*Please delete as appropriate*)

OR My thesis cannot be made publicly available online.

YES / NO (*Please delete as appropriate*)

### 3. GRANTING OF NON-EXCLUSIVE RIGHTS

Whether I deposit my Work personally or through an assistant or other agent, I agree to the following:

Rights granted to the University of Warwick and the British Library and the user of the thesis through this agreement are non-exclusive. I retain all rights in the thesis in its present version or future versions. I agree that the institutional repository administrators and the British Library or their agents may, without changing content, digitise and migrate the thesis to any medium or format for the purpose of future preservation and accessibility.

### 4. DECLARATIONS

(a) I DECLARE THAT:

- I am the author and owner of the copyright in the thesis and/or I have the authority of the authors and owners of the copyright in the thesis to make this agreement. Reproduction of any part of this thesis for teaching or in academic or other forms of publication is subject to the normal limitations on the use of copyrighted materials and to the proper and full acknowledgement of its source.
- The digital version of the thesis I am supplying is the same version as the final, hard-bound copy submitted in completion of my degree, once any minor corrections have been completed.
- I have exercised reasonable care to ensure that the thesis is original, and does not to the best of my knowledge break any UK law or other Intellectual Property Right, or contain any confidential material.
- I understand that, through the medium of the Internet, files will be available to automated agents, and may be searched and copied by, for example, text mining and plagiarism detection software.

(b) IF I HAVE AGREED (in Section 2 above) TO MAKE MY THESIS PUBLICLY AVAILABLE DIGITALLY, I ALSO DECLARE THAT:

- I grant the University of Warwick and the British Library a licence to make available on the Internet the thesis in digitised format through the Institutional Repository and through the British Library via the EThOS service.
- If my thesis does include any substantial subsidiary material owned by third-party copyright holders, I have sought and obtained permission to include it in any version of my thesis available in digital format and that this permission encompasses the rights that I have granted to the University of Warwick and to the British Library.

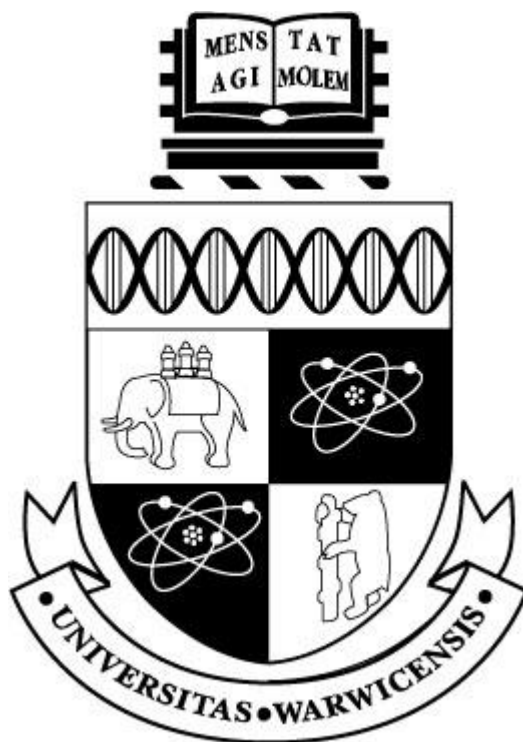
### 5. LEGAL INFRINGEMENTS

I understand that neither the University of Warwick nor the British Library have any obligation to take legal action on behalf of myself, or other rights holders, in the event of infringement of intellectual property rights, breach of contract or of any other right, in the thesis.

---

*Please sign this agreement and return it to the Graduate School Office when you submit your thesis.*

Student's signature: ..... Date: .....



Investigation of the Structure of the  
Perovskite Series  
 $(\text{Na}_{1-x}\text{K}_x)_{1/2}\text{Bi}_{1/2}\text{TiO}_3$

by

Aoife O'Brien

A thesis submitted in partial fulfilment of the requirements for the  
degree of Doctor of Philosophy

University of Warwick,  
Department of Physics

March, 2013



# Contents

Title Page	i
Contents	ii
List of Tables	iv
List of Figures	vi
Declaration and Published Work	xii
Abstract	xiv
List of Abbreviations	xv

## Chapter 1

Introduction and Literature Review	1
1.1 Rationale	1
1.2 Perovskite General Structure	2
1.2.1 Ideal Structure; Distortions	2
1.2.2 Octahedral Tilting	3
1.3 Properties	5
1.3.1 Piezoelectricity	5
1.3.2 Pyroelectricity	6
1.3.3 Ferroelectricity	6
1.4 Functional Perovskites	7
1.4.1 Barium Titanate, BaTiO <sub>3</sub>	8
1.4.2 Lead Titanate, PbTiO <sub>3</sub> , and Lead Zirconate-Titanate (PZT)	10
1.4.3 Sodium Bismuth Titanate, Na <sub>0.5</sub> Bi <sub>0.5</sub> TiO <sub>3</sub>	12
1.4.4 Potassium Bismuth Titanate, K <sub>0.5</sub> Bi <sub>0.5</sub> TiO <sub>3</sub>	16
1.4.5 Potassium Sodium Bismuth Titanate, (K <sub>x</sub> Na <sub>1-x</sub> ) <sub>0.5</sub> Bi <sub>0.5</sub> TiO <sub>3</sub>	16
1.5 Solvothermal and Hydrothermal Synthesis	18
1.5.1 Hydrothermal Synthesis of Perovskites	19
References	21

## Chapter 2

Experimental Methods	26
2.1 Sample Preparation	26
2.1.1 Solid State Synthesis	26
2.1.2 Hydrothermal Synthesis	26
2.2 Thermal Analysis	27
2.3 X-Ray Diffraction	28
2.4 Rietveld Refinement	29
2.4.1 Overview	29
2.4.2 Refinable Parameters	30
2.4.3 Criteria of Fit	32
2.4.4 Multiphase Refinement	33
References	34

<b>Chapter 3</b>	
Solid State KNBT X-Ray Diffraction Study	35
3.1 Room-Temperature Study of NBT	35
3.1.1 Pure NBT	35
3.1.2 NBT doped with 1 at. % Mn	40
3.2 Room-Temperature Study of KNBT	42
3.2.1 Series Overview	42
3.2.2 KNBT05 – KNBT20	45
3.2.3 KNBT25 – KNBT65	51
3.2.4 Series Data Analysis	56
3.3 High-Temperature X-Ray Diffraction Study	68
3.3.1 NBT	68
3.3.2 NBT doped with 1 at. % Mn	81
3.3.3 KNBT10	83
3.3.4 KNBT40	88
3.4 Summary	93
References	96
 <b>Chapter 4</b>	
Hydrothermal KNBT X-Ray Diffraction Study	98
4.1 NBT	98
4.1.1 Room-Temperature X-Ray Diffraction	98
4.1.2 High-Temperature X-Ray Diffraction	103
4.2 KBT	114
4.3 X-Ray Diffraction Study of the KNBT Series	120
4.4 KNBT30	125
References	133
 <b>Chapter 5</b>	
Conclusions and Further Work	134
5.1 NBT	134
5.1.1 NBT Room-Temperature Structure	134
5.1.2 Hydrothermal Synthesis of NBT	134
5.1.3 Temperature-Dependent Behaviour of NBT	136
5.1.4 Mn-doped NBT	137
5.2 Solid State KNBT Series	137
5.2.1 Room-Temperature	137
5.2.2 KNBT10 & KNBT40, High-Temperature	139
5.2.3 Solid State KNBT Phase Diagram	139
5.3 Hydrothermal KNBT Series	139
5.3.1 Room-Temperature	139
5.3.2 Hydrothermal KNBT30, High-Temperature	140
5.4 Hydrothermal KBT	141
References	143

## List of Tables

1.1	Curie temperature ( $T_C$ ) and room-temperature spontaneous polarisation ( $P_S$ ) of Rochelle salt, $\text{KH}_2\text{PO}_4$ and $\text{BaTiO}_3$	8
2.1	Definitions of Gaussian, Lorentzian and TCHZ peak shapes	31
2.2	Goodness-of-fit parameters for Rietveld refinements	32
3.1	Lattice parameters, atomic positions, thermal displacement parameters, and refinement details for solid state NBT, taken at room temperature	39
3.2	Lattice parameters, atomic positions, thermal displacement parameters, and refinement details for Mn-NBT, taken at room temperature	41
3.3	Lattice parameters, atomic positions, thermal displacement parameters, and refinement details for KNBT05 & KNBT10	46
3.4	Lattice parameters, atomic positions, thermal displacement parameters, and refinement details for KNBT15 & KNBT20	47
3.5	Lattice parameters, atomic positions, thermal displacement parameters, and refinement details for KNBT25 and KNBT30	52
3.6	Lattice parameters, atomic positions, thermal displacement parameters, and refinement details for KNBT35 and KNBT40	54
3.7	Lattice parameters, atomic positions, thermal displacement parameters, and refinement details for KNBT45 and KNBT50	55
3.8	Lattice parameters, atomic positions, thermal displacement parameters, and refinement details for KNBT60 and KNBT65	56
3.9	Polarisation values for NBT-KNBT65	61
3.10	Lattice parameters, atomic positions, thermal displacement parameters, and refinement details for solid state NBT at 200 °C	69
3.11	Lattice parameters, atomic positions, thermal displacement parameters, and refinement details for solid state NBT at 450 °C, 530 °C and 600 °C	72
3.12	Lattice parameters and refinement details for solid state NBT at 300 °C	78

3.13	Lattice parameters, atomic positions, thermal displacement parameters, and refinement details for $P4mm$ and $Pm\bar{3}m$ models of KNBT10 at 120 °C	86
3.14	Lattice parameters, atomic positions, thermal displacement parameters, and refinement details for $P4mm$ and $Pm\bar{3}m$ models of KNBT10 at 220 °C and 335 °C	88
3.15	Lattice parameters, atomic positions, thermal displacement parameters, and refinement details for $P4mm$ and $R3m/P4mm$ models of KNBT40 at 280 °C	91
3.16	Lattice parameters, atomic positions, thermal displacement parameters, and refinement details for $Pm\bar{3}m$ , $P4mm$ , and $R3m$ models of KNBT40 at 450 °C	92
4.1	Lattice parameters, atomic positions, thermal displacement parameters, and refinement details for heat-treated hydrothermal NBT, taken at room temperature	96
4.2	Results of polarisation calculations, based on atomic positions and lattice parameters obtained from Rietveld refinement	101
4.3	Lattice parameters, atomic positions, thermal displacement parameters, and refinement details for hydrothermal NBT at 130 °C	106
4.4	Lattice parameters, atomic positions, thermal displacement parameters, and refinement details for hydrothermal NBT at 450 °C, 530 °C and 700 °C	107
4.5	Lattice parameters and statistics for multiphase refinements of hydrothermal NBT at 305 °C in space groups: $R3c/P4bm$ , $Cc/P4bm$	112
4.6	Lattice parameters and statistics for refinements of hydrothermal NBT at 305 °C in space groups: $Pnma$ , $Cmcm$ and $P2_1/m$	112
4.7	Lattice parameters, atomic positions, thermal displacement parameters, and refinement details for heat-treated hydrothermal KNBT30, taken at room temperature	126
4.8	Lattice parameters, atomic positions, thermal displacement parameters, and refinement details for heat-treated hydrothermal KNBT30, taken at 500 °C	131

## List of Figures

1.1	Ideal perovskite structure with $BX_6$ octahedra and A cation in the centre	3
1.2	Anti-phase and in-phase tilting, viewed along the direction of the tilt axis	4
1.3	Example of a dielectric hysteresis loop, showing remanent polarisation ( $P_R$ ), the polarisation remanent in a poled material when the applied field is removed, and the coercive field ( $E_C$ ), that which results in zero net polarisation	7
1.4	Tetragonal barium titanate unit cell, showing displacement of titanium ion relative to the oxygen octahedron centre	9
1.5	Temperature-dependence of lattice parameters and cube root of cell volume of $BaTiO_3$	9
1.6	Phase diagrams of PZT	11
1.7	Piezoelectric coupling in PZT, showing peak close to the morphotropic phase boundary	11
1.8	Polarisation directions on the rhombohedral, tetragonal, and monoclinic phases	12
1.9	Phase diagram of KNBT	17
1.10	Piezoelectric constant $d_{33}$ for KNBT	18
1.11	Unit cell parameter variation with potassium substitution in KNBT, showing rhombohedral and tetragonal regions of the composition spectrum, and intermediate morphotropic region	18
2.1	Schematic diagram of Bragg-Brentano geometry	28
3.1	Room temperature XRD data from solid state synthesised NBT powder, shown on both linear and logarithmic scales	35
3.2	Plot showing fit, XRD data and difference plot for R3c Rietveld refinement of solid state NBT (room temperature)	36
3.3	Section of refinement from Figure 3.2 showing $\{110\}_{pc}$ XRD peak and mismatch between XRD data and model	37

3.4	Plot showing fit, data and difference plot for <i>Cc</i> Rietveld refinement of solid state NBT (room temperature)	37
3.5	Section of refinement from Figure 3.4 showing $\{110\}_{pc}$ peak and mismatch between data and model	38
3.6	XRD patterns of NBT and MnNBT	40
3.7	XRD data from KNBT	42
3.8	$\{100\}_{pc}$ XRD peak from KNBT samples	43
3.9	$\{110\}_{pc}$ XRD peak from KNBT samples	43
3.10	$\{111\}_{pc}$ XRD peak from KNBT samples	44
3.11	XRD patterns of NBT-KNBT30, showing $\frac{1}{2}(311)_{pc}$ peak visible at $\approx 38.5^\circ 2\theta$ in NBT-KNBT20	44
3.12	Simplified section of the <i>R3c</i> unit cell in the <i>ab</i> -plane, showing oxygen atoms and direction of rotation of the oxygen octahedra	48
3.13	Tilting angle, $\omega$ , in relation to lattice parameter <i>a</i>	48
3.14	Tilt angle, $\omega$ , for NBT – KNBT20 ( <i>R3c</i> models). The dashed line is drawn as a guide to the eye	49
3.15	Anisotropic thermal displacement parameters of A-site ions in NBT – KNBT20 ( <i>R3c</i> models)	50
3.16	Rhombohedral unit cell of NBT, showing thermal ellipsoids of the A-site atoms elongated in the $\langle 001 \rangle_R$ direction	50
3.17	Anisotropic thermal displacement parameters of A-site ions in NBT – KNBT20 ( <i>Cc</i> models).	51
3.18	Plot showing fit, XRD data and difference plot for <i>R3m/P4mm</i> refinement of KNBT25.	53
3.19	Plot showing fit, XRD data and difference plot for <i>R3m/P4mm</i> refinement of KNBT25; $\{110\}_{pc}$ XRD peak.	53
3.20	Plot showing fit, XRD data and difference plot for <i>R3m/P4mm</i> refinement of KNBT35.	53
3.21	Plot showing fit, XRD data and difference plot for <i>R3m/P4mm</i>	53

	refinement of KNBT35; $\{110\}_{pc}$ XRD peak.	
3.22	Pseudocubic unit cell volumes across the range NBT to KNBT65, and volumes calculated from published values for KBT lattice parameters	57
3.23	Pseudocubic lattice parameters across the range NBT - KNBT65, and published values for KBT lattice parameters	57
3.24	Tetragonal $c/a$ ratio of KNBT25-65, and reported $c/a$ ratios for KBT	58
3.25	Lattice parameters $a$ and $c$ from the $R3c$ models (NBT – KNBT20), and $a$ and $2c$ from the $R3m$ models (KNBT25 – KNBT65)	59
3.26	Unit cell showing average charge centre in $z$ of oxygen ions ( $'z_O'$ ), A-site cations ( $'z_A'$ ) and titanium ions ( $'z_{Ti}'$ ). $'d_{Ti}'$ is the displacement between the titanium and oxygen charge centres; and $'d_A'$ is the displacement between the A-site and oxygen charge centres	60
3.27	$R3c/R3m$ polarisation across the range: NBT – KNBT65. The dashed line indicates the approximate location of the phase boundary	62
3.28	$P4mm$ polarisation across the range: NBT – KNBT65	63
3.29	Polarisation across the range: NBT – KNBT65. The dashed line indicates the approximate location of the boundary	64
3.30	Relative abundances of rhombohedral and tetragonal phases from NBT – KNBT65. The dashed line indicates the approximate location of the boundary	65
3.31	Relationship between $c/a$ ratio and relative abundance of $P4mm$ phase, with linear fit to the data	65
3.32	$\{220\}_{pc}$ XRD peak from KNBT30, KNBT35 and KNBT50. The coloured bars mark the approximate separation between the $P4mm$ doublet peaks	66
3.33	Fit to the $\{220\}_{pc}$ XRD peak from KNBT30 using Voigt functions to model the underlying rhombohedral and tetragonal peaks	67
3.34	Splitting of the $\{220\}_{pc}$ tetragonal doublet peaks as a function of tetragonal component of peak area.	67
3.35	NBT x-ray diffraction patterns collected at room temperature, 200 °C, 300 °C, 450 °C, 530 °C and 600 °C	68
3.36	Plot showing fit, data and difference plot for $R3c$ refinement of solid	70

state NBT at 200 °C.

3.37	Plot showing fit, data and difference plot for <i>Cc</i> refinement of solid state NBT at 200 °C.	70
3.38	Plot showing fit, data and difference plot for $\{110\}_{pc}$ XRD peak in <i>R3c</i> refinement of solid state NBT at 200 °C.	70
3.39	Plot showing fit, data and difference plot for $\{110\}_{pc}$ XRD peak in <i>Cc</i> refinement of solid state NBT at 200 °C.	71
3.40	Plot showing fit, data and difference plot for <i>P4bm</i> refinement of solid state NBT at 450 °C.	73
3.41	Plot showing fit, data and difference plot for <i>Pm3m</i> refinement of solid state NBT at 530 °C.	73
3.42	Plot showing fit, data and difference plot for <i>Pm3m</i> refinement of solid state NBT at 600 °C.	73
3.43	XRD data from NBT during heating from 100 – 400 °C, showing $\frac{1}{2}\{311\}_{pc}$ peak at $\approx 38^\circ 2\theta$ and $\frac{1}{2}\{310\}_{pc}$ peak at $\approx 36.3^\circ 2\theta$ , indicating phase transition at $\approx 300^\circ\text{C}$	74
3.44	NBT $\{110\}_{pc}$ and $\{111\}_{pc}$ full width at half maximum variation with temperature, showing both heating and cooling data	75
3.45	Intensity of the $\frac{1}{2}\{311\}_{pc}$ and $\frac{1}{2}\{310\}_{pc}$ XRD peaks relative to the intensity of the $\{110\}_{pc}$ peak, heating and cooling. Grey areas indicate the temperature range over which both peaks are seen to coexist.	76
3.46	$\{110\}_{pc}$ peak in NBT XRD patterns collected at room temperature, 200 °C, 300 °C, 450 °C, 530 °C and 600 °C. A sharper peak can be seen at the transition temperature (300 °C) than at 200 °C or 450 °C.	77
3.47	Plot showing fit, data and difference plot for <i>R3c</i> refinement of solid state NBT at 300 °C.	78
3.48	Plot showing fit, data and difference plot for <i>Cc</i> refinement of solid state NBT at 300 °C.	78
3.49	Plot showing fit, data and difference plot for <i>P4bm</i> refinement of solid state NBT at 300 °C.	79
3.50	Plot showing fit, data and difference plot for <i>Pm3m</i> refinement of solid state NBT at 300 °C.	79



3.51	Pseudocubic lattice parameters and pseudocubic unit cell volumes of NBT between room temperature and 600 °C	81
3.52	Relative Intensity of the $\frac{1}{2}\{311\}_{pc}$ and $\frac{1}{2}\{310\}_{pc}$ XRD peaks as a function of temperature	82
3.53	Pseudo-cubic lattice parameters of MnNBT, based on rhombohedral, tetragonal, and cubic models, as a function of temperature	83
3.54	Pseudo-cubic unit cell volume of MnNBT as a function of temperature, based on rhombohedral, cubic, and tetragonal models	83
3.55	FWHM of the $\{110\}_{pc}$ and $\{111\}_{pc}$ peaks in KNBT10 on heating from room temperature to 340 °C. The lines are drawn as a guide to the eye	84
3.56	FWHM of the $\{110\}_{pc}$ and $\{111\}_{pc}$ peaks in KNBT10 on heating from room temperature to 260 °C, focusing on the region of phase transition. The lines indicate linear trends fitted to the data	85
3.57	Intensity of the $\frac{1}{2}\{311\}_{pc}$ XRD peak relative to the intensity of the $\{110\}_{pc}$ XRD peak in KNBT10 when heated from room temperature to 340 °C	85
3.58	FWHM of the $\{110\}_{pc}$ and $\{111\}_{pc}$ XRD peaks in KNBT40 on heating from room temperature to 450 °C. The solid lines represent fits to the data; the dashed line is drawn as a guide to the eye	89
3.59	$\{110\}_{pc}$ XRD peak of KNBT40 at 25 °C, 280 °C, and 450 °C, showing visible splitting at 25 °C only	90
3.60	$\{210\}_{pc}$ XRD peak of KNBT40 at 25 °C, 280 °C, and 450 °C. Although the splitting seen at 25 °C is not as distinct at 280 °C, comparison with the 450 °C data shows that some peak broadening not consistent with cubic symmetry is still present	90
3.61	Phase diagram of the KNBT system	89
4.1	Room temperature XRD data from hydrothermally synthesised NBT, as prepared and after heat-treatment at 950 °C for 6 hours	99
4.2	$\frac{1}{2}\{311\}_{pc}$ XRD peak in hydrothermal NBT, before and after heat-treatment at 950 °C for 6 hours	99
4.3	Log plot of XRD data from heat-treated hydrothermal NBT and solid state NBT, showing greater relative intensity of the $\frac{1}{2}\{311\}_{pc}$ XRD peak in the hydrothermal sample	100

4.4	Polarisation values of solid state NBT – KNBT20 and hydrothermal NBT ( <i>R3c</i> models)	102
4.5	XRD data from hydrothermally synthesised NBT at room temperature, 130 °C, 450 °C, 530 °C, and 700 °C	103
4.6	$\{110\}_{pc}$ XRD peak from hydrothermally synthesised NBT at room temperature, 130 °C, 450 °C, 530 °C, and 700 °C	104
4.7	$\{200\}_{pc}$ peak from hydrothermally synthesised NBT at room temperature, 130 °C, 450 °C, 530 °C, and 700 °C	104
4.8	35 – 41 ° 2 $\theta$ XRD data from hydrothermally synthesised NBT at room temperature, 130 °C, 450 °C, 530 °C, and 700 °C (data offset in the y axis). The $\frac{1}{2}\{311\}_{pc}$ XRD peak can be seen up to 130 °C; the $\frac{1}{2}\{310\}_{pc}$ XRD peak can be seen at 450 °C and 530 °C	105
4.9	Variation in FWHM values of $\{110\}_{pc}$ and $\{111\}_{pc}$ XRD peaks, heating and cooling	108
4.10	Relative intensities of the superstructure reflections in hydrothermal NBT on heating from room temperature to 520 °C	109
4.11	Relative intensities of the superstructure reflections in hydrothermal NBT in the region of the phase transition; a) on heating; b) on cooling. The solid lines show linear best fit to the data; the dashed lines indicate the temperature of phase transition	110
4.12	XRD pattern from hydrothermal NBT at 305 °C, showing coexistence of $\frac{1}{2}\{310\}_{pc}$ in-phase and $\frac{1}{2}\{311\}_{pc}$ antiphase tilt peaks (inset)	111
4.13	Plot showing fit, XRD data and difference plot from <i>Pnma</i> refinement of hydrothermal NBT at 305 °C, showing peaks predicted by the model that are not present in the data.	113
4.14	Plot showing fit, XRD data and difference plot from <i>Cmcm</i> refinement of hydrothermal NBT at 305 °C, showing peaks predicted by the model that are not present in the data.	113
4.15	Plot showing fit, XRD data and difference plot from <i>P2<sub>1</sub>/m</i> refinement of hydrothermal NBT at 305 °C, showing peaks predicted by the model that are not present in the data.	113
4.16	Pseudocubic lattice parameters of hydrothermal NBT between room temperature and 700 °C	114
4.17	Room-temperature XRD pattern of hydrothermal KBT, as-prepared	115

4.18	Room-temperature XRD pattern of hydrothermal KBT, after heat-treatment at 890 °C	115
4.19	Peak centres of the modelled $\{001\}_T$ and $(010)_T$ XRD peaks, as functions of temperature	116
4.20	$\{100\}_{pc}$ XRD peak of hydrothermal KBT at 710 °C and 725 °C, showing gradual assimilation of the $\{001\}_T$ peak into the $\{010\}_T$ peak	117
4.21	The Lorentzian fractions of the low- $2\theta$ side (L1) and the high- $2\theta$ side (L2) of the modelled $\{100\}_{pc}$ peak, between 725 °C – 890 °C	118
4.22	HWHM of the low- and high- $2\theta$ sides of the $(001)_T$ XRD peak of KBT as functions of temperature	118
4.23	$\{100\}_{pc}$ XRD peak of hydrothermal KBT at 25 °C and 605 °C, showing increased asymmetry of the $(001)_T$ peak at 605 °C	119
4.24	TGA-DSC curves of hydrothermal KBT	120
4.25	Room-temperature XRD patterns collected from as-prepared KNBT00-100	121
4.26	$\{110\}_{pc}$ XRD peak in as-prepared KNBT00-100	121
4.27	XRD patterns of as-prepared hydrothermal NBT and KNBT10, showing similar backgrounds and $\frac{1}{2}\{311\}_{pc}$ reflection	122
4.28	Pseudo-cubic lattice parameters of as-prepared hydrothermal KNBT	124
4.29	Room-temperature XRD pattern from hydrothermal KNBT30, heated-treated at 900 °C for 6 hours, showing $\frac{1}{2}\{311\}_{pc}$ peak	125
4.30	$\{110\}_{pc}$ XRD peak from hydrothermal KNBT30, heated-treated at 900 °C for 6 hours	125
4.31	Intensity of the $\frac{1}{2}\{311\}_{pc}$ XRD peak relative to the intensity of the $\{110\}_{pc}$ XRD peak in KNBT30 when heated from 100 °C to 500 °C. The solid line is a linear fit to the data between 100 °C – 230 °C	127
4.32	FWHM of the $\{110\}_{pc}$ and $\{111\}_{pc}$ peaks in KNBT30 on heating from 500 °C to 500 °C. Solid lines show linear fits to the data < 500 °C; dashed lines are drawn at the FWHM values of the 500 °C data. The dotted lines indicate the temperatures at which these intercept	128

4.33	$\{110\}_{pc}$ XRD peak of hydrothermal KNBT30 at 500 °C, showing no peak splitting	128
4.34	$\{321\}_{pc}$ XRD peak of hydrothermal KNBT30 at 500 °C, showing asymmetric peak shape indicative of peak splitting	129
4.35	Williamson-Hall plot of hydrothermal KNBT30 at 500 °C, and cubic hydrothermal and solid state NBT at 700 °C and 600 °C respectively	130

## Declaration and Published Work

This thesis is submitted to the University of Warwick in support of my application for the degree of Doctor of Philosophy. It has been composed by myself and has not been submitted in any previous application for any degree.

The work presented (including data generated and data analysis) was carried out by the author except in the cases outlined below:

Hydrothermal samples were synthesised by Dr. Kripasindhu Sardar;

Thermal analysis was performed by Mr. Dave Hammond.

Parts of this thesis have been published by the author:

A. O'Brien, D. I. Woodward, K. Sardar, R. I. Walton, P. A. Thomas, *App. Phys. Lett.* **101** (14), 2902 (2012).

## Abstract

The structures of the lead-free perovskites in the solid solution range  $(K_xNa_{1-x})_{0.5}Bi_{0.5}TiO_3$  (KNBT100x) have been investigated using high-resolution x-ray diffraction (XRD) on polycrystalline samples. The room-temperature structure of  $Na_{0.5}Bi_{0.5}TiO_3$  (NBT) has been studied, and identified as having monoclinic  $Cc$  symmetry, with distortion very close to that of rhombohedral  $R3c$ . High-temperature XRD has been used to identify a phase transition between the pseudo-rhombohedral phase and a tetragonal  $P4bm$  phase at 300 °C. This transition has been found to occur via a pseudo-cubic structure, although local variations in transition temperatures lead to the coexistence of both phases, with a hysteresis of ~ 30 °C. The Curie temperature,  $T_C$ , has been found to lie in the range 450 °C – 530 °C. The room-temperature structures of compositions from NBT to  $(K_{0.65}Na_{0.35})_{0.5}Bi_{0.5}TiO_3$  have been studied, and a phase boundary identified at  $x \sim 0.2$ . Compositions from NBT – KNBT20 refine as monoclinic  $Cc$ , with pseudo-rhombohedral symmetry, whilst KNBT25-65 were found to have equilibrium phase  $P4mm$ , with a stress-induced  $R3m$  phase also present. A relationship was observed between the spontaneous tetragonal strain and the proportion of tetragonal phase present in these samples. KNBT10 and KNBT40 did not show evidence of the high-temperature  $P4bm$  phase; instead,  $T_C$  values were found to be ~ 225 °C and ~ 300 °C respectively. Experimental data have been combined with data from published literature to construct a phase diagram of the KNBT system.

KNBT synthesised via a hydrothermal method has been investigated. Hydrothermal NBT, once heat-treated, has been found to show similar structure to solid state NBT and undergoes the pseudo-rhombohedral to tetragonal transition at 305 °C, with a hysteresis of ~ 20 °C between heating and cooling.  $T_C$  was found to be higher, in the range 530 °C – 700 °C. The XRD patterns of non-heat-treated hydrothermal KNBT have broader peaks and a more undulating background, indicative of smaller crystallite size and diffuse scattering from a more disordered material. The proposed source of this disorder is the presence of oxygen vacancies,  $OH^-$  groups, or A-site clustering. Significant peak splitting was observed in the XRD patterns of hydrothermal  $K_{0.5}Bi_{0.5}TiO_3$  (KBT) and tetragonal KNBT. This was not the case for solid state KNBT, showing a greater tetragonal distortion in materials prepared via the hydrothermal method. Heat-treating this material was found to effect a significant structural change, with single peaks remaining after cooling. It is proposed that this could be caused by the release of  $OH^-$  groups, recrystallisation, and mixing of the A-site species.

## List of Abbreviations

FWHM	full width at half-maximum
HWHM	half width at half-maximum
XRD	x-ray diffraction
NBT	$\text{Na}_{0.5}\text{Bi}_{0.5}\text{TiO}_3$
KBT	$\text{K}_{0.5}\text{Bi}_{0.5}\text{TiO}_3$
KNBT	$(\text{K}_x\text{Na}_{1-x})_{0.5}\text{Bi}_{0.5}\text{TiO}_3$
PZT	$\text{Pb}(\text{Zr}_x\text{Ti}_{1-x})\text{O}_3$
PEG	polyethylene glycol
TGA	thermo-gravimetric analysis
DSC	differential scanning calorimetry

# Chapter 1

## Introduction and Literature Review

### 1.1 Rationale

Piezoelectric materials have found widespread use in industry, with a broad range of applications including sensors of force or displacement, and actuator devices such as motors and signal generators<sup>1,2</sup>. Metal-oxide based piezoelectric ceramics offer a high degree of control over the composition, shape, and dimensions of a piezoelectric ceramic element, at relatively low manufacturing cost<sup>2</sup>. This has allowed tailoring of piezoelectric ceramics according to specific requirements<sup>2</sup>.

Currently, the most widely-used materials are those based on lead zirconate-titanate (PZT),  $\text{Pb}(\text{Zr}_x\text{Ti}_{1-x})\text{O}_3$ , because of their excellent electromechanical properties<sup>3</sup>. Lead oxide is a toxic material, and vaporises during processing<sup>3</sup>. Lead may be inhaled, or ingested after settling out of the air, and is readily absorbed into the bloodstream<sup>4</sup>. Deleterious effects are suffered by many organ systems including the central nervous system and kidneys<sup>5,6</sup>, and chronic lead exposure in children is known to impair neurological and intellectual development<sup>5,6</sup>. In light of the health risks posed by lead, it has been included in the Restriction of Hazardous Substances directive of the European Union<sup>7</sup>, which limits the use of certain substances in electrical and electronic equipment. This directive calls for the substitution of environmentally-friendly alternatives, making exemptions where this is “not possible from the scientific and technical point of view”, with a specific mention of electronic ceramics<sup>7</sup>. Despite the temporary clemency, considerable research effort has been devoted to the search for a lead-free alternative to PZT<sup>1,3,8,9</sup>. This is also motivated by demand for high-temperature applications, for which none of the currently-available lead-based materials are suitable<sup>3</sup>.



Electromechanical response has been found to be composition-dependent, with enhanced properties found close to the boundary between different crystallographic phases of PZT<sup>10,11</sup>. Research into lead-free piezoelectric materials has therefore centred around metal-oxide solutions with analogous phase diagrams<sup>1</sup>, including perovskite titanates<sup>1</sup>, niobates<sup>1</sup>, and bismuth ferrite (BiFeO<sub>3</sub>)<sup>9</sup>. The following work is a structural study into one such range of materials, the sodium bismuth titanate–potassium bismuth titanate solid solution range. This solid solution has attracted attention for possessing a phase boundary between apparently rhombohedral and tetragonal structures at which physical properties, including piezoelectric coefficients, are maximised. However, structural studies of this system have reported wildly varying phase fields and a reliable phase diagram remains elusive. This work combines high-resolution x-ray diffraction and Rietveld refinements with materials fabricated by solid state and hydrothermal methods to obtain such a phase diagram.

## 1.2 Perovskite General Structure

### 1.2.1 Ideal Structure; Distortions

Perovskite-type compounds have general formula ABX<sub>3</sub>, A and B being cations and X an anion, usually oxygen. They can be considered as a framework of BX<sub>6</sub> octahedra, with the A cations occupying the interstices between them<sup>12</sup>. The A and B cations have 12-fold and 6-fold coordination to the oxygen ions, respectively. In the ideal form (Figure 1.1), perovskites have cubic  $Pm\bar{3}m$  symmetry and unit cell of side  $\sim 4 \text{ \AA}$ . The structure must also have a neutral overall charge, normally attained by a charge distribution of A<sup>1+</sup>B<sup>5+</sup>O<sub>3</sub>, A<sup>2+</sup>B<sup>4+</sup>O<sub>3</sub> or A<sup>3+</sup>B<sup>3+</sup>O<sub>3</sub>.

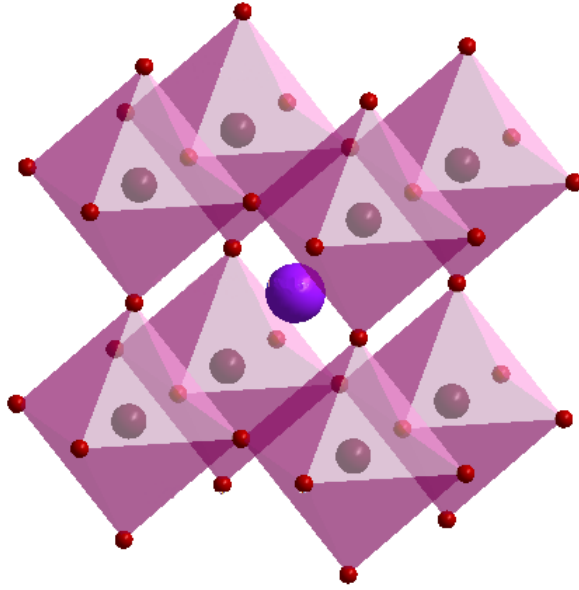


**Figure 1.1.** Ideal perovskite structure with  $BX_6$  octahedra and A cation in the centre.

A tolerance factor of the size of ions in perovskite oxides is defined<sup>13</sup>:

$$t = \frac{(r_A + r_X)}{\sqrt{2}(r_B + r_X)} \quad (1.1)$$

where  $r_A$ ,  $r_B$  and  $r_X$  are the radii of the A, B, and X ions. The ideal perovskite structure has a tolerance factor equal to 1, and usually occurs at high temperatures<sup>14</sup>. If the tolerance factor  $> 1$ , the B cation is too small for the oxygen octahedron, allowing a small polar distortion, as in  $BaTiO_3$ . In the case of a tolerance factor less than 1, the A cation would be too small to maintain 12-fold coordination in the ideal cubic structure. The  $BO_6$  octahedra distort little, thanks to the high electrostatic valence of the B-O bond, but are able to tilt, maintaining B-O distances but reducing A-O distances<sup>15</sup>. Tilting leads to a reduction in the volume of the pseudo-cubic unit cell<sup>15,16</sup>. In the more extreme cases, tolerance factors smaller than 1 lead to a lowering of the A cation coordination number<sup>17</sup>.

### 1.2.2 Octahedral Tilting

A notation system of the form  $a^+b^-c^0$  was devised by Glazer<sup>18</sup> to describe octahedral tilting in perovskites. The letters are used to refer to tilting around the pseudocubic [100], [010] and [001] axes respectively, repeated letters being used to denote tilts of equal

magnitude about two or more axes (e.g.  $aac$ ). Positive, or 'in-phase', tilting describes the situation in which successive octahedra parallel to the tilt axis in question are rotated in the same sense, and this is denoted by a superscript '+'. Negative ('antiphase') tilting is that in which successive octahedra parallel to the tilt axis are rotated in the opposite sense (denoted by the superscript '-') (Figure 1.2). An axis about which there is no tilting is given the superscript '0'. Classifying the tilt systems in this way, Glazer produced a list of 23 possible tilt systems corresponding to 15 different space groups<sup>18</sup>. Howard and Stokes<sup>19</sup> reduced this list to 15 possible tilt systems by eliminating those with higher symmetry than that required by the corresponding space group. The notation was later modified to include subscripts +, - and 0 indicating B cation displacement along a given axis. For example,  $a^0_0a^0_0c^0_+$  represents the tetragonal ferroelectric structure of  $\text{BaTiO}_3$ , the + subscript denoting B-cation displacement in the + direction along the z axis<sup>20</sup>. Structures with tolerance factors below  $t \sim 0.985$  tend to show anti-phase tilting, and below  $t \sim 0.965$  both in- and anti-phase tilting occur<sup>16</sup>.

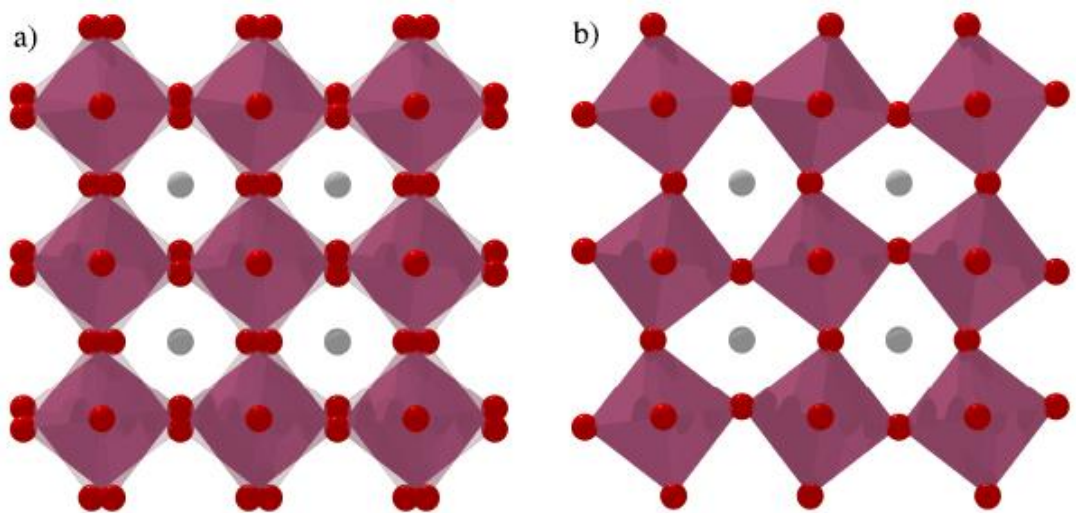


**Figure 1.2.** a) anti-phase tilting and b) in-phase tilting, viewed along the direction of the tilt axis.

Antiphase tilting causes the pseudocubic unit cell axis to double parallel to the tilt axis. There is also a doubling of the repeat distances perpendicular to the axis of tilt<sup>21</sup>. In-phase tilting also doubles the repeat distance in the direction perpendicular to the tilt axis, but not parallel. In both cases, cell volume is increased by an integer, producing diffraction peaks that can be indexed to half-integer reciprocal lattice planes with respect to the ideal structure. These 'extra' peaks can be useful in determining crystal structure and studying phase transitions<sup>18,21</sup>. With reference to a pseudo-cubic unit cell, the main reflections will be indexed with integer indices, whilst the 'extra' reflections may be indexed with half-integer numbers. Anti-phase tilting gives reflections of the type  $\frac{1}{2}\{ooo\}_{pc}$ ; in-phase tilting gives  $\frac{1}{2}\{ooe\}_{pc}$  reflections, the even index being  $h$  for  $a^+$ ,  $k$  for  $b^+$ , and  $l$  for  $c^+$  tilting<sup>21</sup>. The intensities of the tilt peaks are related to the angle through which the octahedra are tilted<sup>21</sup>.

## 1.3 Properties

### 1.3.1 Piezoelectricity

Of the 32 crystallographic point groups, 21 are non-centrosymmetric. The absence of a centre of symmetry is a requirement in order to produce a dipole moment by the application of stress, and so only non-centrosymmetric crystals may be piezoelectric. Of the 21 non-centrosymmetric point groups, 20 are piezoelectric. Piezoelectricity is a charge produced in response to mechanical stress and, conversely, a mechanical deformation in response to an applied electric field. The direct piezoelectric effect can be described thus:

$$P_i = d_{ijk}\sigma_{jk} \quad (1.2)$$

and the converse:

$$\epsilon_{ij} = d_{ijk}E_k \quad (1.3)$$

$\sigma$  is the applied stress,  $E$  the applied electric field,  $P$  is the induced polarisation, and  $\epsilon$  is induced strain.  $d$  is a piezoelectric coefficient linking these properties. The ability to couple

electrical and mechanical displacements makes piezoelectric materials useful for sensor and actuator technologies<sup>9</sup>.

### 1.3.2 Pyroelectricity

Of the 20 piezoelectric point groups, 10 are pyroelectric. Pyroelectricity is the generation of a temporary polarisation in response to a change in temperature. Temperature-sensitive spontaneous polarisation makes pyroelectric materials suitable for a range of applications including detection of radiation and infra-red imaging<sup>17</sup>.

### 1.3.3 Ferroelectricity

When cooled, most perovskite structures undergo a transition from cubic  $Pm\bar{3}m$  to a lower symmetry structure. This transition is known as the Curie transition, and takes place at the ferroelectric Curie temperature,  $T_C$ . Below this temperature ferroelectric properties may be present.

Of the 10 pyroelectric point groups, some are ferroelectric. Ferroelectricity is defined as a spontaneous electric polarisation, reversible in an applied electric field; ferroelectric materials therefore show dielectric hysteresis loops (Figure 1.3). As ferroelectrics are both pyroelectric and piezoelectric, hysteresis loops serve as useful indicators of the existence of piezoelectricity in a material.

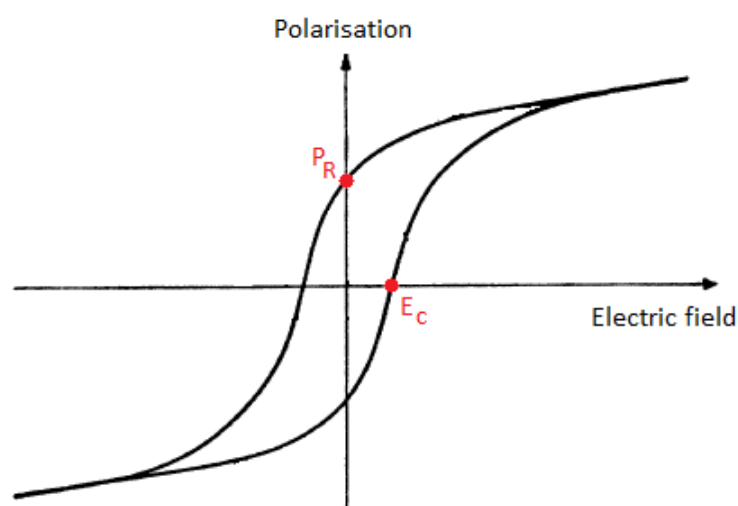


**Figure 1.3.** Example of a dielectric hysteresis loop, showing remanent polarisation ( $P_R$ ), the polarisation remanent in a poled material when the applied field is removed, and the coercive field ( $E_c$ ), that which results in zero net polarisation.

Ceramics, existing as randomly oriented grains, may be poled using an applied field to give a net polarisation in a particular direction. This allows access to piezoelectric materials without the need for single crystals, which require careful preparation with regard to their crystal orientation and may be brittle or difficult to grow.

## 1.4 Functional Perovskites

Perovskite compounds exhibit manifold properties including ferroelectricity, piezoelectricity and pyroelectricity, rendering them desirable for a wide range of applications. This is due in part to the impressive array of suitable constituents, with over 90% of natural metallic elements known to be stable in perovskite oxide structures<sup>14</sup>. Further variation is possible by partial substitution of the A and B cations, allowing compounds to be ‘tuned’ for optimum properties<sup>22</sup>.

### 1.4.1 Barium Titanate, BaTiO<sub>3</sub>

BaTiO<sub>3</sub>, was discovered in 1941 to have a very high dielectric constant<sup>23</sup> and later found to exhibit ferroelectricity<sup>24</sup>. This was the first case of ferroelectricity found in a perovskite material. Hitherto, the phenomenon was thought to relate to hydrogen bonding and was known only in Rochelle salt and potassium dihydrogen phosphate, KH<sub>2</sub>PO<sub>4</sub><sup>25</sup>. Both of these materials have low Curie points, are water soluble, and have lower spontaneous polarisation values than BaTiO<sub>3</sub> (Table 1). By contrast, barium titanate is ferroelectric up to 120 °C and can be easily prepared as a polycrystalline ceramic and shaped as desired<sup>23</sup>. These physical properties were more favourable for practical application, and its simple structure made it attractive as a material in which to study ferroelectricity<sup>26, 27</sup>.

	Rochelle Salt	KH <sub>2</sub> PO <sub>4</sub>	BaTiO <sub>3</sub>
T <sub>C</sub> (°C)	24; -18	-150	120
P <sub>S</sub> (μC cm <sup>-2</sup> )	12 <sup>[28]</sup>	---	26 <sup>[29]</sup>

**Table 1.1.** Curie temperature (T<sub>C</sub>) and room-temperature spontaneous polarisation (P<sub>S</sub>) of Rochelle salt, KH<sub>2</sub>PO<sub>4</sub> and BaTiO<sub>3</sub>.

At the Curie point, the ideal cubic structure changes to give a tetragonal unit cell,  $a = 3.995 \text{ \AA}$ ,  $c = 4.034 \text{ \AA}$ <sup>30</sup> at room temperature (Figure 1.4). The titanium ion is displaced from the centre of the oxygen octahedron by about 6% of the Ti-O distance. The barium ions are displaced in the same direction, by a smaller amount; the relative displacement of the cations and anions results in a large dipole moment throughout the structure. In an applied electric field, the titanium ion can shift to any of the other corners of the octahedron, changing the orientation of the dipole<sup>30</sup>.

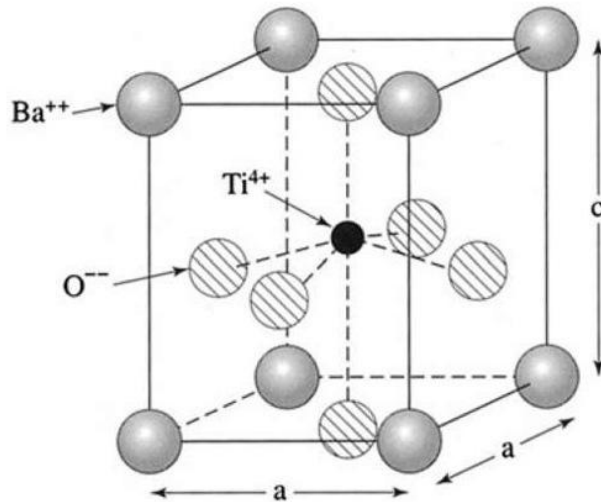


**Figure 1.4.** Tetragonal barium titanate unit cell, showing displacement of titanium ion relative to the oxygen octahedron centre, from West<sup>30</sup>.

Kay and Vousden identified two further phase transitions, both ferroelectric-to-ferroelectric: tetragonal ( $P4mm$ ) to orthorhombic ( $Bmm2$ ) at 5 °C; and orthorhombic to rhombohedral ( $R3m$ ) at -90 °C (Figure 1.5)<sup>31</sup>. The titanium ions are displaced along the  $\langle 110 \rangle$  direction in the orthorhombic structure, and the  $\langle 111 \rangle$  direction in the rhombohedral structure. Kay's and Vousden's data<sup>31</sup> show evidence of phase coexistence, hysteresis, and discontinuous change in cell volume at all three transitions.

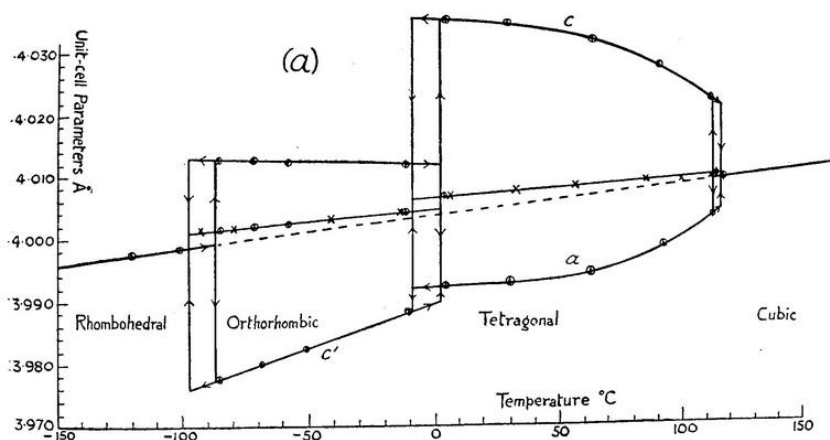


**Figure 1.5.** Temperature-dependence of lattice parameters and cube root of cell volume of  $\text{BaTiO}_3$ , from Kay and Vousden<sup>31</sup>.



### 1.4.2 Lead Titanate, $\text{PbTiO}_3$ , and Lead Zirconate-Titanate (PZT)

In the early 1950s,  $\text{PbTiO}_3$  was investigated<sup>32,33</sup> for its known ferroelectricity<sup>34</sup> and its analogy to  $\text{BaTiO}_3$ <sup>32</sup>. It was found to undergo a paraelectric-to-ferroelectric transition similar to that of  $\text{BaTiO}_3$  but at a higher temperature (490 °C) and to a more strongly tetragonal structure ( $c/a = 1.063$ <sup>33</sup>, compared with  $c/a = 1.01$  in  $\text{BaTiO}_3$ <sup>30</sup>).

Around this time, the solid solution range  $\text{PbZr}_{1-x}\text{Ti}_x\text{O}_3$  (PZT; specific compositions referred to as *PZT100x*) was also studied<sup>35,36,37</sup>. Shirane and Suzuki<sup>36</sup> identified a region in the PZT phase diagram between PZT40-PZT45 in which lay the boundary between the tetragonal structure of lead titanate and the structure of Zr-rich solutions, which they found to be rhombohedral (pure  $\text{PbZrO}_3$ , however, is orthorhombic<sup>38</sup>). Sawaguchi<sup>37</sup> found the phase boundary to lie between PZT44-PZT46, and also concluded that this boundary was “nearly parallel to the temperature axis”. This was later described as a “morphotropic” phase boundary by Jaffe *et al.*<sup>39</sup> (Figure 1.6a). A monoclinic phase bridging the rhombohedral and tetragonal phases has since been reported<sup>40</sup>, and the phase diagram modified (Figure 1.6b). Compositions in the region of the morphotropic phase boundary are known to have enhanced physical properties including higher piezoelectric coupling and dielectric constants<sup>10</sup> (Figure 1.7). The pronounced piezoelectric effect, high Curie temperature (350 °C) and near-temperature-independence of the phase boundary rendered these compositions suitable for applications over a wide range of ambient temperatures<sup>10</sup>.

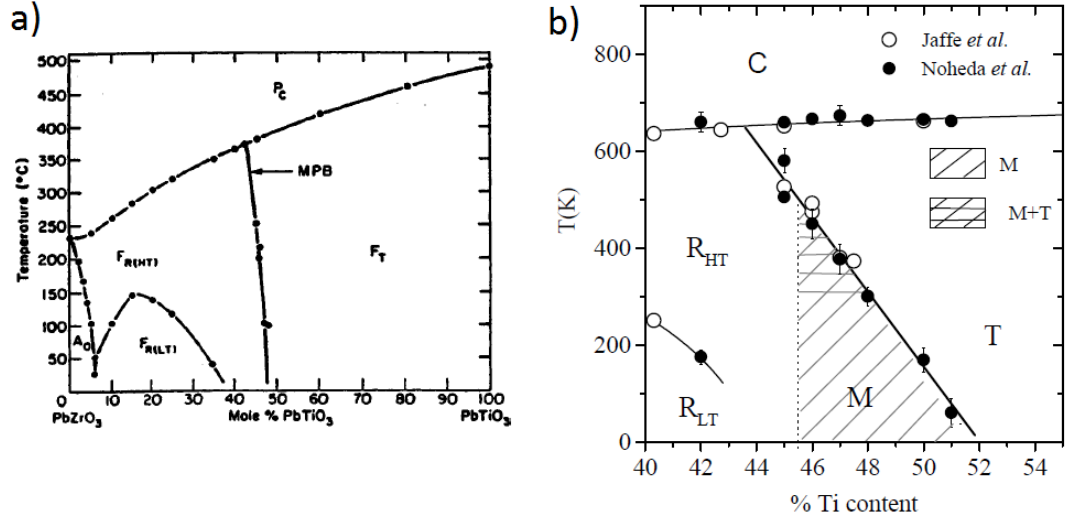


**Figure 1.6.** a) Phase diagram of PZT from Jaffe *et al.*<sup>11</sup>; b) modified phase diagram in the region of the morphotropic phase boundary, including monoclinic phase (from Noheda and Cox)<sup>41</sup>.

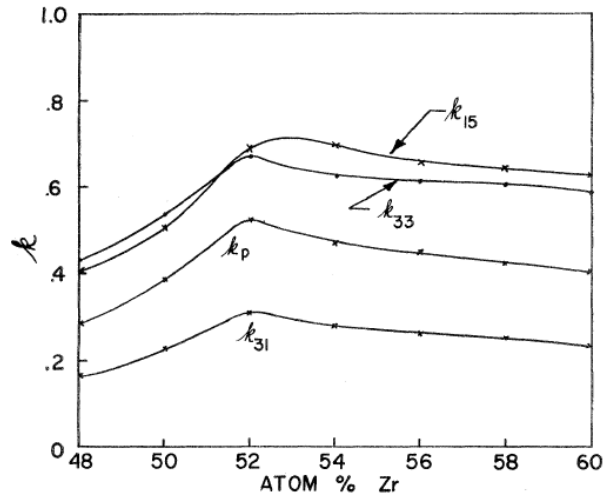


**Figure 1.7.** Piezoelectric coupling in PZT, showing peak close to the morphotropic phase boundary (from Berlincourt *et al.*<sup>10</sup>).

An explanation put forward by Guo *et al.*<sup>42</sup> and Noheda *et al.*<sup>43</sup> attributes the high piezoelectric response largely to the presence of the monoclinic phase. According to this explanation, local displacements in the rhombohedral and tetragonal phases are responsible for the observed long-range monoclinic structure. Polarisation occurs along  $\langle 111 \rangle$  directions in the rhombohedral phase, and along  $\langle 100 \rangle$  directions in the tetragonal phase. Polarisation in the monoclinic cell, however, may take a range of directions within the  $\{110\}$  planes (Figure 1.8). The rotation of the polar axis in the monoclinic plane is

accompanied by monoclinic distortion of the unit cell. These large atomic displacements, necessary to produce the high piezoelectric response, only occur in compositions close to the morphotropic phase boundary<sup>42</sup>.

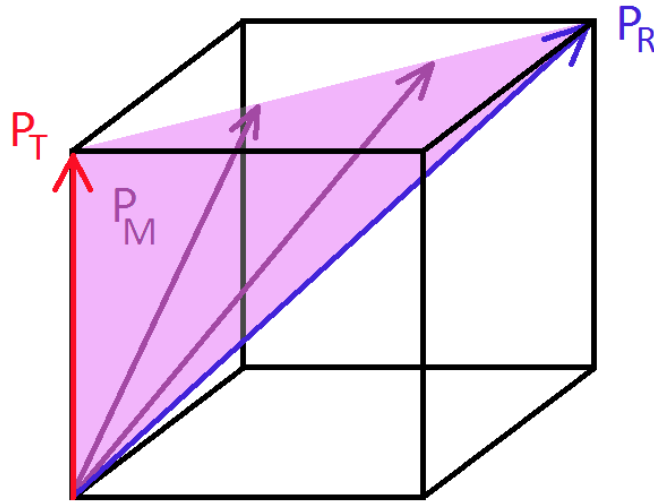


**Figure 1.8.** Polarisation directions on the rhombohedral ( $P_R$ ), tetragonal ( $P_T$ ) and monoclinic (shaded) phases. The range of possible monoclinic polarisation directions forms a ‘bridge’ between the directions  $P_R$  and  $P_T$ .

### 1.4.3 Sodium Bismuth Titanate, $\text{Na}_{0.5}\text{Bi}_{0.5}\text{TiO}_3$

In 1961, Smolenskii *et al.* reported a new ferroelectric material,  $\text{Na}_{1/2}\text{Bi}_{1/2}\text{TiO}_3$  (NBT).  $\text{Bi}^{3+}$  ions, having the same electronic configuration as  $\text{Pb}^{2+}$  ions, had been conjectured as a potential component of new perovskites featuring spontaneous polarisation<sup>44</sup>. An anomaly in the linear thermal expansion coefficient was used to assign a phase transition at 320 °C as the Curie temperature<sup>44</sup>. Zvirgzds *et al.* investigated the temperature-dependent structure and found the sequence of phase transitions on cooling to be: cubic  $Pm3m \rightarrow$  tetragonal  $P4mm$  at 520 °C;  $P4mm \rightarrow$  rhombohedral  $R3m$  at 260 °C. The latter phase transition showed a large temperature hysteresis (approximately 60 °C higher on heating)<sup>45</sup>. A similar value for the hysteresis was found by Pronin *et al.*<sup>46</sup>, who reported the transition temperature as 304 °C on heating and 243 °C on cooling. Analysis of lattice parameters in the tetragonal phase revealed the  $c/a$  ratio to be greatest in the

middle of the  $P4mm$  region, decreasing towards the phase transitions<sup>45</sup>. Vakhrushev *et al.* identified the room temperature structure as  $R3c$ <sup>47</sup>.  $R3c$  differs from  $R3m$  in that  $R3c$  includes a glide plane along the  $c$  direction. This doubles the pseudo-cubic unit cell and gives an anti-phase tilted structure with a  $\frac{1}{2}$ <sub>pc</sub><sup>48</sup> reflection.

A thorough neutron diffraction investigation by Jones and Thomas<sup>49,50</sup> found the room-temperature structure to be  $R3c$  with  $a^-a^-a^-$  tilting and parallel cation displacement along the  $[111]$  axis. The tetragonal phase was found to be  $P4bm$ , with  $a^0a^0c^+$  tilting and unequal antiparallel cation displacements along the  $[001]$  axis. The  $Ti^{4+}$  ions are displaced along the  $c$  axis, but in the opposite direction from the sodium and bismuth displacements. This produces a ferrielectric arrangement in the unit cell, giving a weakly polar tetragonal phase<sup>50</sup>. The rhombohedral and tetragonal structures were found to coexist in the temperature range 300-320 °C, giving way to a purely tetragonal structure up until 500 °C. Above 500 °C the cubic phase overlaps the tetragonal one, before the structure becomes completely cubic by 540 °C<sup>50</sup>. The cubic phase they found to be  $Pm\bar{3}m$ , showing there is no ordering of the  $Na^+$  and  $Bi^{3+}$  cations.

Work on both single crystals<sup>51</sup> and powdered ceramics<sup>52</sup> has recently indicated that the average structure of room-temperature NBT is monoclinic. By analysing the  $2\theta$  splitting of high-resolution XRD peaks, Gorfman and Thomas found the lattice symmetry to be lower than rhombohedral<sup>51</sup>. Modelling the splitting, they found the best match came from a C-centred monoclinic lattice. They predicted this to be  $Cc$  which, being a sub-group of  $R3c$ , has the required superstructure peaks. An additional superstructure peak  $\{\frac{1}{2} \frac{1}{2} \frac{1}{2}\}_{pc}$ , potential evidence of the  $Cc$  space group, was found to be a double diffraction effect, leaving the assignment of the  $Cc$  space group unproven. Aksel *et al.*<sup>52</sup> used Rietveld refinement of x-ray diffraction data to compare  $R3c$  with  $Cc$  models. A  $Cc$  structure with  $a^-a^-c^-$  tilting was found to give the best fit. They did not rule out the possibility of two  $R3c$  phases, but considered it unlikely as one of these phases refined as highly bismuth-

deficient – this was not thought to be a likely outcome of the sample preparation method used<sup>52</sup>.

Gorfman *et al.*<sup>53</sup> carried out further work on single crystal NBT, using birefringence microscopy to investigate optical properties as a function of temperature. The orientations of the optical axes present in the sample were measured, and the distribution of these used to infer the crystal symmetry. For either rhombohedral or tetragonal symmetries, a clustering of these orientations at right angles to each other would be expected, whereas monoclinic symmetry would allow a more evenly spread distribution. The observed room temperature distribution indicates monoclinic symmetry, tending towards a rhombohedral distribution as the temperature increases. An apparent rhombohedral distribution at 317 °C precedes the transition to tetragonal symmetry, which begins at 326 °C. On cooling, the tetragonal phase is present until 277 °C. However, the clear domain boundaries that would be expected for rhombohedral symmetry were not observed. Between the “quasi-rhombohedral” and tetragonal phases, the crystal was found to be optically isotropic. Characteristic of cubic symmetry, the isotropy could, alternatively, be explained by the presence of small, optically anisotropic domains. A purely tetragonal structure was observed above 340 °C, up until the Curie temperature at 556 °C. The Curie transition was found to be unaffected by thermal hysteresis.

Rao and Ranjan found evidence of a room-temperature monoclinic *Cc* phase in NBT, which undergoes a transformation to *R3c* when poled<sup>54</sup>. They suggested that the macroscopic monoclinic symmetry may comprise twinned rhombohedral nanodomains.

Dorcet *et al.*<sup>55</sup> found, using electron microscopy, evidence of an orthorhombic phase intermediate to the rhombohedral and tetragonal phases. This was seen in the form of elongated electron diffraction reflections interpreted as belonging to the space group *Pnma*, suggesting a modulated formation of orthorhombic sheets between twinned *R3c* domains. Sakata and Masuda<sup>56</sup> found the remanent polarisation to fall to zero at 200 °C.

They considered this evidence of an antiferroelectric phase, detailing the sequence of phase transitions as ferroelectric-antiferroelectric-paraelectric at elevated temperatures, with transitions at 200 °C and 320 °C. However, there is little other evidence for an antiferroelectric phase in NBT.

NBT is part of a group of materials known as ‘relaxor’ ferroelectrics. Relaxors show a broad maximum in the dielectric permittivity curve, shifting to higher temperatures as the measuring frequency is increased<sup>11</sup>. Solid solution ranges having relaxors such as  $\text{Pb}(\text{Mg}_{1/3}\text{Nb}_{2/3})\text{O}_3$ ,  $\text{Pb}(\text{Ni}_{1/3}\text{Nb}_{2/3})\text{O}_3$ , and  $\text{Pb}(\text{Fe}_{1/2}\text{Nb}_{1/2})\text{O}_3$  as an end-member with lead titanate have been found to show substantial piezoelectric effects<sup>11</sup>. Relaxor characteristics are thought to be linked to the existence of polar nano-regions within the structure<sup>57</sup>, which are known to give rise to diffuse x-ray and neutron scattering<sup>57</sup>. Evidence of polar planar defects has been found in diffuse x-ray scattering experiments on NBT<sup>58</sup>.

Ceramic NBT, when poled, has  $d_{33} \approx 70 \text{ pC N}^{-1}$ <sup>59</sup>. The depoling temperature has been found to be 210 °C, as taken from *ex situ* measurements of the direct piezoelectric coefficient, or 160 °C, as taken from *in situ* measurements of the converse piezoelectric coefficient<sup>59</sup>. Doping with small amounts of manganese ( $\leq 1$  atomic %, abbreviated as ‘MnNBT’) has been shown<sup>60,61</sup> to increase the piezoelectric coefficient and electromechanical coupling factor of single crystal NBT. This doping does not significantly change the structure, with only a slight variation in lattice parameters being reported between NBT and MnNBT<sup>60</sup>. However, a broad, extra, low- $2\theta$  peak can be seen in the x-ray diffraction pattern of MnNBT, possibly indicative of nanostructure<sup>62</sup>.

#### 1.4.4 Potassium Bismuth Titanate, $\text{K}_{0.5}\text{Bi}_{0.5}\text{TiO}_3$

1960 Smolenskii *et al.* in 1960<sup>44</sup> first synthesised  $\text{K}_{1/2}\text{Bi}_{1/2}\text{TiO}_3$  (KBT), which they identified as a ferroelectric perovskite with  $T_c \sim 380^\circ\text{C}$ . At room temperature, the structure is tetragonal  $P4mm$ , with reported lattice parameters:  $a = 3.913 \text{ \AA}$ ,  $c = 3.99 \text{ \AA}$ <sup>63</sup>;  $a = 3.936 \text{ \AA}$ ,  $c = 3.9884 \text{ \AA}$ <sup>64</sup>;  $a = 3.922 \text{ \AA}$ ,  $c = 4.006 \text{ \AA}$ <sup>65</sup>.

#### 1.4.5 Potassium Sodium Bismuth Titanate, $(\text{K}_x\text{Na}_{1-x})_{0.5}\text{Bi}_{0.5}\text{TiO}_3$

The range of solid solutions  $(\text{K}_x\text{Na}_{1-x})_{0.5}\text{Bi}_{0.5}\text{TiO}_3$  (denoted: KNBT100x) was first described by Buhrer in 1962<sup>66</sup>. Compositions in the range from the potassium-rich end-member, KBT, to KNBT20 were found to show tetragonal distortion and ferroelectricity<sup>66</sup>. A more detailed study<sup>67</sup> of the phase diagram was carried out in 1996, motivated by the observation that compositions near a morphotropic phase boundary between rhombohedral and tetragonal structures, such as that found in PZT, gave the best electromechanical properties<sup>67</sup>. In addition to rhombohedral and tetragonal regions at the sodium- and potassium-rich ends respectively, this study found a bi-phasic region at  $0.16 < x < 0.6$  (Figure 1.9). Investigation of temperature-dependent dielectric permittivity found it to go through a large maximum at approximately  $320^\circ\text{C}$  in rhombohedral compositions, and  $380^\circ\text{C}$  in tetragonal compositions. A small shoulder on the low-temperature side of the permittivity curve of NBT was attributed to an antiferroelectric phase. Of the sodium-rich materials, the composition closest to the boundary between the 'rhombohedral' and 'bi-phasic' regions ( $x = 0.16$ ) showed the highest  $d_{33}$  value,  $96 \text{ pC N}^{-1}$  compared with  $70 \text{ pC N}^{-1}$  for NBT<sup>67</sup>.

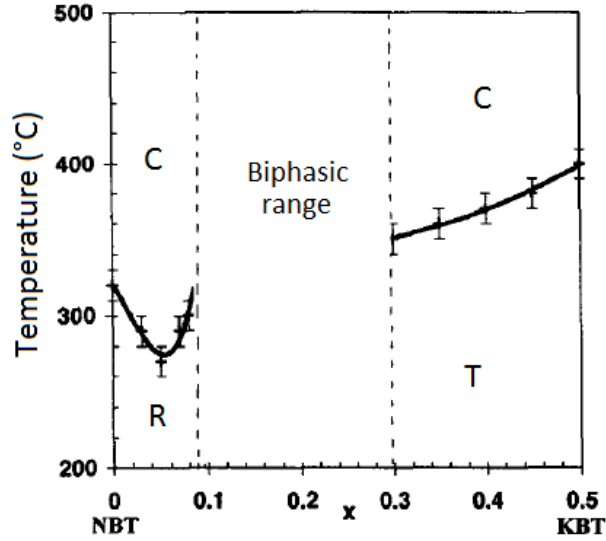


**Figure 1.9.** KNBT phase diagram (from Elkechai *et al.*<sup>67</sup>). 'C', 'R' and 'T' denote cubic, rhombohedral and tetragonal phases, respectively.

A more recent study by Otoničar *et al.*<sup>68</sup> confirmed the enhanced piezoelectric constant in the phase boundary region (Figure 1.10). However, they found the morphotropic region intermediate to rhombohedral and tetragonal regions to be considerably narrower, lying within  $0.17 < x < 0.25$  (Figure 1.11). The  $d_{33}$  maximum at  $x = 0.2$  they found to be  $134 \text{ pCn}^{-1}$ , compared with  $68 \text{ pCn}^{-1}$  for NBT<sup>68</sup>. Summarising various studies, they note that a morphotropic phase boundary has been reported in the range  $0.16 < x < 0.2$ <sup>69</sup>, and that intermediate phases have also been reported instead, including: an intermediate phase in the region  $0.5 \leq x \leq 0.8$ <sup>64</sup>; an  $R3m$  phase at  $x = 0.5$  and  $0.6$ <sup>70</sup>; a pseudocubic phase between  $x = 0.18$  and  $x = 0.4$ <sup>71</sup>. They account for this variation in reports by pointing out that different preparation methods were used in each study<sup>68</sup>.



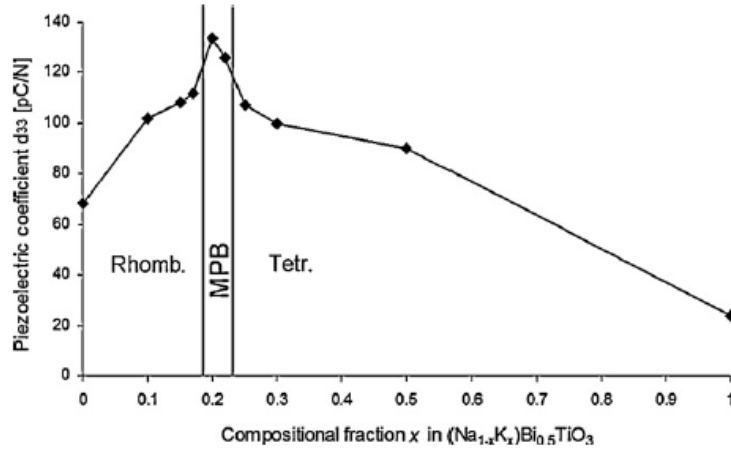


**Figure 1.10.** Piezoelectric constant  $d_{33}$  for KNBT, measured at 100 kHz at room temperature (from Otoničar *et al.* <sup>68</sup>).

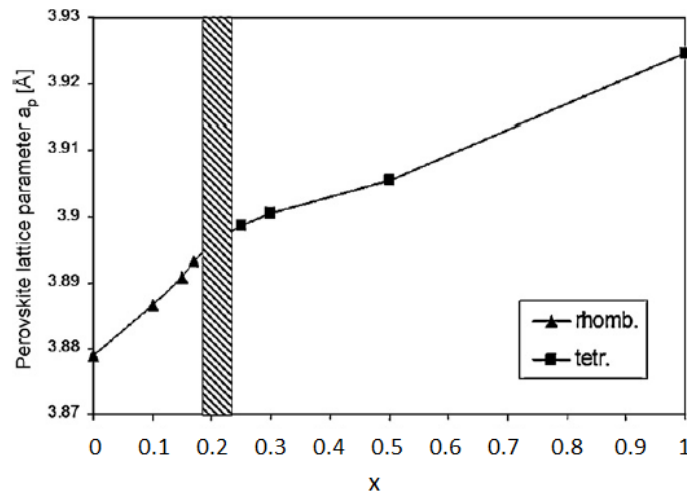


**Figure 1.11.** Unit cell parameter variation with potassium substitution in KNBT, showing rhombohedral and tetragonal regions of the composition spectrum, and intermediate morphotropic region (shaded) (from Otoničar *et al.* <sup>68</sup>).

## 1.5 Solvothermal and Hydrothermal Synthesis

Whilst conventional solid state preparation routes have traditionally been used to create highly crystalline materials, they offer little control over crystallite size and shape, and produce only those phases that are most thermodynamically stable<sup>72</sup>. Solvothermal synthesis allows crystalline materials to be produced without the need for high temperatures. The reagents are dissolved and heated in an autoclave above the boiling

point of the solvent. This method is advantageous when working with volatile elements as they cannot escape from the system, maintaining the initial stoichiometry. Solvothermal synthesis allows the production of metastable phases that cannot withstand high temperatures<sup>72</sup>. The choice of solvent<sup>73</sup> and the molar ratio of initial reactants<sup>74</sup> have been reported to affect the morphology of the resulting crystallites. Wei *et al.* produced  $\text{Ba}_{1-x}\text{Sr}_x\text{TiO}_3$  single crystals of 5-20 nm using a mixture of ethylenediamine ( $\text{NH}_2\text{CH}_2\text{CH}_2\text{NH}_2$ ) and ethanolamine ( $\text{NH}_2\text{CH}_2\text{CH}_2\text{OH}$ ) as the solvent<sup>74</sup>. By varying the ratio of Ba:Sr in the reactant, spherical, polygonal, or cuboid crystals could be produced. Yang *et al.*<sup>73</sup> used a polyethylene glycol (PEG) solvent to produce hollow, sub-micrometer-sized cubes of perovskite  $\text{CaTiO}_3$ . Introduction of water into the solvent in a ratio of 1:9 ( $\text{H}_2\text{O}$  : PEG) resulted in formation of prismatic rectangular single crystal rods, and a 1:1 ratio resulted in “butterfly-shaped” crystals. A purely hydrothermal synthesis resulted in irregular  $\text{CaTiO}_3$  crystals<sup>73</sup>.

### 1.5.1 Hydrothermal Synthesis of Perovskites

Solvothermal synthesis has been used to produce A-site substituted complex perovskites<sup>74</sup>, including hydrothermal synthesis of NBT<sup>75,76,77</sup> and KBT<sup>77,78,79</sup>. Hydrothermal synthesis of NBT has been found to result in cubic crystals of composition  $\text{Na}_{0.50}\text{Bi}_{0.45}\text{H}_{0.05}\text{TiO}_3$ , containing  $\text{OH}^-$  groups<sup>76</sup>. After heating to 1180 °C, no evidence of  $\text{OH}^-$  groups was found and the observed symmetry was rhombohedral. Thermo-gravimetric analysis (TGA) shows significant mass loss between 300 °C – 500 °C, attributed to removal of  $\text{OH}^-$  groups as  $\text{H}_2\text{O}$ . The resultant phase was found to have a shorter *c* parameter than solid state NBT, attributed to cation and oxygen deficiencies<sup>76</sup>. A broad peak in the permittivity of the heat-treated sample was observed at 300 °C – 350 °C, as observed in solid state NBT<sup>80</sup>. This was not observed in the as-prepared material<sup>76</sup>. The size of the crystals ranged between ~ 0.3 – 1 mm, and increased with higher reaction temperature.

Temperatures below 180 °C did not lead to a complete reaction<sup>76</sup>. Lencka *et al.* synthesised NBT using the starting reagents  $\text{Bi}(\text{NO}_3)_3 \cdot 5\text{H}_2\text{O}$ ,  $\text{TiO}_2$  and  $\text{NaOH}$ <sup>77</sup>. Ma *et al.* used  $\text{Bi}(\text{NO}_3)_3$ ,  $(\text{Ti}(\text{O}-i\text{-C}_3\text{H}_7)_4)$ ,  $(\text{Ti}(\text{O}-n\text{-C}_4\text{H}_9)_4)$ , and  $\text{Na}_2\text{CO}_3$ <sup>75</sup>. Kumada *et al.* used  $\text{Bi}_2\text{O}_3$ ,  $\text{TiO}_2$  (anatase) and  $\text{NaOH}$ <sup>76</sup>.

Difficulty has been reported in producing phase-pure hydrothermal KBT, with some unidentified, broad, low-intensity peaks present in XRD patterns<sup>77</sup>. The intensity of these peaks decreased with an increase in the concentration of the precursor  $\text{KOH}$ <sup>77</sup>, suggesting potassium may not be as readily taken into the structure. Tetragonal lattice parameters were found to be in good agreement with literature on solid state KBT. A decrease in  $c$  and an increase in  $a$  was observed after calcinations of the sample<sup>77</sup>. Using  $\text{KOH}$  as a mineraliser, KBT nanowires of 5x200 nm have been produced hydrothermally<sup>78</sup>, and a sol-gel-hydrothermal method has been used to produce nanowires of 4x100 nm<sup>79</sup>, and 1  $\mu\text{m}$  x 100 nm<sup>81</sup>.

The following work is a structural study into the sodium bismuth titanate–potassium bismuth titanate solid solution range. This solid solution has attracted attention for possessing a phase boundary between apparently rhombohedral and tetragonal structures at which physical properties, including piezoelectric coefficients, are maximised. However, structural studies of this system have reported wildly varying phase fields and a reliable phase diagram remains elusive. This work combines high-resolution x-ray diffraction and Rietveld refinements with materials fabricated by solid state and hydrothermal methods to obtain such a phase diagram.

## References

- <sup>1</sup> S. O. Leontsev and R. E. Eitel, *Sci. Technol. Adv. Mat.* **11**, 44302 (2010).
- <sup>2</sup> APC International, *Piezoelectric Ceramics: Principles and Applications*, 2nd Edition ed. (Mackeyville, PA, 2011).
- <sup>3</sup> D. M. Maeder, D. Damjanovic, and N. Setter, *J. Electroceram.* **13**, 385 (2004).
- <sup>4</sup> L. L. Bergeson, *Envir. Qual. Management* **18**, 79 (2008).
- <sup>5</sup> J. N. Gordon, A. Taylor, and P. N. Bennett, *Br. J. Clin. Pharm.* **53**, 451 (2002).
- <sup>6</sup> P. J. Landrigan and A. C. Todd, *West. J. Med.* **161**, 153 (1994).
- <sup>7</sup> DIRECTIVE 2002/95/EC, edited by European Parliament (Official Jour. EU. L, 2003), pp. 19.
- <sup>8</sup> P. K. Panda, *J. Mat. Sci.* **44**, 5049 (2009).
- <sup>9</sup> E. Aksel and J. L. Jones, *Sensors* **10** (3), 1935 (2010).
- <sup>10</sup> D. A. Berlincourt, C. Cmolik, and H. Jaffe, *Proc. IRE* **48**, 220 (1960).
- <sup>11</sup> B. Jaffe, W. R Cook, and H. Jaffe, *Piezoelectric ceramics*. (Academic Press, London, New York, 1971).
- <sup>12</sup> A Navrotsky, *Chem. Mater* **10**, 2787 (1998).
- <sup>13</sup> V. M. Goldschmidt, *Naturwissenschaften* **14**, 477 (1926).
- <sup>14</sup> L. G. Tejuca, J. L. G Fierro, and J. M. D. Tascon, *Structure and Reactivity of Perovskite-Type Oxides*. (Academic Press, London, 1970).
- <sup>15</sup> H. D. Megaw, *Ferroelectricity in Crystals*. (Methuen & Co. Ltd., London, 1957).
- <sup>16</sup> I. M. Reaney, E. L. Colla, and N. Setter, *Jpn. J. Appl. Phys* **33**, 3984 (1994).
- <sup>17</sup> K. M. Rabe, C. H. Ahn, and J-M. Triscone, in *Topics in Applied Physics*, edited by C. E. Ascheron and W. Skolaut (Springer, Heidelberg, 2007), Vol. 105.
- <sup>18</sup> A. M. Glazer, *Acta Cryst. B* **28**, 3384 (1972).
- <sup>19</sup> C. J. Howard and H. T Stokes, *Acta Cryst. B* **54**, 782 (1998).

- 20 H. T. Stokes, E. H. Kisi, D. M. Hatch, and C. J. Howard, *Acta Cryst. B* **58**, 934 (2002).
- 21 A. M. Glazer, *Acta Cryst A* **31**, 756 (1975).
- 22 D. Lin, K. W. Kwok, and L. W. Chan, *J. Appl. Phys.* **102**, 74113 (2007).
- 23 H. Thurnauer and J. Deaderick, USA Patent no. 2429588 (1947).
- 24 A. von Hippel, R. G. Breckenridge, F. G. Chesley, and L. Tisza, *Ind. Eng. Chem.* **38**,  
1097 (1946).
- 25 R. E. Newnham and L. E. Cross, *MRS Bull* **30**, 845 (2005).
- 26 A. von Hippel, *Rev. Modern Phys.* **22**, 221 (1950).
- 27 F. Jona and G. Shirane, *Ferroelectric Crystals*. (Pergamon Press, Oxford, 1962),  
p.402.
- 28 J. Hablützel, *Helv. phys. Acta* **12** (6), 489 (1939).
- 29 J. C. Burfoot, *Ferroelectrics: an Introduction to the Physical Principles*. (Butler &  
Tanner Ltd., London, 1967), p.261.
- 30 A. R. West, *Basic Solid State Chemistry*, Second Edition ed. (John Wiley & Sons, Ltd.,  
Chichester, 1999), p.479.
- 31 H. F. Kay and P. Vousden, *Phil. Mag. Series 7* **40** (309), 1019 (1949).
- 32 H. H. Rogers, Technical Report - Massachusetts Inst. Tech. Lab. Insulation Res.  
(1952).
- 33 G. Shirane and S. Hoshino, *J. Phys. Soc. Jap.* **6**, 265 (1950).
- 34 S. Roberts, *J. Am. Ceram. Soc.* **33**, 63 (1950).
- 35 G. Shirane and A. Takeda, *J. Phys. Soc. Jap.* **7**, 5 (1952).
- 36 G. Shirane and K. Suzuki, *J. Phys, Soc. Jap.* **7**, 333 (1952).
- 37 E. Sawaguchi, *J. Phys. Soc. Jap.* **8**, 615 (1953).
- 38 E. Sawaguchi, H. Maniwa, and S. Hoshino, *Phys. Rev.* **83**, 1078 (1951).
- 39 B. Jaffe, R. S. Roth, and S. Marzullo, *J. Res. Nat. Bur. Stds.* **55**, 239 (1955).

- 40 B. Noheda, D. E. Cox, G. Shirane, J. A. Gonzalo, L. E. Cross, and S. E. Park, Appl.  
Phys. Lett. **74**, 2059 (1999).
- 41 B. Noheda and D. E. Cox, Phase Transitions **79**, 5 (2006).
- 42 R. Guo, L. E. Cross, S. E. Park, B. Noheda, D. E. Cox, and G. Shirane, Phys. Rev. Lett.  
**84**, 5423 (2000).
- 43 B. Noheda, J. A. Gonzalo, L. E. Cross, R. Guo, S.-E. Park, D. E. Cox, and G. Shirane,  
Phys. Rev. B **61**, 8687 (2000).
- 44 G. A. Smolenskii, V. A. Isupov, A. I. Agranovskaya, and N. N. Krainik, Soviet Physics -  
Solid State **2**, 2651 (1961).
- 45 J. A. Zvirgzds, P. P. Kapostins, J. V. Zvirgzde, and T. V. Kruzina, Ferroelectrics **40**, 75  
(1982).
- 46 I. P. Pronin, P. P. Syrnikov, V. A. Isupov, V. M. Egorov, and N. V. Zaitseva,  
Ferroelectrics **25**, 395 (1980).
- 47 S. B. Vakhrushev, B. G. Ivanitskii, B. E. Kvyatkovskii, A. N. Maistrenko, N. M.  
Malysheva, and N. N. Parfenova, Sov. Phys. Solid State **25**, 1504 (1983).
- 48 P. A. Thomas, S. Trujillo, M. Boudard, S. Gorfman, and J. Kreisel, Solid State Sci. **12**,  
311 (2010).
- 49 G. O. Jones and P. A. Thomas, Acta Cryst. B **56**, 426 (2000).
- 50 G. O. Jones and P. A. Thomas, Acta Cryst. B **58**, 168 (2002).
- 51 S. Gorfman and P. A. Thomas, J. Appl. Cryst. **43**, 1409 (2010).
- 52 E. Aksel, J. S. Forrester, J. L. Jones, P. A. Thomas, K. Page, and M. R. Suchomel, Appl.  
Phys. Lett. (2011), Vol. 98.
- 53 S. Gorfman, A. M. Glazer, Y. Noguchi, M. Miyayama, H. Luo, and P. A. Thomas, J.  
Appl. Cryst. **45**, 444 (2012).
- 54 B. N. Rao and R. Ranjan, Phys. Rev. B **86**, 4103 (2012).
- 55 V. Dorcet, G. Trolliard, and P. Boullay, Chem. Mater. **20**, 5061 (2008).

- 56 K. Sakata and Y. Masuda, *Ferroelectrics* **7**, 347 (1974).
- 57 M. Pasciak, T. R. Welberry, J. Kulda, M. Kempa, and J. Hlinka, *Phys. Rev. B.* **85** 4109 (2012).
- 58 J. Kreisel, P. Bouvier, B. Dkhil, P. A. Thomas, A. M. Glazer, T. R. Welberry, B. Chaabane, and M. Mezouar, *Phys. Rev. B* **68**, 14113 (2003).
- 59 M. Davies, E. Aksel, and J. L. Jones, *J. Am. Ceram. Soc. (Blackwell Publishing Inc., 2011), Vol. 94, pp. 1316.*
- 60 W. W. Ge, H. Liu, X. Y. Zhao, W. Z. Zhong, X. M. Pan, T. H. He, D. Lin, H. Q. Xu, X. P. Jiang, and H. S. Luo, *J. Alloys Comp.* **462**, 256 (2008).
- 61 H. Liu, W. Ge, X. Jiang, X. Zhao, and H. Luo, *Mater. Lett.* **62**, 2721 (2008).
- 62 C.-S. Tu, S.-H. Huang, C.-S. Ku, H.-Y. Lee, R. R. Chien, V. H. Schmidt, and H. Luo, *Appl. Phys. Lett.* **96**, 062903 (2010).
- 63 V. A. Isupov, *Ferroelectrics* **315**, 123 (2005).
- 64 J. Kreisel, A. M. Glazer, G. Jones, P. A. Thomas, L. Abello, and G. Lucazeau, *J. Phys. - Condens. Matt.* **12**, 3267 (2000).
- 65 S. M. Emel'yanov, I. P. Raevskii, and F. I. Savenko, *Fiz. Tverd. Tela.* **29**, 2511 (1987).
- 66 C. F. Buhrer, *J. Chem. Phys.* **36**, 798 (1962).
- 67 O. Elkechai, M. Manier, and J. P. Mercurio, *Phys. Status Solidi A* **157**, 499 (1996).
- 68 M. Otonicar, S. D. Skapin, M. Spreitzer, and D. Suvorov, *J. Am. Ceram. Soc.* **30**, 971 (2010).
- 69 A. Sasaki, T. Chiba, Y. Mamiya, and E. Otsuki, *Jpn. J. Appl. Phys.* **38**, 5564 (1999).
- 70 G. O. Jones, J. Kreisel, and P. A. Thomas, *Powder Diffr.* **17**, 301 (2002).
- 71 I. P. Pronin, N. N. Parfenova, N. V. Zaitseva, V. A. Isupov, and G. A. Smolenskii, *Sov. Phys. Solid State* **24**, 1060 (1982).
- 72 D. R. Modeshia and R. I. Walton, *Chem. Soc. Rev.* **39**, 4303 (2010).

- <sup>73</sup> X. Yang, I. D. Williams, J. Chen, J. Wang, H. Xu, H. Konishi, Y. Pan, C. Liang, and M. Wu, *J. Mat. Chem.* **18**, 3543 (2008).
- <sup>74</sup> X. Wei, G. Xu, Z. Ren, Y. Wang, G. Shen, and G. Han, *J. Cryst. Growth* **310**, 4132 (2008).
- <sup>75</sup> Y. J. Ma, J. H. Cho, Y. H. Lee, and B. I. Kim, *Mat. Chem. & Phys.* **98**, 5 (2006).
- <sup>76</sup> N. Kumada, Y. Morozumi, Y. Yonesaki, T. Takei, N. Kinomura, and T. Hayashi, *J. Ceram. Soc. Jap.* **116**, 1238 (2008).
- <sup>77</sup> M. M. Lencka, M. Oledzka, and R. E. Riman, *Chem. Mater.* **12**, 1323 (2000).
- <sup>78</sup> X.-P. Jiang, M. Lin, N. Tu, C. Chen, and Y.-M. Li, *Mat. Sci. Eng. B* **175**, 90 (2010).
- <sup>79</sup> Y.-D. Hou, L. Hou, S.-Y. Huang, M.-K. Zhu, H. Wang, and H. Yan, *Sol. Stat. Comm.* **137**, 658 (2006).
- <sup>80</sup> J. Suchanicz, K. Roleder, J. Kwapulinski, and I. Jankowska-Sumara, *Phase Trans.* **57** (4), 173 (1996).
- <sup>81</sup> L. Hou, Y.-D. Hou, X.-M. Song, M.-K. Zhu, H. Wang, and H. Yan, *Mat. Res. Bull.* **41**, 1330 (2006).



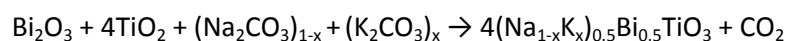
## Chapter 2

### Experimental Methods

#### 2.1 Sample Preparation

##### 2.1.1 Solid State Synthesis

Polycrystalline compounds were prepared from starting reagents Na<sub>2</sub>CO<sub>3</sub> (99.9%), Bi<sub>2</sub>O<sub>3</sub> (99.975%), TiO<sub>2</sub> (99.6%) and K<sub>2</sub>CO<sub>3</sub> (99.6%) (Alfa Aesar). These were reacted in stoichiometric quantities according to the formula:



Starting materials were mixed by ball-milling in ethanol for 24 hours with 5 mm zirconia grinding balls. Samples were then oven-dried at 70 °C until all ethanol evaporated, ground with an agate pestle and mortar to improve homogeneity and calcined at 800 °C for 6 hours to form the perovskite phase. Following phase identification by powder x-ray diffraction (XRD), the re-ground samples were then heat-treated at temperatures in the range 1000-1110 °C to further increase homogeneity. Calcination and heat-treatment were carried out in air in platinum crucibles with either platinum or alumina lids. Heating and cooling rates were 180 °C h<sup>-1</sup> and 120 °C h<sup>-1</sup> respectively.

A manganese-doped NBT sample was made using the above method of NBT synthesis with the addition of 1 mol % manganese in the form MnO<sub>2</sub> (98%) (Alfa Aesar).

##### 2.1.2 Hydrothermal Synthesis

Hydrothermal synthesis was carried out in a Teflon-lined stainless-steel autoclave using a 1:4 molar ratio of Bi<sub>2</sub>O<sub>3</sub> (99.9%, Janssen Chimica): TiO<sub>2</sub> (>98%, Janssen Chimica). Typically 1-1.3 mmol solid Bi<sub>2</sub>O<sub>3</sub> was added to an autoclave. TiO<sub>2</sub> was then added in a quantity appropriate to maintain the requisite ratio. 10 ml 10 M NaOH (aq) solution was

added and the suspension stirred for 3 hours. The autoclave was then sealed and placed in a preheated oven at 240 °C for 120 hours. Once cooled, the precipitate was separated using filter paper and washed in distilled water to remove any excess hydroxide before oven-drying at 80 °C for 12 hours. Following initial characterisation using XRD to identify the phase formed, the sample was heat-treated in air in a closed platinum crucible at 950 °C for 6 hours to increase crystallite size (as indicated by sharper peaks in the diffraction pattern). Heating and cooling rates were 180 °C h<sup>-1</sup> and 120 °C h<sup>-1</sup> respectively.

KBT was produced using the above method, but with 10 ml 10 M KOH (aq) in place of NaOH solution. KNBT was produced by mixing the NaOH and KOH solutions in stoichiometric quantities; the ratio of K:Na in the final material was assumed to be the same as the ratio in the aqueous solution.

## 2.2 Thermal Analysis

Thermal analysis was performed on a Mettler Toledo TGA/DSC 1 STARe System with 70 µl Pt sample holders, using a heating rate of 10 °C min<sup>-1</sup>. The reference material was an identical, empty sample holder.

In TGA (thermogravimetric analysis) the mass of the sample is recorded whilst it is heated at a constant rate<sup>1</sup>. Decomposition or re-crystallisation can be monitored as a function of temperature by observing mass loss or gain over a temperature range.

In differential scanning calorimetry (DSC), the behaviour of the sample is compared with that of an inert reference material<sup>1</sup>. The sample and reference are maintained at the same temperature during heating. If the sample undergoes a thermal event, such as decomposition or phase change, the heat inputs required by the reference and sample in order to maintain an equal temperature in both will differ. In the case of an endothermic event, the sample will require a greater heat input; during an exothermic event, the

reference will require the greater input. The quantity measured is the difference between the heat inputs to the sample and reference.

## 2.3 X-ray Diffraction

The primary technique used in this study was XRD from powder samples. XRD scans were performed using a Panalytical X'Pert Pro multipurpose XRPD system with a PIXcel detector and germanium curved Johansson monochromator, giving Cu-K $\alpha_1$  radiation. For scans intended for structural refinements, minimum  $2\theta$  values were typically  $10^\circ$ - $20^\circ$ , maximum  $2\theta$  values were typically  $90^\circ$ - $120^\circ$ . Scan time was 10-20 hours, using a step size of  $0.06^\circ$   $2\theta$ . An Anton Paar HTK1200N furnace was used in the collection of variable-temperature data. Heating and cooling rates were  $3^\circ\text{C min}^{-1}$  or  $5^\circ\text{C min}^{-1}$ . Prior to collecting data at a given temperature, the sample stage was held at that temperature for 10 minutes to ensure even temperature throughout the sample.

A schematic diagram of the Bragg-Brentano geometry of the x-ray diffractometer is shown in Figure 2.1. During a powder scan measurements are taken at successive steps in  $2\theta$ , each at position  $2\theta_i$ . The measurement at each step,  $y_i$ , is the number of counts recorded in a preset time interval.

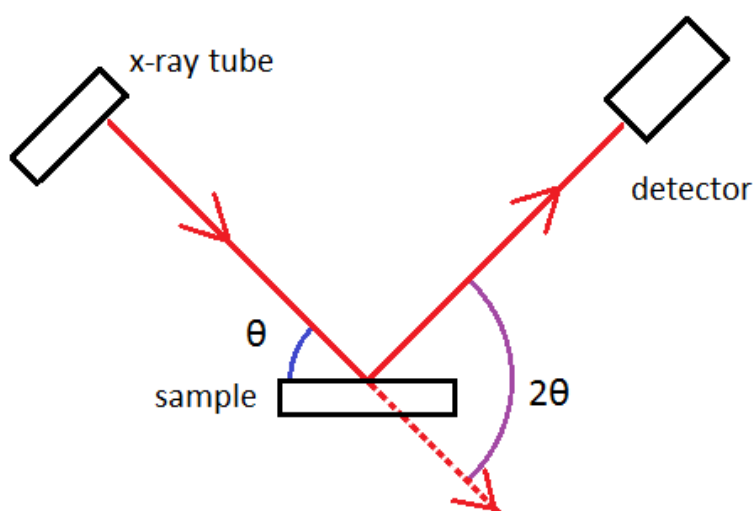


**Figure 2.1.** Schematic diagram of Bragg-Brentano geometry.

## 2.4 Rietveld Refinement

### 2.4.1 Overview

The intensity,  $y_i$ , is recorded at incremental steps of  $\sim 0.06^\circ 2\theta$ ,  $i$ , in the powder pattern. Rietveld refinement uses a least squares procedure to fit a calculated pattern to the observed  $y_i$  values, minimising the residual,  $S_y$  (ref. <sup>2</sup>):

$$S_y = \sum_i w_i (y_i - y_{ci})^2 \quad 2.1$$

where:  $y_i$  is the observed intensity at the  $i^{\text{th}}$  step;  $w_i$  is a statistical weight assigned to  $y_i$ ;  $w_i = 1/y_i$ ;  $y_{ci}$  is the calculated intensity at the  $i^{\text{th}}$  step.

The Rietveld method<sup>3</sup> is used for refining patterns containing overlapping Bragg reflections, each of which has: peak height; peak position; breadth; tails, which decay gradually with distance from peak position; and an integrated area, which is proportional to the Bragg intensity,  $I_K$ .  $I_K$  is proportional to the square of the absolute value of the structure factor,  $|F_K|^2$ . A close starting model is needed as the overlapped reflections are not resolved in advance of refinement. The calculated intensity is determined from the  $|F_K|^2$  values calculated from the structural model by summing calculated contributions from overlapping Bragg peaks and the background:

$$y_{ci} = s \sum_K L_K |F_K|^2 \phi(2\theta_i - 2\theta_K) P_K A + y_{bi} \quad 2.2$$

where:  $s$  is the scale factor;  $K$  represents Miller indices,  $h,k,l$ ;  $L_K$  contains the Lorentz, polarisation and multiplicity factors;  $\phi(2\theta_i - 2\theta_K)$  is the reflection profile function;  $P_K$  is the preferred orientation function;  $A$  is an absorption factor;  $F_K$  is the structure factor for the  $K^{\text{th}}$  Bragg reflection;  $y_{bi}$  is the background intensity at the  $i^{\text{th}}$  step.

The model parameters are refined to minimise  $S_y$ , leading to a set of normal equations involving derivatives of  $y_{ci}$  with respect to each parameter. The normal equations are soluble by inversion of the normal matrix with elements  $M_{jk}$ :

$$M_{jk} = -\sum_i 2w_i \left[ (y_i - y_{ci}) \frac{\partial^2 y_{ci}}{\partial x_j \partial x_k} - \left( \frac{\partial y_{ci}}{\partial x_j} \right) \left( \frac{\partial y_{ci}}{\partial x_k} \right) \right] \quad 2.3$$

where the parameters  $x_j$  and  $x_k$  are the adjustable parameters. The matrix elements can be approximated by deletion of the term  $(y_i - y_{ci}) \frac{\partial^2 y_{ci}}{\partial x_j \partial x_k}$ . The elements  $M_{jk}$  form an  $m$  by  $m$  matrix, where  $m$  is the number of parameters being refined. The solution is found using an iterative procedure in which the shifts,  $\Delta x_k$ , are given by:

$$\Delta x_k = \sum M_{jk}^{-1} \frac{\partial S_y}{\partial x_k}. \quad 2.4$$

The shifts are applied to the initial parameters, and the process repeated to minimise  $S_y$ . Because the relationships between parameters and intensities are non-linear, a close starting model is required to avoid false minima.

### 2.4.2 Refinable Parameters

Parameters that may be refined include those describing atomic positions and thermal displacement, background, lattice, instrument geometry, specimen displacement, and sample-related peak-broadening, such as crystallite size and strain.

The background intensity at the  $i^{\text{th}}$  step,  $y_{bi}$ , is obtained from a refinable background function; in TOPAS-Academic<sup>4</sup> this is a Chebyshev polynomial with the number of coefficients specified by the user.

The Bragg reflection profiles are related to the diffraction angle  $\theta$ , and are described by  $\phi$ , which approximates both instrumental (e.g. profile asymmetry) and sample (e.g. crystallite size, strain) effects. The reflection profile used in this study was a modified Thompson-Cox-Hastings pseudo-Voigt, TCHZ. This is a mixture of Gaussian and Lorentzian peak shape functions, the proportions of each described by the parameter  $\eta$  (Table 2.1).

Peak shape function	Definition
Gaussian	$G(x) = \left( \frac{2\sqrt{\frac{\ln 2}{\pi}}}{\Gamma_G} \right) e^{-\frac{4 \ln 2 x^2}{\Gamma_G^2}}$
Lorentzian	$L(x) = \frac{2/\pi\Gamma_L}{\left( 1 + 4x^2/\Gamma_L^2 \right)}$
TCHZ	$F(x) = \eta L(x) + (1 - \eta)G(x)$

**Table 2.1.** Definitions of Gaussian, Lorentzian and TCHZ peak shapes.  $x$  is  $(\theta_i - \theta_k)$ ;  $\Gamma_G$  and  $\Gamma_L$  are the FWHM of the Gaussian and Lorentzian peak shapes, given by:  $\Gamma_G = (U \tan^2\theta + V \tan\theta + W + Z/\cos^2\theta)^{1/2}$  and  $\Gamma_L = X \tan\theta + Y/\cos\theta$ .

The parameter  $\eta$  is given by  $\eta = 1.36603q - 0.47719q^2 + 0.1116q^3$ , where  $q = \Gamma_L/\Gamma$  and  $\Gamma$  is the FWHM of the TCHZ peak shape:  $\Gamma = (\Gamma_G^5 + A\Gamma_G^4\Gamma_L + B\Gamma_G^3\Gamma_L^2 + C\Gamma_G^2\Gamma_L^3 + D\Gamma_G\Gamma_L^4 + \Gamma_L^5)^{0.2}$ , where:  $A = 2.69269$ ;  $B = 2.42843$ ;  $C = 4.47163$ ;  $D = 0.07842$ .  $U, V, W, X, Y, Z$  are refinable parameters.

The structure factor is given by:

$$F_K = \sum_j N_j f_j e^{[2\pi i(hx_j + ky_j + lz_j)]} e^{-M_j} \quad 2.5$$

where:  $N_j$  is the site occupancy divided by the site multiplicity for the  $j^{\text{th}}$  atom site;  $f_j$  is the x-ray scattering factor for the  $j^{\text{th}}$  atom;  $h, k, l$  are Miller indices;  $(x_j, y_j, z_j)$  is the position of the  $j^{\text{th}}$  atom ;

$$M_j = 8\pi^2 \overline{u_s^2} \sin^2 \left( \frac{\theta}{\lambda^2} \right) \quad 2.6$$

$\overline{u_s^2}$  is the root-mean-square displacement of the  $j$ th atom parallel to the diffraction vector.

This factor accounts for thermal displacement, and can be modelled as isotropic or anisotropic. In the case of isotropic thermal displacement, a single parameter describes the radius of a sphere, with units of  $B_j$ , where

$$B_j = 8\pi^2 \overline{u_s^2}. \quad 2.7$$

Anisotropic thermal displacement may be modelled by six parameters defining an ellipsoid, which can be represented by the symmetric tensor

$$\mathbf{u} = \begin{bmatrix} u_{11} & u_{12} & u_{13} \\ u_{12} & u_{22} & u_{23} \\ u_{13} & u_{23} & u_{33} \end{bmatrix}. \quad 2.8$$

### 2.4.3 Criteria of Fit

In addition to a visual inspection of the fit, various criteria are used to assist one in judging the quality of a refinement. These ‘*R*-factors’ are summarised in Table 2.2<sup>4</sup>.

Criteria of fit	Definition	
<i>R</i> -pattern, $R_p$	$R_p = \sqrt{\frac{\sum  y_i - y_{ci} }{\sum y_i}}$	$R'_p = \sqrt{\frac{\sum  y_i - y_{ci} }{\sum  y_i - bkg_i }}$
<i>R</i> -weighted pattern, $R_{wp}$	$R_{wp} = \sqrt{\frac{\sum w_i (y_i - y_{ci})^2}{\sum w_i y_i^2}}$	$R'_{wp} = \sqrt{\frac{\sum w_i (y_i - y_{ci})^2}{\sum w_i (y_i - y_{bi})^2}}$
<i>R</i> -expected, $R_{exp}$	$R_{exp} = \sqrt{\frac{M - m}{\sum w_i y_i^2}}$	$R'_{exp} = \sqrt{\frac{M - m}{\sum w_i (y_i - y_{bi})^2}}$
Goodness of fit, $\chi^2$	$\chi^2 = \frac{R_{wp}}{R_{exp}} = \sqrt{\frac{\sum w_i (y_i - y_{ci})^2}{M - m}}$	
<i>R</i> -Bragg	$R_B = \frac{\sum  I_k - I_{ck} }{\sum I_k}$	

**Table 2.2.** Goodness-of-fit parameters for Rietveld refinements, as used by TOPAS-Academic<sup>4</sup>. *Bkg<sub>i</sub>* = background intensity at the *i*<sup>th</sup> step, *m* = number of refinable parameters, *M* = number of step in the pattern, *I<sub>ck</sub>* = calculated intensity of *k*<sup>th</sup> Bragg reflection.

The *R*-expected value gives an idea of how well the data could, in theory, be modelled, based on the number of parameters and the number of steps in the pattern. *R*-pattern and *R*-weighted pattern are based on summing the difference between the

observed and calculated data at each step in the pattern; in the case of  $R_{wp}$ , the numerator is the residual being minimised in the least squares procedure.  $R_{wp}$  is weighted according to the observed intensity of each step, so that a greater absolute difference between observed and calculated intensities is allowed where the observed intensity is high. The goodness of fit is defined as the ratio of  $R_{wp}$  and  $R_{exp}$ ; a value of  $\chi^2 = 1$  would describe a perfect fit. The  $R$ -Bragg value is concerned only with how well the Bragg peaks have been modelled, and can be useful in fitting patterns that contain peaks not belonging to the phase(s) being modelled.

#### **2.4.4. Multiphase Refinement**

It is possible to use Rietveld refinement to model more than one phase in a data set. In this study, two close starting models were obtained by carrying out single-phase refinements using both phases individually, then carrying out a two-phase refinement with both models combined. Lattice parameters and atomic positions were fixed whilst the background and peak shapes were refined. Lattice parameters were then refined. Before allowing these to refine freely, it was sometimes necessary to adjust them manually, using the graphical output to match the calculated peak positions to the multiplet peaks seen in the data. Atomic positions were then refined. Isotropic thermal displacement parameters were initially fixed at  $1.5 \text{ \AA}^2$ . After refining all other parameters, thermal displacements were refined for the A-site, then the B-site. If the thermal displacement parameters contributed reasonably to the model – that is to say, offered visual or statistical improvement in the fit whilst converging to a sensible (non-negative) value – then they were retained in the model. It was not possible to refine anisotropic thermal displacement parameters through multiphase refinements.



## References

- <sup>1</sup> A. R. West, *Basic Solid State Chemistry*, Second Edition ed. (John Wiley & Sons, Ltd., Chichester, 1999), p.479.
- <sup>2</sup> R. A. Young, *The Rietveld Method*, *IUCr Monographs on Crystallography* (Oxford University Press, United States, 1995), p. 298.
- <sup>3</sup> H. M. Rietveld, *J. Appl. Cryst.* **2**, 65 (1968).
- <sup>4</sup> A. A. Coelho, TOPAS-Academic (<http://www.topas-academic.net/>, Brisbane, 2007).

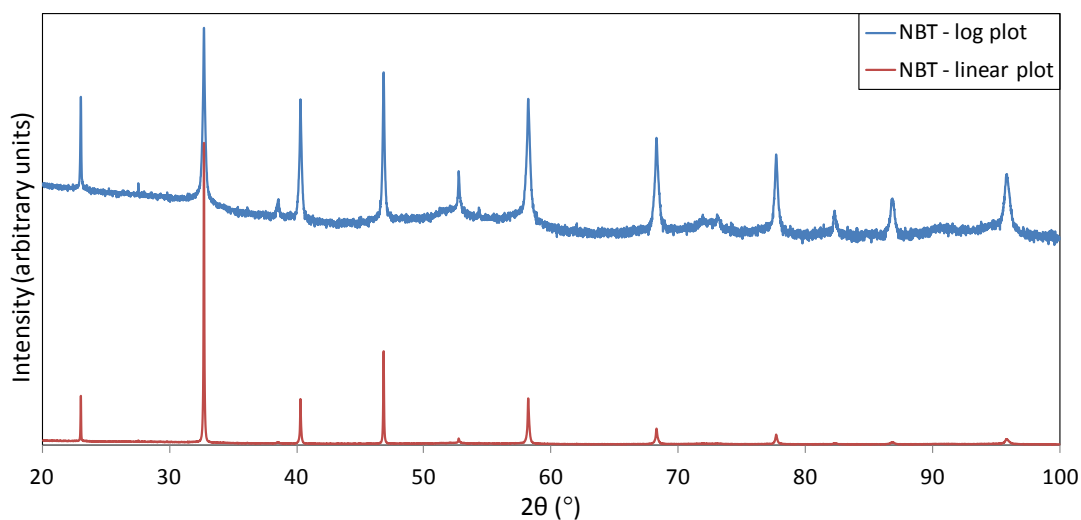
## Chapter 3

### Solid State KNBT X-Ray Diffraction Study

#### 3.1 Room-Temperature Study of NBT

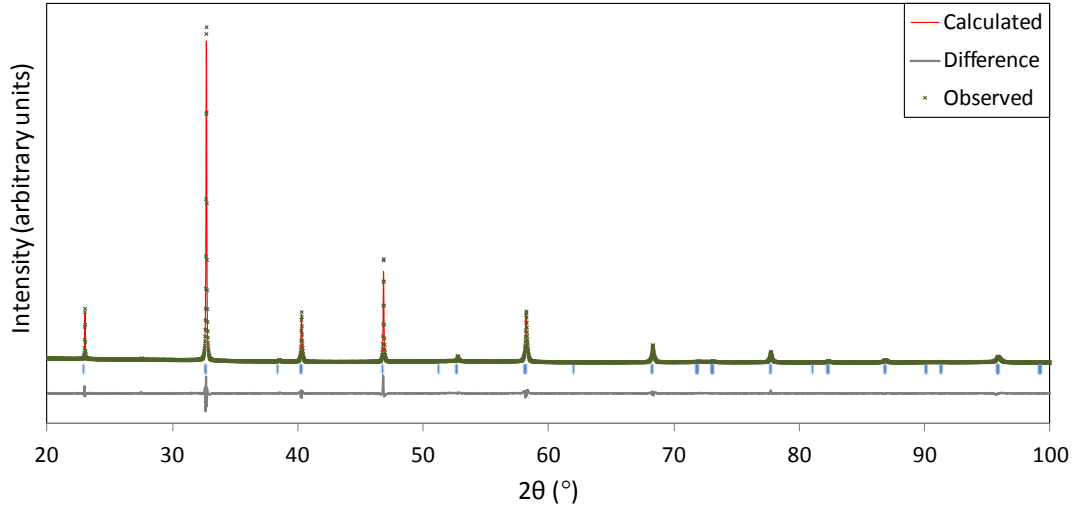
##### 3.1.1 Pure NBT

Figure 3.1 shows the XRD pattern from NBT produced via solid state reaction at 800 °C, followed by heat treatment at 1100°C. Visually, the data appear similar to those of a cubic pattern. This is best illustrated by the linear plot, demonstrating an absence of peak splitting. The presence of a superstructure peak at 38.5 °2 $\theta$ , associated with antiphase tilting of oxygen octahedra, shows the structure is not cubic. This peak can be most easily seen in the logarithmic plot, which also shows the fluctuating background, indicating disorder in the sample.



**Figure 3.1.** Room temperature XRD data from solid state synthesised NBT powder, shown on both linear and logarithmic scales.

A Rietveld refinement was carried out using an *R3c* model as this has historically been recognised as the structure of NBT<sup>1</sup> (Figure 3.2).



**Figure 3.2.** Plot showing fit, XRD data and difference plot for R3c Rietveld refinement of solid state NBT (room temperature). Tick marks indicate positions of peaks as determined by refinement.

The combination of Cu  $K\alpha_1$  radiation and a long scan time has produced data of very high quality. This has enabled a very close fit between model and data to be obtained by Rietveld refinement. The match between the model and data is systematically poorest in the centres of the peaks, with a calculated intensity below that of the observed peak maximum (Figure 3.3). Additionally, the calculated peak is narrower than the observed peak at the base, and slightly wider nearer the centre of the peak, whilst the FWHM values are approximately equivalent. These subtle discrepancies of peak shape fitting may be due to microstructural elements such as anisotropic strain or crystallographic defects. However, analysis of microstructure is beyond the scope of this thesis, and the fitting is adequate for the ensuing structural investigation. Splitting of the  $\{110\}_{pc}$  peak (Figure 3.3) is not clearly visible, indicating planar spacings of the different planes are very similar in magnitude. Peak broadness, owing to both sample and machine effects, does not allow peaks with this separation to be clearly resolved.

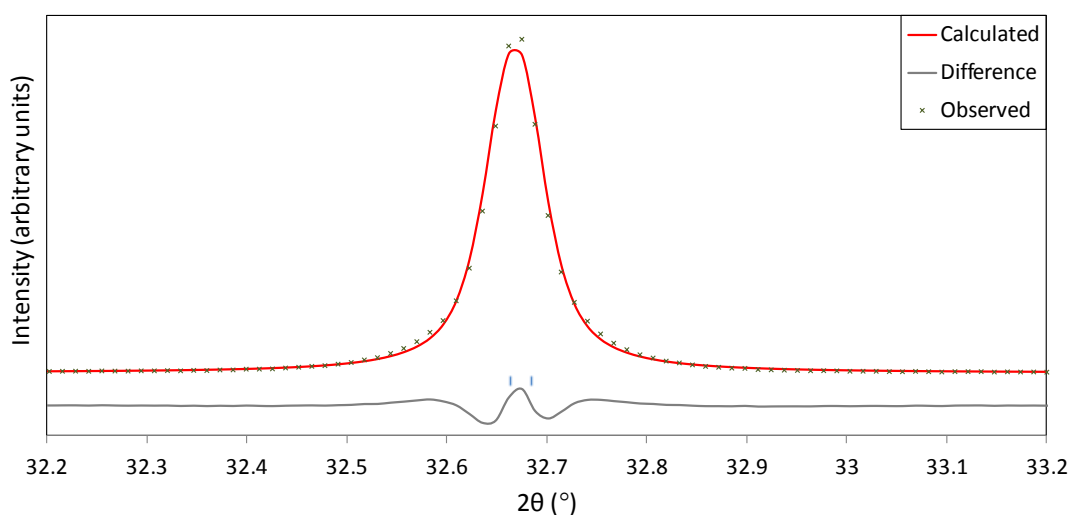


**Figure 3.3.** Section of refinement from Figure 3.2 showing  $\{110\}_{pc}$  XRD peak and mismatch between XRD data and model.

A refinement was also carried out using a  $Cc$  model (Figure 3.4), prompted by recent studies suggesting this symmetry for  $NBT^{2, 3}$ . Detail of the most intense peak is shown in Figure 3.5. It can be seen from Figures 3.4 and 3.5 that this model does not offer a visible improvement in the fit. This may indicate that the limitations of the original fit are not caused by the choice of space group.

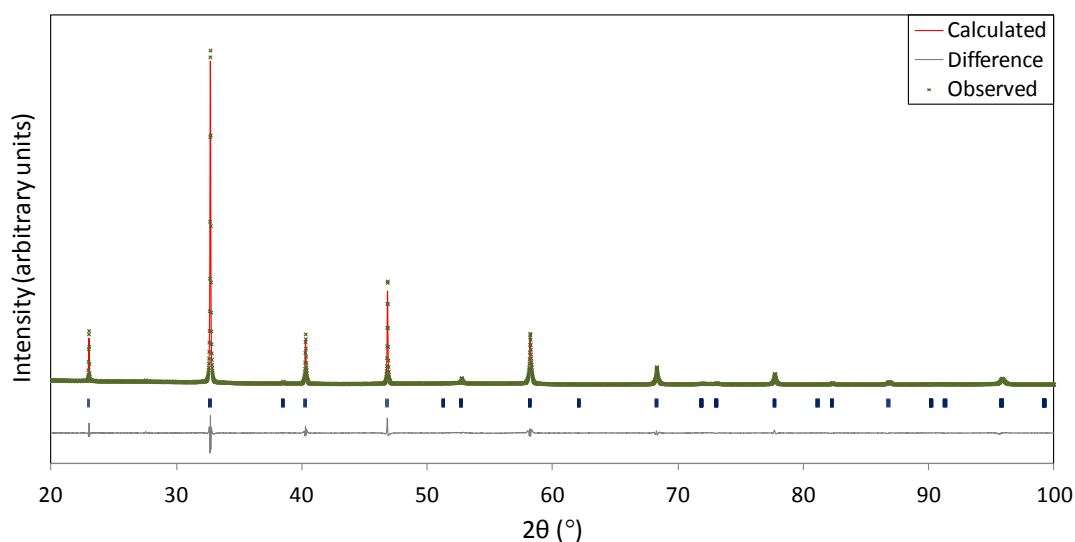


**Figure 3.4.** Plot showing fit, data and difference plot for  $Cc$  Rietveld refinement of solid state NBT (room temperature). Tick marks indicate positions of peaks as determined by refinement.

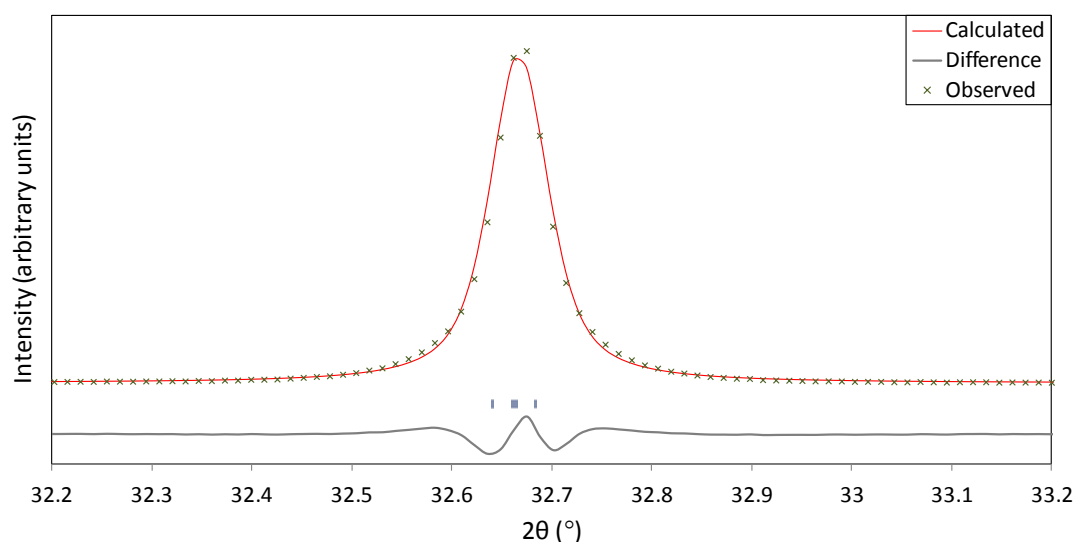


**Figure 3.5.** Section of refinement from Figure 3.4 showing  $\{110\}_{pc}$  peak and mismatch between data and model.

Table 3.1 shows values produced by *R3c* and *Cc* refinements. It can be seen from Table 3.1, as it can from Figures 3.1-3.5, that the quality of the fit to the data is similar for both models. It can also be seen that cation positions and anisotropic displacement parameters can generally be refined to a greater level of accuracy using the *R3c* model.

In order that the refinements converged sensibly it was necessary to link the sodium and bismuth positions together. In addition, it was not possible to refine anisotropic thermal displacement parameters for any atoms other than sodium and bismuth. In fitting the pattern, no fewer than nineteen parameters were needed to model the background. Such diffuse scattering has been previously observed in NBT<sup>4,5</sup>, and has been suggested to be the result of local structure different from the long-range order<sup>4</sup>.

Crystal system		Rhombohedral	Monoclinic
Space group		$R\bar{3}c$	$Cc$
Tilt system		$a^-a^-a^-$	$a^-a^-c^-$
$a$ (Å)		5.4963(1)	9.5191(6)
$b$ (Å)		-	5.4969(6)
$c$ (Å)		13.4744(5)	5.4972(6)
$\alpha, \beta, \gamma$ (°)		90, 90, 120	90, 125.226(4), 90
Pseudo-cubic unit cell volume (Å <sup>3</sup> )		58.753(3)	58.74(1)
No. Refined parameters		34	46
$R_{exp}$		4.291	4.287
$R_p$ (%)		6.398	6.281
$R_{wp}$ (%)		8.426	8.328
$R_{bragg}$ (%)		1.840	2.166
$\chi^2$		1.964	1.943
Na/Bi	$x$	0	0
	$y$	0	0.25
	$z$	0.2427(5)	0
	U11 (Å <sup>2</sup> )	0.039(1)	0.022(3)
	U22 (Å <sup>2</sup> )		0.08(3)
	U33 (Å <sup>2</sup> )	0.108(5)	0.09(2)
	U12 (Å <sup>2</sup> )	0.0199(6)	-0.001(6)
	U13 (Å <sup>2</sup> )	0	0.031(4)
	U23 (Å <sup>2</sup> )	0	0.00(1)
Ti	$x$	0	0.249(5)
	$y$	0	0.265(2)
	$z$	0	0.767(7)
O (I)	$x$	0.220(3)	0.00(2)
	$y$	0.375(2)	0.24(2)
	$z$	0.0702(9)	0.48(2)
O (II)	$x$	-	0.25(1)
	$y$	-	0.56(1)
	$z$	-	0.96(2)
O (III)	$x$	-	0.277(8)
	$y$	-	0.94(1)
	$z$	-	0.99(3)

**Table 3.1.** Lattice parameters, atomic positions, thermal displacement parameters, and refinement details for solid state NBT, taken at room temperature.

### 3.1.2 NBT doped with 1 at. % Mn

Figure 3.6 shows the XRD pattern from MnNBT produced via solid state reaction at 1100 °C, compared with that of NBT. It is clear that there is very little difference between these two scans, with no obvious peak splitting and a superstructure peak at 38.5 °2 $\theta$ . Rietveld refinement was carried out using the NBT *R3c* and *Cc* models as starting points. These refinements are summarised in Table 3.2.

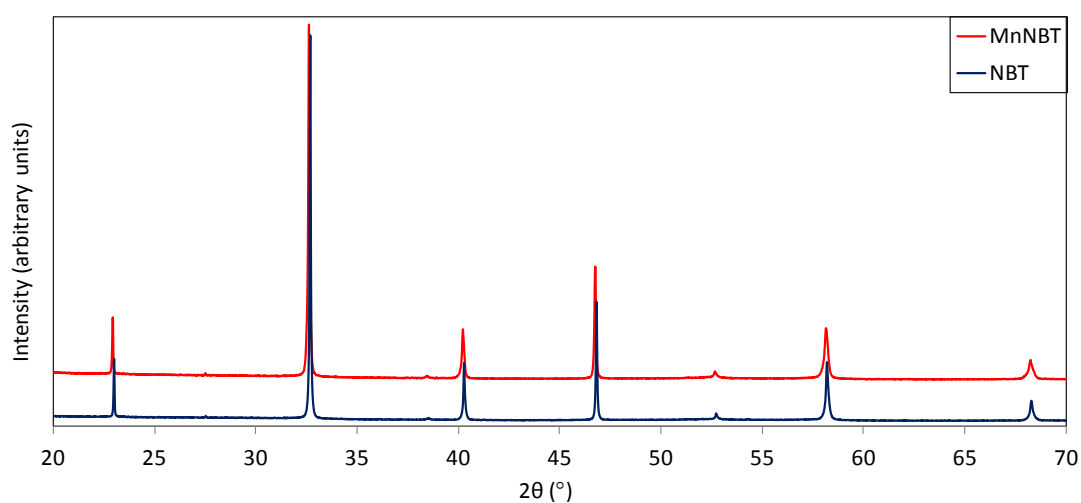


**Figure 3.6.** XRD patterns of NBT and MnNBT (data have been scaled and offset in intensity).

Crystal system		Rhombohedral	Monoclinic
Space group		$R3c$	$Cc$
Tilt system		$a^-a^-a^-$	$a^-a^-c^-$
$a$ (Å)	5.49248(7)	9.512(6)	
$b$ (Å)			5.4919(8)
$c$ (Å)	13.4787(5)	5.4971(8)	
$\alpha, \beta, \gamma$ (°)		90, 90, 120	90, 125.29(5), 90
Pseudo-cubic unit cell volume (Å <sup>3</sup> )		58.683(2)	58.60(5)
No. Refined parameters		30	31
$R_{exp}$		4.368	4.368
$R_p$ (%)		7.513	9.800
$R_{wp}$ (%)		9.984	12.737
$R_{bragg}$ (%)		2.291	4.774
$\chi^2$		2.285	2.916
Na/Bi	$x$	0	0
	$y$	0	0.25
	$z$	0.258(1)	0
	U11 (Å <sup>2</sup> )	0.017(1)	-
	U22 (Å <sup>2</sup> )		
	U33 (Å <sup>2</sup> )	0.137(4)	
	U12 (Å <sup>2</sup> )	0.0087(5)	
	U13 (Å <sup>2</sup> )	0	
	U23 (Å <sup>2</sup> )	0	
	$b$ (Å <sup>2</sup> )	-	
Ti/Mn	$x$	0	
	$y$	0	0.25(3)
	$z$	0	0.8(4)
	$b$ (Å <sup>2</sup> )	0.44(9)	-
O (I)	$x$	0.204(2)	0.958(8)
	$y$	0.325(4)	0.25(1)
	$z$	0.083(3)	0.5(3)
O (II)	$x$	-	0.19(2)
	$y$	-	0.5(7)
	$z$	-	0.9(7)
O (III)	$x$	-	0.30(2)
	$y$	-	0.0(7)
	$z$	-	0.1(7)

**Table 3.2.** Lattice parameters, atomic positions, thermal displacement parameters, and refinement details for Mn-NBT, taken at room temperature.

The refinements favour the rhombohedral model. This has a unit cell volume 0.1% smaller than that for NBT, and  $a$  and  $c$  lattice parameters 0.07% smaller and 0.03% larger respectively. These differences are minimal, as might be expected given the similar sizes of the Mn and Ti radii<sup>6</sup>, and the low percentage Mn doping.



## 3.2 Room-Temperature Study of KNBT

### 3.2.1 Series Overview

Polycrystalline samples of  $(K_xNa_{1-x})_{0.5}Bi_{0.5}TiO_3$  were prepared in the range  $0 < x < 0.65$ , via solid state synthesis. XRD data across the range are shown in Figure 3.7.

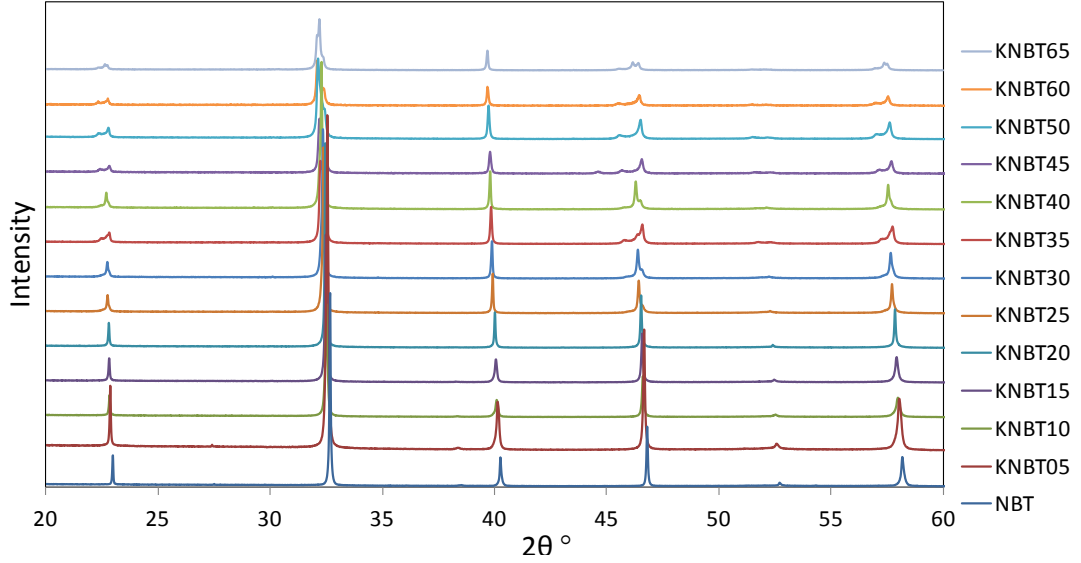


**Figure 3.7.** XRD data from KNBT (patterns offset in the y axis).

The  $\{100\}_{pc}$  peak (Figure 3.8) shows broadening and splitting with increasing potassium content. NBT-KNBT20 show a single, narrow peak, characteristic of rhombohedral or monoclinic symmetry with a very low spontaneous strain. The peak broadens asymmetrically in KNBT25-KNBT30, and three distinct triplet peaks can be made out in KNBT65. This is a possible indication of a bi-phasic region between the symmetry of NBT, and the  $P4mm$  structure seen in KBT<sup>7</sup>. Another possibility is the presence of a single, distinct phase, such as orthorhombic  $Amm2$  or  $Cm$ . The  $\{110\}_{pc}$  peak shows splitting and broadening consistent with that of the  $\{100\}_{pc}$  peak (Figure 3.9).

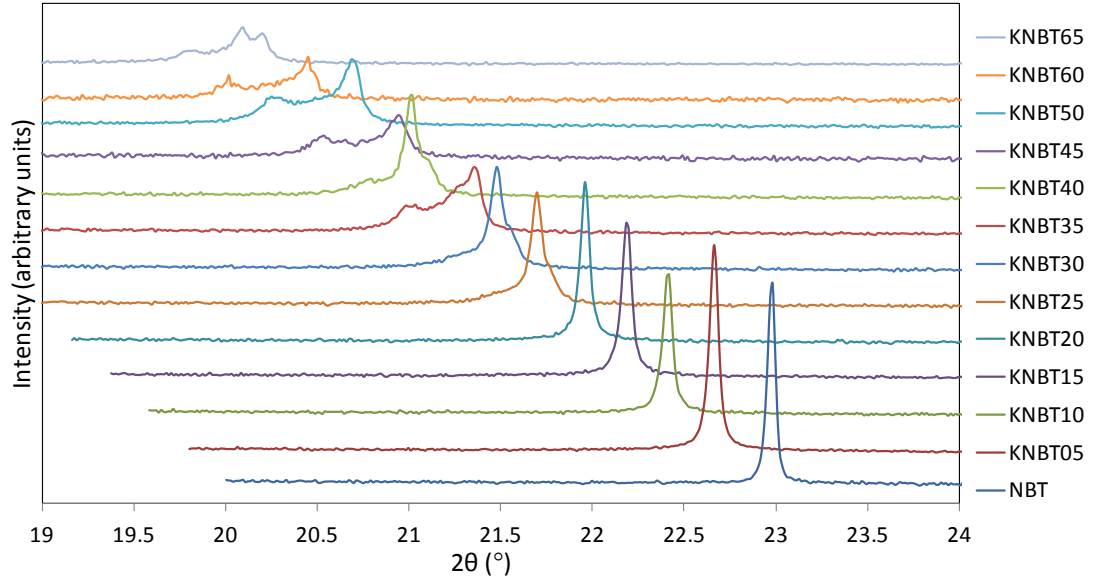


**Figure 3.8.**  $\{100\}_{pc}$  XRD peak from KNBT samples (data have been scaled and in intensity and offset in intensity and  $2\theta$  for clarity).

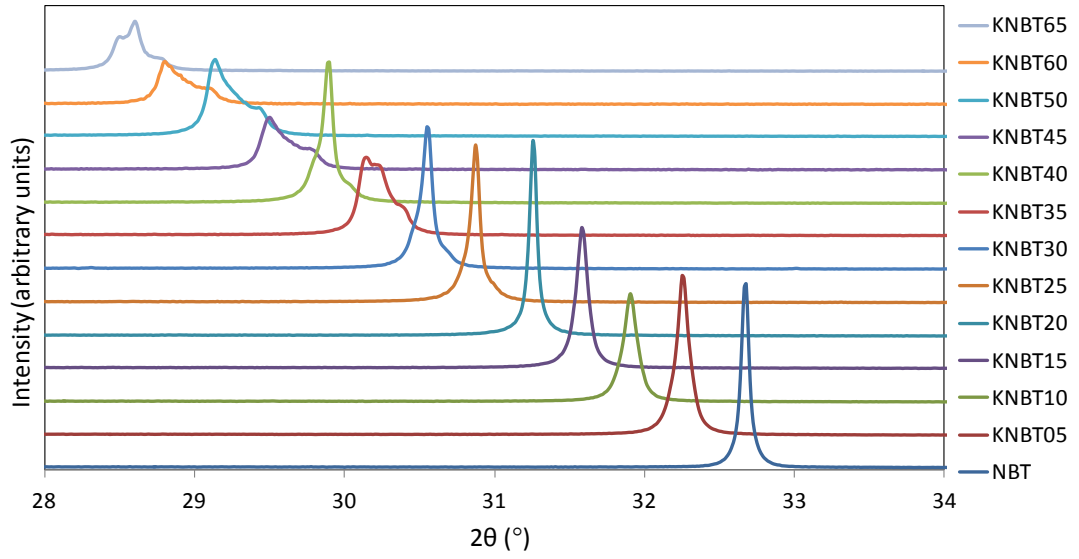


**Figure 3.9.**  $\{110\}_{pc}$  XRD peak from KNBT samples (data have been scaled in intensity and and offset in intensity and  $2\theta$  for clarity).

The  $\{111\}_{pc}$  peak remains a singlet across the series (Figure 3.10), consistent with orthorhombic or tetragonal phases, or rhombohedral or monoclinic phases with very low spontaneous strain.

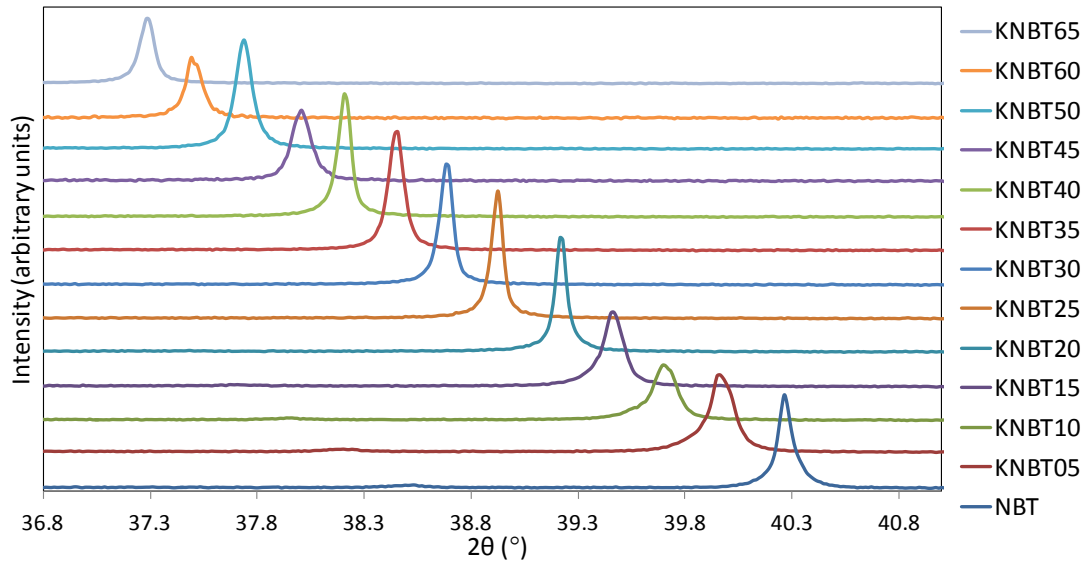


**Figure 3.10.**  $\{111\}_{pc}$  XRD peak from KNBT samples (data have been scaled in intensity and offset in intensity and  $2\theta$  for clarity).

The  $\frac{1}{2}\{311\}_{pc}$  peak at approximately  $38^\circ 2\theta$  is absent in KNBT25 and above (Figure 3.11). This indicates that compositions of KNBT25 and above do not contain antiphase tilting and so cannot have the same symmetry as KNBT20 and below. No other superstructure peaks are present in KNBT25 and above, showing there is no in-phase tilting either.

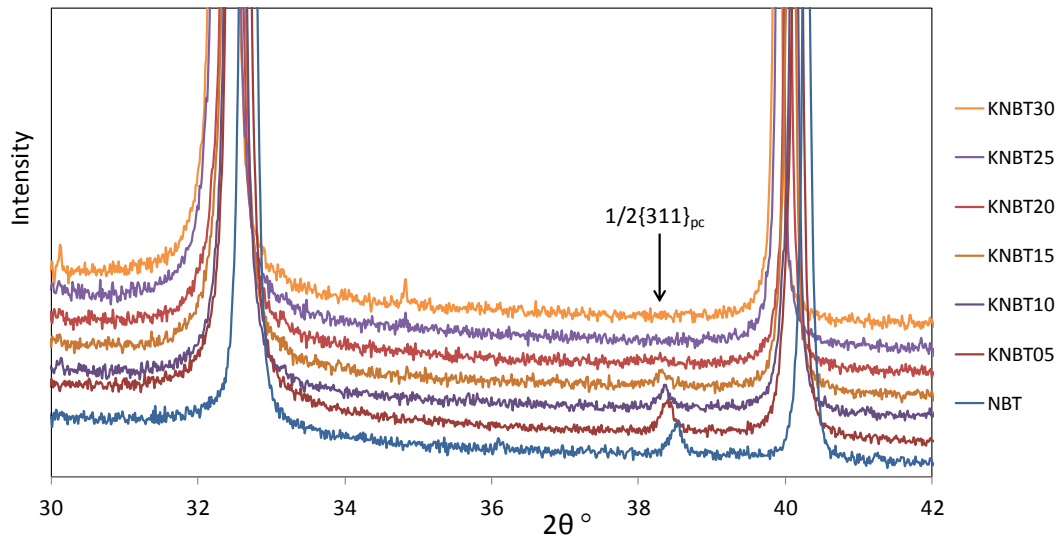


**Figure 3.11.** XRD patterns of NBT-KNBT30, showing  $\frac{1}{2}\{311\}_{pc}$  peak visible at  $\approx 38.5^\circ 2\theta$  in NBT-KNBT20 (data have been scaled and offset in intensity and  $2\theta$  for clarity).

### 3.2.2 KNBT05 – KNBT20

Rietveld refinements were carried out in both monoclinic *Cc* and rhombohedral *R3c* space groups. Tables 3.3 and 3.4 give details of these refinements, including lattice parameters, atomic positions, thermal displacement parameters (where these could be refined), and fit statistics.

		KNBT05		KNBT10	
Crystal system		Rhombohedral	Monoclinic	Rhombohedral	Monoclinic
Space group		<i>R3c</i>	<i>Cc</i>	<i>R3c</i>	<i>Cc</i>
Tilt system		<i>a<sup>-</sup>a<sup>-</sup>a<sup>-</sup></i>	<i>a<sup>-</sup>a<sup>-</sup>c<sup>-</sup></i>	<i>a<sup>-</sup>a<sup>-</sup>a<sup>-</sup></i>	<i>a<sup>-</sup>a<sup>-</sup>c<sup>-</sup></i>
<i>a</i> (Å)	5.49907(1)	9.5288(3)	5.50233(9)	9.5389(3)	
<i>b</i> (Å)					5.4950(2)
<i>c</i> (Å)	13.4986(4)	5.5117(2)	13.5049(5)	5.5176(2)	
$\alpha$ (°)	90	90	90	90	
$\theta$ (°)	90	125.268(4)	90	125.258(2)	
$\gamma$ (°)	120	90	120	90	
Pseudo-cubic unit cell volume (Å <sup>3</sup> )		58.918(2)	58.907(4)	59.015(3)	59.096(4)
No. Refined parameters		32	47	31	47
<i>R</i> <sub>exp</sub>		2.614	2.611	4.445	4.439
<i>R</i> <sub>p</sub> (%)		5.262	4.943	6.744	6.021
<i>R</i> <sub>wp</sub> (%)		7.255	6.729	8.949	7.708
<i>R</i> <sub>bragg</sub> (%)		1.568	1.650	3.069	2.070
$\chi^2$		2.775	2.578	2.013	1.736
Na/Bi	<i>x</i>	0	0	0	0
	<i>y</i>	0	0.25	0	0.25
	<i>z</i>	0.2567(5)	0	0.2533(9)	0
	U11 (Å <sup>2</sup> )	0.029(1)	0.021(2)	0.033(1)	0.024(3)
	U22 (Å <sup>2</sup> )		0.041(4)		0.033(3)
	U33 (Å <sup>2</sup> )	0.138(4)	0.135(7)	0.115(4)	0.125(5)
	U12 (Å <sup>2</sup> )	0.0144(5)	0.016(4)	0.0164(5)	0.003(7)
	U13 (Å <sup>2</sup> )	0	0.038(5)	0	0.036(4)
U23 (Å <sup>2</sup> )	0.021(8)		0.01(1)		
Ti/Mn	<i>x</i>	0	0.256(2)	0	0.2536(7)
	<i>y</i>	0	0.246(2)	0	0.2520(0)
	<i>z</i>	0	0.759(7)	0	0.7617(8)
	<i>b</i> (Å <sup>2</sup> )	-	0.52(8)	-	0.65(7)
O (I)	<i>x</i>	0.180(1)	0.019(5)	0.223(1)	0.015(7)
	<i>y</i>	0.892(1)	0.217(9)	0.843(2)	0.207(8)
	<i>z</i>	0.0918(8)	0.55(1)	0.086(1)	0.558(8)
O (II)	<i>x</i>	-	0.2017)	-	0.206(7)
	<i>y</i>	-	0.51(1)	-	0.51(1)
	<i>z</i>	-	0.95(1)	-	0.03(1)
O (III)	<i>x</i>	-	0.228(7)	-	0.234(8)
	<i>y</i>	-	0.01(2)	-	0.01(1)
	<i>z</i>	-	0.00(2)	-	0.02(1)

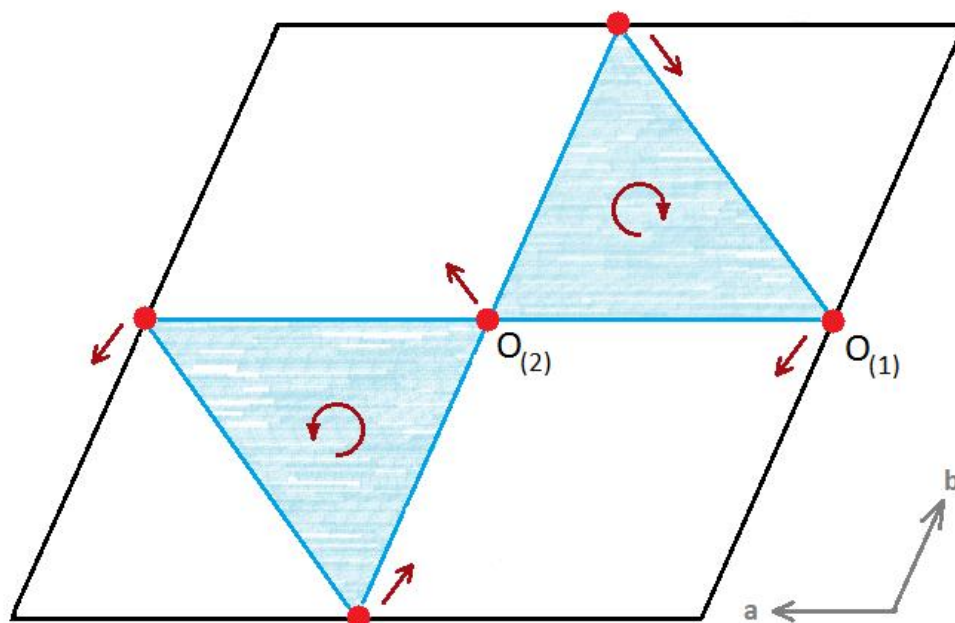
**Table 3.3.** Lattice parameters, atomic positions, thermal displacement parameters, and refinement details for KNBT05 & KNBT10.

		KNBT15		KNBT20	
Crystal system		Rhombohedral	Monoclinic	Rhombohedral	Monoclinic
Space group		<i>R3c</i>	<i>Cc</i>	<i>R3c</i>	<i>Cc</i>
Tilt system		<i>a<sup>-</sup>a<sup>-</sup>a<sup>-</sup></i>	<i>a<sup>-</sup>a<sup>-</sup>c<sup>-</sup></i>	<i>a<sup>-</sup>a<sup>-</sup>a<sup>-</sup></i>	<i>a<sup>-</sup>a<sup>-</sup>c<sup>-</sup></i>
<i>a</i> (Å)	5.5096(4)		9.5461(7)	5.5155(1)	9.560(1)
<i>b</i> (Å)			5.5076(2)		5.5181(9)
<i>c</i> (Å)			13.494(2)	5.5162(3)	13.4996(6)
$\alpha$ (°)	90	90	90	90	
$\beta$ (°)	90	125.266(6)	90	125.269(7)	
$\gamma$ (°)	120	90	120	90	
Pseudo-cubic unit cell volume (Å <sup>3</sup> )		59.12(1)	59.199(7)	59.275(3)	59.40(3)
No. Refined parameters		39	47	28	40
<i>R</i> <sub>exp</sub>		4.200	4.196	4.200	4.196
<i>R</i> <sub>p</sub> (%)		6.132	5.667	8.739	6.705
<i>R</i> <sub>wp</sub> (%)		8.106	7.331	12.361	8.684
<i>R</i> <sub>bragg</sub> (%)		1.511	1.970	4.266	1.644
$\chi^2$		1.930	1.747	2.943	2.070
Na/Bi	<i>x</i>	0	0	0	0
	<i>y</i>	0	0.25	0	0.25
	<i>z</i>	0.239(1)	0	0.250(1)	0
	U11 (Å <sup>2</sup> )	0.054(7)	0.027(3)	0.045(2)	0.08(2)
	U22 (Å <sup>2</sup> )		0.045(4)		0.06(1)
	U33 (Å <sup>2</sup> )	0.08(2)	0.106(6)	0.168(8)	0.08(3)
	U12 (Å <sup>2</sup> )	0.027(4)	0.00(2)	0.0227(9)	-0.005(9)
	U13 (Å <sup>2</sup> )	0	0.027(9)	0	0.04(4)
	U23 (Å <sup>2</sup> )		0.00(3)		-0.00(3)
Ti/Mn	<i>x</i>	0	0.253(4)	0	0.268(8)
	<i>y</i>	0	0.25(2)	0	0.24(1)
	<i>z</i>	0	0.755(7)	0	0.78(3)
	<i>b</i> (Å <sup>2</sup> )	-	0.9(1)	1.4(1)	-
O (I)	<i>x</i>	0.203(5)	0.00(4)	0.193(3)	0.01(5)
	<i>y</i>	0.846(5)	0.21(1)	0.850(2)	0.3(1)
	<i>z</i>	0.069(2)	0.54(4)	0.104(2)	0.52(8)
O (II)	<i>x</i>	-	0.21(2)	-	0.23(8)
	<i>y</i>	-	0.52(2)	-	0.52(8)
	<i>z</i>	-	0.03(1)	-	0.96(7)
O (III)	<i>x</i>	-	0.22(1)	-	0.21(4)
	<i>y</i>	-	0.01(2)	-	0.96(7)
	<i>z</i>	-	0.02(2)	-	0.92(7)

**Table 3.4.** Lattice parameters, atomic positions, thermal displacement parameters, and refinement details for KNBT15 & KNBT20.

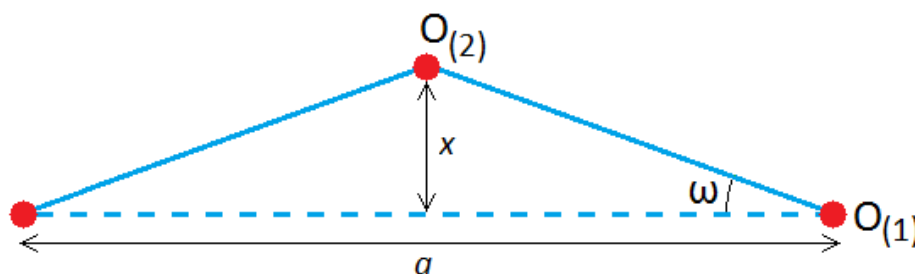
A value for  $\omega$ , the angle of tilt of the oxygen octahedra about the *c*-axis, has been calculated from the refinements in the *R3c* models of NBT – KNBT20. The *R3c* models were chosen for this analysis because they have lower uncertainty in the oxygen positions than

the refinements in  $Cc$  (Tables 3.3 and 3.4). Figure 3.12 gives a simplified representation of a slice through the  $R3c$  cell parallel to the  $c$ -axis, showing the faces of two oxygen octahedra and their directions of rotation.



**Figure 3.12.** Simplified section of the  $R3c$  unit cell in the  $ab$ -plane, showing oxygen atoms (red), and direction of rotation of the oxygen octahedra (faces shown in blue).

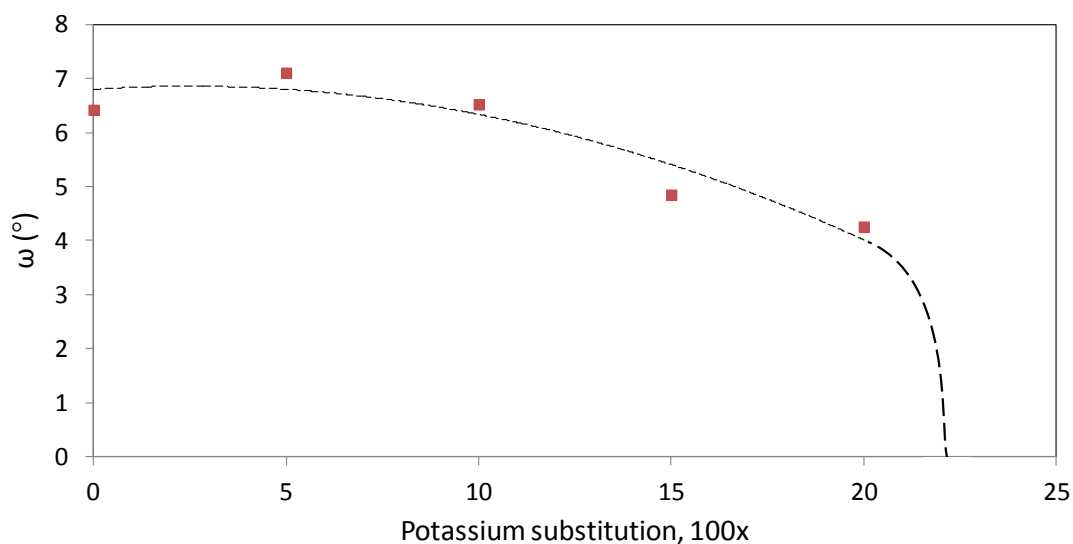
The angle through which the octahedra are rotated is calculated using trigonometry. The distance  $x$ , shown in Figure 3.13, is the separation, in the direction perpendicular to the  $a$ -axis, of the oxygen atoms  $O_{(1)}$  and  $O_{(2)}$ .



**Figure 3.13.** Tilting angle,  $\omega$ , in relation to lattice parameter  $a$ .

It can be seen that the distance  $x = |y_1 - y_2|a \cos 30^\circ$ , where  $y_1$  and  $y_2$  are the fractional atomic coordinates along  $y$  of oxygens  $O_{(1)}$  and  $O_{(2)}$  respectively. It therefore

follows that  $\tan \omega = \sqrt{3}|y_1 - y_2|$ . In calculating  $\omega$  via this method, it has been assumed that all oxygen-oxygen bond lengths are equal and there is no distortion of the octahedra.



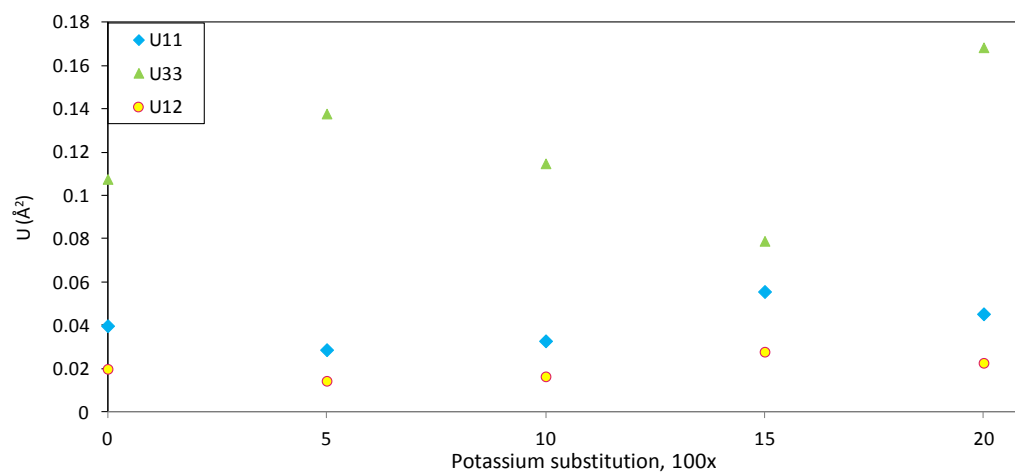
**Figure 3.14.** Tilt angle,  $\omega$ , for NBT – KNBT20 (*R3c* models). The dashed line is drawn as a guide to the eye.

Figure 3.14 shows calculated  $\omega$  values for NBT – KNBT20. A neutron diffraction study has previously found a tilt angle of  $8.24^\circ$  NBT<sup>8</sup>. The data show a general decrease in the tilting angle as potassium content is increased. The larger ionic radius of potassium (compared with sodium) leads to a larger *a* lattice parameter, accommodating octahedra without requiring as great a degree of tilting. Because of the uncertainties inherent in using XRD to analyse oxygen positions, it is unsurprising that the points are significantly scattered about the overall trend. Furthermore, only a general trend in the relationship between  $\omega$  and potassium content can be described; it is not possible to fit a quantitative model based on these data.

A value of  $\omega = 8.18^\circ$  has been calculated for MnNBT. This is comparable with the calculated tilt angle of NBT ( $\omega = 6.42^\circ$ ), and lies between this value and the published value for NBT ( $\omega = 8.24^\circ$ ). This indicates, as expected, that very little extra distortion appears as a result of Mn substitution.



Analysis of the A-site anisotropic thermal displacement parameters reveals the presence of a preferred displacement direction in both *R3c* and *Cc* models. U33 is the largest parameter in the rhombohedral models (Figure 3.15), giving thermal ellipsoids elongated along the *c* axis (Figure 3.16).



**Figure 3.15.** Anisotropic thermal displacement parameters of A-site ions in NBT – KNBT20 (*R3c* models).

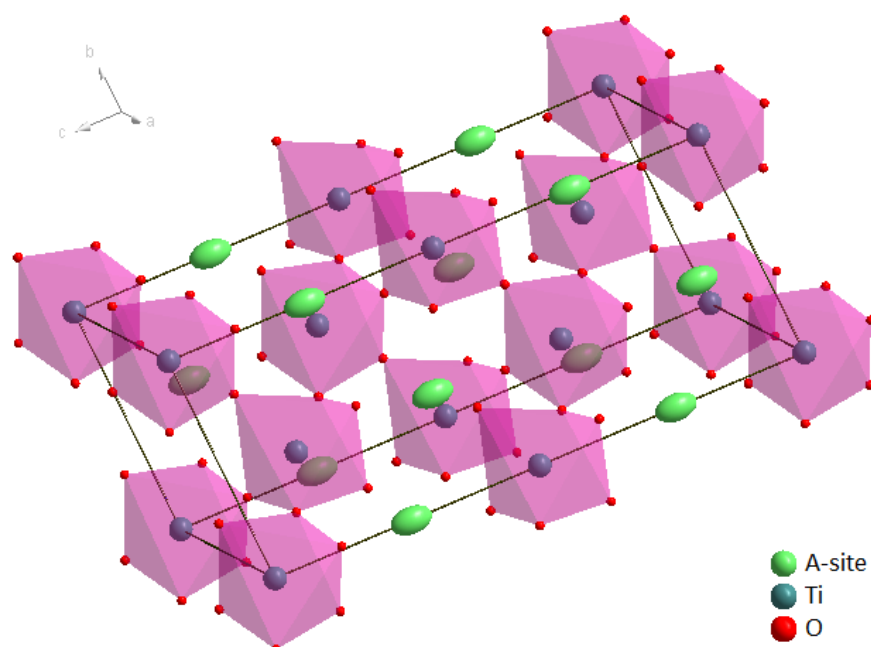


**Figure 3.16.** Rhombohedral unit cell of NBT, showing thermal ellipsoids of the A-site atoms elongated in the  $\langle 001 \rangle_R$  direction.

The monoclinic models show a general trend to have U33 as the largest parameter (Figure 3.17). In both rhombohedral and monoclinic models, U33 is equivalent to the  $\langle 111 \rangle_{pc}$  direction, and so both models are in agreement that thermal displacement is greatest along this direction. In the rhombohedral unit cell, the z-direction is the only one in which charge displacement is permitted by symmetry constraints; it is therefore unsurprising that the thermal parameters show a relative ease of movement in this direction.

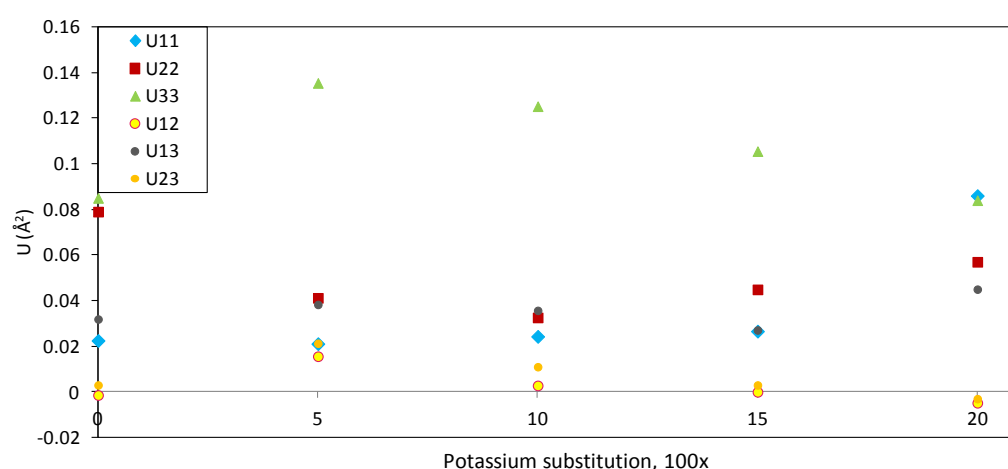


**Figure 3.17.** Anisotropic thermal displacement parameters of A-site ions in NBT – KNBT20 (Cc models).

### 3.2.3 KNBT25 – KNBT65

In KNBT25 and KNBT30, significant asymmetric peak broadening is observed in the  $\{100\}_{pc}$  and  $\{110\}_{pc}$  peaks (Figures 3.8 and 3.9). The peak shape suggests underlying contributions from a rhombohedral/monoclinic structure and a tetragonal  $P4mm$  structure, such as that expected for KBT<sup>7</sup>. In the absence of any visible superstructure peaks, the refinement has been carried out using a combined  $P4mm$  &  $R3m$  model, rather than  $R3c$  (Table 3.5). Attempts to refine a single model with space groups  $Amm2$  or  $Cm$  gave poor fits to the data. The sharp peak centres and relatively low shoulders to either side of the  $\{100\}_{pc}$  and  $\{110\}_{pc}$  peaks suggest a predominantly rhombohedral/monoclinic structure with

a lesser proportion of *P4mm*. This is supported by the values for relative percentages obtained from the refinements ( $\approx 74$  % for both samples). The combination of *R3m* with *P4mm* was found to give the best fit for all compositions in the range KNBT25-KNBT65 (Tables 3.5-3.8; Figures 3.18-3.21). In KNBT25 and KNBT30, it has been possible to refine isotropic thermal displacement parameters for the A-site atoms in both the *R3m* and *P4mm* structures, and for the Ti atoms in the *R3m* structure, of which there is a greater proportion. For KNBT35 – KNBT65, isotropic thermal displacement parameters have been refined for the A-site only, except KNBT40, for which it has been possible to refine thermal parameters for both the titanium and oxygen atoms in the *R3m* structure.

Composition		KNBT25		KNBT30	
Crystal systems		Rhombohedral & Tetragonal			
Space group		<i>R3m</i>	<i>P4mm</i>	<i>R3m</i>	<i>P4mm</i>
Relative abundance (%)		74.3	25.7	73.5	26.5
<i>a</i> , <i>b</i> (Å)		5.53018(6)	3.8978(1)	5.5360(1)	3.9009(1)
<i>c</i> (Å)		6.7715(2)	3.9428(2)	6.7797(3)	3.9489(2)
$\alpha, \beta, \gamma$ (°)		90, 90, 120	90, 90, 90	90, 90, 120	90, 90, 90
Pseudo-cubic unit cell volume (Å <sup>3</sup> )		59.782(2)	59.902(3)	59.981(3)	60.090(3)
No. Refined parameters		50		50	
<i>R</i> <sub>exp</sub>		4.094		4.040	
<i>R</i> <sub>p</sub> (%)		4.185		4.888	
<i>R</i> <sub>wp</sub> (%)		5.546		6.654	
<i>R</i> <sub>bragg</sub> (%)		1.481	1.730	1.541	2.235
$\chi^2$		1.355		1.647	
Na/K/Bi	<i>x</i> , <i>y</i>	0	0	0	0
	<i>z</i>	0.994(3)	0	0.18(1)	0
	<i>b</i> (Å <sup>2</sup> )	6.4(1)	1.72(8)	7.2(1)	2.3(1)
Ti	<i>x</i>	0	0.5	0	0.5
	<i>y</i>	0	0.5	0	0.5
	<i>z</i>	0.5	0.537(2)	0.5	0.538(3)
	<i>b</i> (Å <sup>2</sup> )	1.14(5)	-	0.34(9)	-
O (I)	<i>x</i>	0.167(1)	0.5	0.188(2)	0.5
	<i>y</i>	0.833(1)	0	0.812(2)	0
	<i>z</i>	0.35(2)	0.611(3)	0.369(3)	0.602(4)
O (II)	<i>x</i>	-	0.5	-	0.5
	<i>y</i>	-	0.5	-	0.5
	<i>z</i>	-	0.142(4)	-	0.131(5)

**Table 3.5.** Lattice parameters, atomic positions, thermal displacement parameters, and refinement details for KNBT25 and KNBT30.

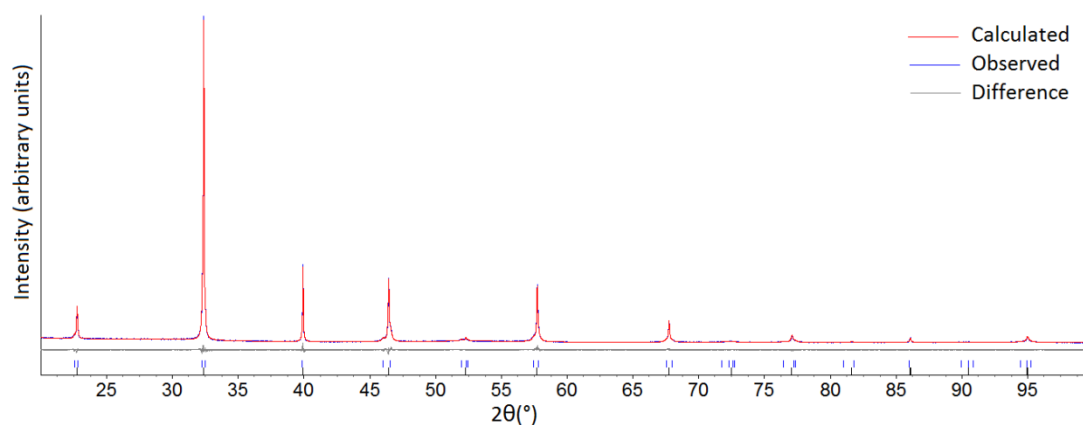


**Figure 3.18.** Plot showing fit, XRD data and difference plot for  $R3m/P4mm$  refinement of KNBT25.

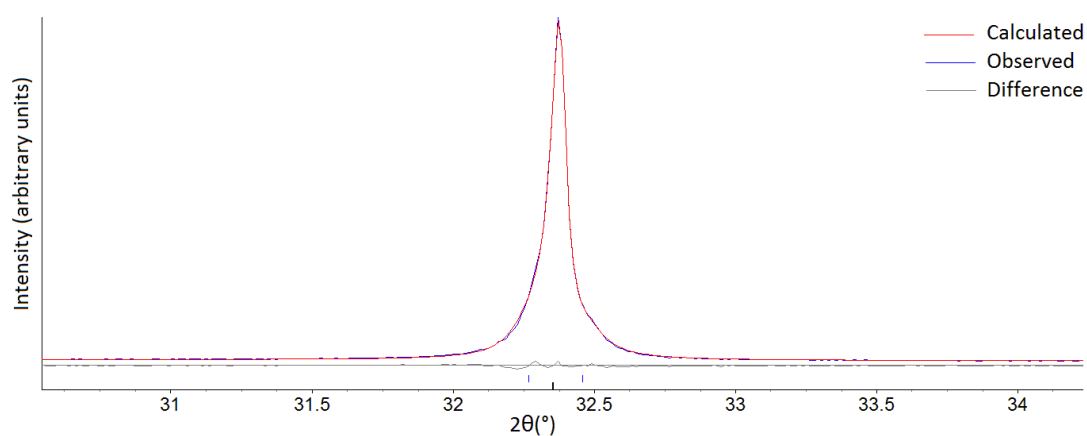


**Figure 3.19.** Plot showing fit, XRD data and difference plot for  $R3m/P4mm$  refinement of KNBT25; {110}<sub>pc</sub> XRD peak.

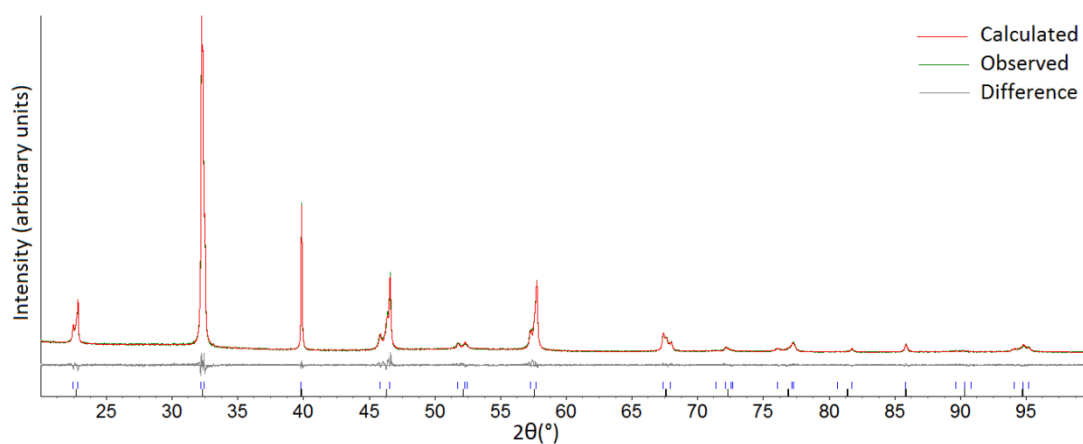


**Figure 3.20.** Plot showing fit, XRD data and difference plot for  $R3m/P4mm$  refinement of KNBT35.

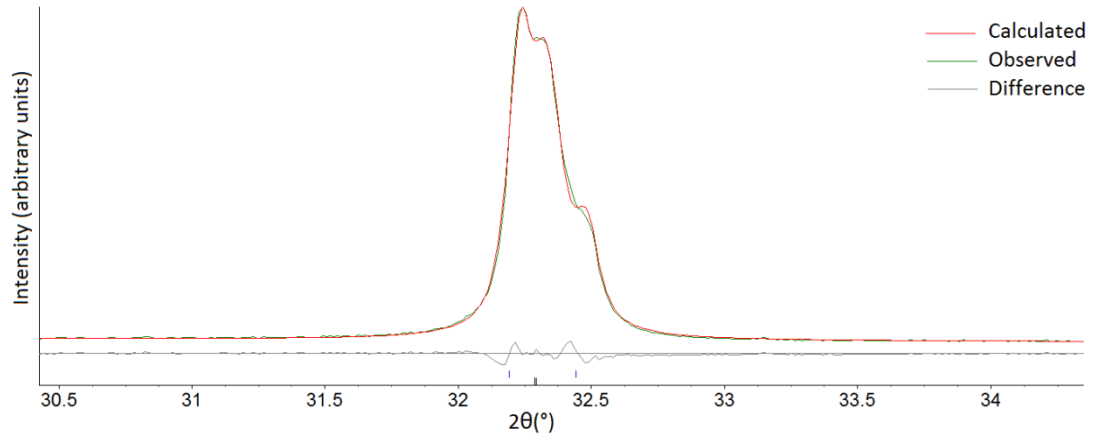


**Figure 3.21.** Plot showing fit, XRD data and difference plot for  $R3m/P4mm$  refinement of KNBT35;  $\{110\}_{pc}$  XRD peak.

Composition		KNBT35		KNBT40	
Crystal systems		Rhombohedral & Tetragonal			
Space group		<i>R3m</i>	<i>P4mm</i>	<i>R3m</i>	<i>P4mm</i>
Relative abundance (%)		53.0	47.0	67.0	33.0
<i>a, b</i> (Å)		5.5396(2)	3.89961(6)	5.54461(8)	3.90648(9)
<i>c</i> (Å)		6.7874(4)	3.9596(1)	6.7954(2)	3.9587(2)
$\alpha, \beta, \gamma$ (°)		90, 90, 120	90, 90, 90	90, 90, 120	90, 90, 90
Pseudo-cubic unit cell volume (Å <sup>3</sup> )		60.127(6)	60.213(2)	60.307(2)	60.412(3)
No. Refined parameters		54		50	
<i>R</i> <sub>exp</sub>		3.885		3.944	
<i>R</i> <sub><i>p</i></sub> (%)		4.236		4.424	
<i>R</i> <sub><i>wp</i></sub> (%)		5.613		5.825	
<i>R</i> <sub><i>bragg</i></sub> (%)		1.072	2.314	1.261	1.987
$\chi^2$		1.445		1.477	
Na/K/Bi	<i>x, y</i>	0	0	0	0
	<i>z</i>	0.019(1)	0	0.984(2)	0
	<i>b</i> (Å <sup>2</sup> )	8.6(2)	3.07(7)	7.3(1)	2.40(8)
Ti	<i>x</i>	0	0.5	0	0.5
	<i>y</i>	0	0.5	0	0.5
	<i>z</i>	0.5	0.541(1)	0.5	0.524(3)
	<i>b</i> (Å <sup>2</sup> )	-	-	1.00(9)	-
O (I)	<i>x</i>	0.200(2)	0.5	0.151(4)	0.5
	<i>y</i>	0.800(2)	0	0.849(4)	0
	<i>z</i>	0.374(3)	0.591(2)	0.312(3)	0.614(3)
	<i>b</i> (Å <sup>2</sup> )	-	-	1.7(4)	-
O (II)	<i>x</i>	-	0.5	-	0.5
	<i>y</i>	-	0.5	-	0.5
	<i>z</i>	-	0.096(3)	-	0.153(4)

**Table 3.6.** Lattice parameters, atomic positions, thermal displacement parameters, and refinement details for KNBT35 and KNBT40.

Composition		KNBT45		KNBT50	
Crystal systems		Rhombohedral & Tetragonal			
Space group		<i>R3m</i>	<i>P4mm</i>	<i>R3m</i>	<i>P4mm</i>
Relative abundance (%)		31.5	68.5	35.3	64.7
<i>a</i> , <i>b</i> (Å)		5.545(1)	3.9031(1)	5.5503(3)	3.90600(7)
<i>c</i> (Å)		6.810(2)	3.9713(2)	6.8193(5)	3.9761(1)
$\alpha, \beta, \gamma$ (°)		90, 90, 120	90, 90, 90	90, 90, 120	90, 90, 90
Pseudo-cubic unit cell volume (Å <sup>3</sup> )		60.44(3)	60.500(3)	60.643(8)	60.663(2)
No. Refined parameters		52		52	
<i>R</i> <sub>exp</sub>		5.112		3.875	
<i>R</i> <sub><i>p</i></sub> (%)		4.958		4.777	
<i>R</i> <sub><i>wp</i></sub> (%)		6.579		6.297	
<i>R</i> <sub><i>bragg</i></sub> (%)		1.160	1.607	1.990	2.541
$\chi^2$		1.287		1.625	
Na/K/Bi	<i>x</i> , <i>y</i>	0	0	0	0
	<i>z</i>	0.012(6)	0	0.017(2)	0
	<i>b</i> (Å <sup>2</sup> )	5.6(5)	3.0(1)	9.2(4)	3.06(5)
Ti	<i>x</i>	0	0.5	0	0.5
	<i>y</i>	0	0.5	0	0.5
	<i>z</i>	0.5	0.540(2)	0.5	0.539(1)
O (I)	<i>x</i>	0.198(3)	0.5	0.216(1)	0.5
	<i>y</i>	0.802(3)	0	0.784(1)	0
	<i>z</i>	0.36(1)	0.593(3)	0.357(4)	0.586(2)
O (II)	<i>x</i>	-	0.5	-	0.5
	<i>y</i>	-	0.5	-	0.5
	<i>z</i>	-	0.103(4)	-	0.092(3)

**Table 3.7.** Lattice parameters, atomic positions, thermal displacement parameters, and refinement details for KNBT45 and KNBT50.

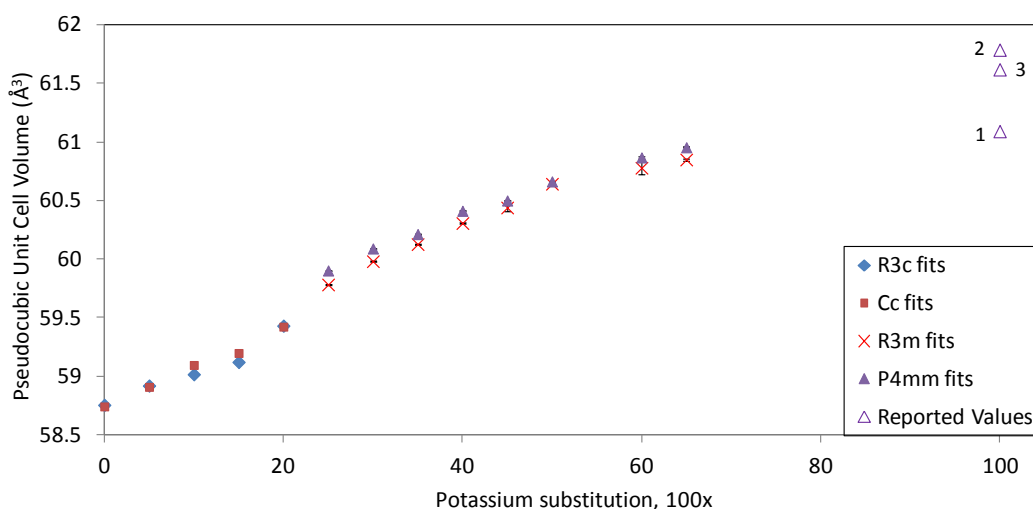
Composition		KNBT60		KNBT65	
Crystal systems		Rhombohedral & Tetragonal			
Space group		<i>R3m</i>	<i>P4mm</i>	<i>R3m</i>	<i>P4mm</i>
Relative abundance (%)		37.8	62.2	52.3	47.2
<i>a</i> , <i>b</i> (Å)		5.558(2)	3.9102(2)	5.5629(4)	3.9144(2)
<i>c</i> (Å)		6.816(5)	3.9810(3)	6.812(1)	3.9781(2)
$\alpha,\beta,\gamma$ (°)		90, 90, 120	90, 90, 90	90, 90, 120	90, 90, 90
Pseudo-cubic unit cell volume (Å <sup>3</sup> )		60.78(6)	60.868(6)	60.85(1)	60.955(4)
No. Refined parameters		48		52	
<i>R</i> <sub>exp</sub>		12.583		4.435	
<i>R</i> <sub><i>p</i></sub> (%)		7.018		4.935	
<i>R</i> <sub><i>wp</i></sub> (%)		9.116		6.490	
<i>R</i> <sub><i>bragg</i></sub> (%)		1.860	3.006	0.987	2.097
$\chi^2$		0.725		1.463	
Na/K/Bi	<i>x,y</i>	0	0	0	0
	<i>z</i>	0.977(6)	0	0.99(3)	0
	<i>b</i> (Å <sup>2</sup> )	7.2(8)	3.5(2)	6.7(8)	3.8(2)
Ti	<i>x</i>	0	0.5	0	0.5
	<i>y</i>	0	0.5	0	0.5
	<i>z</i>	0.5	0.535(4)	0.5	0.468(8)
O (I)	<i>x</i>	0.114(3)	0.5	0.134(2)	0.5
	<i>y</i>	0.886(3)	0	0.866(2)	0
	<i>z</i>	0.305(9)	0.583(6)	0.33(4)	0.593(5)
O (II)	<i>x</i>	-	0.5	-	0.5
	<i>y</i>	-	0.5	-	0.5
	<i>z</i>	-	0.113(8)	-	0.06(1)

**Table 3.8.** Lattice parameters, atomic positions, thermal displacement parameters, and refinement details for KNBT60 and KNBT65.

### 3.2.4 Series Data Analysis

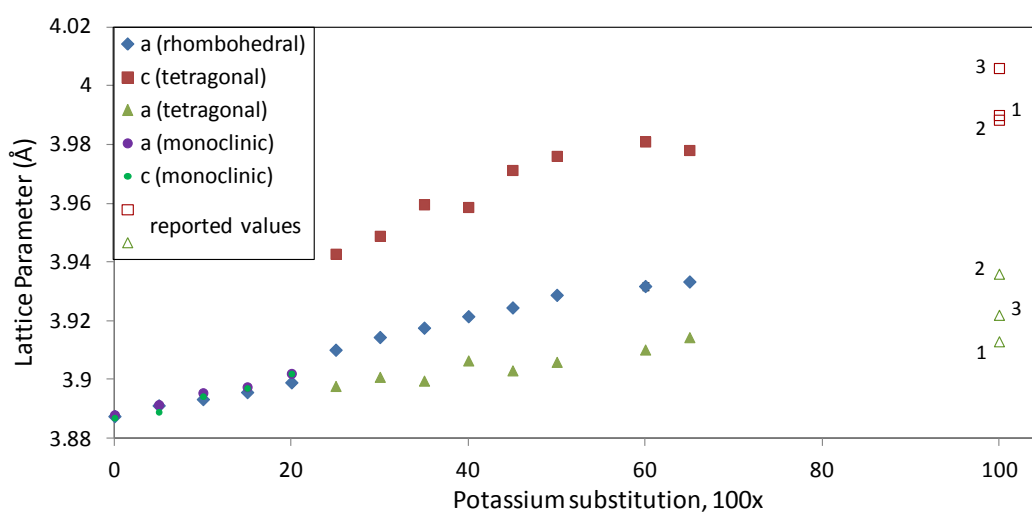
Figure 3.22 shows the pseudocubic unit cell volumes across the range NBT – KNBT65, calculated from rhombohedral, monoclinic and tetragonal models. Also shown are volumes calculated from published values for KBT lattice parameters<sup>9, 10, 11</sup>. For all models, an increase in cell volume is observed with increasing potassium concentration: a consequence of the larger average radius of the A-site ion<sup>6</sup>. The published values agree with this trend. Two approximately linear relationships can be seen: the first, from NBT – KNBT20; and the second, from KNBT25-65. A break in the linear trend occurs between KNBT20 and KNBT25, coinciding with the phase boundary between the *R3c* (or *Cc*) structure and the multiphase *R3m/P4mm* structure. This is also the region with the highest

$d_{33}$  values<sup>12</sup>.



**Figure 3.22.** Pseudocubic unit cell volumes across the range NBT to KNBT65, and volumes calculated from published values for KBT lattice parameters (1<sup>[9]</sup>; 2<sup>[10]</sup>; 3<sup>[11]</sup>).

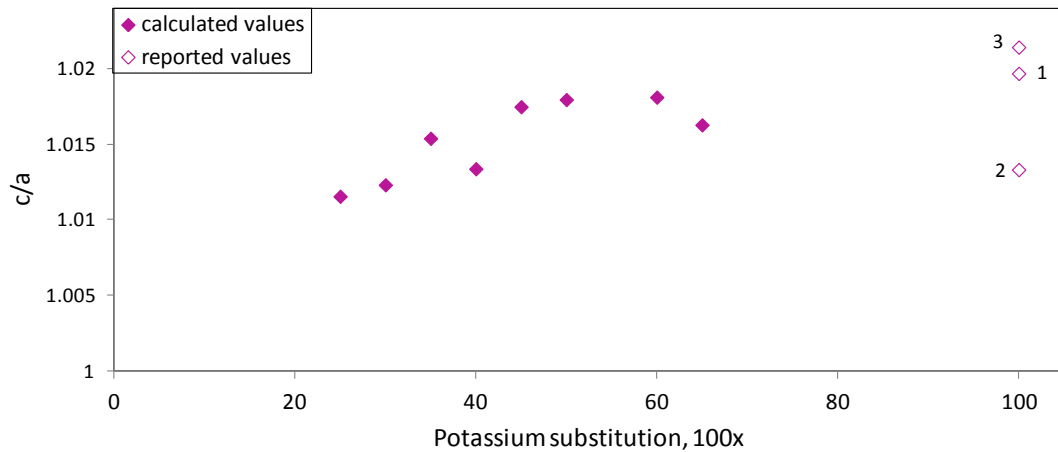
Figure 3.23 shows pseudocubic lattice parameters of NBT – KNBT65, using rhombohedral, tetragonal and monoclinic models. Like the pseudocubic unit cell volumes, these show an approximately linear increase with potassium content, with a break at the phase boundary between the *R3c* (or *Cc*) and *R3m/P4mm* structures. Also shown are published values for KBT lattice parameters<sup>9, 10, 11</sup>, which agree broadly with this relationship although there is significant variability.



**Figure 3.23.** Pseudocubic lattice parameters across the range NBT - KNBT65, and published values for KBT lattice parameters (1<sup>[9]</sup>; 2<sup>[10]</sup>; 3<sup>[11]</sup>).

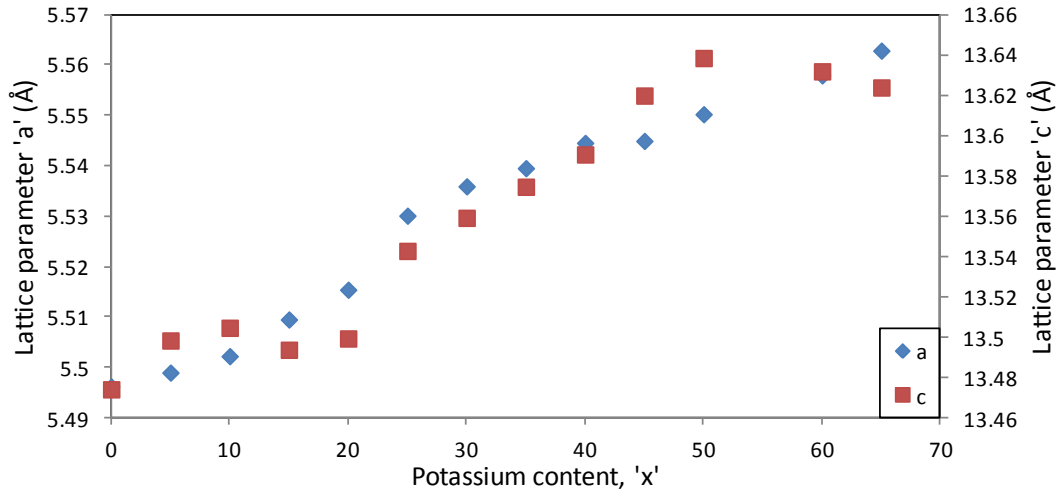


Figure 3.24 shows the  $c/a$  ratios of the tetragonal phase in KNBT25-65, as well as those calculated from published lattice parameters for KBT<sup>9, 10, 11</sup>. The greatest  $c/a$  ratio is found between KNBT50-60, indicating that these compositions have the greatest spontaneous tetragonal strain.



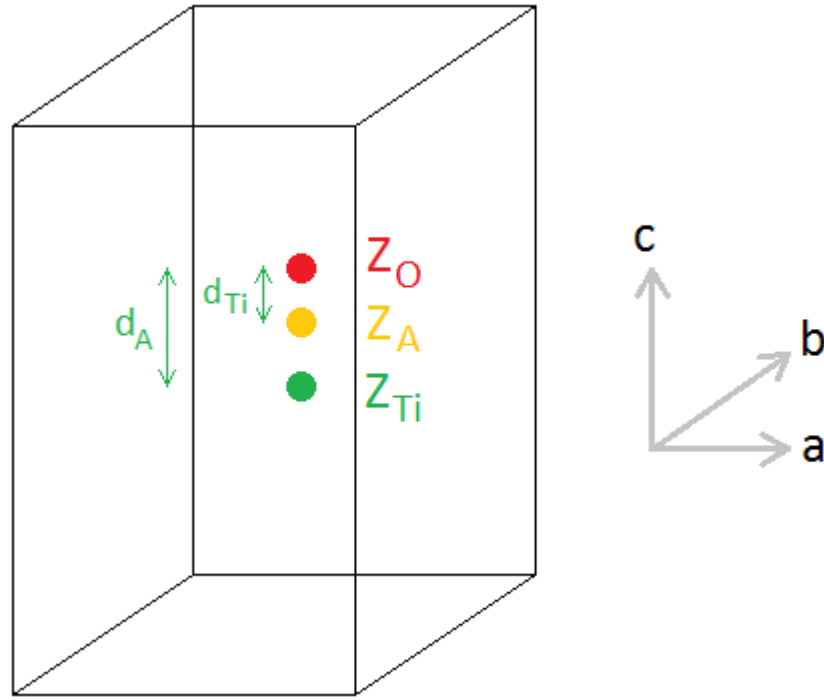
**Figure 3.24.** Tetragonal  $c/a$  ratio of KNBT25-65, and reported  $c/a$  ratios for KBT (1<sup>[9]</sup>, 2<sup>[10]</sup>, 3<sup>[11]</sup>).

Figure 3.25 shows the  $a$  and  $c$  parameters from the  $R3c$  model, and  $a$  and  $2c$  from the  $R3m$  model. In general, a linear increase in these parameters is seen with increasing potassium content, a consequence of the larger average ionic radius of the A-site atom. A break in the linear trends occurs between KNBT20 and KNBT25, coinciding with the phase boundary between the  $R3c$  structure and the multiphase  $R3m/P4mm$  structure. The regions with the greatest difference between  $a$  and  $2c$  occur between KNBT05-15, and KNBT45-50, indicating greater rhombohedral strain in these compositions.



**Figure 3.25.** Lattice parameters  $a$  and  $c$  from the  $R3c$  models (NBT – KNBT20), and  $a$  and  $2c$  from the  $R3m$  models (KNBT25 – KNBT65).

Polarisation of the unit cell as a function of  $x$  was calculated from the refined structures. In proceeding with the series analysis, consideration was given to the choice of rhombohedral or monoclinic models for NBT-KNBT20. Although the rhombohedral fit was better only for NBT, the  $R3c$  fits clearly provide reasonable models of the KNBT05-20 unit cells, as the  $R$ -factors indicate. For purposes of comparison it was desirable to use a consistent model across the range NBT-KNBT20; the  $R3c$  unit cell was selected as it provides a simpler model for analysis of polarisation, allowing charge displacement only in the  $z$  direction. Additionally, this choice provides continuity with the  $R3m$  polarisation found in KNBT25-KNBT65. The average charge location in the  $z$ -direction (Figure 3.26) was determined for the A, B and O sites.



**Figure 3.26.** Unit cell showing average charge centre in  $z$  of oxygen ions ( $z_O$ ), A-site cations ( $z_A$ ) and titanium ions ( $z_{Ti}$ ). ' $d_{Ti}$ ' is the displacement between the titanium and oxygen charge centres; and ' $d_A$ ' is the displacement between the A-site and oxygen charge centres.

As symmetry constraints only allow charge separation in the  $z$ -direction, the distance between these locations was used to calculate the magnitude of polarisation. This was done for the A and B sites separately in both the rhombohedral and tetragonal structures. For the case of the polarisation arising from the titanium-oxygen separation, the following formula was used:

$$P = \frac{4cne}{V} [z_O - z_{Ti}] \quad (3.1)$$

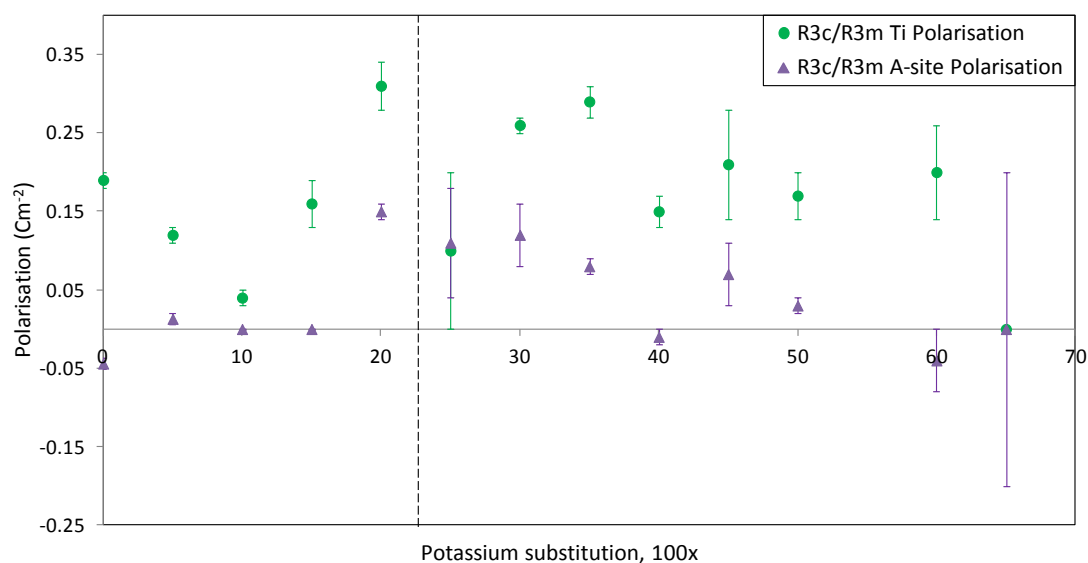
where:  $P$  = polarisation ( $\text{Cm}^{-2}$ );  $c$  =  $c$  lattice parameter ( $\text{\AA}$ );  $n$  = number of formula units in unit cell;  $e$  = electronic charge (C);  $V$  = unit cell volume, ( $\text{\AA}^3$ );  $z_{Ti}$  = average titanium  $z$  position;  $z_O$  = average oxygen  $z$  position.

An equivalent formula was used for calculating separately the polarisation arising from the A-site cation-oxygen separation. For convention, the value for Ti-site polarisation has been taken as positive.

x	Rhombohedral model Polarisation (Cm <sup>-2</sup> )			Tetragonal model Polarisation (Cm <sup>-2</sup> )		
	A-site	B-site	Total	A-site	B-site	Total
0	0.044(7)	0.19(1)	0.15(1)			
05	0.013(7)	0.12(1)	0.13(1)			
10	0	0.04(1)	0.04(1)			
15	0	0.16(3)	0.16(3)			
20	0.15(1)	0.31(3)	0.46(3)			
25	0.11(7)	0.1(1)	0.2(1)	0.26(1)	0.36(3)	0.62(3)
30	0.12(4)	0.26(1)	0.38(4)	0.23(2)	0.31(3)	0.54(4)
35	0.08(1)	0.29(2)	0.37(2)	0.195(8)	0.22(2)	0.42(2)
40	-0.01(1)	0.15(2)	0.14(2)	0.27(1)	0.43(3)	0.70(3)
45	0.07(4)	0.21(7)	0.28(8)	0.20(1)	0.24(3)	0.44(3)
50	0.03(1)	0.17(3)	0.16(3)	0.185(8)	0.21(2)	0.40(2)
60	-0.04(4)	0.20(6)	0.0(7)	0.02(2)	0.24(4)	0.26(4)
65	0.0(2)	0	0.0(2)	0.02(2)	0.44(4)	0.46(4)

**Table 3.9.** Polarisation values for NBT-KNBT65.

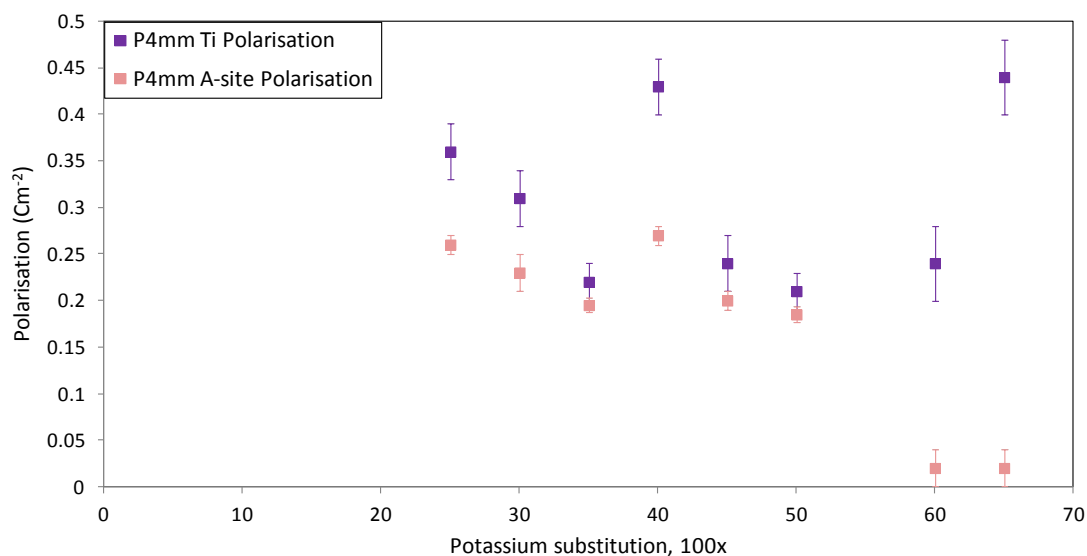
Table 3.9 and Figures 3.27 and 3.28 show the separate A-site and Ti-site polarisation values, for the rhombohedral and tetragonal phases. These values are comparable with that of BaTiO<sub>3</sub>, 0.26 Cm<sup>-2</sup> [13]. The largest contribution to the polarisation comes from the Ti-O separation; this is especially true of the rhombohedral phases. To the left of the phase boundary (Figure 3.27), a ‘dip’ in polarisation is seen at KNBT10.



**Figure 3.27.** *R3c/R3m* polarisation across the range: NBT – KNBT65. The dashed line indicates the approximate location of the phase boundary.

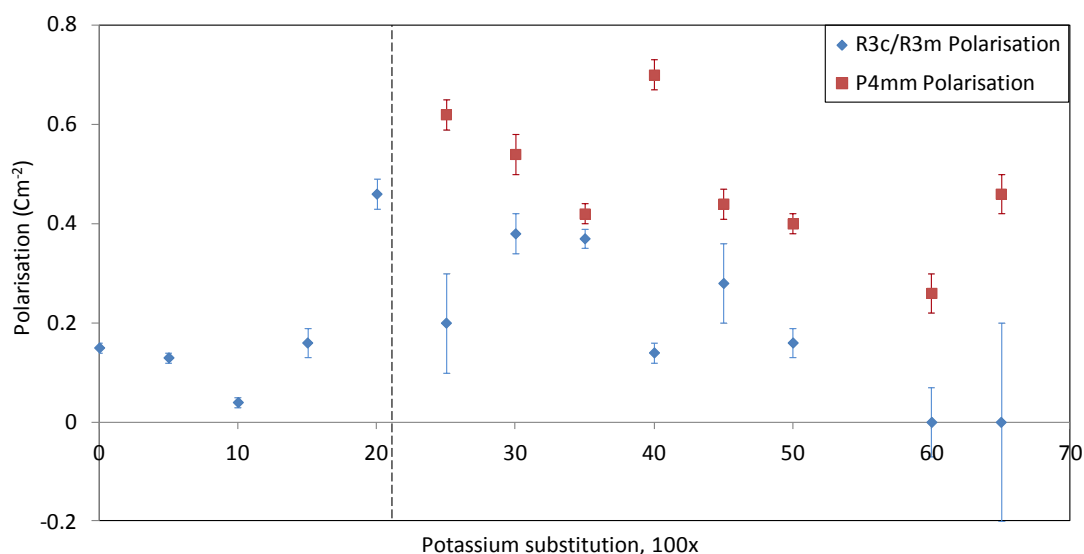
The calculated polarisation values for MnNBT are 0.044(7) Cm<sup>-2</sup> and 0.00(1) Cm<sup>-2</sup> for the A-site and B-site respectively. Unlike NBT, the main contribution comes from the A-site. From these values, it appears that the addition of Mn to the structure lowers the polarisation of NBT. This seems unlikely, given the similarity between the NBT and MnNBT structures (Tables 3.1 and 3.2). Further work, such as neutron diffraction, would be required to provide more reliable oxygen positions from which to verify the polarisation values.

To the right of the phase boundary (Figures 3.27 & 3.28) no clear trend of the polarisation values is observed with increasing potassium substitution.



**Figure 3.28.** *P4mm* polarisation across the range: NBT – KNBT65.

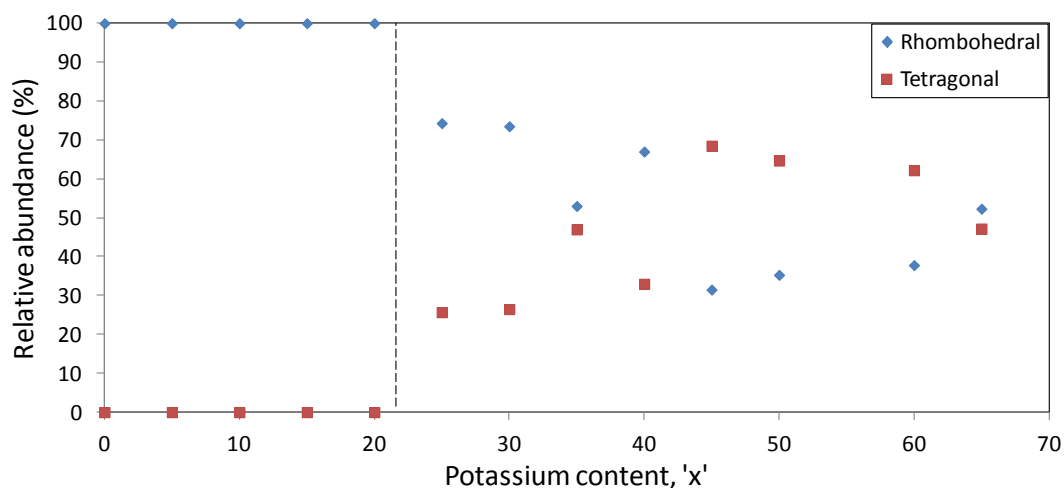
Figure 3.29 gives the overall polarisation (the sum of the A-site and Ti-site polarisation values) from the rhombohedral and tetragonal phases as a function of composition. The data show that the tetragonal phase is more polarised than the rhombohedral phases. The rhombohedral values show a peak at KNBT20. The presence of enhanced polarisation here lends further support to the drawing of a phase boundary<sup>14</sup>. However, the data appear highly scattered because of the uncertainty in using XRD to analyse oxygen positions. The tetragonal polarisation values also appear to show a peak, at KNBT40. This is a possible consequence of the noisy data, or may be related to the shift in structure that occurs near this composition; between KNBT40 and KNBT45, the structure changes from being predominantly rhombohedral, to predominantly tetragonal (Figure 3.30).



**Figure 3.29.** Polarisation across the range: NBT – KNBT65. The dashed line indicates the approximate location of the boundary.

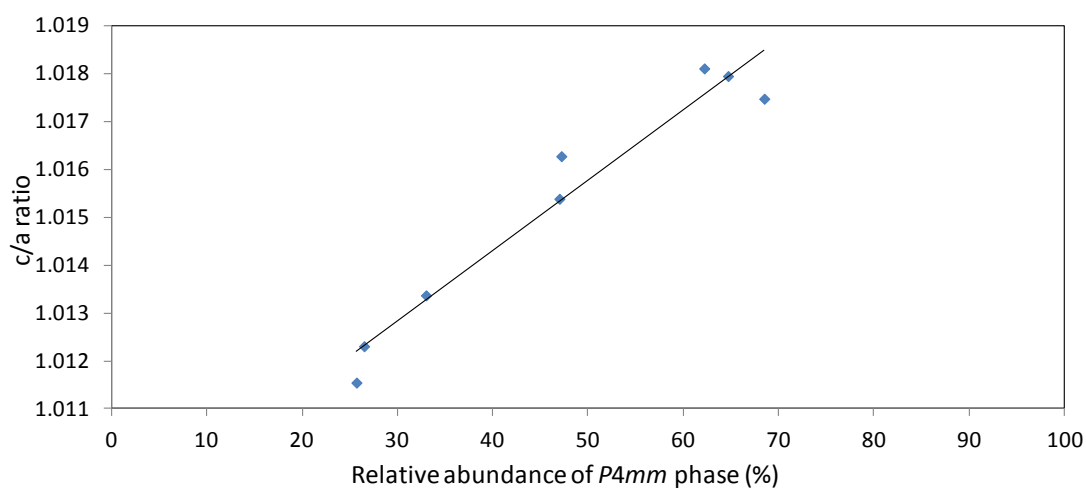
The error bars in Figures 3.27 and 3.29 suggest that the values to the left of the phase boundary have been ascertained with a greater degree of confidence than those in the multi-phase region. Larger errors are to be expected from multi-phase refinements, as a greater number of parameters must be refined from the data. In the multi-phase region, greater errors are seen in the rhombohedral phase polarisation. A possible reason for this is that the *R3m* phase may be less uniform and more prone to variation in atomic positions, giving larger errors in the Rietveld refinement.

Figure 3.30 shows the relative abundances of the rhombohedral and tetragonal phases as a function of composition, using the values generated by Rietveld refinement. Between KNBT25-45, the proportion of rhombohedral phase decreases (excepting KNBT40); between KNBT45-65, the proportion of rhombohedral phase gradually increases, becoming the predominant phase by a small amount in KNBT65.



**Figure 3.30.** Relative abundances of rhombohedral and tetragonal phases from NBT – KNBT65. The dashed line indicates the approximate location of the boundary.

A correlation can be observed between the  $c/a$  ratio (Figure 3.24) and the proportions of rhombohedral and tetragonal phases present (Figure 3.30). This correlation is shown in Figure 3.31.



**Figure 3.31.** Relationship between  $c/a$  ratio and relative abundance of  $P4mm$  phase. The line indicates a linear fit to the data.

The correlation is supported by a visual analysis of the diffraction patterns. Figure 3.32 shows the  $\{220\}_{pc}$  XRD peak from KNBT30, KNBT35 and KNBT50. KNBT30 contains the lowest amount of tetragonal phase; this is shown by the high-intensity, rhombohedrally-generated peak centre and lower-intensity, tetragonally-generated peak shoulders.



KNBT35 contains a more significant tetragonal contribution, and in KNBT50 the rhombohedral contribution cannot be visually distinguished from the tetragonal peaks. The coloured bars illustrating peak separation show that, with increasing overall tetragonal contribution, an increased peak splitting is observed.

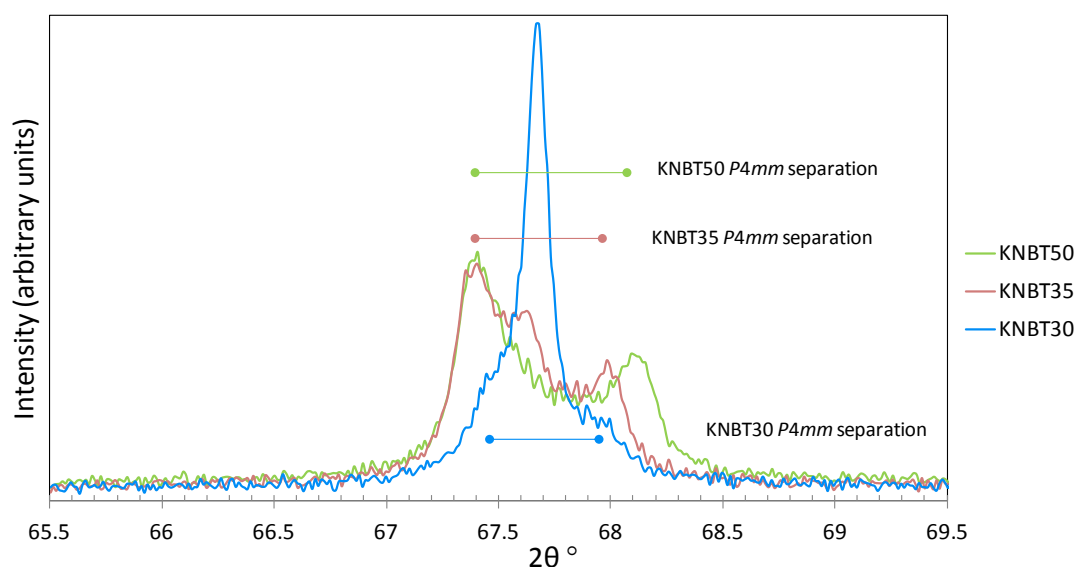


**Figure 3.32.**  $\{220\}_{pc}$  XRD peak from KNBT30, KNBT35 and KNBT50. The coloured bars mark the approximate separation between the  $P4mm$  doublet peaks.

To investigate the possibility that the enhanced central-peak intensity was a consequence of its proximity to the flanking peaks, rather than a result of the rhombohedral structure, the  $\{220\}_{pc}$  peak was fitted using three Voigt peak functions in OriginPro 8.5<sup>15</sup>, as shown in Figure 3.33.

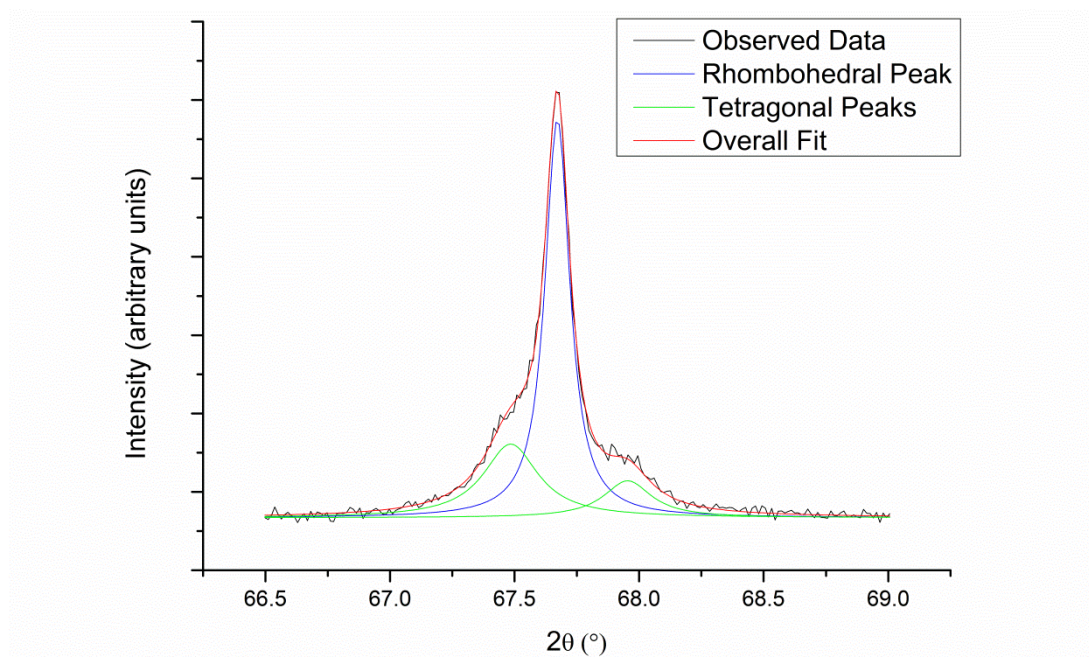


**Figure 3.33.** Fit to the  $\{220\}_{pc}$  XRD peak from KNBT30 using Voigt functions to model the underlying rhombohedral and tetragonal peaks.

The separation in  $2\theta$  between the tetragonal doublet peaks has been plotted as a function of the tetragonal component of peak area (Figure 3.34).

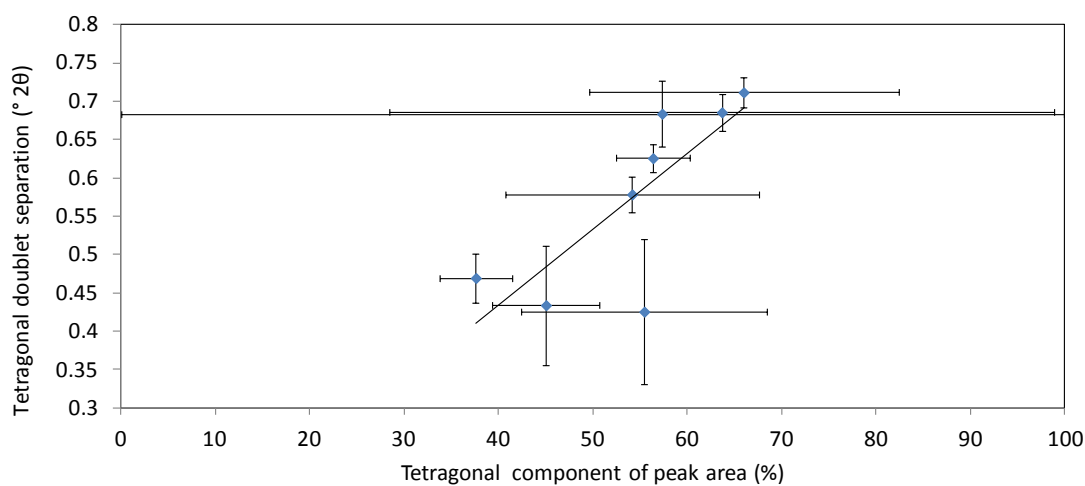


**Figure 3.34.** Splitting of the  $\{220\}_{pc}$  tetragonal doublet peaks as a function of tetragonal component of peak area.

Despite the capacious nature of the error bars, a trend corroborating that of Figure 3.31 is apparent, indicating that the relationship between  $c/a$  and the relative abundance

of tetragonal phase has a physical basis and is not an artefact of the data processing method.

The two-phase region observed from KNBT25-65 is unusual, as only one equilibrium phase is normally encountered in perovskites. The tetragonal phase could be expected to be in equilibrium in this region, as KBT is tetragonal and a phase boundary occurs at around KNBT20<sup>12</sup>. The non-equilibrium rhombohedral phase may be the result of stress-induced phase transition, occurring as samples were ground.

### 3.3 High-Temperature X-Ray Diffraction Study

#### 3.3.1 NBT

NBT structure as a function of temperature was investigated using high-temperature x-ray diffraction. Initially, data were collected at 200 °C, 300 °C, 450 °C, 530 °C and 600 °C (Figure 3.35), this range being sufficient to observe the high-temperature cubic phase in addition to the tetragonal phase intermediate to the cubic and room-temperature phases.

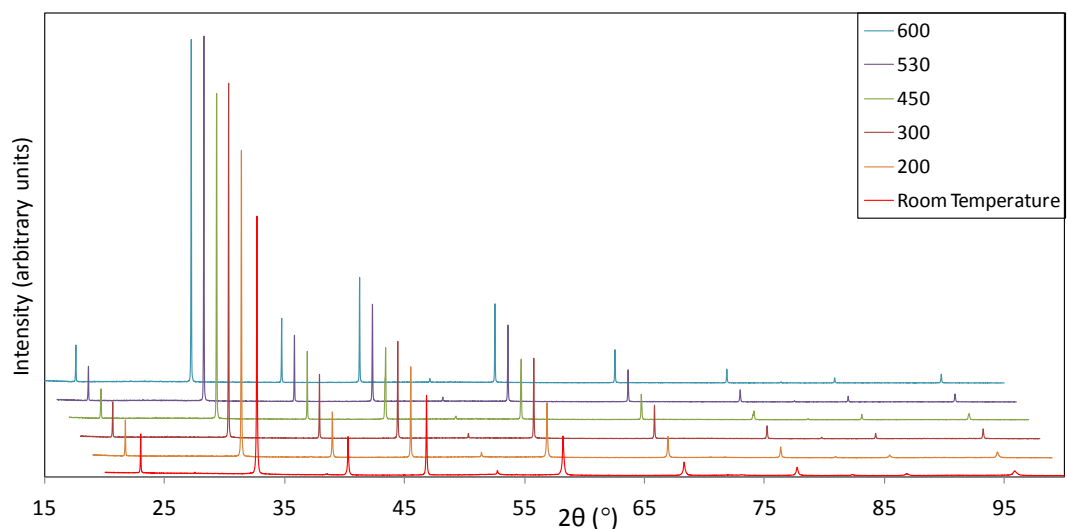


**Figure 3.35.** NBT x-ray diffraction patterns collected at room temperature, 200 °C, 300 °C, 450 °C, 530 °C and 600 °C (data offset in the x and y axes for clarity).

In addition to the Rietveld refinement already reported for the room-temperature data, refinements were carried out on data collected at 200 – 600 °C. The results of these are summarised in Tables 3.10 and 3.11, and Figures 3.36-

Crystal system		Rhombohedral	Monoclinic
Space group		$R3c$	$Cc$
Tilt system		$\bar{a}\bar{a}\bar{a}$	$\bar{a}\bar{a}\bar{c}$
$a$ (Å)		5.50156(6)	9.5412(3)
$b$ (Å)		$= a$	5.5051(2)
$c$ (Å)		13.4858(3)	5.5048(2)
$\alpha, \beta, \gamma$ (°)		90, 90, 120	90, 125.305(3), 90
Pseudo-cubic unit cell volume (Å <sup>3</sup> )		58.915(2)	58.991(3)
No. Refined parameters		31	38
$R_{exp}$		6.653	6.649
$R_p$ (%)		7.404	8.640
$R_{wp}$ (%)		9.483	11.233
$R_{bragg}$ (%)		1.767	2.460
$\chi^2$		1.426	1.690
Na/Bi	$x$	0	0
	$y$	0	0.25
	$z$	0.2577(8)	0
	U11 (Å <sup>2</sup> )	0.055(2)	0.07(2)
	U22 (Å <sup>2</sup> )		0.06(1)
	U33 (Å <sup>2</sup> )	0.087(4)	0.057(8)
	U12 (Å <sup>2</sup> )	0.129(1)	0.01(1)
	U13 (Å <sup>2</sup> )	0	0.022(9)
	U23 (Å <sup>2</sup> )	0	0.00(1)
Ti	$x$	0	0.2681(8)
	$y$	0	0.250(5)
	$z$	0	0.764(3)
	$b$ (Å <sup>2</sup> )	0.64(9)	-
O (I)	$x$	0.126(3)	0.018(8)
	$y$	0.302(6)	0.24(2)
	$z$	0.094(1)	0.51(1)
O (II)	$x$	-	0.210(8)
	$y$	-	0.54(2)
	$z$	-	0.92(1)
O (III)	$x$	-	0.249(9)
	$y$	-	0.97(2)
	$z$	-	0.97(1)

**Table 3.10.** Lattice parameters, atomic positions, thermal displacement parameters, and refinement details for solid state NBT at 200 °C.

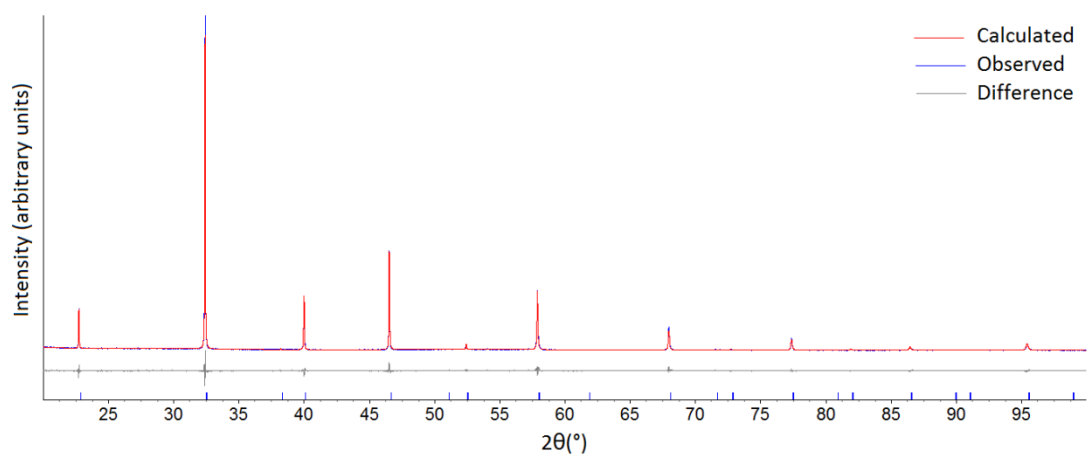


**Figure 3.36.** Plot showing fit, data and difference plot for  $R3c$  refinement of solid state NBT at 200 °C.

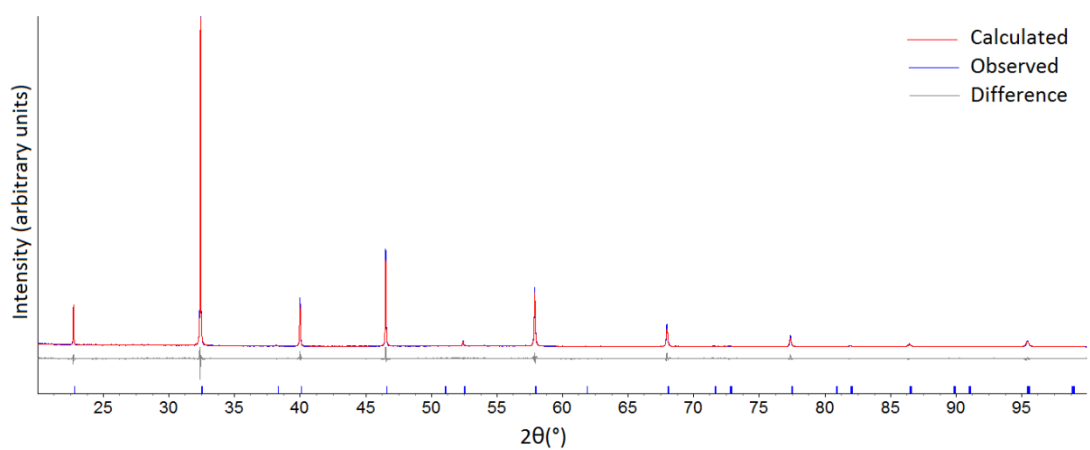


**Figure 3.37.** Plot showing fit, data and difference plot for  $Cc$  refinement of solid state NBT at 200 °C.

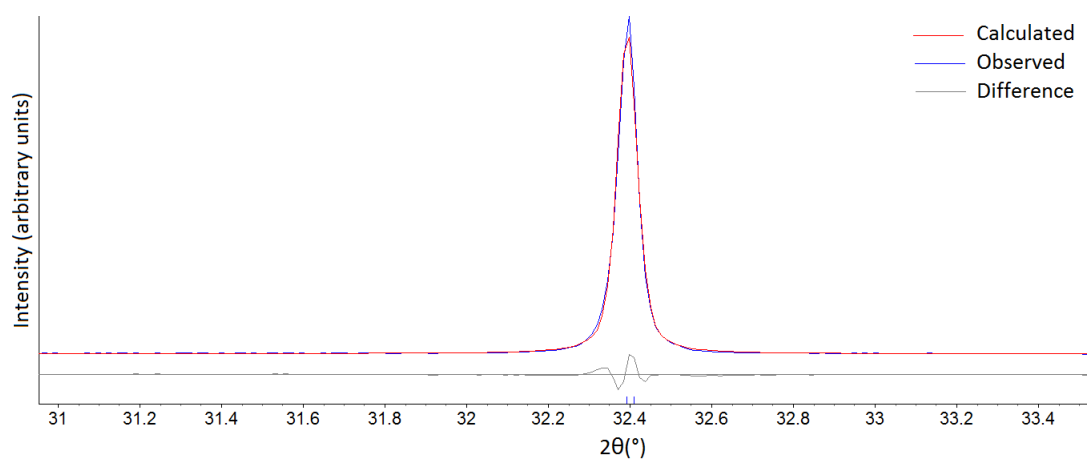


**Figure 3.38.** Plot showing fit, data and difference plot for  $\{110\}_{pc}$  XRD peak in  $R3c$  refinement of solid state NBT at 200 °C.

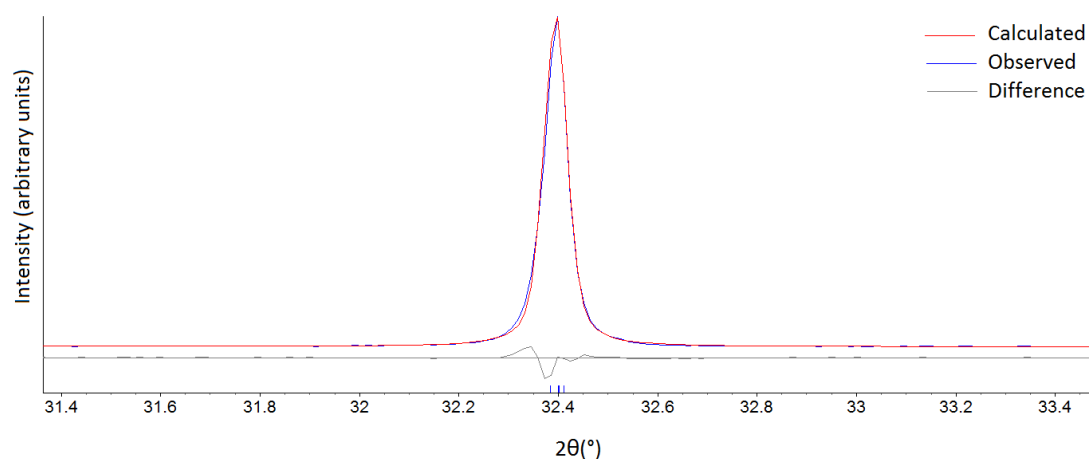


**Figure 3.39.** Plot showing fit, data and difference plot for  $\{110\}_{pc}$  XRD peak in  $Cc$  refinement of solid state NBT at 200 °C.

An analysis of data collected at 300 °C has also been carried out; this will be discussed later, in the context of the phase transition between the pseudo-rhombohedral symmetry seen at room temperature, and the tetragonal symmetry seen at 450 °C.

Temperature		450 °C	530 °C	600 °C
Crystal system		Tetragonal	Cubic	Cubic
Space group		$P4bm$	$Pm\bar{3}m$	$Pm\bar{3}m$
Tilt system		$a^0a^0c^+$	$a^0a^0c^0$	$a^0a^0c^0$
$a$ (Å)		5.52266(7)	3.91103(1)	3.91485(1)
$b$ (Å)				
$c$ (Å)				
$\alpha, \beta, \gamma$ (°)		90, 90, 90	90, 90, 90	90, 90, 90
Pseudo-cubic unit cell volume (Å <sup>3</sup> )		59.626(1)	59.8237(5)	59.9999(5)
No. Refined parameters		33	23	18
$R_{exp}$		6.607	6.619	6.672
$R_p$ (%)		7.844	7.429	8.383
$R_{wp}$ (%)		10.675	9.374	10.453
$R_{bragg}$ (%)		3.142	2.056	2.265
$\chi^2$		1.616	1.416	1.567
Na/Bi	$x$	0	0	0
	$y$	0.5	0	0
	$z$	0.507(5)	0	0
	U11 (Å <sup>2</sup> )	0.066(2)	0.0777(6)	0.0787(7)
	U22 (Å <sup>2</sup> )			
	U33 (Å <sup>2</sup> )			
	U12 (Å <sup>2</sup> )	0.001(2)	0	0
	U13, U23 (Å <sup>2</sup> )	0	0	0
Ti	$x$	0	0.5	0.5
	$y$	0	0.5	0.5
	$z$	0	0.5	0.5
	U11 (Å <sup>2</sup> )	-	0.0194(5)	0.0194(6)
	U22 (Å <sup>2</sup> )	-		
	U33 (Å <sup>2</sup> )	-		
	U12, U23, U23 (Å <sup>2</sup> )	-	0	0
	$b$ (Å <sup>2</sup> )	1.3(1)	-	-
O (I)	$x$	0	0.5	0.5
	$y$	0	0.5	0.5
	$z$	0.121(7)	0	0
	U11 (Å <sup>2</sup> )	-	0.038(1)	0.040(1)
	U22 (Å <sup>2</sup> )	-		
	U33 (Å <sup>2</sup> )	-		
	U12, U13, U23 (Å <sup>2</sup> )	-	0	0
	$b$ (Å <sup>2</sup> )	1.4(5)	-	-
O (II)	$x$	0.256(2)	-	-
	$y$	0.278(2)	-	-
	$z$	0.951(5)	-	-
	$b$ (Å <sup>2</sup> )	2.5(2)	-	-

**Table 3.11.** Lattice parameters, atomic positions, thermal displacement parameters, and refinement details for solid state NBT at 450 °C, 530 °C and 600 °C.

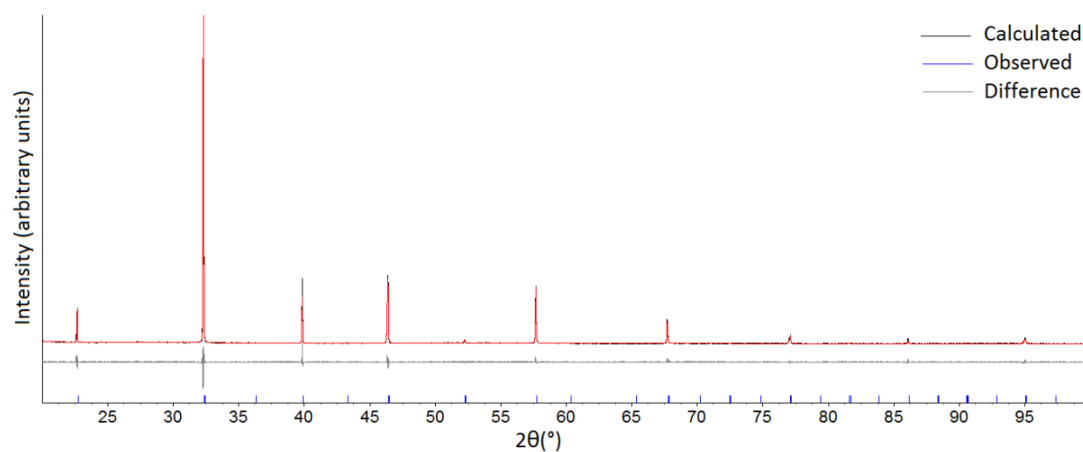


**Figure 3.40.** Plot showing fit, data and difference plot for  $P4bm$  refinement of solid state NBT at 450 °C.

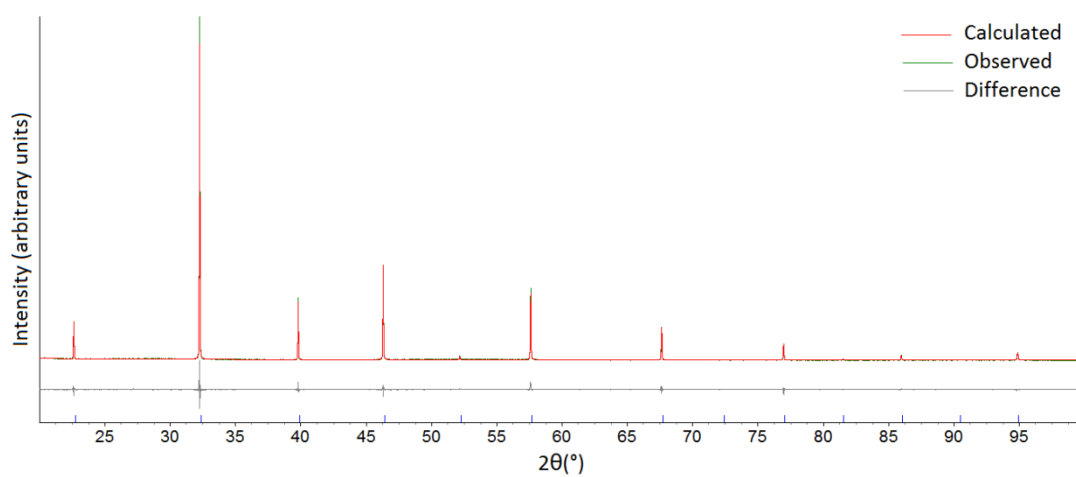


**Figure 3.41.** Plot showing fit, data and difference plot for  $Pm\bar{3}m$  refinement of solid state NBT at 530 °C.

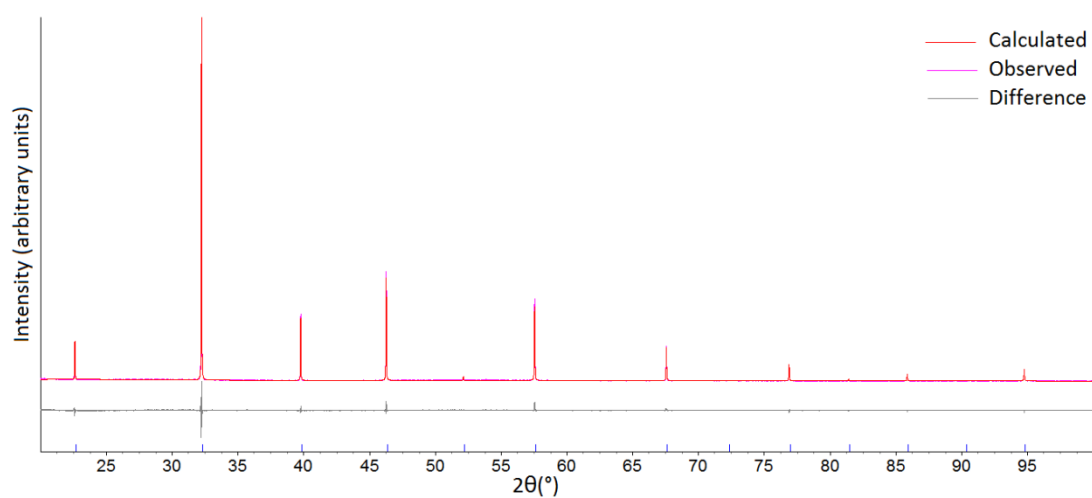


**Figure 3.42.** Plot showing fit, data and difference plot for  $Pm\bar{3}m$  refinement of solid state NBT at 600 °C.



Closer analysis of the  $2\theta$  range  $31^\circ - 41^\circ$  was employed to elucidate the phase transition, this range covering the  $\{110\}_{pc}$  and  $\{111\}_{pc}$  peaks as well as the  $\frac{1}{2}\{311\}_{pc}$  and  $\frac{1}{2}\{310\}_{pc}$  peaks seen in the room-temperature and tetragonal phases respectively (Figure 3.43). A step size of  $0.0131^\circ 2\theta$  and counting times of between 1000 – 3750 s were used; longer counting times were used in proximity to the phase transition, as a greater signal-to-noise ratio was desirable to observe the low-intensity superstructure peaks. Heating and cooling data were collected to investigate hysteresis.

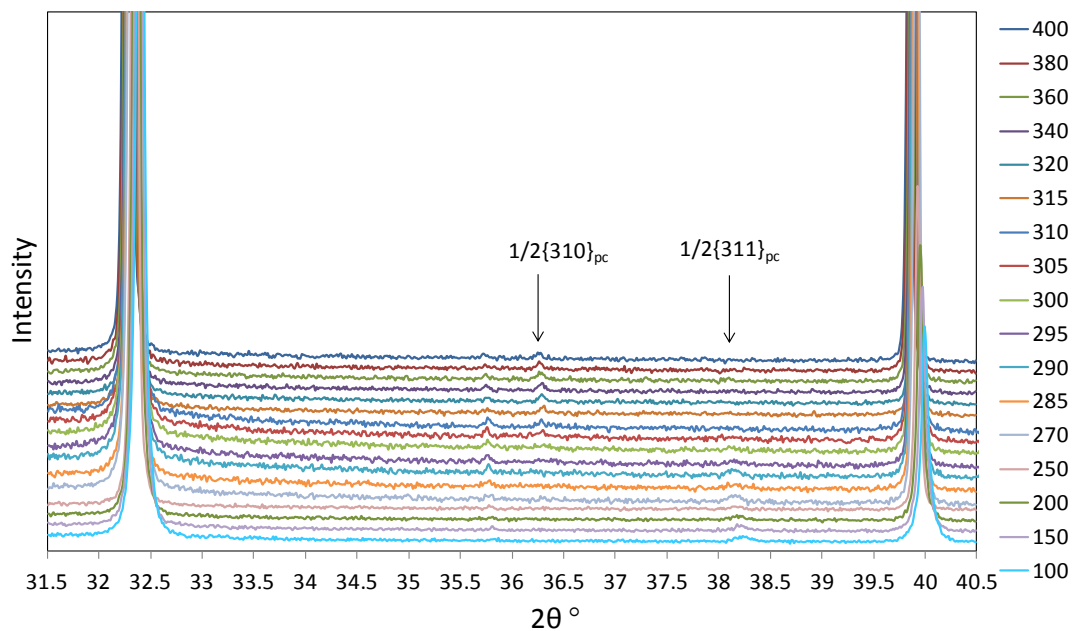


**Figure 3.43.** XRD data from NBT during heating from 100 – 400 °C, showing  $\frac{1}{2}\{311\}_{pc}$  peak at  $\approx 38^\circ 2\theta$  and  $\frac{1}{2}\{310\}_{pc}$  peak at  $\approx 36.3^\circ 2\theta$ , indicating phase transition at  $\approx 300^\circ\text{C}$ . The peak seen at  $\approx 35.8^\circ 2\theta$  arises from an impurity in the sample (data offset in the y axis).

The main peaks are observed to narrow with increasing temperature (Figure 3.44a). Both  $\{110\}_{pc}$  and  $\{111\}_{pc}$  peaks are observed to reach a minimum width in the range  $295\text{--}305^\circ\text{C}$ , clearly indicating this as a phase transition temperature. The increase in the  $\{110\}_{pc}$  peak width above this phase transition is consistent with emerging tetragonal symmetry. Cooling data (Figure 3.44b) show hysteresis in the phase transition temperature, with the peak widths converging at approximately  $280^\circ\text{C}$ , and narrow peak widths persisting until  $240^\circ\text{C}$ . This hysteresis effect has been observed in other studies<sup>16</sup>.

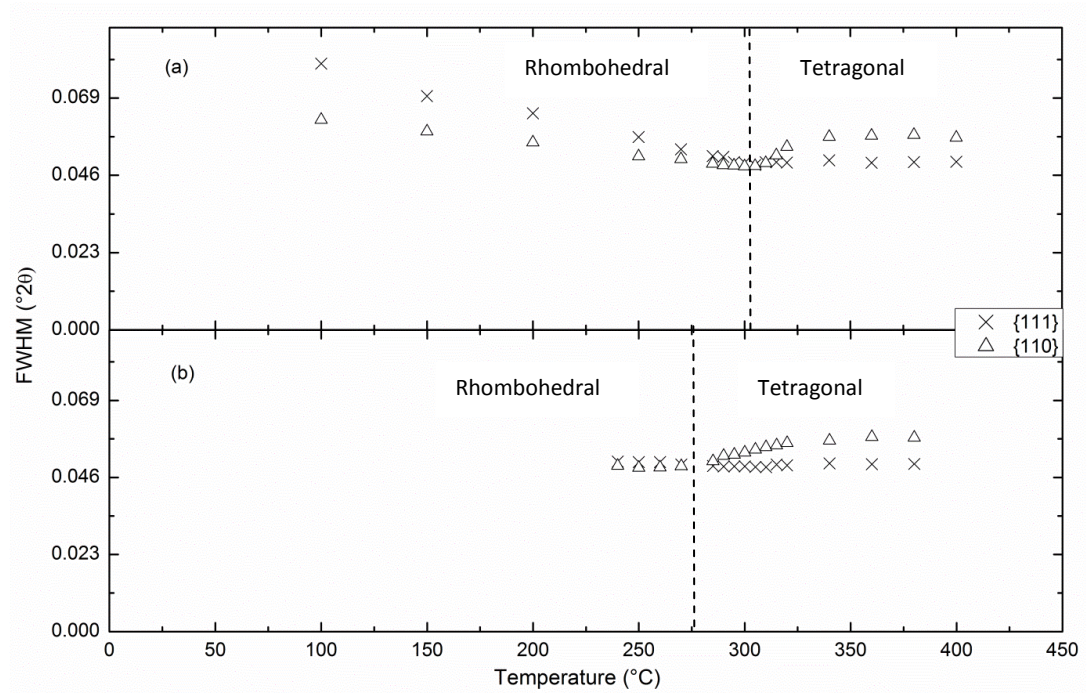


**Figure 3.44.** NBT  $\{110\}_{pc}$  and  $\{111\}_{pc}$  full width at half maximum variation with temperature a) on heating; b) on cooling.

Above  $\approx 300$  °C,  $\frac{1}{2}\{310\}_{pc}$  superstructure reflections associated with in-phase tilting are observed at  $36.5^\circ 2\theta$ , consistent with the tilted tetragonal structure with polar space group  $P4bm$ <sup>8</sup>. The intensities of the weak antiphase and in-phase superstructure reflections were measured using an iterative method after Sonneveld & Visser<sup>17</sup> in PANalytical HighScore Plus<sup>18</sup> and normalised against the most intense reflection. Plotted as a function of temperature (Figure 3.45), these follow the same trends as the peak widths. The intensities of the superstructure reflections reflect the octahedral tilt angle,<sup>19</sup> showing that the angle of tilt in the rhombohedral phase decreases as the phase transition is approached. The presence of both  $\frac{1}{2}\{311\}_{pc}$  and  $\frac{1}{2}\{310\}_{pc}$  peaks indicates the presence of either an intermediate phase or a phase coexistence region at 295-300 °C on heating, and 280-260 °C on cooling.

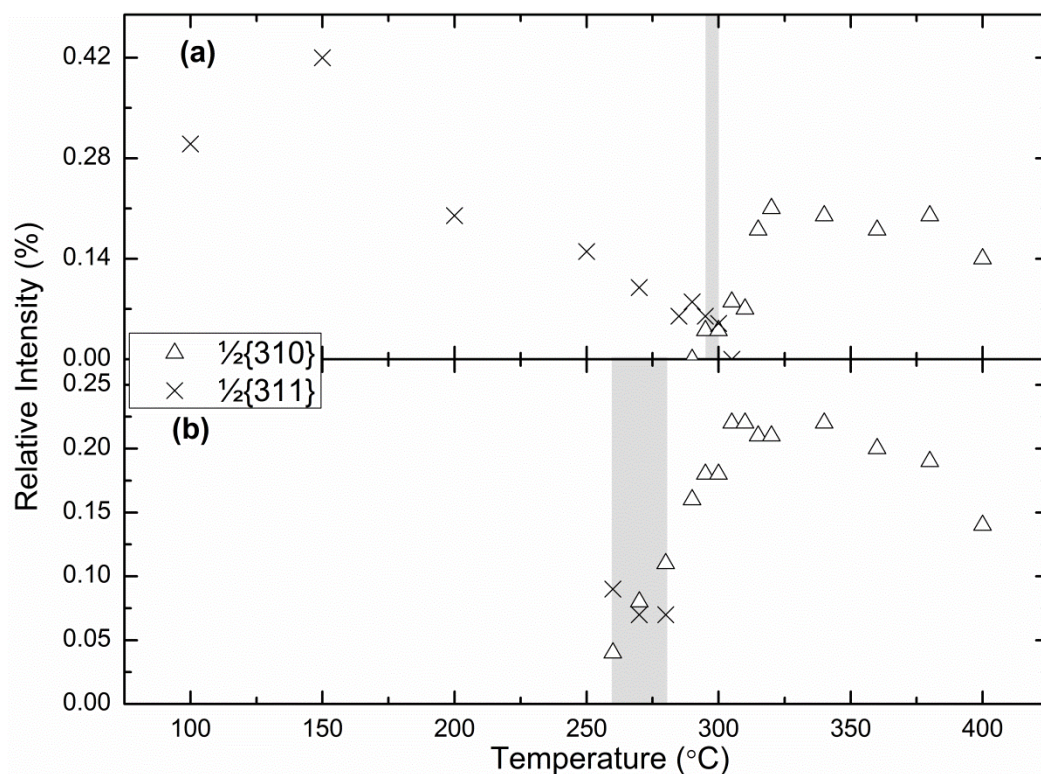


**Figure 3.45.** Intensity of the  $\frac{1}{2}\{311\}_{pc}$  and  $\frac{1}{2}\{310\}_{pc}$  XRD peaks relative to the intensity of the  $\{110\}_{pc}$  peak during: a) heating to 400 °C; b) cooling from 400 °C. Grey areas indicate the temperature range over which both peaks are seen to coexist.

Rietveld refinement was performed on a 20 – 100 °2 $\theta$  scan taken at 300 °C (heating), a temperature at which both superstructure peaks have been seen (Figure 3.45). As the counting time needed to distinguish these peaks from the background was 3750 s, these peaks cannot be observed in the scan from which the refinement was carried out, as it was necessary to reduce the counting time to 1750 s in order to scan a larger 2 $\theta$  range. The lack of distinguishable superstructure peaks (Figure 3.45), and narrow peak widths (Figures 3.44a and 3.46), gave a pattern that appeared cubic. Although it was possible to refine this pattern using distorted structural models they did not give a significantly better fit than a cubic refinement, neither visually nor based on *R*-factors.

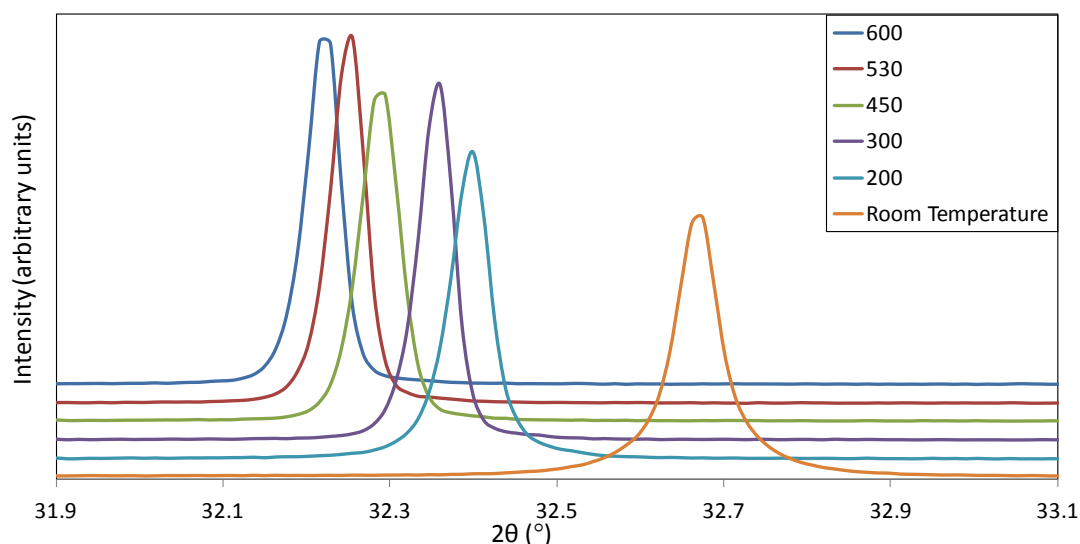


**Figure 3.46.**  $\{110\}_{pc}$  peak in NBT XRD patterns collected at room temperature, 200 °C, 300 °C, 450 °C, 530 °C and 600 °C. A sharper peak can be seen at the transition temperature (300 °C) than at 200 °C or 450 °C.

The possibility of an intermediate phase was considered;  $Pnma$ ,  $P2_1/m$ , or  $Cmcm$  would give both  $\frac{1}{2}\{311\}_{pc}$  and  $\frac{1}{2}\{310\}_{pc}$  peaks, but would also give rise to many additional peaks not seen in the pattern. Combinations of  $P4bm$  with  $R3c$ , and  $P4bm$  with  $Cc$  were tried as models for refinement. However, the data contained insufficient information on the distortion of the structure to support a multiphase refinement. Therefore, these refinements converged using one structure almost exclusively to fit the pattern, with the other having very broad peaks of almost no intensity. Using a single-phase model, it was possible to refine the data in any of these three space groups. Details of these refinements are compared with the cubic refinement in Table 3.12. These refinements are shown in Figures 3.47-3.50.

Crystal system	Rhombohedral	Monoclinic	Tetragonal	Cubic
Space group	$R3c$	$Cc$	$P4bm$	$Pm\bar{3}m$
Tilt system	$a^-a^-a^-$	$a^-a^-c^-$	$a^0a^0c^+$	$a^0a^0a^0$
$a$ (Å)	5.5137(1)	9.5506(4)	5.51307(4)	3.89872(2)
$b$ (Å)		5.5128(5)		
$c$ (Å)	13.5050(6)	5.5128(5)	3.89996(6)	
$\alpha, \beta, \gamma$ (°)	90, 90, 120	90, 125.243(4), 90	90, 90, 90	90, 90, 90
Pseudo-cubic unit cell volume (Å <sup>3</sup> )	59.260(3)	59.263(9)	59.268(1)	59.2606(9)
No. Refined parameters	22	40	25	20
$R_{exp}$	6.663	6.669	6.677	6.680
$R_p$ (%)	7.713	8.378	9.127	8.065
$R_{wp}$ (%)	9.738	10.907	11.328	10.081
$R_{bragg}$ (%)	2.590	4.924	2.415	2.083
$\chi^2$	1.461	1.635	1.697	1.509

**Table 3.12.** Lattice parameters and refinement details for solid state NBT at 300 °C.

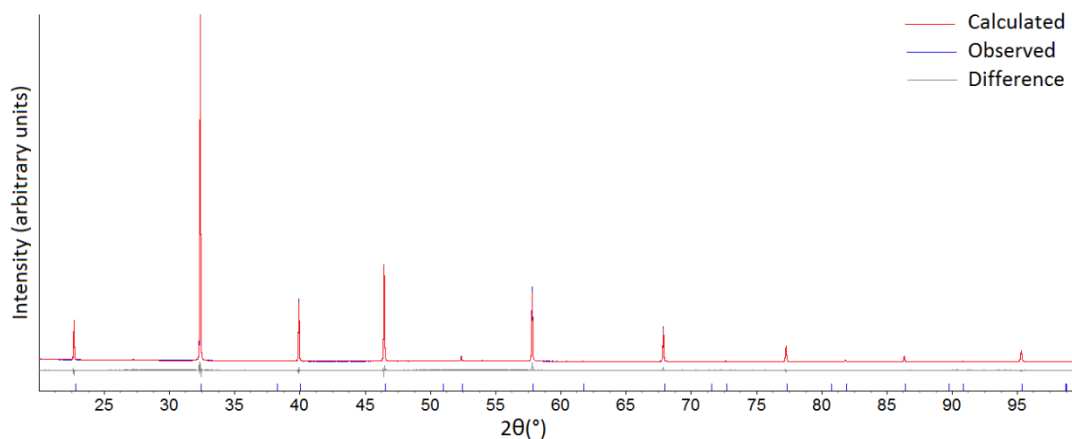


**Figure 3.47.** Plot showing fit, data and difference plot for  $R3c$  refinement of solid state NBT at 300 °C.

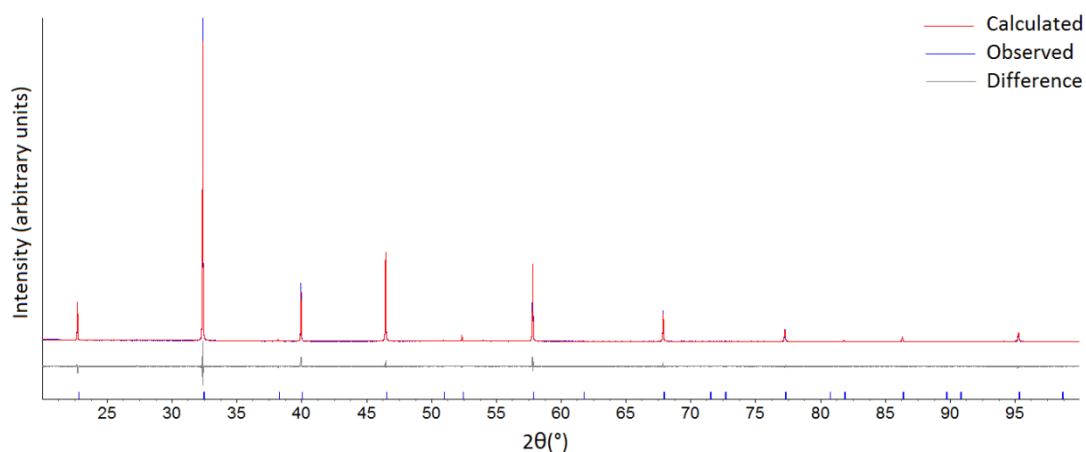


**Figure 3.48.** Plot showing fit, data and difference plot for  $Cc$  refinement of solid state NBT at 300 °C.

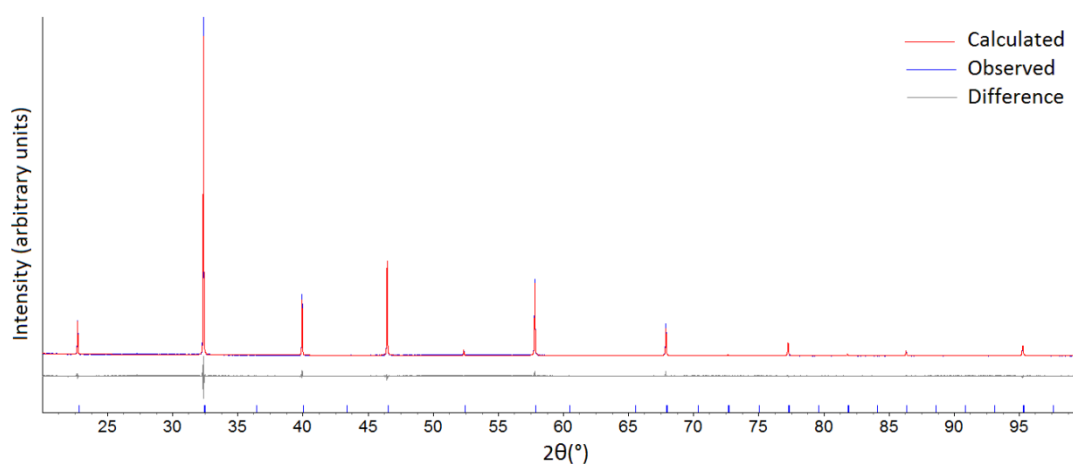


**Figure 3.49.** Plot showing fit, data and difference plot for *P4bm* refinement of solid state NBT at 300 °C.

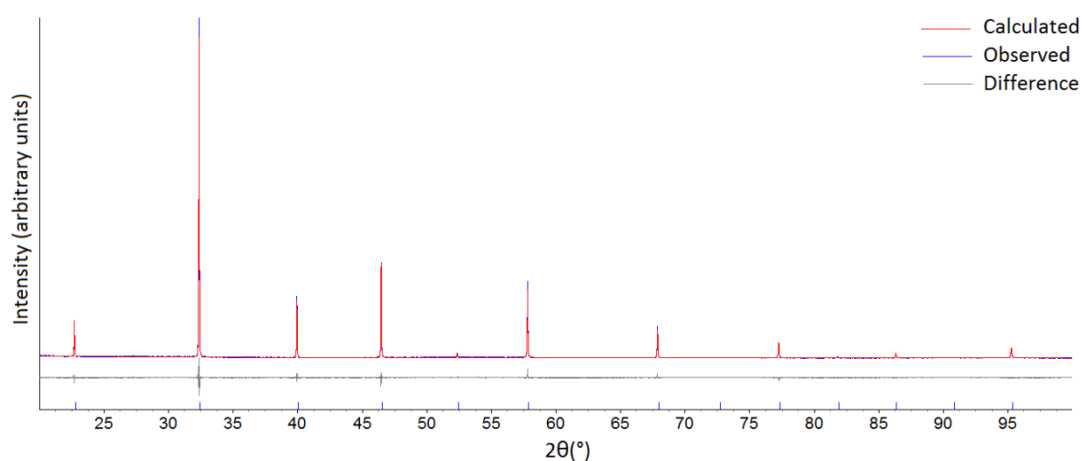


**Figure 3.50.** Plot showing fit, data and difference plot for *Pm3m* refinement of solid state NBT at 300 °C.

The cubic refinement is supported by the narrow peak widths shown in Figures 3.44a and 3.46. The superstructure peaks seen at this temperature (Figure 3.45a) establish the presence of distorted structure in at least part of the sample. However, as Figure 3.45a shows, these peaks are smallest at the transition temperature. A number of possible models of the behaviour at the transition temperature have been considered:

#### Model A:

Approaching the transition temperature, cubic domains form within the pseudo-rhombohedral bulk. These increase in size until the sample is entirely cubic. Tetragonal

domains form above the transition temperature, growing to form an entirely tetragonal sample. This is not considered a viable model as Figure 3.45 shows the overlap of rhombohedral/monoclinic and tetragonal superstructure peaks, not allowing for an intermediate cubic phase.

#### Model B:

Ingrowth of cubic domains occurs as in model A, but this time the tetragonal domains appear before the rhombohedral/monoclinic domains have been entirely erased. This model does not account for the narrowing of peaks seen as the transition temperature is approached (Figure 3.44), because the distorted structure on either side of the transition would be expected to contribute consistently broad peaks.

#### Model C:

The degree of rhombohedral/monoclinic distortion decreases towards the transition temperature. The rhombohedral angle approaches 90 and the angle of oxygen octahedral tilting approaches zero. After reaching an undistorted structure, tetragonal distortions appear, increasing to give the *P4bm* structure seen at 450 °C (Table 3.11). This is not considered a viable model as Figure 3.45 shows the overlap of rhombohedral/monoclinic and tetragonal superstructure peaks, not allowing for an intermediate cubic phase.

#### Model D:

At room temperature, rhombohedral/monoclinic distortion is present to different degrees in different domains within the sample. As in model C, this distortion decreases towards the transition temperature, becoming metrically cubic at  $\approx 300$  °C, before the onset of tetragonal distortion. However, the phase transition occurs at different rates or temperatures in different domains, leading to the overlap of rhombohedral/monoclinic and tetragonal symmetry evidenced in the superstructure peaks, and the suggestion of cubic structure seen in the narrow peak widths. The inconsiderable size of the distortions approaching the phase transition gives a diffraction pattern that appears cubic, with the



superstructure peaks contributing very little intensity. This is considered the most likely model, as it provides the most complete explanation of the data collected.

Figure 3.36 shows the pseudocubic lattice parameters and unit cell volumes of NBT between room temperature and 600 °C, using rhombohedral, monoclinic, tetragonal and cubic models. These show an approximately linear increase between 200 °C – 600 °C.

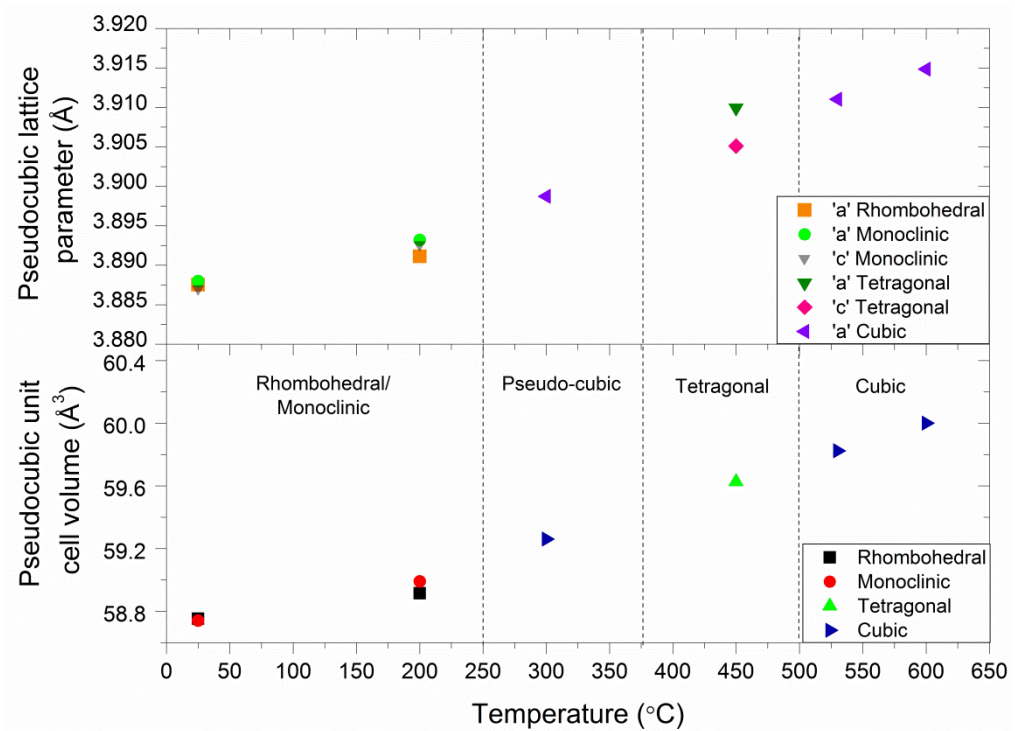


**Figure 3.51.** Pseudocubic lattice parameters and pseudocubic unit cell volumes of NBT between room temperature and 600 °C.

### 3.3.2 NBT doped with 1 at. % Mn

The temperature-dependent behaviour of MnNBT was investigated using XRD from 26 °C – 625 °C. Figure 3.52 shows the intensity of the  $\frac{1}{2}\{311\}_{pc}$  and  $\frac{1}{2}\{310\}_{pc}$  peaks relative to the intensity of the  $\{110\}_{pc}$  peak. It can be seen from this graph that the phase transition from rhombohedral to tetragonal symmetry occurs at 300 °C. As in NBT, the transition occurs via a coexistence of weakly-distorted rhombohedral and tetragonal structures. The  $\frac{1}{2}\{310\}_{pc}$  intensity reaches a maximum between 350 °C – 400 °C, indicating greatest



octahedral tilting angle in this temperature range, before decreasing as  $T_C$  is approached.

The absence of the  $\frac{1}{2}\{310\}_{pc}$  peak at 575 °C indicates  $T_C$  is approximately 550 °C.

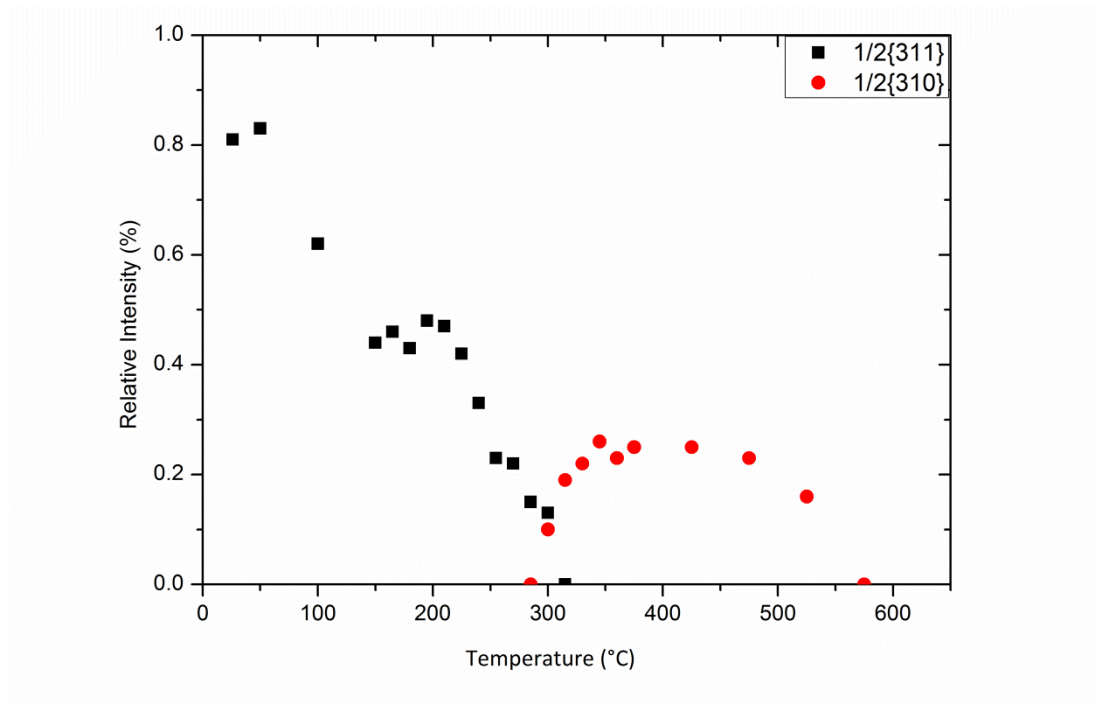


**Figure 3.52.** Relative Intensity of the  $\frac{1}{2}\{311\}_{pc}$  and  $\frac{1}{2}\{310\}_{pc}$  XRD peaks as a function of temperature.

Figures 3.53 and 3.54 show how the pseudo-cubic lattice parameters and unit cell volumes vary with temperature. Both of these graphs show an approximately linear increase with temperature. A splitting of the lattice parameters occurs on entering the tetragonal phase at 300 °C. A slight “bump” in the volume increase can be seen between 300 °C – 400 °C.  $T_C \sim 550$  °C. This is slightly higher than predicted for NBT, although it may be as low as  $\sim 525$  °C, which would allow  $T_C$  to be equal for both samples. Overall, the addition of 1% Mn to NBT appears to alter the structure and temperature-dependent behaviour very little.

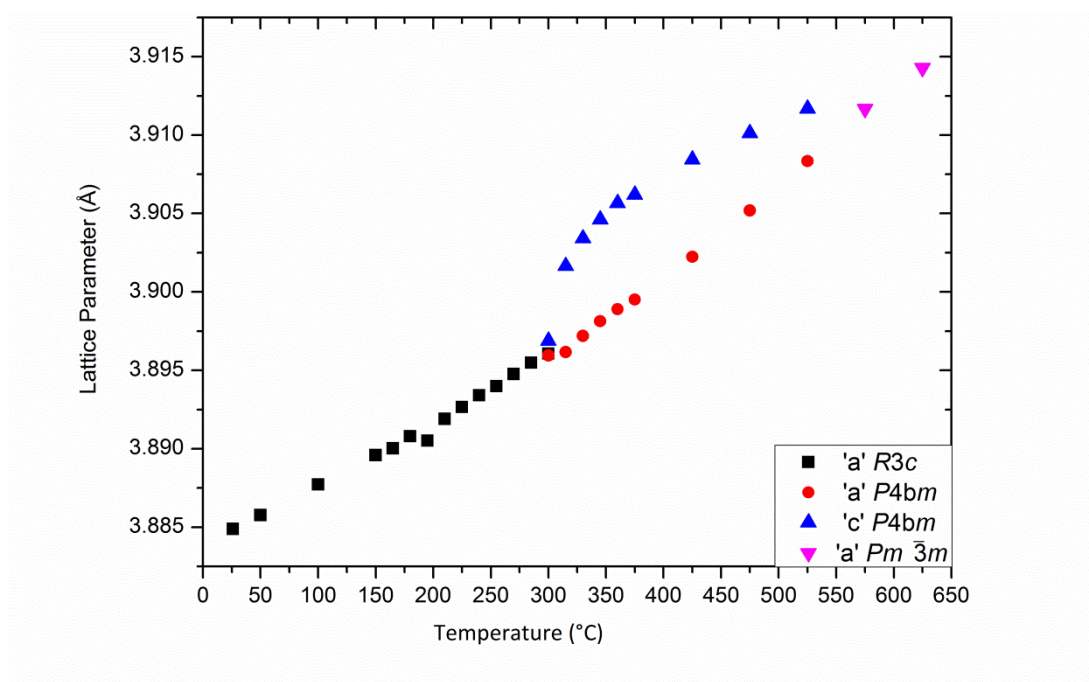


**Figure 3.53.** Pseudo-cubic lattice parameters of MnNBT, based on rhombohedral, tetragonal, and cubic models, as a function of temperature.

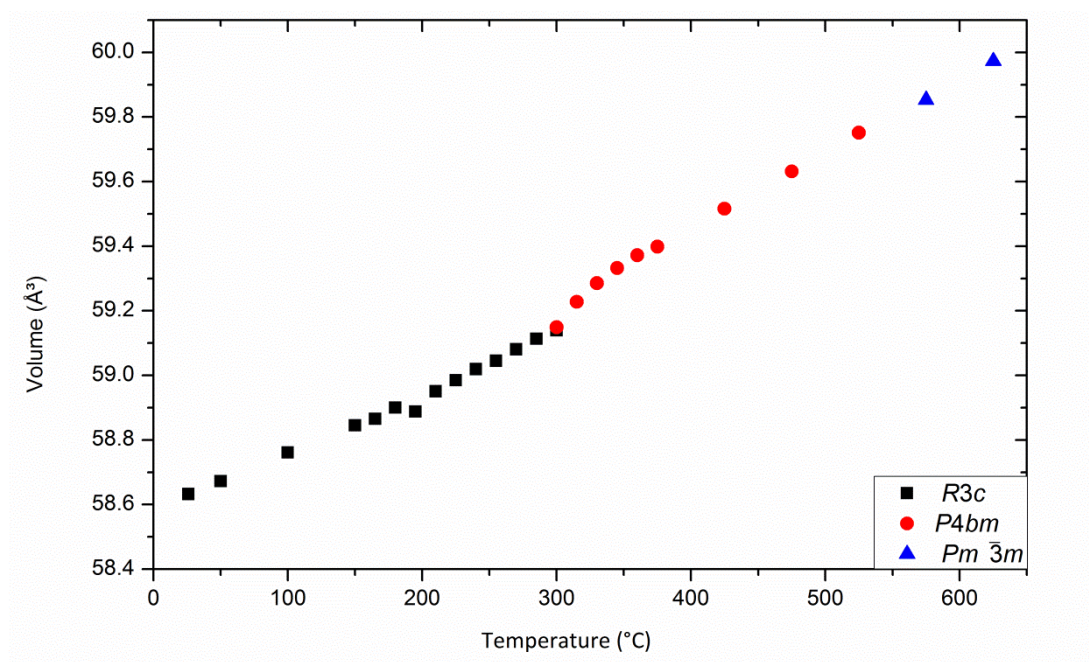


**Figure 3.54.** Pseudo-cubic unit cell volume of MnNBT as a function of temperature, based on rhombohedral, cubic, and tetragonal models.

### 3.3.3 KNBT10

KNBT10 structure as a function of temperature was investigated using XRD

between room temperature and 340 °C. Scans of the 31 - 41° 2θ range were collected at

temperatures up to 340 °C, as well as a 20 – 63.5° 2 $\theta$  scan at 335 °C. In subsequent experiments, 20 – 100° 2 $\theta$  scans were collected at 120 °C and 220 °C. The {110}<sub>pc</sub> and {111}<sub>pc</sub> peaks were fitted using a pseudo-Voigt peak function in OriginPro 8.5<sup>15</sup>; Figure 3.55 shows the FWHM. On heating from 25 °C - 220 °C, the {110}<sub>pc</sub> and {111}<sub>pc</sub> peak widths converge, indicating a decrease of the pseudo-rhombohedral distortion. At 220 °C the peak widths are equal. Above this temperature, the peak widths remain constant, indicating no change in the lattice parameters with increased temperature. Straight lines fitted by eye serve to illustrate the transition between the two trends, implying a phase transition at 220 °C. Following the initial experiment, 31 - 41° 2 $\theta$  scans were collected at finer temperature intervals of 10 °C between 170 – 260 °C (Figure 3.56), confirming 220 °C as the transition temperature.

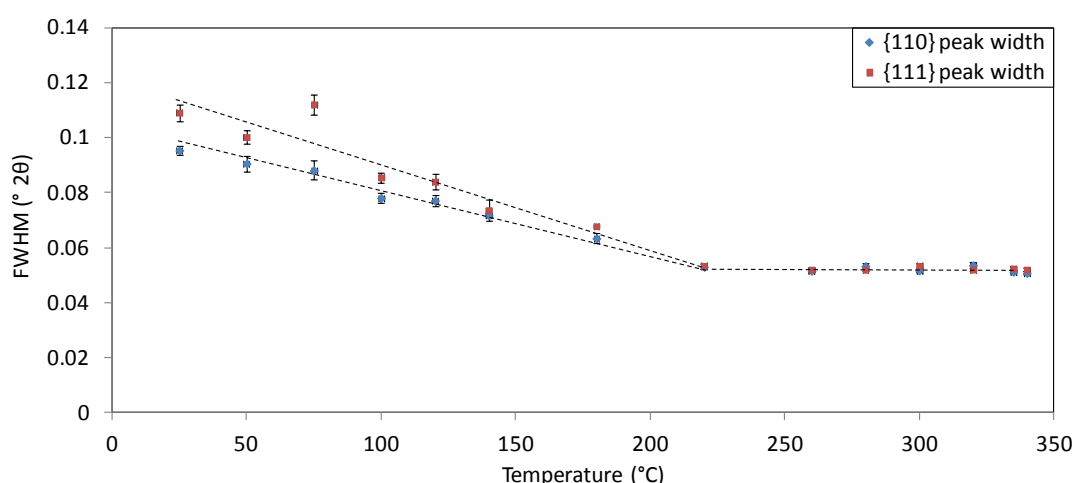


**Figure 3.55.** FWHM of the {110}<sub>pc</sub> and {111}<sub>pc</sub> peaks in KNBT10 on heating from room temperature to 340 °C. The lines are drawn as a guide to the eye.

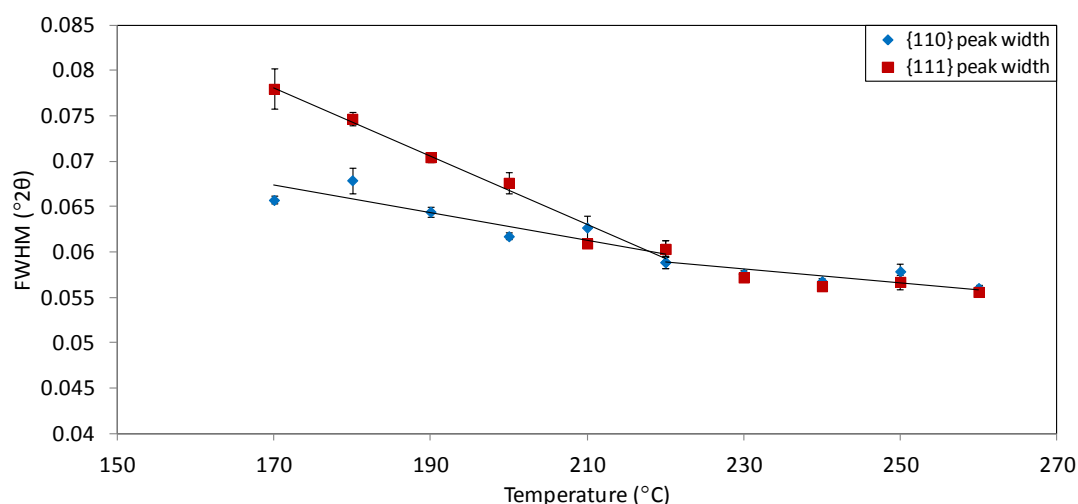


**Figure 3.56.** FWHM of the  $\{110\}_{pc}$  and  $\{111\}_{pc}$  peaks in KNBT10 on heating from room temperature to 260 °C, focusing on the region of phase transition. The lines indicate linear trends fitted to the data.

The intensity of the  $\frac{1}{2}\{311\}_{pc}$  peak relative to that of the  $\{110\}_{pc}$  was measured as a function of temperature (Figure 3.57). This is seen to decrease as the phase transition is approached, indicating a diminution in octahedral rotation leading to a phase transition at  $\approx 225$  °C. Unlike the 300 °C phase transition in NBT, the KNBT10 220 °C phase transition does not involve the emergence of the in-phase tilting  $\frac{1}{2}\{310\}_{pc}$  peak, indicating either a cubic or un-tilted tetragonal phase.

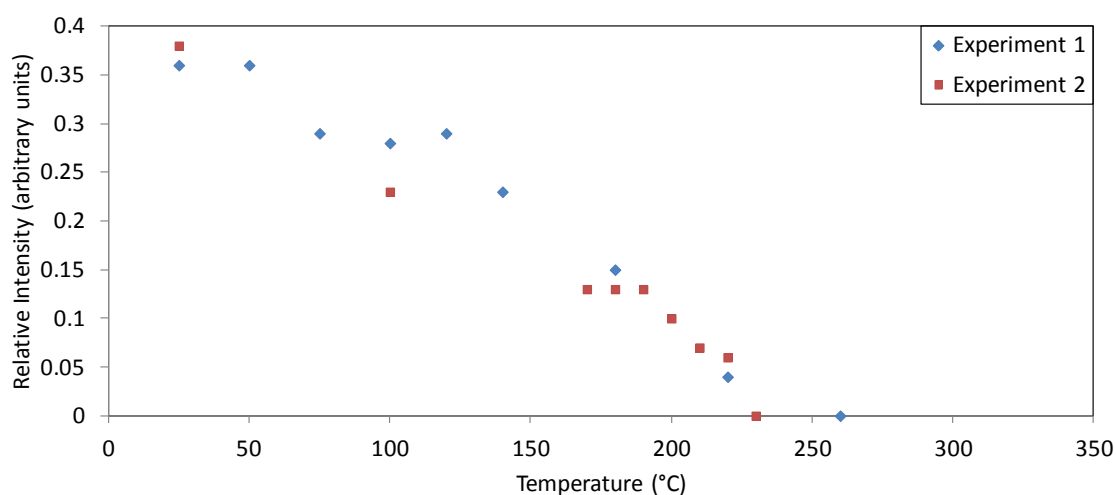


**Figure 3.57.** Intensity of the  $\frac{1}{2}\{311\}_{pc}$  XRD peak relative to the intensity of the  $\{110\}_{pc}$  XRD peak in KNBT10 when heated from room temperature to 340 °C.

Rietveld refinements have been carried out on data collected at 120 °C, 220 °C, and 335 °C. At 120 °C, refinements were performed using the *R3c* and *Cc* starting models obtained from the room temperature refinement. The details of these refinements are summarised in Tables 3.13 and 3.14. As with the room temperature refinements, there is little difference between the quality of the rhombohedral and monoclinic fits.

Temperature		120 °C	
Crystal system		Rhombohedral	Monoclinic
Space group		<i>R3c</i>	<i>Cc</i>
Tilt system		<i>a</i> <sup>−</sup> <i>a</i> <sup>−</sup> <i>a</i> <sup>−</sup>	<i>a</i> <sup>−</sup> <i>a</i> <sup>−</sup> <i>c</i> <sup>−</sup>
<i>a</i> (Å)		5.5118(1)	9.5478(5)
<i>b</i> (Å)			5.5100(2)
<i>c</i> (Å)		13.5135(5)	5.5166(3)
<i>α,β,γ</i> (°)		90, 90, 120	90, 125.253(4), 90
Pseudo-cubic unit cell volume (Å <sup>3</sup> )		59.256(2)	59.248(6)
No. Refined parameters		26	38
<i>R</i> <sub>exp</sub>		4.626	4.621
<i>R</i> <sub><i>p</i></sub> (%)		7.886	8.279
<i>R</i> <sub><i>wp</i></sub> (%)		10.118	10.642
<i>R</i> <sub><i>bragg</i></sub> (%)		2.686	5.600
<i>χ</i> <sup>2</sup>		2.187	2.303
Na/K/Bi	<i>x</i>	0	0
	<i>y</i>	0	0.25
	<i>z</i>	0.258(1)	0
	U11 (Å <sup>2</sup> )	0.043(2)	0.037(6)
	U22 (Å <sup>2</sup> )		0.053(5)
	U33 (Å <sup>2</sup> )	0.112(6)	0.064(7)
	U12 (Å <sup>2</sup> )	0.0216(9)	0.007(6)
	U13 (Å <sup>2</sup> )	0	0.01(1)
	U23 (Å <sup>2</sup> )	0	0.00(2)
Ti	<i>x</i>	0	0.25(1)
	<i>y</i>	0	0.251(5)
	<i>z</i>	0	0.75(9)
	<i>b</i> (Å <sup>2</sup> )	0.6(1)	-
O (I)	<i>x</i>	0.195(2)	0.2(1)
	<i>y</i>	0.860(2)	0.5(6)
	<i>z</i>	0.079(4)	0.0(4)
	<i>b</i> (Å <sup>2</sup> )	1.8(3)	-
O (II)	<i>x</i>	-	0.3(1)
	<i>y</i>	-	0.5(6)
	<i>z</i>	-	0.0(4)
O (III)	<i>x</i>	-	0.2(2)
	<i>y</i>	-	0.0(9)
	<i>z</i>	-	0.0(7)

**Table 3.13.** Lattice parameters, atomic positions, thermal displacement parameters, and refinement details for *P4mm* and *Pm3m* models of KNBT10 at 120 °C.

As the  $\frac{1}{2}\{310\}_{pc}$  peak seen above 300 °C in NBT is not present in KNBT10, an un-tilted  $P4mm$  structure was considered for the temperature range above 220 °C.

Alternatively, 220 °C may mark the Curie transition to a cubic structure. This theory is supported by the trend in the  $\{110\}_{pc}$  and  $\{111\}_{pc}$  peak widths, which do not diverge, as would be expected from a strained tetragonal structure, but remain constant after meeting at the transition temperature. For 220 °C and 335 °C, refinements have been carried out using both  $P4mm$  and  $Pm\bar{3}m$  models. It will be noted that at 220 °C the  $\frac{1}{2}\{311\}_{pc}$  peak is still present, confirming that the structure cannot purely be either of these; however, the intensity of this peak is very low, suggesting that if the structure is bi-phasic then a basic refinement should be possible using either of these phases. It can be seen from Table 3.14 that the quality of the fits is equivalent for cubic and tetragonal structures. At 335 °C, the structure is cubic, based on the observation of narrow peak widths and the absence of superstructure peaks. At 220 °C, there is evidence (the  $\frac{1}{2}\{311\}_{pc}$  peak) of a weakly distorted rhombohedral/monoclinic structure. As with the NBT 300 °C phase transition, it is proposed that the distorted structure seen at room temperature tends towards metrically cubic as the transition temperature is approached (explaining the converging  $\{110\}_{pc}$  and  $\{111\}_{pc}$  peak widths, and the diminishing  $\frac{1}{2}\{311\}_{pc}$  peak). However, unlike in NBT, this is not accompanied by the formation of tetragonal domains, but by the onset of cubic symmetry.

Temperature		220 °C		335 °C	
Crystal system		Tetragonal	Cubic	Tetragonal	Cubic
Space group		<i>P4mm</i>	<i>Pm</i> 3 <i>m</i>	<i>P4mm</i>	<i>Pm</i> 3 <i>m</i>
<i>a</i> (Å)	3.9032(1)	3.90322(2)	3.90851(8)	3.90871(3)	
<i>b</i> (Å)			3.9094(2)		
<i>c</i> (Å)					
$\alpha,\beta,\gamma$ (°)	90, 90, 90	90, 90, 90	90, 90, 90	90, 90, 90	
Pseudo-cubic unit cell volume (Å <sup>3</sup> )		59.468(3)	59.4660(9)	59.722(3)	59.717(1)
No. Refined parameters		29	24	18	16
<i>R</i> <sub>exp</sub>		4.366	4.367	4.538	4.540
<i>R</i> <sub><i>p</i></sub> (%)		5.144	5.147	7.311	7.040
<i>R</i> <sub><i>wp</i></sub> (%)		6.590	6.617	9.087	8.757
<i>R</i> <sub><i>bragg</i></sub> (%)		1.339	1.496	2.510	0.989
$\chi^2$		1.510	1.515	2.002	1.929
Na/K/Bi	<i>x</i>	0	0	0	0
	<i>y</i>	0	0	0	0
	<i>z</i>	0.975(3)	0	0.99(1)	0
	U11 (Å <sup>2</sup> )	0.08(2)	0.0705(4)	0.060(6)	0.0652(9)
	U22 (Å <sup>2</sup> )				
	U33 (Å <sup>2</sup> )			0.08(1)	
	U12 (Å <sup>2</sup> )	0	0	0	0
	U13 (Å <sup>2</sup> )	0	0	0	0
	U23 (Å <sup>2</sup> )	0	0	0	0
Ti	<i>x</i>	0.5	0.5	0.5	0.5
	<i>y</i>	0.5	0.5	0.5	0.5
	<i>z</i>	0.5	0.5	0.5	0.5
	<i>b</i> (Å <sup>2</sup> )	0.77(5)	1.22(3)	-	0.46(8)
O (I)	<i>x</i>	0.5	0.5	0	0.5
	<i>y</i>	0.5	0.5	0	0.5
	<i>z</i>	0.01(1)	0	0.07(2)	0
	<i>b</i> (Å <sup>2</sup> )	3(2)	3.10(6)	-	2.3(1)
O (II)	<i>x</i>	0.5	-	0.5	-
	<i>y</i>	0	-	0	-
	<i>z</i>	0.430(5)	-	0.45(2)	-
	<i>b</i> (Å <sup>2</sup> )	1.8(8)	-	-	-

**Table 3.14.** Lattice parameters, atomic positions, thermal displacement parameters, and refinement details for *P4mm* and *Pm3m* models of KNBT10 at 220 °C and 335 °C.

### 3.3.4 KNBT40

The previously-used method of high-temperature XRD analysis was applied to KNBT40, a composition which was refined at room-temperature as a combination of rhombohedral and tetragonal structures. In this case, tilt peak analysis was not applicable, as both structures are un-tilted. The linear decreases with temperature observed in both

the  $\{110\}_{pc}$  and  $\{111\}_{pc}$  FWHM converge at approximately 280 °C (Figure 3.58). Between 280 °C and 450 °C, a small decrease in FWHM is observed. From Figure 3.58, a phase transition can be inferred at approximately 280 °C.

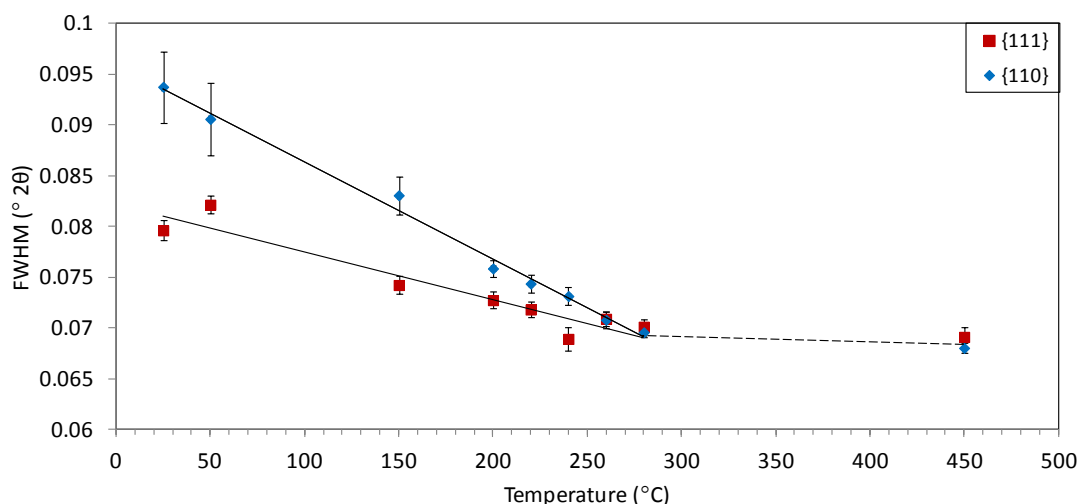


**Figure 3.58.** FWHM of the  $\{110\}_{pc}$  and  $\{111\}_{pc}$  XRD peaks in KNBT40 on heating from room temperature to 450 °C. The solid lines represent fits to the data; the dashed line is drawn as a guide to the eye.

As the tetragonal structure does not give a split  $\{111\}_{pc}$  peak, the decrease in  $\{111\}_{pc}$  peak width observed up to 280 °C can be attributed only to the rhombohedral phase. It has been assumed that the transition to cubic takes place at the same temperature in both phases, although this may not necessarily be the case.

The structures at 280 °C and 450 °C were analysed by Rietveld refinement. At 280 °C, the peak shape characteristic of the room-temperature  $R3m/P4mm$  structure is no longer visible (Figure 3.59). However, as the  $\{110\}_{pc}$  FWHM shows a continuous decrease to 280 °C with no evidence of a phase transition below this temperature, the  $R3m/P4mm$  combination has been considered a potential model. To investigate the possibility of a phase transition at 280 °C, refinement was also carried out using a single-phase  $P4mm$  model, beginning with the unit cell generated from the multiphase refinement. A single phase  $R3m$  structure was also tried, and was rejected on the basis of its poor visual fit and



higher  $R$ -factors. Subtle evidence of peak splitting indicates a non-cubic symmetry (Figure 3.60), so a cubic refinement has not been performed. The results of the 280 °C refinements are given in Table 3.14.

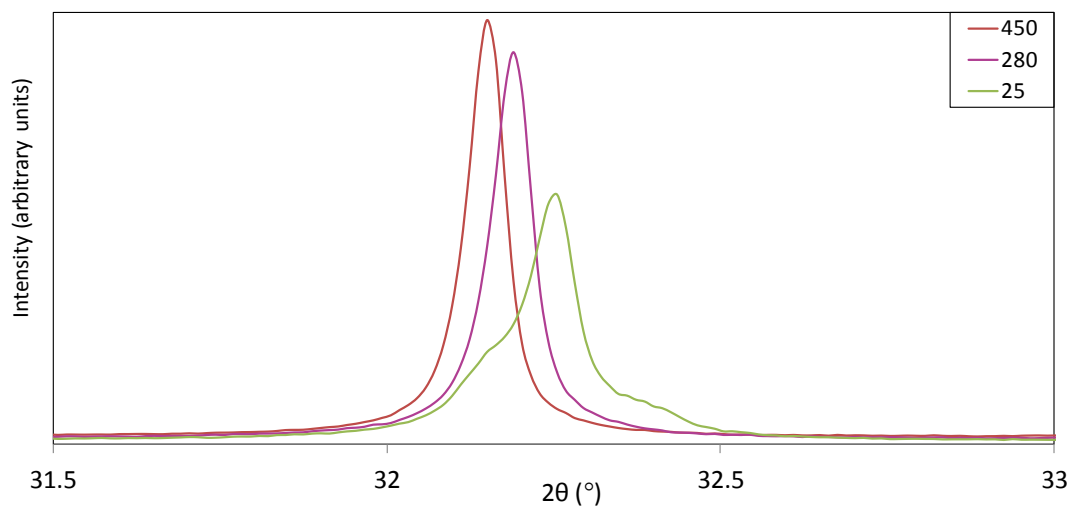


**Figure 3.59.** {110}<sub>pc</sub> XRD peak of KNBT40 at 25 °C, 280 °C, and 450 °C, showing visible splitting at 25 °C only.

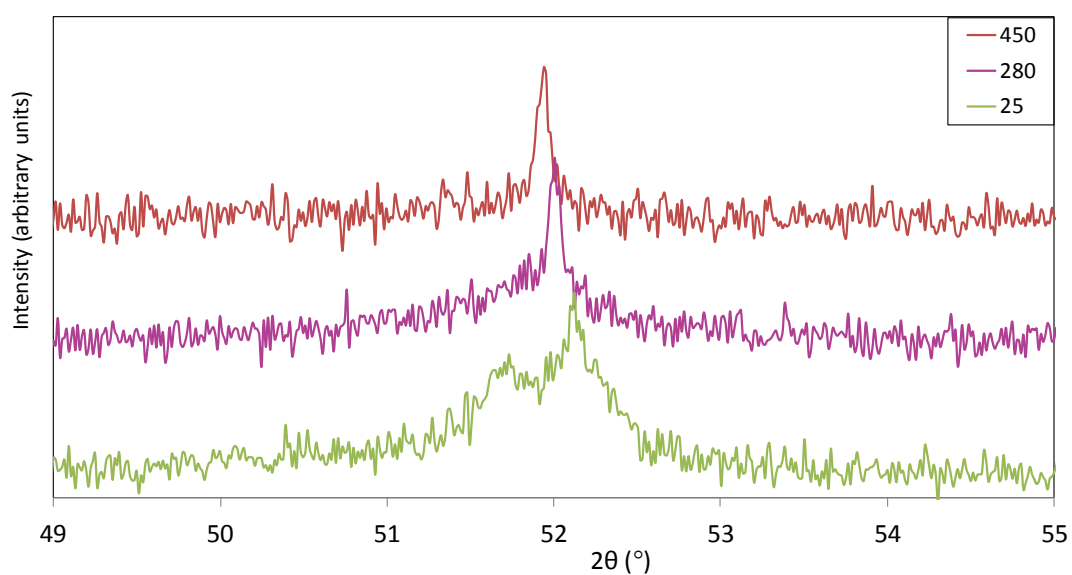


**Figure 3.60.** {210}<sub>pc</sub> XRD peak of KNBT40 at 25 °C, 280 °C, and 450 °C. Although the splitting seen at 25 °C is not as distinct at 280 °C, comparison with the 450 °C data shows that some peak broadening not consistent with cubic symmetry is still present.

Crystal systems		Rhombohedral & Tetragonal		Tetragonal	Rhombohedral
Space group		<i>R3m</i>	<i>P4mm</i>	<i>P4mm</i>	<i>R3m</i>
Relative abundance (%)		74.9	25.1	100.0	100.0
<i>a</i> , <i>b</i> (Å)		5.5571(8)	3.9245(3)	3.92898(4)	5.55690(4)
<i>c</i> (Å)		6.806(2)	3.9490(7)	3.93117(8)	6.8082(2)
$\alpha, \beta, \gamma$ (°)		90, 90, 120	90, 90, 90	90, 90, 90	90, 90, 120
Pseudo-cubic unit cell volume (Å <sup>3</sup> )		60.67(2)	60.82(1)	60.685(1)	60.689(2)
No. Refined parameters		35		27	28
<i>R</i> <sub>exp</sub>		4.962		4.965	4.965
<i>R</i> <sub>p</sub> (%)		7.035		7.428	7.880
<i>R</i> <sub>wp</sub> (%)		8.975		9.905	10.148
<i>R</i> <sub>bragg</sub> (%)		1.860	2.526	2.356	2.358
$\chi^2$		1.809		1.995	2.044
Na/K/Bi	<i>x, y</i>	0	0	0	0
	<i>z</i>	0.991(2)			0.992(1)
	<i>b</i> (Å <sup>2</sup> )	7.0(1)	5.2(3)	-	-
	U11, U22 (Å <sup>2</sup> )	-	-	0.074(1)	0.070(2)
	U33 (Å <sup>2</sup> )	-	-	0.146(5)	0.172(8)
	U12 (Å <sup>2</sup> )	-	-	0	0.0352(8)
	U13, U23 (Å <sup>2</sup> )	-	-	0	0
Ti	<i>x</i>	0	0.5	0.5	0
	<i>y</i>	0	0.5	0.5	0
	<i>z</i>	0.5	0.568(5)	0.5	0.5
	<i>b</i> (Å <sup>2</sup> )	1.1(1)	2.3(6)	-	1.53(6)
O (I)	<i>x</i>	0.154(2)	0.5	0.5	0.1678(9)
	<i>y</i>	0.886(3)	0.5	0.5	0.8322(9)
	<i>z</i>	0.846(2)	0.668(6)	0.03(1)	0.367(2)
O (II)	<i>x</i>	-	0.5	0.5	-
	<i>y</i>	-	0.5	0	-
	<i>z</i>	-	0.27(1)	0.431(4)	-

**Table 3.15.** Lattice parameters, atomic positions, thermal displacement parameters, and refinement details for *P4mm* and *R3m/P4mm* models of KNBT40 at 280 °C.

Table 3.15 shows that the *R*-factors for the *P4mm* fit are only slightly higher than those for the *R3m/P4mm* fit. However, the *P4mm* model does not adequately describe the peak asymmetry at  $\approx 52^\circ 2\theta$ . It is concluded that the structure is still *R3m/P4mm*, and the phase transition inferred from the FWHM data takes place at a temperature above 280 °C.

At 450 °C, the peak asymmetry characteristic of the multiphase structure is gone (Figures 3.59 and 3.60). Single phase refinements have been carried out using *Pm $\bar{3}$ m*, *P4mm*, and *R3m* models. The results of these refinements are summarised in Table 3.16.

Crystal systems		Cubic	Tetragonal	Rhombohedral
Space group		$Pm\bar{3}m$	$P4mm$	$R3m$
Relative abundance (%)		100.0	100.0	100.0
$a, b$ (Å)		3.93264(3)	3.93221(7)	5.56294(4)
$c$ (Å)			3.9336(1)	6.8175(2)
$\alpha, \beta, \gamma$ (°)		90, 90, 90	90, 90, 90	90,90,120
Pseudo-cubic unit cell volume (Å <sup>3</sup> )		60.821(1)	60.822(2)	60.904(2)
No. Refined parameters		23	29	32
$R_{exp}$		4.960	4.958	4.957
$R_p$ (%)		6.372	6.296	7.098
$R_{wp}$ (%)		8.069	8.014	9.334
$R_{bragg}$ (%)		1.583	1.730	2.677
$\chi^2$		1.627	1.625	1.883
Na/K/Bi	$x, y$	0	0	0
	$z$	0	0.983(3)	0.998(1)
	U11 (Å <sup>2</sup> )	0.0903(7)	0.098(5)	0.094(3)
	U22 (Å <sup>2</sup> )			
	U33 (Å <sup>2</sup> )		0.10(1)	0.097(7)
	U12 (Å <sup>2</sup> )	0	0	0.047(1)
	U13, U23 (Å <sup>2</sup> )			0
Ti	$x$	0.5	0.5	0
	$y$	0.5	0.5	0
	$z$	0.5	0.5	0.5
	$b$ (Å <sup>2</sup> )	1.76(4)	1.57(6)	1.72(5)
O (I)	$x$	0.5	0	0.1672(8)
	$y$	0.5	0	0.8328(8)
	$z$	0	0.028(8)	0.295(2)
	$b$ (Å <sup>2</sup> )	2.3(1)	1.9(9)	-
O (II)	$x$	-	0.5	-
	$y$	-	0.417(4)	-
	$z$	-	1.0(5)	-

**Table 3.16.** Lattice parameters, atomic positions, thermal displacement parameters, and refinement details for  $Pm\bar{3}m$ ,  $P4mm$ , and  $R3m$  models of KNBT40 at 450 °C.

The fit produced by the  $R3m$  model is inferior to that of the cubic or tetragonal models, as evidenced by the  $R$ -factor values. There is little difference in quality between the  $Pm\bar{3}m$  and  $P4mm$  models. The use of the lower symmetry model to describe the structure cannot, therefore, be justified, and it is concluded that the structure is cubic;  $T_c$  must lie between 280 °C – 450 °C. The decrease in FWHM over this temperature range is very small in comparison with the fitted trends below 280 °C, indicating that  $T_c$  is at the

lower end of the range. Based on these refinements and the FWHM data, it is suggested that  $T_c \approx 300^\circ\text{C}$ .

### 3.4 Summary

A tentative phase diagram has been proposed, using published phase transition temperatures<sup>20</sup> in combination with those determined by this study (Figure 3.61).

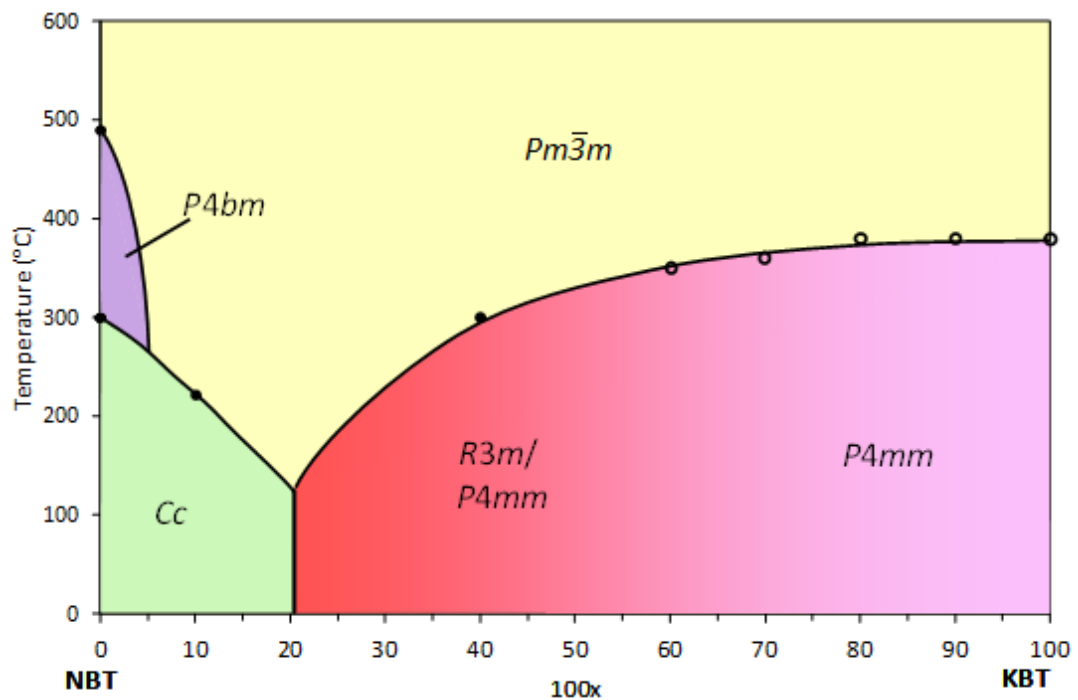


**Figure 3.61.** Phase diagram of the KNBT system. Filled circles represent results collected in this study; hollow circles represent results from Elkechai *et al.*, 1996<sup>20</sup>

The room-temperature phase of NBT – KNBT20 has been assigned monoclinic *Cc* symmetry. Although good *R3c* refinements of KNBT05-20 XRD data have been produced, those in *Cc* have better *R*-factors (Tables 3.3 and 3.4). The refinements in this study favour *R3c* for the NBT end-member but, as recent published literature supports a monoclinic model<sup>2, 3, 16, 21, 22</sup>, the *Cc* phase region has been extended to include NBT.

A phase boundary has been drawn close to KNBT20. Between KNBT20-25, a change in phase was shown using Rietveld refinement, supported by the discontinuous changes in

pseudo-cubic unit cell volume and lattice parameter (Figures 3.22 & 3.23). Enhanced electromechanical properties, associated with morphotropic phase boundaries<sup>14</sup>, have been observed in compositions of  $x \approx 0.2$ <sup>12</sup>, suggesting this boundary to be such. High-temperature data from compositions close to this point would be required to confirm minimal temperature-dependence of this boundary.

Whilst there is a consensus in the literature on the tetragonal symmetry of the KBT end-member<sup>9, 10, 11, 20</sup>, there is considerable disagreement regarding the mid-range compositions. Reported possibilities include a bi-phasic region at KNBT20-60<sup>20</sup>, morphotropic regions at KNBT16-20<sup>23</sup> and KNBT17-25<sup>12</sup>, and intermediate phase regions at KNBT50-80<sup>10</sup> and KNBT18-40<sup>24</sup>. It has been suggested that this discord is a result of sensitivity to the preparation conditions<sup>12</sup>. This study has found no evidence of an intermediate phase, but instead found bi-phasic  $R3m/P4mm$  compositions extending as far as KNBT65. It is proposed that stress-induced phase transition is responsible for the presence of  $R3m$  material in this region of the phase diagram. This would account for the fluctuation in the amount of rhombohedral material seen in KNBT25-65 (Figure 3.30). The  $R3m$  component decreases inconsistently with higher potassium substitution, suggesting that the structure is not effected purely by composition but also by processing conditions. The overall decrease indicates that compositions near the phase boundary may be more susceptible to phase transition.

The rhombohedral-tetragonal phase transition temperature in NBT has been determined as 300 °C. Evidence of this phase transition was not seen in KNBT10, which appeared to become cubic, with a much lower  $T_c$  than NBT. A narrow  $P4bm$  region has therefore been drawn, extending upwards to 490 °C. This temperature has not been conclusively determined, but lies halfway between the temperatures at which tetragonal and cubic structures were observed (450 °C and 530 °C). KNBT40 did not show evidence of high-temperature phase transition other than the Curie transition, at  $T_c \approx 300$  °C. On the

basis of the  $T_c$  values found for KNBT10 and KNBT40, and those reported in the literature<sup>20</sup>, curves have been drawn marking the upper boundaries of the monoclinic and tetragonal/multiphase regions. Similar curved line shapes, with a dip in the location of the phase boundary, are reported by Hiruma *et al.* (2008)<sup>25</sup>.

The addition of 1 at. % Mn to NBT was not found to have a marked effect on the room temperature structure, or the transition to tetragonal symmetry, which occurred at 300 °C. In MnNBT, the Curie transition was found to lie between 525 °C – 575 °C, while in NBT  $450\text{ °C} < T_c < 530\text{ °C}$ . Although differing values of  $T_c$  have been assigned to NBT and MnNBT (490 °C and 550 °C respectively), it is possible that  $T_c$  occurs in the range 525 °C – 530 °C in both materials.

## References

- <sup>1</sup> S. B. Vakhrushev, B. G. Ivanitskii, B. E. Kvyatkovskii, A. N. Maistrenko, N. M. Malysheva, and N. N. Parfenova, *Sov. Phys. Solid State* **25**, 1504 (1983).
- <sup>2</sup> S. Gorfman and P. A. Thomas, *J. Appl. Cryst.* **43**, 1409 (2010).
- <sup>3</sup> E. Aksel, J. S. Forrester, B. Kowalski, J. L. Jones, and P. A. Thomas, *Appl. Phys. Lett.* **99**, 222901 (2011).
- <sup>4</sup> J. Kreisel, P. Bouvier, B. Dkhil, P. A. Thomas, A. M. Glazer, T. R. Welberry, B. Chaabane, and M. Mezouar, *Phys. Rev. B* **68**, 14113 (2003).
- <sup>5</sup> P. A. Thomas, S. Trujillo, M. Boudard, S. Gorfman, and J. Kreisel, *Solid State Sci.* **12**, 311 (2010).
- <sup>6</sup> R. D. Shannon and C. T. Prewitt, *Acta. Cryst. B* **25**, 925 (1969).
- <sup>7</sup> C. F. Buhner, *J. Chem. Phys.* **36**, 798 (1962).
- <sup>8</sup> G. O. Jones and P. A. Thomas, *Acta Cryst. B* **58**, 168 (2002).
- <sup>9</sup> V. A. Isupov, *Ferroelectrics* **315**, 123 (2005).
- <sup>10</sup> J. Kreisel, A. M. Glazer, G. Jones, P. A. Thomas, L. Abello, and G. Lucazeau, *J. Phys. Condens. Mat.* **12**, 3267 (2000).
- <sup>11</sup> S. M. Emel'yanov, I. P. Raevskii, and F. I. Savenko, *Fiz. Tverd. Tela.* **29**, 2511 (1987).
- <sup>12</sup> M. Otonicar, S. D. Skapin, M. Spreitzer, and D. Suvorov, *J. Am. Ceram. Soc.* **30**, 971 (2010).
- <sup>13</sup> J. C. Burfoot, *Ferroelectrics: an Introduction to the Physical Principles*. (Butler & Tanner Ltd., London, 1967), p.261.
- <sup>14</sup> D. A. Berlincourt, C. Cmolik, and H. Jaffe, *Proc. IRE* **48**, 220 (1960).
- <sup>15</sup> OriginLab Corporation, OriginPro (Northampton, MA USA, 2010).
- <sup>16</sup> S. Gorfman, A. M. Glazer, Y. Noguchi, M. Miyayama, H. Luo, and P. A. Thomas, *J. Appl. Cryst.* **45**, 444 (2012).

- <sup>17</sup> E. J. Sonneveld and J. W. Visser, *J. Appl. Cryst.* **8**, 1 (1975).
- <sup>18</sup> PANalytical B. V., X'Pert HighScore Plus (Almelo, The Netherlands, 2008).
- <sup>19</sup> A. M. Glazer, *Acta Cryst. A* **31**, 756 (1975).
- <sup>20</sup> O. Elkechai, M. Manier, and J. P. Mercurio, *Phys. Status Solidi A* **157**, 499 (1996).
- <sup>21</sup> E. Aksel, J. S. Forrester, J. L. Jones, P. A. Thomas, K. Page, and M. R. Suchomel, *Appl. Phys. Lett.* **98**, 222901 (2011).
- <sup>22</sup> B. N. Rao and R. Ranjan, *Phys. Rev. B* **86**, 4103 (2012).
- <sup>23</sup> A. Sasaki, T. Chiba, Y. Mamiya, and E. Otsuki, *Jpn. J. Appl. Phys.* **38**, 5564 (1999).
- <sup>24</sup> G. O. Jones, J. Kreisel, and P. A. Thomas, *Powder Diffr.* **17**, 301 (2002).
- <sup>25</sup> Y. Hiruma, H. Nagata, and T. Takenaka, *J. Appl. Phys.* **104** (2008).



## Chapter 4

### Hydrothermal KNBT X-Ray Diffraction Study

#### 4.1 NBT

##### 4.1.1 Room-Temperature X-Ray Diffraction

Figure 4.1 shows XRD data from hydrothermal NBT prepared as described, both before and after heat-treatment at 950 °C for 6 hours. As the as-prepared sample gives broader, lower-intensity peaks, heat-treatment was deemed necessary to produce a diffraction pattern suitable for Rietveld refinement. The heat-treated sample gave a smoother background, indicative of a reduction in diffuse scattering. The XRD peaks are thinner after heat-treatment, indicating that grain growth has taken place. Visible peak splitting is not observed following heat-treatment, but a superstructure reflection resulting from antiphase tilting of the oxygen octahedra is visible at  $38.5^\circ 2\theta$ , corresponding to Miller indices of type  $\frac{1}{2}\{311\}_{pc}$ , consistent with either rhombohedral  $R3c$  or monoclinic  $Cc$  structures. This peak is also visible in data from the as-prepared material, but is more obvious after heat-treatment (Figure 4.2). The higher intensity following heat-treatment suggests that it is not only grain growth that has occurred, but possibly a reduction in defects. This would account for the lower background. The  $\frac{1}{2}\{311\}_{pc}$  peak shows greater intensity relative to the  $\{110\}_{pc}$  peak in hydrothermal than in solid state NBT (Figure 4.3).

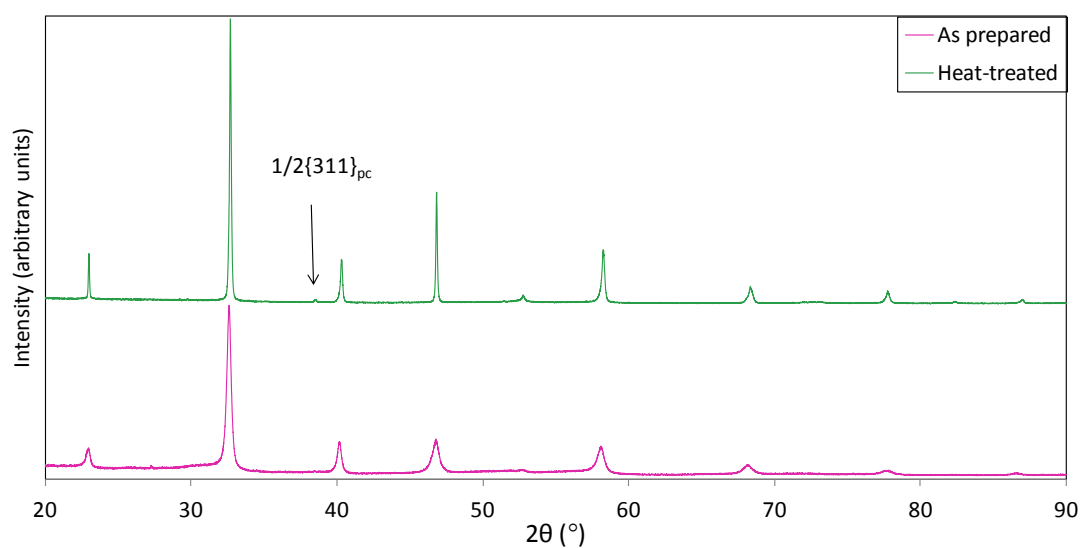


**Figure 4.1.** Room temperature XRD data from hydrothermally synthesised NBT, as prepared and after heat-treatment at 950 °C for 6 hours (data have been offset in intensity).

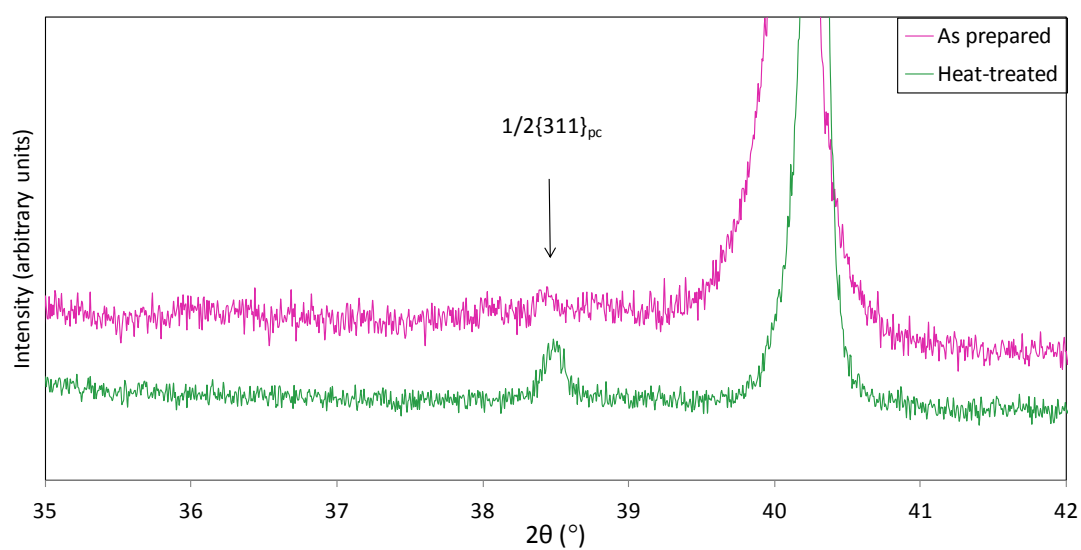


**Figure 4.2.**  $\frac{1}{2}\{311\}_{pc}$  XRD peak in hydrothermal NBT, before and after heat-treatment at 950 °C for 6 hours.

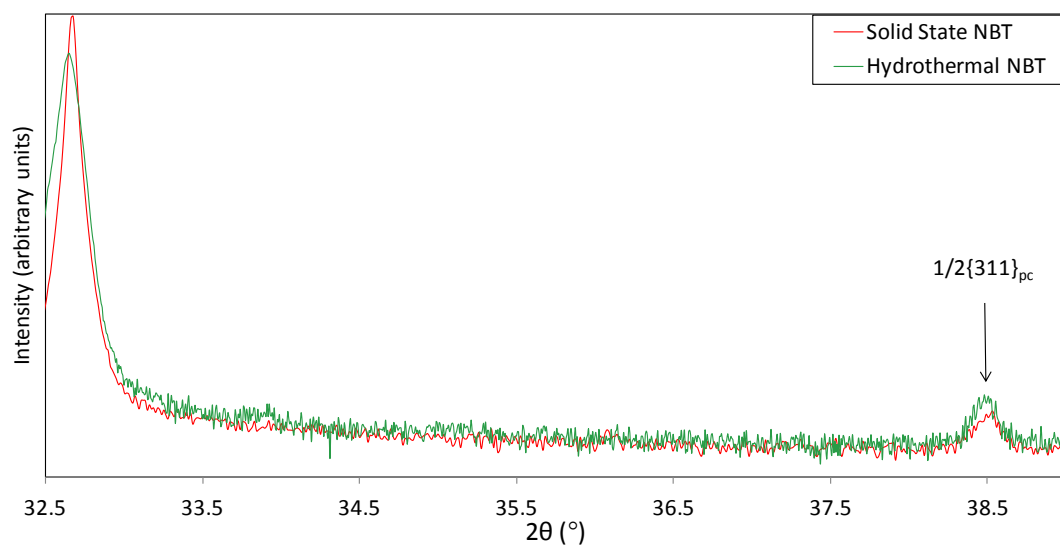


**Figure 4.3.** Log plot of XRD data from heat-treated hydrothermal NBT and solid state NBT, showing greater relative intensity of the  $\frac{1}{2}\{311\}_{pc}$  XRD peak in the hydrothermal sample (data have been scaled in intensity).

Structural refinements in both  $R3c$  and  $Cc$  space groups were performed, the results of which (Table 4.1) do not conclusively favour one or other of these symmetries.

Crystal system		Rhombohedral	Monoclinic
Space group		$R\bar{3}c$	$Cc$
Tilt system		$a^-a^-a^-$	$a^-a^-c^-$
$a$ (Å)		5.4897(2)	9.5324(2)
$b$ (Å)		-	5.4833(1)
$c$ (Å)		13.4914(6)	5.5104(2)
$\alpha, \beta, \gamma$ (°)		90, 90, 120	90, 125.417(1), 90
Pseudo-cubic unit cell volume (Å <sup>3</sup> )		58.686(5)	58.682(3)
No. Refined parameters		27	40
$R_{exp}$		5.770	5.767
$R_p$ (%)		7.093	6.376
$R_{wp}$ (%)		9.566	8.716
$R_{bragg}$ (%)		1.934	2.500
$\chi^2$		1.658	1.511
Na/Bi	$x$	0	0
	$y$	0	0.25
	$z$	0.2529(3)	0
	U11 (Å <sup>2</sup> )	0.0203(7)	0.014(1)
	U22 (Å <sup>2</sup> )		0.030(2)
	U33 (Å <sup>2</sup> )	0.144(3)	0.075(3)
	U12 (Å <sup>2</sup> )	0.0101(4)	0.011(3)
	U13 (Å <sup>2</sup> )	0	-0.031(2)
	U23 (Å <sup>2</sup> )	0	0.017(5)
Ti	$x$	0	0.253(1)
	$y$	0	0.256(2)
	$z$	0	0.781(1)
O (I)	$x$	0.117(1)	0.984(3)
	$y$	0.320(3)	0.202(4)
	$z$	0.091(1)	0.522(6)
	$b$ (Å <sup>2</sup> )	1.5(1)	-
O (II)	$x$	-	0.193(3)
	$y$	-	0.517(7)
	$z$	-	0.951(7)
O (III)	$x$	-	0.237(4)
	$y$	-	0.978(7)
	$z$	-	0.971(6)

**Table 4.1.** Lattice parameters, atomic positions, thermal displacement parameters, and refinement details for heat-treated hydrothermal NBT, taken at room temperature.

The polarisation values for hydrothermal NBT are given in Table 4.2, and plotted alongside those of solid state KNBT in Figure 4.4. The magnitude of polarisation is roughly half that of solid state NBT, but the major contribution still comes from the Ti-O polarisation.

	Na <sup>1+</sup> /Bi <sup>3+</sup>	Ti <sup>4+</sup>	O <sup>2-</sup>
Charge centre along z	0.505	0.5	0.508
Separation from O <sup>2-</sup> charge centre	0.003	0.008	-
Corresponding polarisation	0.019 Cm-2	0.113 Cm-2	

**Table 4.2.** Results of polarisation calculations, based on atomic positions and lattice parameters obtained from Rietveld refinement.

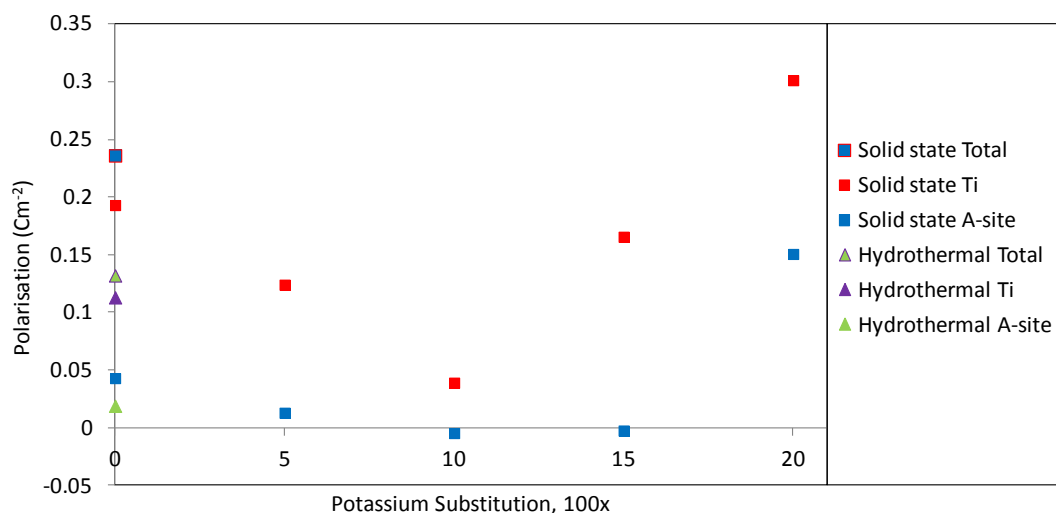


**Figure 4.4.** Polarisation values of solid state NBT – KNBT20 and hydrothermal NBT (*R3c* models).

The tilt angle was calculated to be  $\omega = 8.47^\circ$ , comparable with that of solid state NBT (calculated  $\omega = 6.42^\circ$ ; published  $\omega = 8.24^\circ$  <sup>[1]</sup>) and MnNBT (calculated  $\omega = 8.18^\circ$ ). The larger tilt angle seen in hydrothermal NBT may be due to the uncertainties inherent in using XRD to analyse oxygen positions, rather than a structural difference. However, the  $\frac{1}{2}\{311\}_{pc}$  peak is more intense in heat-treated hydrothermal NBT than in solid state NBT, supporting the more strongly tilted model of hydrothermal NBT.

### 4.1.2 High-Temperature X-Ray Diffraction

NBT structure as a function of temperature was investigated using high-temperature XRD on a sample annealed at 950 °C for 6 hours. Initially, data were collected at 130 °C, 450 °C, 530 °C and 700 °C (Figure 4.5), this range being sufficient to observe the high-temperature cubic phase in addition to the tetragonal phase intermediate to the cubic and room-temperature phases.

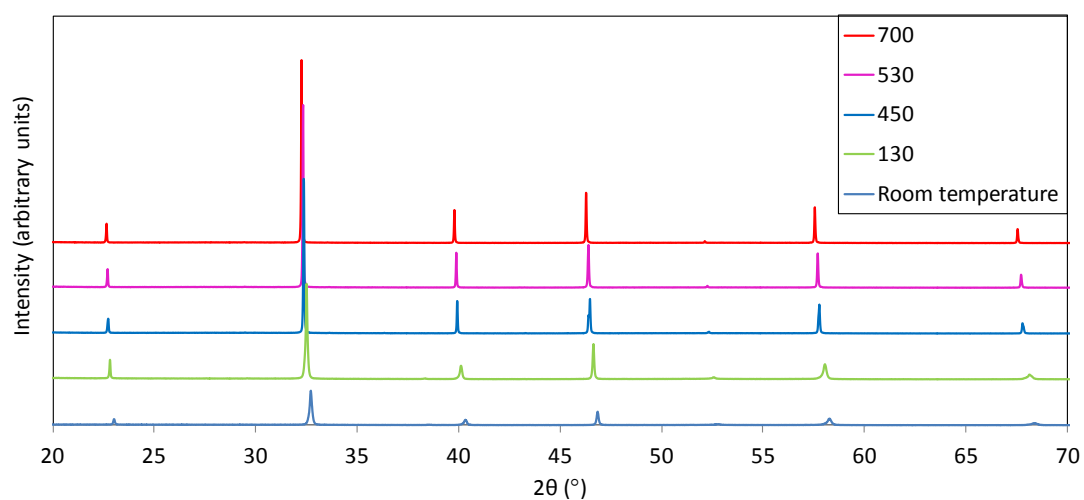


**Figure 4.5.** XRD data from hydrothermally synthesised NBT at room temperature, 130 °C, 450 °C, 530 °C, and 700 °C (data offset in the y axis).

The  $\{110\}_{pc}$  peak narrows with increasing temperature (Figure 4.6), and appears noticeably broader at 450 °C than at 530 °C and 700 °C. This indicates greater spontaneous strain at 450 °C than at 530 °C and 700 °C, possibly because the structure has become cubic by 530 °C. Figure 4.7 shows the clear tetragonal splitting of the  $\{200\}_{pc}$  peak at 450 °C. Figure 4.8 shows the low-intensity features of the  $2\theta$  range 35 – 41°. At room temperature and 130 °C, the  $\frac{1}{2}\{311\}_{pc}$  peak can be seen at 38.5 ° $2\theta$ . The  $\frac{1}{2}\{310\}_{pc}$  peak, a product of the  $a^0a^0c^+$  tilting in  $P4bm$  can be seen at both 450 °C and 530 °C, but not 700 °C. This shows the cubic transition is not complete until above 530 °C.

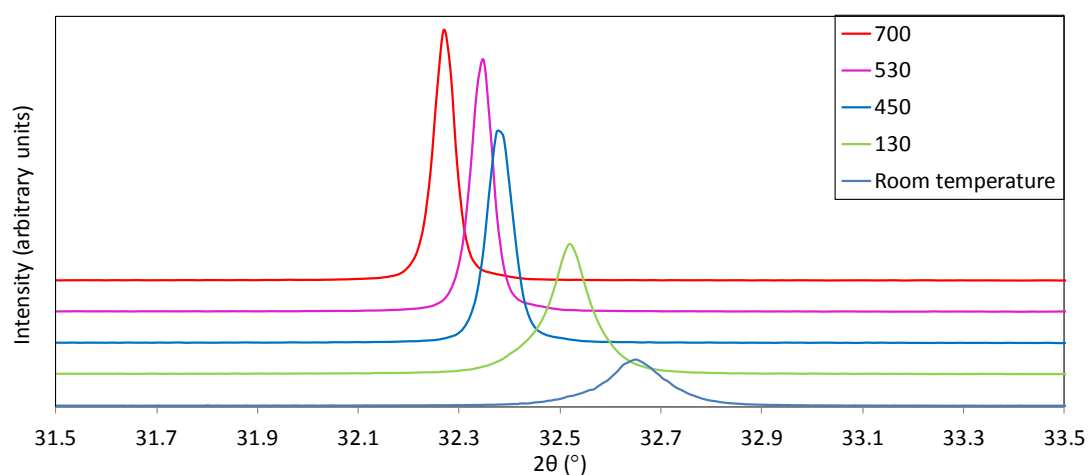


**Figure 4.6.** {110}<sub>pc</sub> XRD peak from hydrothermally synthesised NBT at room temperature, 130 °C, 450 °C, 530 °C, and 700 °C (data offset in the y axis).

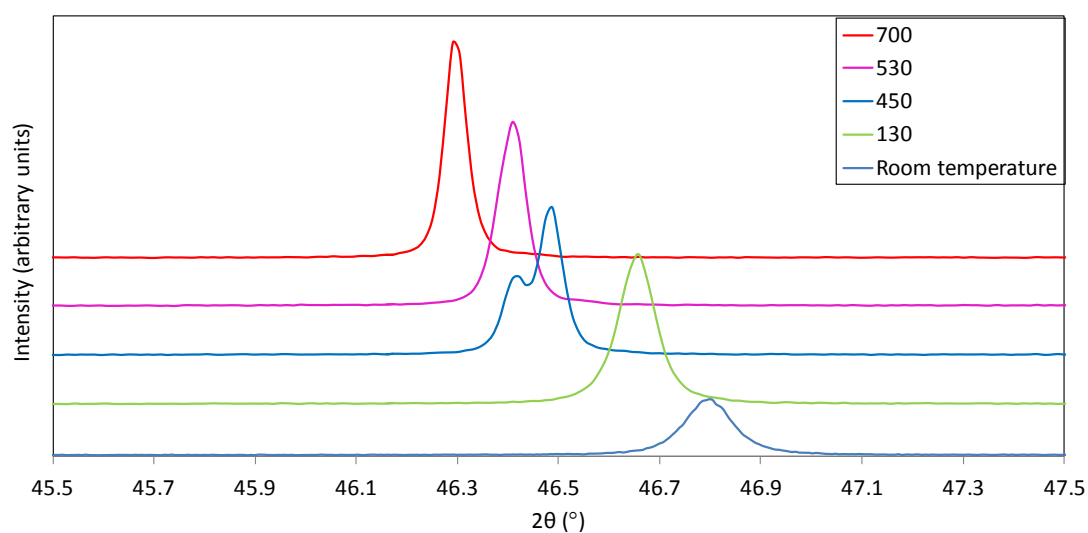


**Figure 4.7.** {200}<sub>pc</sub> peak from hydrothermally synthesised NBT at room temperature, 130 °C, 450 °C, 530 °C, and 700 °C (data offset in the y axis).

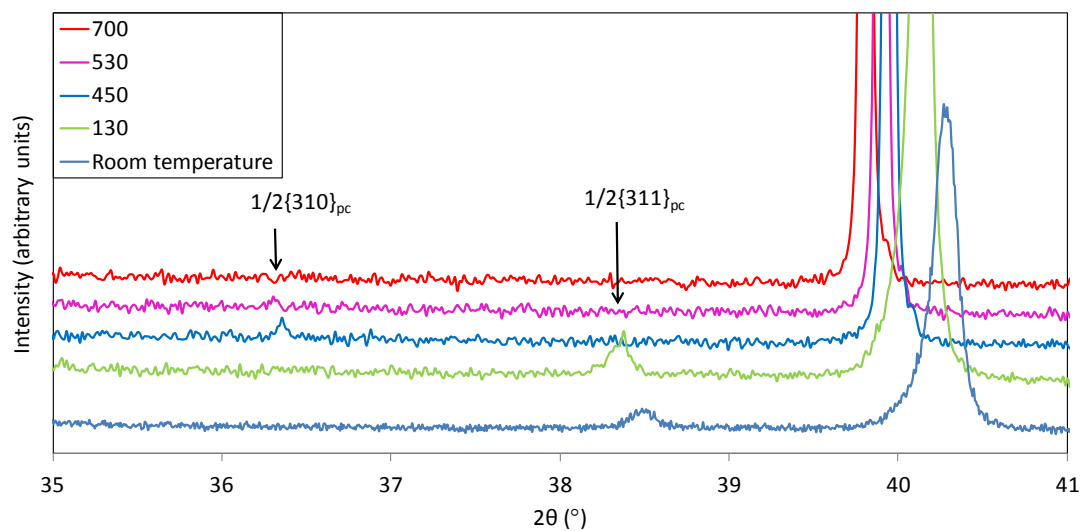


**Figure 4.8.** 35 – 41 ° 2 $\theta$  XRD data from hydrothermally synthesised NBT at room temperature, 130 °C, 450 °C, 530 °C, and 700 °C (data offset in the y axis). The  $\frac{1}{2}\{311\}_{pc}$  XRD peak can be seen up to 130 °C; the  $\frac{1}{2}\{310\}_{pc}$  XRD peak can be seen at 450 °C and 530 °C.

Rietveld refinement has been used to investigate the structures, summarised in Tables 4.3 & 4.4.



Crystal system		Rhombohedral	Monoclinic
Space group		$R3c$	$Cc$
Tilt system		$a^-a^-a^-$	$a^-a^-c^-$
$a$ (Å)	5.5029(1)		9.5339(3)
$b$ (Å)			5.4908(1)
$c$ (Å)	13.4542(3)		5.5110(1)
$\alpha, \beta, \gamma$ (°)	90, 90, 120		90, 125.375(2), 90
Pseudo-cubic unit cell volume (Å <sup>3</sup> )		58.806(3)	58.81(1)
No. Refined parameters		29	45
$R_{exp}$		4.621	4.615
$R_p$ (%)		8.560	7.050
$R_{wp}$ (%)		11.295	9.185
$R_{bragg}$ (%)		2.983	3.375
$\chi^2$		2.444	1.990
Na/Bi	$x$	0	0
	$y$	0	0.25
	$z$	0.254(1)	0
	U11 (Å <sup>2</sup> )	0.110(2)	0.021(2)
	U22 (Å <sup>2</sup> )		0.038(2)
	U33 (Å <sup>2</sup> )	0.004(1)	0.095(4)
	U12 (Å <sup>2</sup> )	0.055(1)	-0.010(3)
	U13 (Å <sup>2</sup> )	0	-0.011(4)
	U23 (Å <sup>2</sup> )	0	-0.014(6)
Ti	$x$	0	0.249(4)
	$y$	0	0.254(3)
	$z$	0	0.727(5)
	$b$ (Å <sup>2</sup> )	1.11(9)	0.9(1)
O (I)	$x$	0.772(1)	0.00(1)
	$y$	0.613(3)	0.206(7)
	$z$	0.426(1)	0.49(2)
	$b$ (Å <sup>2</sup> )	1.0(2)	-
O (II)	$x$	-	0.267(6)
	$y$	-	0.50(2)
	$z$	-	0.2(1)
O (III)	$x$	-	0.301(5)
	$y$	-	0.99(1)
	$z$	-	0.02(1)

**Table 4.3.** Lattice parameters, atomic positions, thermal displacement parameters, and refinement details for hydrothermal NBT at 130 °C.

Temperature		450 °C	530 °C	700 °C
Crystal system		Tetragonal	Tetragonal	Cubic
Space group		$P4bm$	$P4bm$	$Pm\bar{3}m$
Tilt system		$a^0a^0c^+$	$a^0a^0c^+$	$a^0a^0a^0$
$a$ (Å)	5.51867(2)	5.52676(3)	3.91668(3)	
$b$ (Å)				
$c$ (Å)				
$\alpha, \beta, \gamma$ (°)	90, 90, 90	90, 90, 90	90, 90, 90	
Pseudo-cubic unit cell volume (Å <sup>3</sup> )		59.5082(4)	59.7161(7)	60.083(1)
No. Refined parameters		34	36	19
$R_{exp}$		4.621	4.586	4.606
$R_p$ (%)		5.388	4.978	6.948
$R_{wp}$ (%)		7.030	6.502	8.709
$R_{bragg}$ (%)		3.193	2.088	1.320
$\chi^2$		1.521	1.418	1.891
Na/Bi	$x$	0	0	0
	$y$	0.5	0.5	0
	$z$	0.495(2)	0.504(4)	0
	U11 (Å <sup>2</sup> )	0.073(1)	0.073(2)	0.0859(6)
	U22 (Å <sup>2</sup> )			
	U33 (Å <sup>2</sup> )	0.076(1)	0.097(3)	
	U12 (Å <sup>2</sup> )	0.001(2)	-0.002(2)	0
	U13, U23 (Å <sup>2</sup> )	0	0	0
Ti	$x$	0	0	0.5
	$y$	0	0	0.5
	$z$	0	0	0.5
	U11 (Å <sup>2</sup> )	-	-	0.0260(5)
	U22 (Å <sup>2</sup> )	-		
	U33 (Å <sup>2</sup> )	-		
	U12 (Å <sup>2</sup> )	-	-	0
	U13, U23 (Å <sup>2</sup> )	-	-	0
$b$ (Å <sup>2</sup> )	1.34(8)	1.45(9)	-	
O (I)	$x$	0	0	0.5
	$y$	0	0	0.5
	$z$	0.076(6)	0.874(7)	0
	U11 (Å <sup>2</sup> )	-	-	0.047(1)
	U22 (Å <sup>2</sup> )	-		
	U33 (Å <sup>2</sup> )	-		
	U12, U13, U23 (Å <sup>2</sup> )	-	-	0
	$b$ (Å <sup>2</sup> )	7.8(6)	8.5(7)	-
O (II)	$x$	0.261(1)	0.26(5)	-
	$y$	0.283(1)	0.24(5)	-
	$z$	0.922(2)	0.061(4)	-
	$b$ (Å <sup>2</sup> )	2.0(1)	4.1(2)	-

**Table 4.4.** Lattice parameters, atomic positions, thermal displacement parameters, and refinement details for hydrothermal NBT at 450 °C, 530 °C and 700 °C.

Closer analysis of the  $2\theta$  range  $31^\circ - 41^\circ$  was employed to elucidate the phase transition. The  $\{110\}_{pc}$  and  $\{111\}_{pc}$  peaks are observed to narrow with increasing temperature (Figure 4.9a). On heating, both peaks reach a minimum width in the range 300-320 °C, clearly indicating this as a phase transition. The increase in the  $\{110\}_{pc}$  peak width above this phase transition is consistent with emerging tetragonal symmetry, indicating  $\approx 300^\circ\text{C}$  as the rhombohedral – tetragonal phase transition temperature, in agreement with optical birefringence measurements<sup>2</sup>. Figure 4.9b shows evidence of hysteresis in the phase transition, with the  $\{110\}_{pc}$  peak width continuing to decrease on cooling to 285-290 °C.

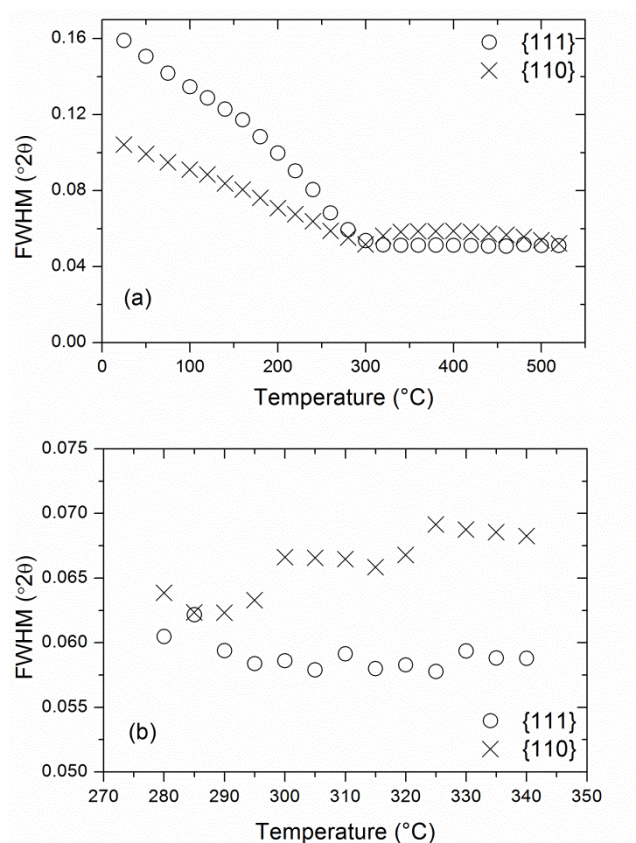


**Figure 4.9.** Variation in FWHM values of  $\{110\}_{pc}$  and  $\{111\}_{pc}$  XRD peaks (a) on heating; (b) on cooling.

Above  $\approx 300^\circ\text{C}$ ,  $\frac{1}{2}\{310\}_{pc}$ , a superstructure reflection associated with in-phase tilting is observed at  $36.5^\circ 2\theta$ , consistent with the tilted tetragonal space group  $P4bm$ <sup>1</sup>. The

intensities of the weak antiphase and in-phase superstructure reflections were measured and normalised against the most intense ( $\{110\}_{pc}$ ) reflection. Plotted as a function of temperature (Figure 4.10), these follow the same trends as the peak widths. The intensities of the superstructure peaks reflect the octahedral tilt angle<sup>3</sup>, showing that the angle of tilt in the rhombohedral phase decreases as the phase transition is approached and that the angle of tilt in the tetragonal phase reaches a maximum at  $\approx 400\text{ }^{\circ}\text{C}$ , consistent with the maximum width of the  $\{110\}_{pc}$  peak (Figure 4.9a).

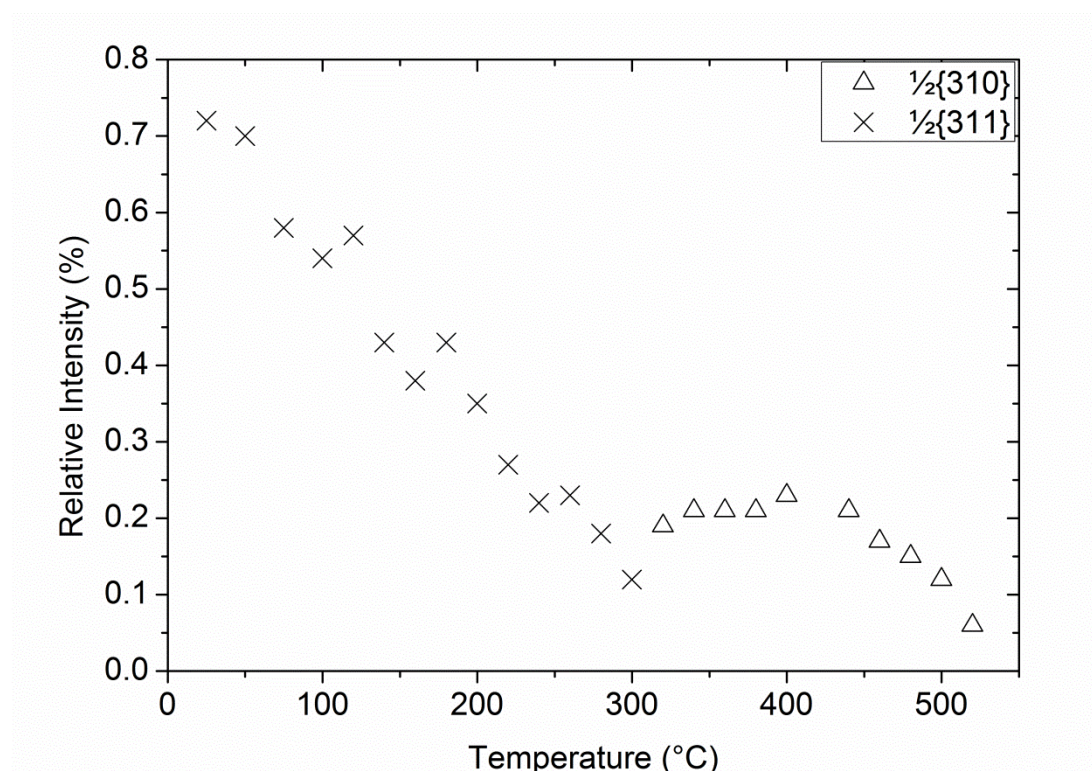


**Figure 4.10.** Relative intensities of the superstructure reflections in hydrothermal NBT on heating from room temperature to 520 °C.

Further data acquired in the region of the phase transition (Figure 4.11) show an apparent coexistence of the rhombohedral and tetragonal phases between 300 °C – 310 °C, as indicated by the presence of both superstructure peaks.

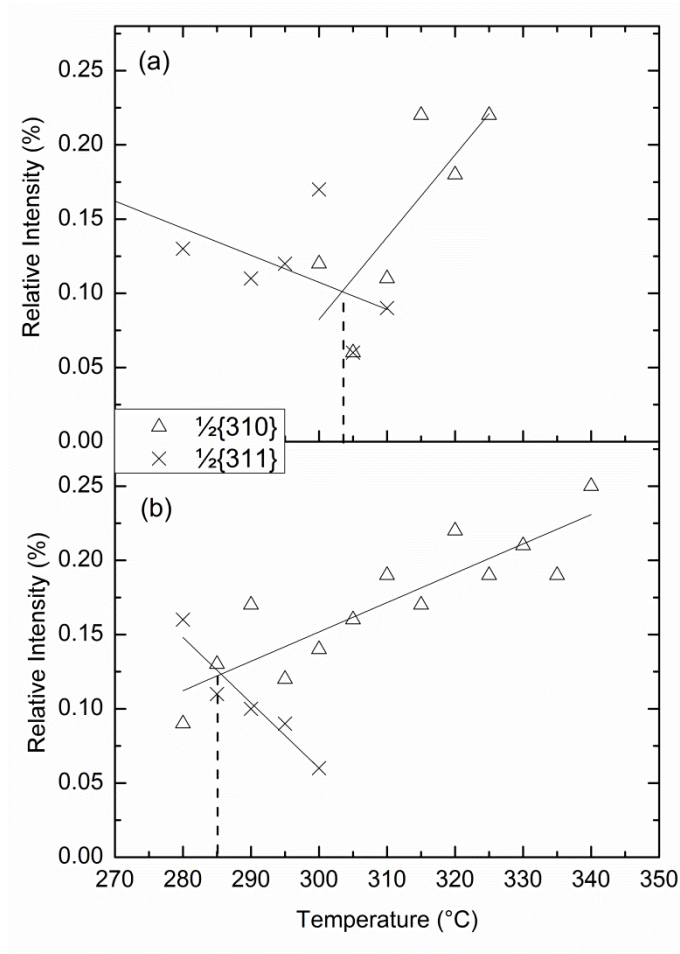


**Figure 4.11.** Relative intensities of the superstructure reflections in hydrothermal NBT in the region of the phase transition; a) on heating; b) on cooling. The solid lines show linear best fit to the data; the dashed lines indicate the temperature of phase transition.

The phase transition temperatures have been chosen as the temperature at which the best fit lines to the  $\frac{1}{2}\{310\}_{pc}$  and  $\frac{1}{2}\{311\}_{pc}$  intensities intersect: 305 °C on heating and 285 °C on cooling. These values show hysteresis of the phase transition, which is 20 °C lower on cooling than heating.

XRD data were collected at the phase transition temperature, 305 °C, for the purpose of Rietveld refinement, and show the presence of peaks from both antiphase and in-phase tilting, consistent with phase coexistence or an intermediate phase (Figure 4.12). Structural refinements carried out against these data show a better fit for phase coexistence than for intermediate phases with the mixed tilt systems required to give both superstructure peaks (space groups  $Pnma$ ,  $Cmcm$  and  $P2_1/m$ <sup>4</sup>) (Tables 4.5 and 4.6). The

best single-phase refinement was in space group *Pnma*; however, this space group would give rise to additional diffraction peaks that are not seen in the pattern. Based on these data, the appearance of both in-phase and antiphase tilt peaks is due to coexistence of both rhombohedral and tetragonal phases. However, the trends in peak widths and superstructure peak intensities indicate that at 305 °C, an un-tilted cubic structure is approached. The trend in  $\{110\}_{pc}$  peak widths and superstructure peak intensities in the tetragonal phase indicate that tetragonal distortion is maximised in the middle of the phase field, while at both the upper and lower temperatures of the tetragonal regime, it appears that the structure tends towards a metrically cubic phase.

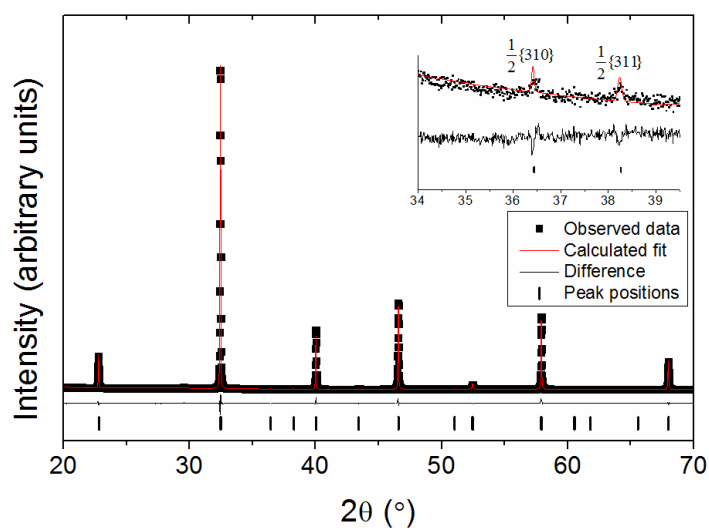


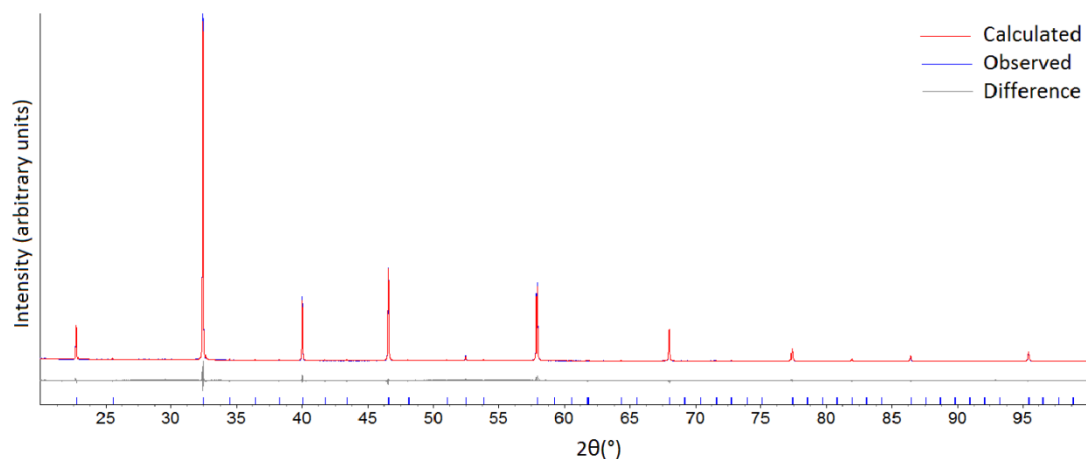
**Figure 4.12.** XRD pattern from hydrothermal NBT at 305 °C, showing coexistence of  $\frac{1}{2}\{310\}_{pc}$  in-phase and  $\frac{1}{2}\{311\}_{pc}$  antiphase tilt peaks (inset).

Crystal system	Rhombohedral/Tetragonal		Monoclinic/Tetragonal	
Space group	<i>R3c</i>	<i>P4bm</i>	<i>Cc</i>	<i>P4bm</i>
Tilt system	$a^-a^-a^-$	$a^0a^0c^+$	$a^-a^-c^-$	$a^0a^0c^+$
<i>a</i> (Å)	5.5114(1)	5.50870(2)	9.5407(4)	5.50962(4)
<i>b</i> (Å)			5.5107(1)	
<i>c</i> (Å)	13.504(1)	3.89738(3)	5.5130(2)	3.89531(7)
$\alpha, \beta, \gamma$ (°)	90, 90, 120	90, 90, 90	90, 125.282(4), 90	90, 90, 90
Pseudo-cubic unit cell volume (Å <sup>3</sup> )	59.206(5)	59.1345(5)	59.153(5)	59.123(1)
No. Refined parameters	52		62	
<i>R</i> <sub>exp</sub>	3.337		3.334	
<i>R</i> <sub>p</sub> (%)	3.786		3.979	
<i>R</i> <sub>wp</sub> (%)	4.925		5.713	
<i>R</i> <sub>bragg</sub> (%)	1.185		2.245	
$\chi^2$	1.476		1.714	

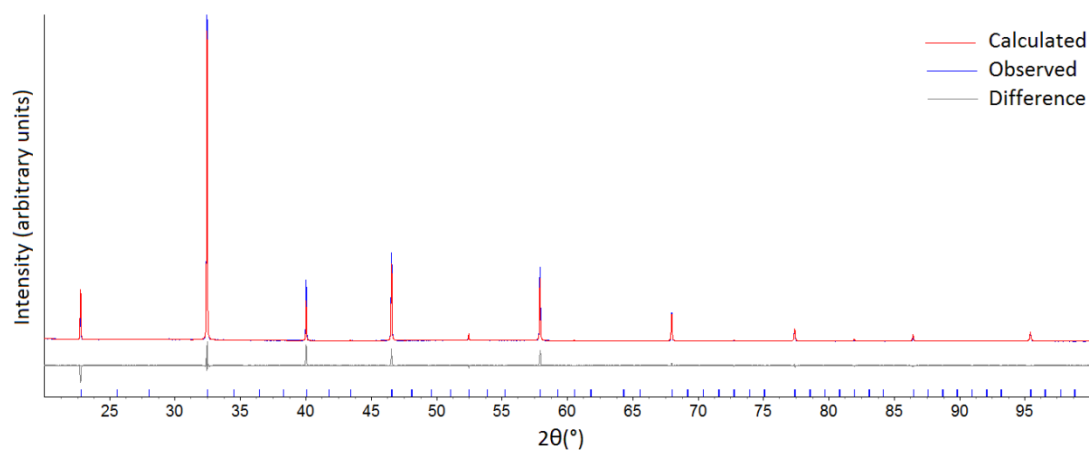
**Table 4.5.** Lattice parameters and statistics for multiphase refinements of hydrothermal NBT at 305 °C in space groups: *R3c/P4bm*, *Cc/P4bm*.

Crystal system	Orthorhombic	Monoclinic	
Space group	<i>Pnma</i>	<i>Cmcm</i>	<i>P2<sub>1</sub>/m</i>
Tilt system	$a^-b^+c^-$	$a^0b^-c^+$	$a^+b^-c^-$
<i>a</i> (Å)	5.5085(2)	7.78988(5)	5.51186(4)
<i>b</i> (Å)	7.79472(6)		7.79683(5)
<i>c</i> (Å)	5.5083(2)	7.7953(1)	5.5249(1)
$\alpha, \beta, \gamma$ (°)	90, 90, 90	90, 90, 90	90, 90.056(3), 90
Pseudo-cubic unit cell volume (Å <sup>3</sup> )	59.128(3)	59.130(1)	59.358(2)
No. Refined parameters	39	46	63
<i>R</i> <sub>exp</sub>	3.341	3.339	3.334
<i>R</i> <sub>p</sub> (%)	4.365	7.118	7.492
<i>R</i> <sub>wp</sub> (%)	5.991	12.050	13.380
<i>R</i> <sub>bragg</sub> (%)	2.606	11.875	6.811
$\chi^2$	1.793	3.609	4.013

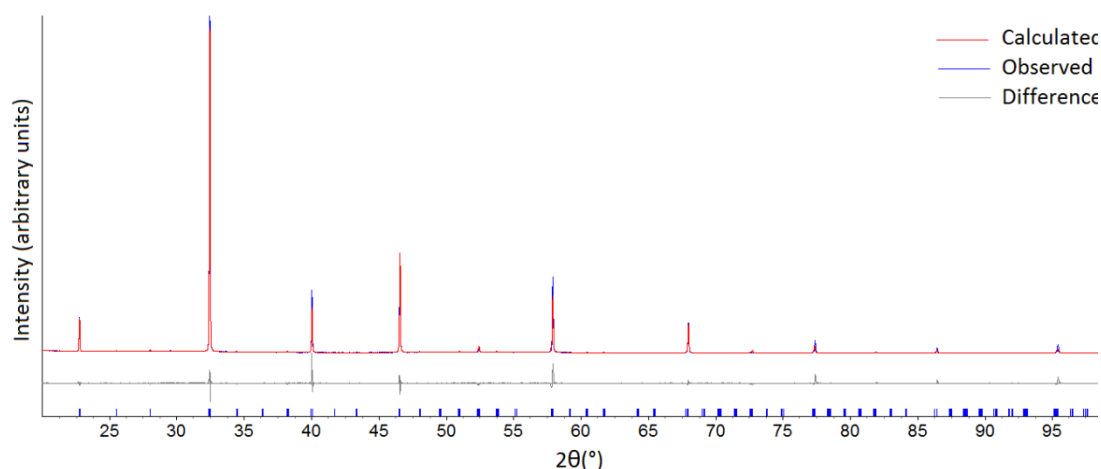
**Table 4.6.** Lattice parameters and statistics for refinements of hydrothermal NBT at 305 °C in space groups: *Pnma*, *Cmcm* and *P2<sub>1</sub>/m*.



**Figure 4.13.** Plot showing fit, XRD data and difference plot from *Pnma* refinement of hydrothermal NBT at 305 °C, showing peaks predicted by the model that are not present in the data.



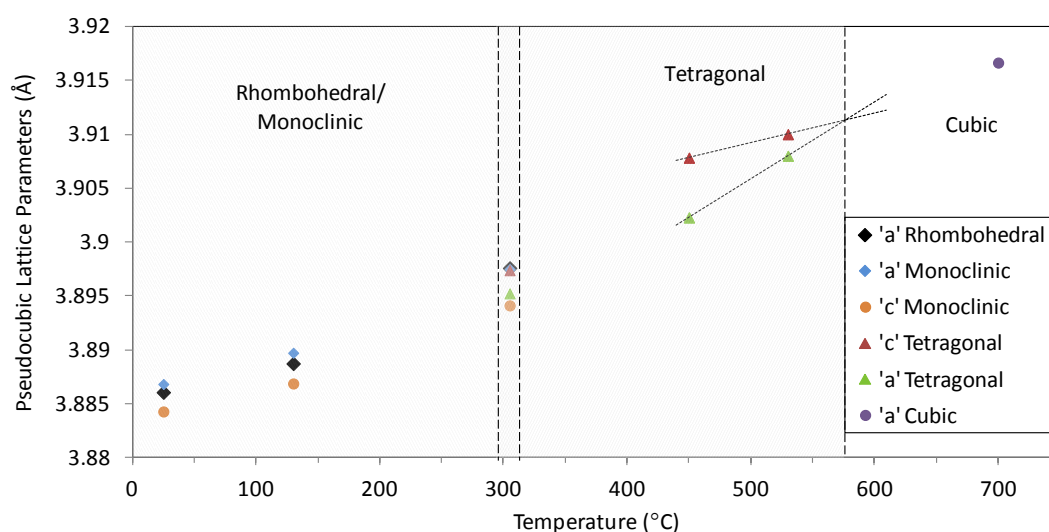
**Figure 4.14.** Plot showing fit, XRD data and difference plot from *Cmcm* refinement of hydrothermal NBT at 305 °C, showing peaks predicted by the model that are not present in the data.



**Figure 4.15.** Plot showing fit, XRD data and difference plot from *P2<sub>1</sub>/m* refinement of hydrothermal NBT at 305 °C, showing peaks predicted by the model that are not present in the data.



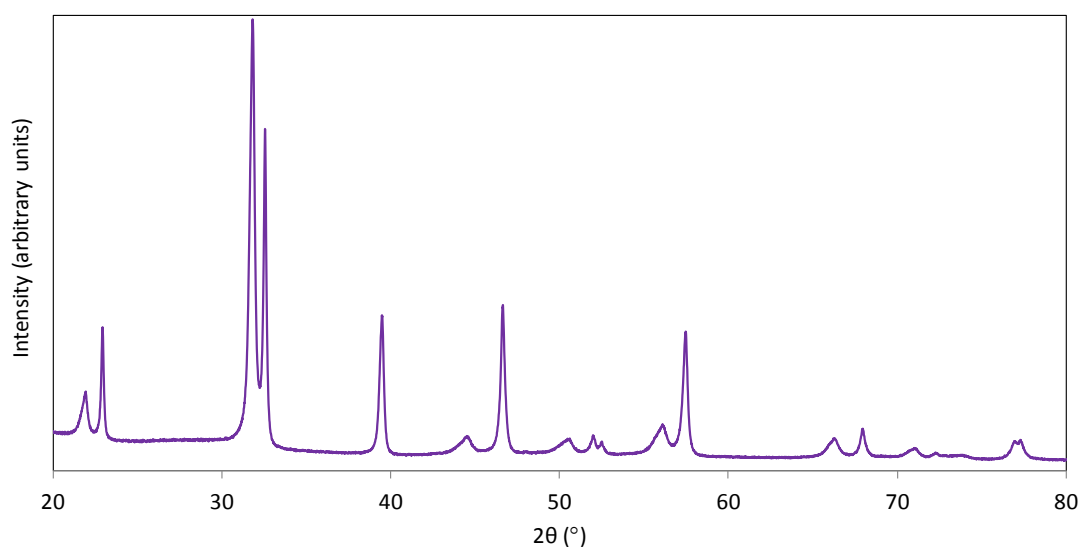
Figure 4.16 shows the pseudocubic lattice parameters of hydrothermal NBT between room temperature and 700 °C, using rhombohedral, monoclinic, tetragonal and cubic models. The approximately linear increase is comparable to that for solid state NBT (Figure 3.51). An approximate  $T_c$  has been marked, taken as the temperature at which linear fits to the tetragonal data intercept. This is not an ideal method of determining  $T_c$ , as the tetragonal data are insufficient to give good trend lines, and is only intended as a rough estimate.



**Figure 4.16.** Pseudocubic lattice parameters of hydrothermal NBT between room temperature and 700 °C.

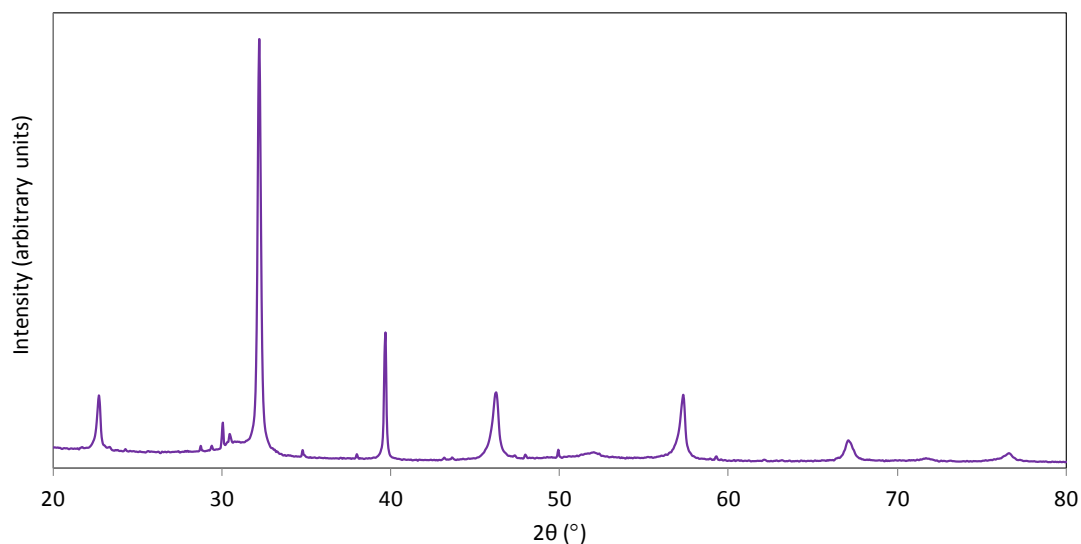
## 4.2 KBT

Figure 4.17 shows the XRD pattern collected from hydrothermal KBT, prepared as described. The tetragonal structure is seen clearly in the split  $\{100\}_{pc}$  and  $\{110\}_{pc}$  peaks.



**Figure 4.17.** Room-temperature XRD pattern of hydrothermal KBT, as-prepared.

This sample was later heat-treated at 890 °C for 1 hour, with a heating rate of 180 °C h<sup>-1</sup>, and cooling rates of 10 °C h<sup>-1</sup> to 400 °C, and 20 °C h<sup>-1</sup> to room temperature. Figure 4.18 shows the room-temperature XRD pattern collected.



**Figure 4.18.** Room-temperature XRD pattern of hydrothermal KBT, after heat-treatment at 890 °C.

The tetragonal splitting is no longer apparent after heating and cooling the sample. A possible explanation for this is the presence of OH<sup>-</sup> groups in the as-prepared material, released when the sample is heated, altering the material structure. This effect has been

seen in hydrothermal NBT<sup>5</sup>. Other possible defects in the as-prepared sample include H<sub>2</sub>O in the structure, oxygen vacancies, or inhomogeneous clustering of the A-site ions. These may contribute to tetragonal strain, giving rise to the split peaks seen in the XRD pattern. The impurity peaks seen at  $\approx 30^\circ 2\theta$  and  $38^\circ 2\theta$  after heat-treatment match those seen in Bi<sub>4</sub>Ti<sub>3</sub>O<sub>12</sub>,<sup>[6]</sup> suggesting that potassium has been lost through volatilisation, or that the original material was non-stoichiometric. Small peaks at  $35^\circ 2\theta$  and  $50^\circ 2\theta$ , which could not be identified, have been attributed to the presence of impurity phases, also indicating non-stoichiometry.

To investigate the annealing process in KBT, the behaviour of the  $\{100\}_{pc}$  peak in as-prepared material was studied using high-temperature XRD. Static scans were collected in the range  $20^\circ 2\theta - 23.2^\circ 2\theta$ , each with a counting time of 70 minutes. Data were collected from  $25^\circ\text{C} - 890^\circ\text{C}$ , with a heating rate of  $1^\circ\text{C min}^{-1}$ . The  $(001)_T$  and  $\{010\}_T$  peaks were modelled using two split pseudo-Voigt peak functions in TOPAS-Academic<sup>7</sup>. Figure 4.19 shows the positions of the  $(001)_T$  and  $\{010\}_T$  XRD peaks as a function of temperature.

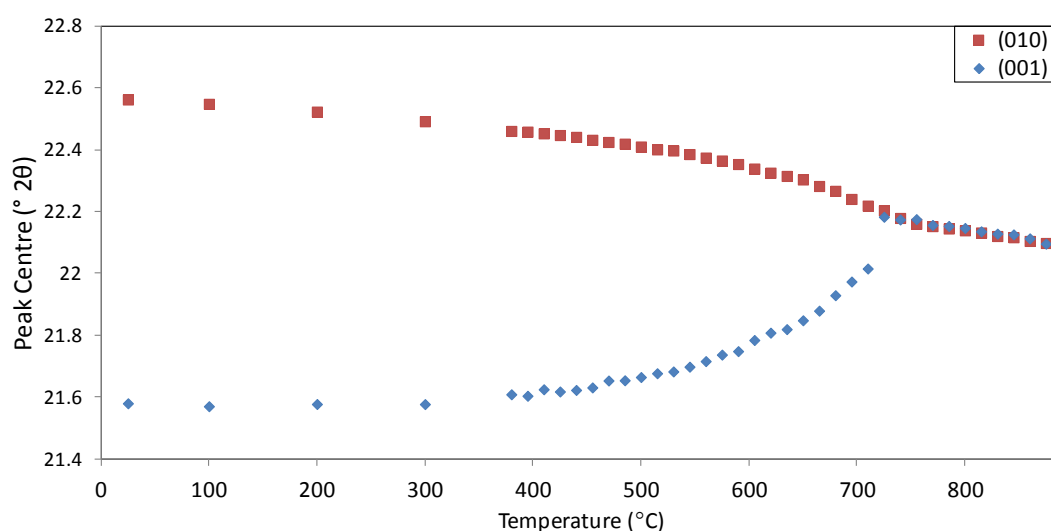


**Figure 4.19.** Peak centres of the modelled  $\{010\}_T$  and  $(001)_T$  XRD peaks, as functions of temperature.

The  $\{010\}_T$  and  $(001)_T$  peaks become closer with increasing temperature, converging as the sample is heated. The upward trend in the  $(001)_T$  peak centre shows a

sharp increase between 710 °C – 725 °C. However, visual analysis of the data shows that this does not indicate the occurrence of a phase transition; rather, the combination of two split pseudo-Voigt peaks is no longer an appropriate model, as the  $\{001\}_T$  peak has been assimilated into the higher-intensity  $\{010\}_T$  peak. This is shown in Figure 4.20.

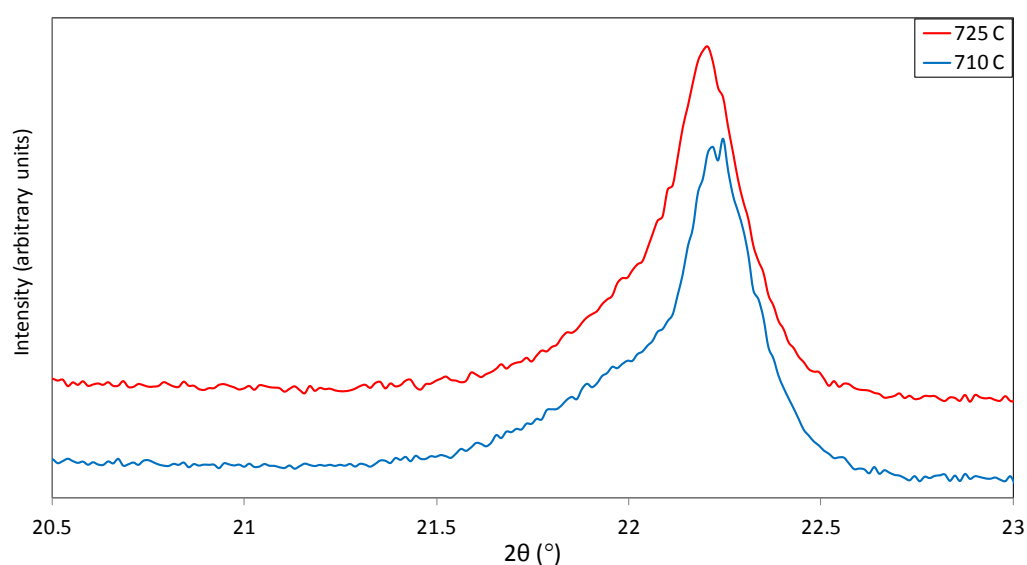


**Figure 4.20.**  $\{100\}_{pc}$  XRD peak of hydrothermal KBT at 710 °C and 725 °C, showing gradual assimilation of the  $\{001\}_T$  peak into the  $\{010\}_T$  peak (data have been offset in the y-axis for clarity).

From 725 °C – 890 °C, a single split pseudo-Voigt peak was used in fitting the  $\{100\}_{pc}$  peak. The peak asymmetry shown in Figure 4.20 is reflected in the differing Lorentzian fractions of the left and right side of the peak (Figure 4.21). These meet at 800 °C, indicating that the peak is not asymmetric; this is interpreted as showing that annealing was complete when this scan was taken. As annealing occurs as a function of time<sup>8</sup> as well as temperature, it is unclear whether 800 °C represents the optimum annealing temperature.

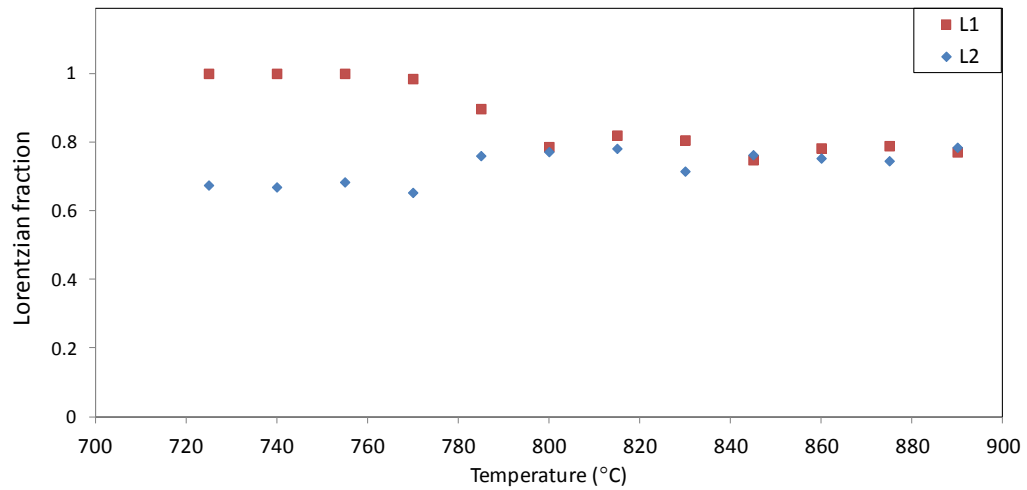


**Figure 4.21.** The Lorentzian fractions of the low-2 $\theta$  side (L1) and the high-2 $\theta$  side (L2) of the modelled  $\{100\}_{pc}$  peak, between 725 °C – 890 °C.

Evidence of anisotropic strain can be seen from the  $(001)_T$  peak, which has a larger half-width at half-maximum (HWHM) on the low-2 $\theta$  side (Figure 4.22). The low-angle HWHM increases with temperature, reaching a maximum at 600 °C. This can be seen from the XRD patterns (Figure 4.23). Increasing HWHM up to 600 °C suggests anisotropic strain increases with temperature. The decrease in HWHM above 600 °C may indicate the onset of annealing at this temperature.

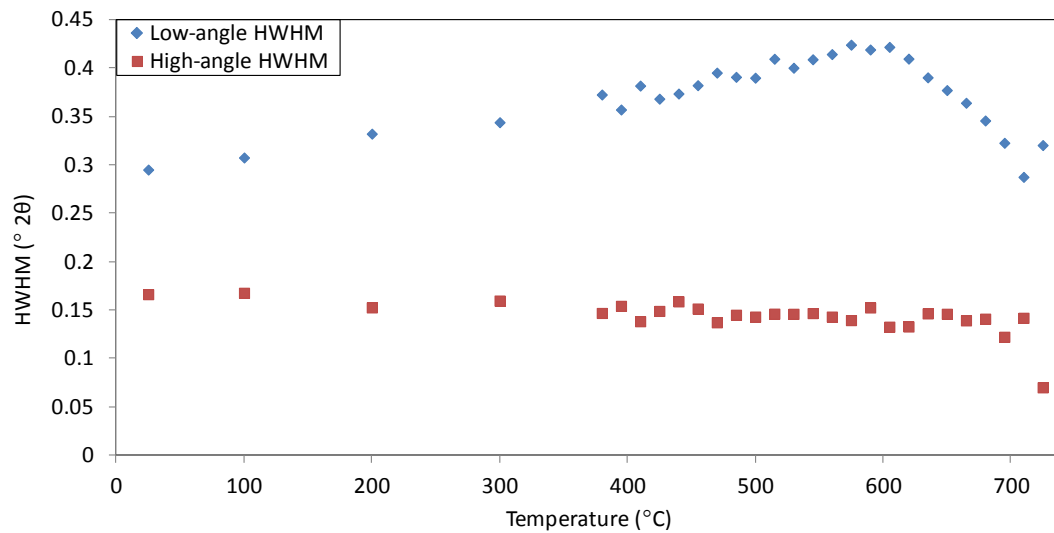


**Figure 4.22.** HWHM of the low- and high-2 $\theta$  sides of the  $(001)_T$  XRD peak of KBT as functions of temperature.

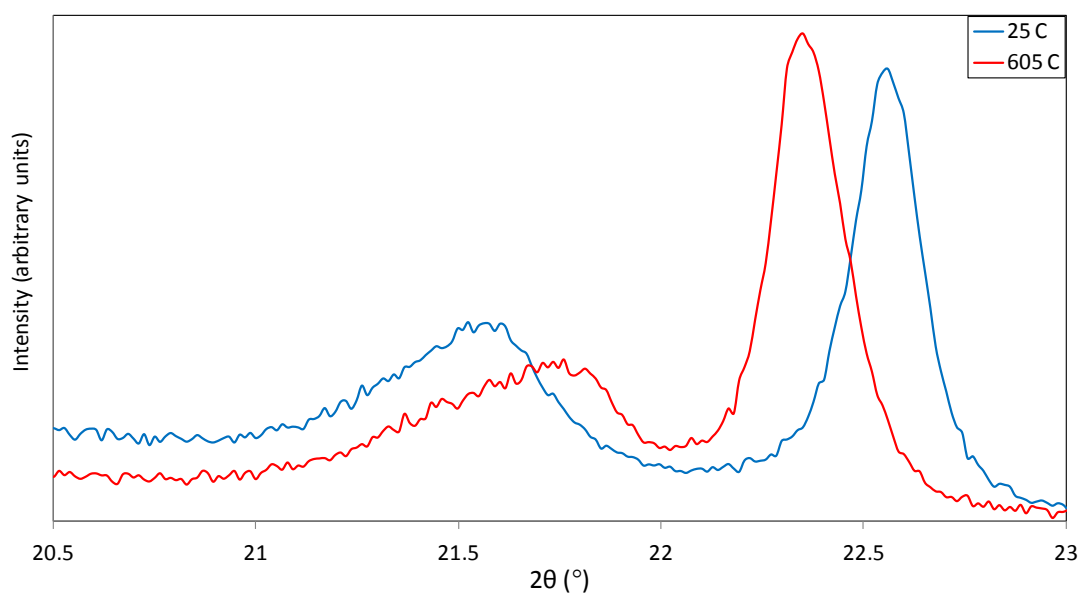


**Figure 4.23.**  $\{100\}_{pc}$  XRD peak of hydrothermal KBT at 25 °C and 605 °C, showing increased asymmetry of the  $(001)_T$  peak at 605 °C (data have been scaled in intensity for clarity).

TGA-DSC was performed on a sample of as-prepared hydrothermal KBT (Figure 4.24). Mass loss occurs as the sample is heated to 175 °C, and then continues at a slower rate until 900 °C. This may be caused by the loss of OH groups as  $H_2O$  molecules, as has been seen in hydrothermal NBT<sup>5</sup>. An increase in mass occurs between 900 °C – 1025 °C. This possibly indicates the uptake of oxygen from the atmosphere to occupy vacancies. The heat curve shows the onset of melting at  $\approx 1050$  °C. The decrease in heat flow begins at  $\approx 900$  °C, coinciding with the increase in sample mass.

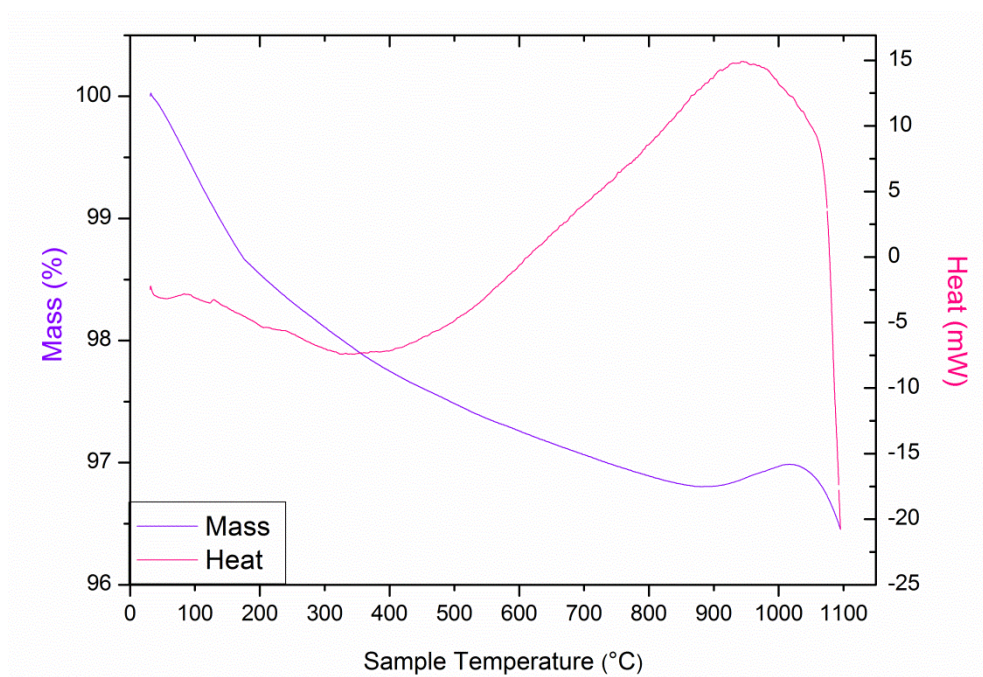


**Figure 4.24.** TGA-DSC curves of hydrothermal KBT.

### 4.3 X-Ray Diffraction Study of the KNBT Series

As-prepared samples across the KNBT range were investigated to ascertain characteristics of materials prepared via hydrothermal method, in contrast with those prepared via solid state reaction. Figures 4.25 and 4.26 show the room-temperature XRD patterns collected.

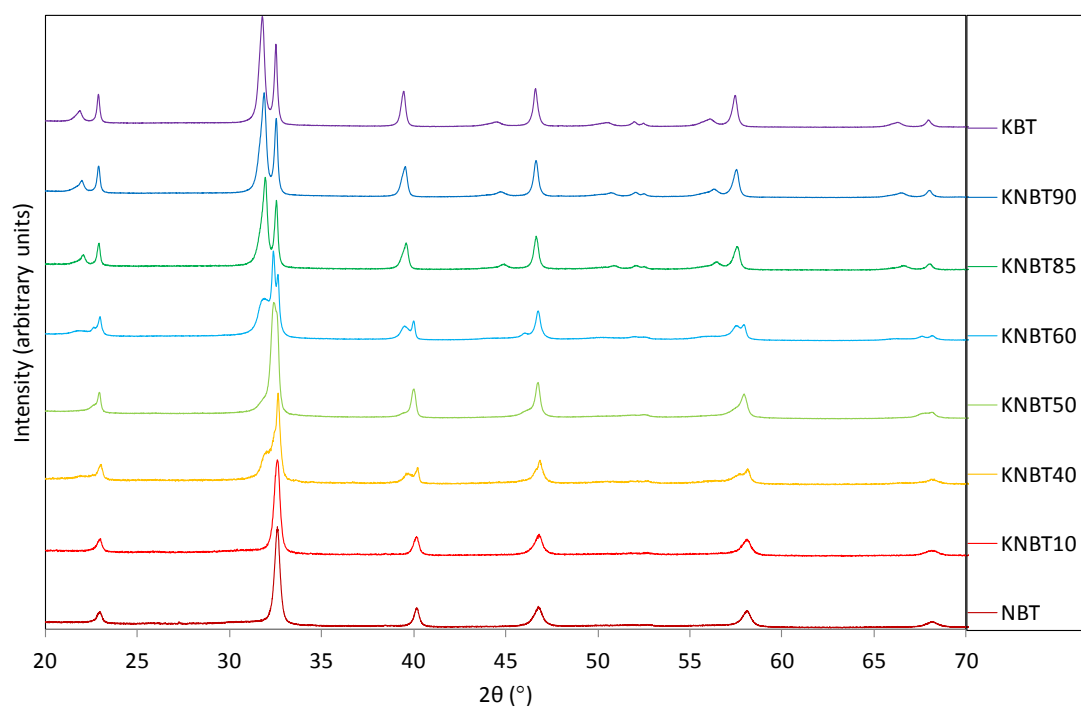


**Figure 4.25.** Room-temperature XRD patterns collected from as-prepared KNBT00-100 (data have been offset in intensity).

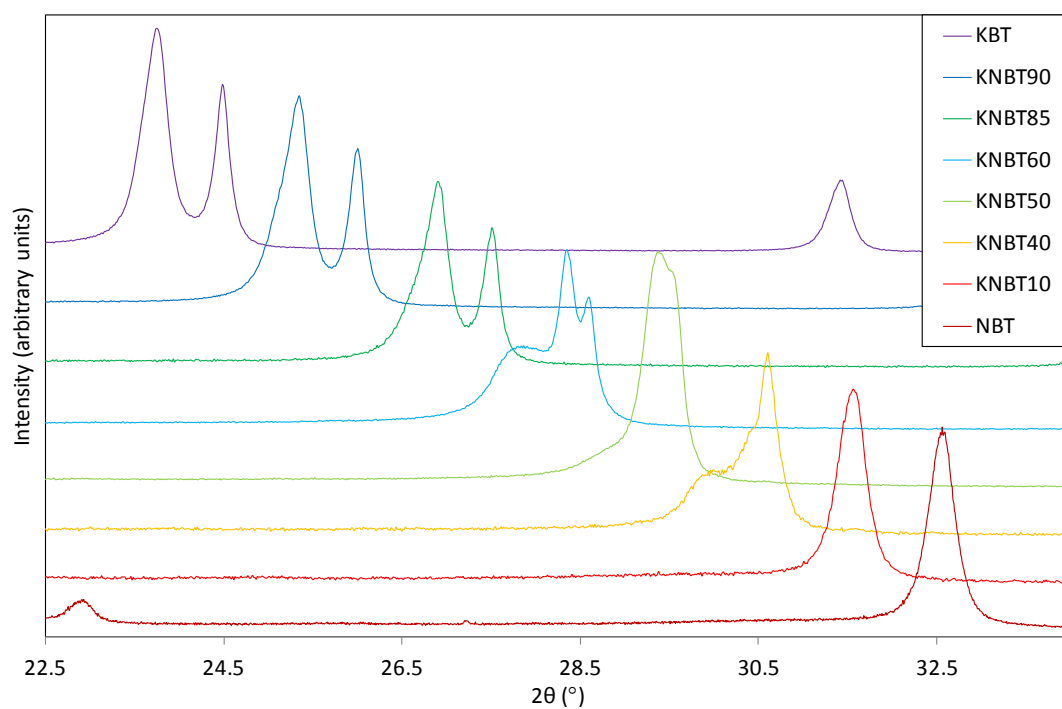


**Figure 4.26.**  $\{110\}_{pc}$  XRD peak in as-prepared KNBT00-100 (data have offset in  $2\theta$  and scaled and offset intensity).



The XRD patterns of NBT and KNBT10 show similar peak shapes and backgrounds, and exhibit the  $\frac{1}{2}\{311\}_{pc}$  reflection (Figures 4.25 – 4.27).

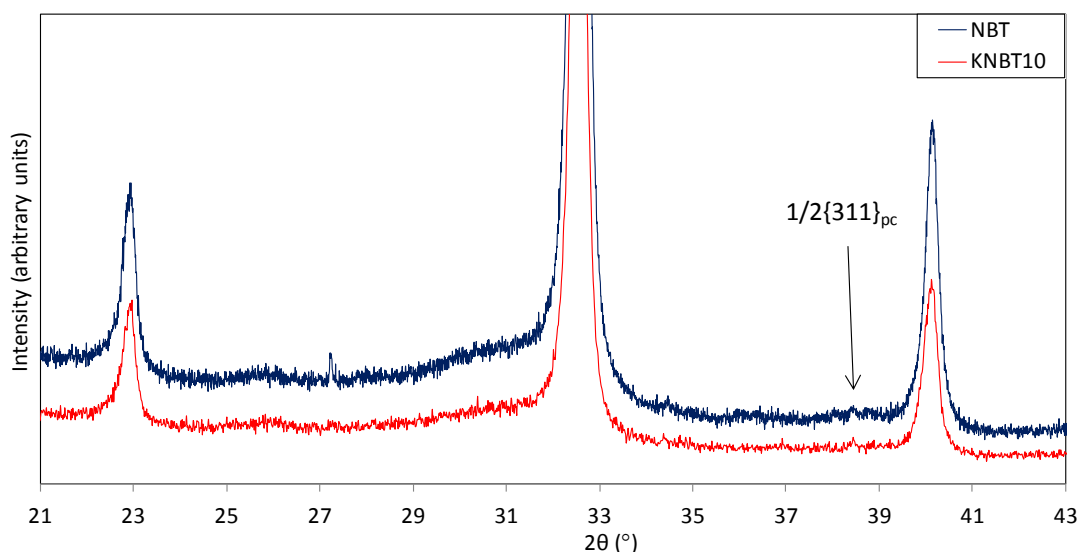


**Figure 4.27.** XRD patterns of as-prepared hydrothermal NBT and KNBT10, showing similar backgrounds and  $\frac{1}{2}\{311\}_{pc}$  reflection. The impurity peak at  $\approx 27^\circ 2\theta$  in NBT has been identified as belonging to  $\text{TiO}_2$  <sup>9</sup>.

Although the as-prepared hydrothermal material is not acquiescent to Rietveld refinement, lattice parameters have been derived in this manner using the *R3c* refinement of heat-treated hydrothermal NBT as a starting point. *Cc* refinements of these data were not necessary, as very close pseudo-cubic lattice parameter trends would be expected for either model (as seen in solid state KNBT, Figure 3.23), and the use of the lower symmetry space group was not justified in refining patterns of comparatively poor clarity.

KNBT85-90 and KBT show evidence of tetragonal peak splitting (Figures 4.25 – 4.26). The *P4mm* structure refined from solid state KNBT65 was used as a starting point to refine lattice parameters from these patterns.

The XRD patterns of KNBT40-60 suggest a multiphase structure (Figures 4.25 – 4.26). The  $\{110\}_{pc}$  peak shows evidence of the tetragonal doublet as well as the rhombohedral contribution: in this case, a single peak with no visible splitting. The  $\frac{1}{2}\{311\}_{pc}$  peak is not visible, suggesting the rhombohedral phase to be *R3m*. Several attempts were

made to refine the patterns as such: initially, using the solid state KNBT  $R3m/P4mm$  models as starting points; subsequently, fitting each phase in a separate refinement and combining them. Despite repeated attempts, it was not possible to reach a satisfactory refinement from which lattice parameters could be drawn. One reason for this was the difficulty in determining peak positions. The low- $2\theta$  triplet of the  $\{110\}_{pc}$  peak in KNBT60 (Figure 4.26) is broad, and may be caused by asymmetric strain or by the presence of a split  $R3m$  peak. Another reason was the difficulty in fitting correct peak shapes, also a result of the asymmetric split peaks. As Rietveld refinement was not a suitable method of obtaining lattice parameters, a fit of the  $\{100\}_{pc}$  reflection only was used to provide estimated values. This was fitted using three Voigt peak functions in OriginPro 8.5<sup>10</sup>. Pseudo-cubic lattice parameters are approximately equal to the  $d$ -spacings corresponding to the positions of the peak centres.

The derived pseudo-cubic lattice parameters are shown in Figure 4.28. The lattice parameters show a broad tendency to increase with potassium substitution, a consequence of the larger average radius of the A-site ion<sup>11</sup>. This is in agreement with the trends observed for solid state KNBT (Figure 3.23). Whilst the  $a$  parameters are of similar magnitude in both hydrothermal and solid state series, the tetragonal  $c$  parameter is larger for hydrothermal KNBT, indicating a greater spontaneous strain. The KBT lattice parameters fall slightly outside the range of the published values for solid state KBT (Figure 3.23); again, a greater strain is seen in the hydrothermal material.

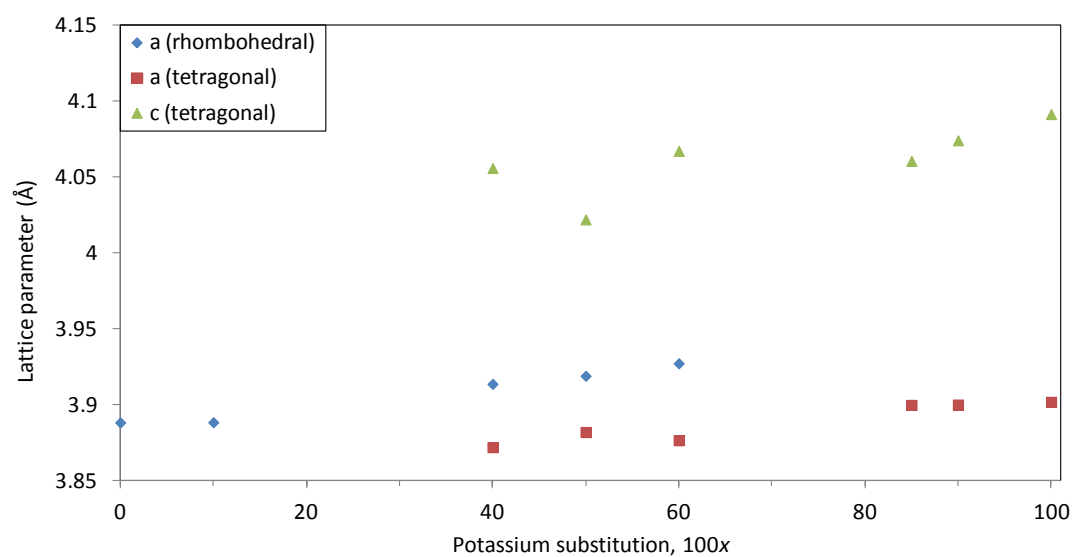


**Figure 4.28.** Pseudo-cubic lattice parameters of as-prepared hydrothermal KNBT.

## 4.4 KNBT30

Hydrothermal KNBT30 was heat-treated at 900 °C for 6 hours in order to anneal the sample and to produce sharper Bragg and superstructure reflections. The room-temperature XRD pattern is shown in Figures 4.29. The XRD peaks show no visible splitting, and the peak shapes do not imply a multiphase structure as is seen in solid state KNBT30 (Figure 4.30). The  $\frac{1}{2}\{311\}_{pc}$  peak is present, with an intensity of 0.78% relative to the  $\{110\}_{pc}$  peak, close to that of hydrothermal NBT (Figure 4.10).

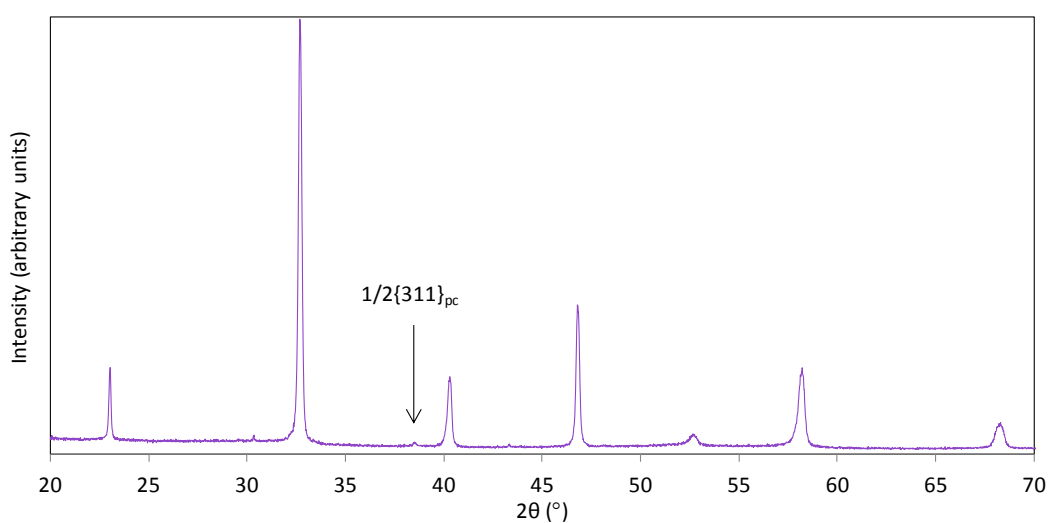


**Figure 4.29.** Room-temperature XRD pattern from hydrothermal KNBT30, heated-treated at 900 °C for 6 hours, showing  $\frac{1}{2}\{311\}_{pc}$  peak.

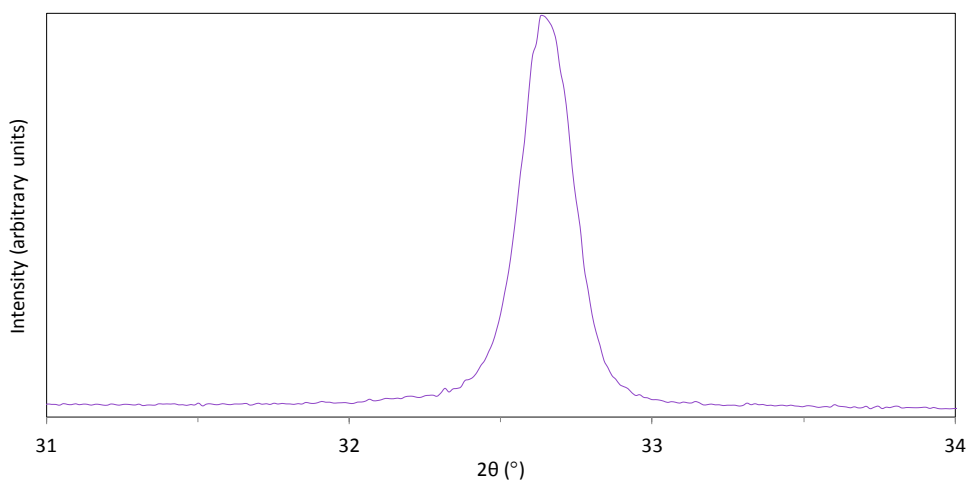


**Figure 4.30.**  $\{110\}_{pc}$  XRD peak from hydrothermal KNBT30, heated-treated at 900 °C for 6 hours.

As the XRD pattern suggests a structure close to that of hydrothermal NBT, refinements were carried out using the NBT  $R3c$  and  $Cc$  models as starting points (Table 4.7).

Crystal system		Rhombohedral	Monoclinic
Space group		$R3c$	$Cc$
Tilt system		$\bar{a} \bar{a} \bar{a}$	$\bar{a} \bar{a} \bar{c}$
$a$ (Å)		5.4970(1)	9.523(1)
$b$ (Å)			5.4958(4)
$c$ (Å)		13.5157(5)	5.5154(4)
$\alpha, \beta, \gamma$ (°)		90, 90, 120	90, 125.300(8), 90
Pseudo-cubic unit cell volume (Å <sup>3</sup> )		58.948(3)	58.90(1)
No. Refined parameters		32	41
$R_{exp}$		5.874	5.871
$R_p$ (%)		6.352	6.885
$R_{wp}$ (%)		8.537	9.074
$R_{bragg}$ (%)		1.849	3.110
$\chi^2$		1.453	1.545
Na/Bi	$x$	0	0
	$y$	0	0.25
	$z$	0.2383(3)	0
	$b$ (Å <sup>2</sup> )	3.30(4)	2.65(5)
Ti	$x$	0	0.25(3)
	$y$	0	0.25(1)
	$z$	0	0.76(2)
O (I)	$x$	0.131(1)	0.00(5)
	$y$	0.349(2)	0.21(2)
	$z$	0.0868(3)	0.47(5)
O (II)	$x$	-	0.23(3)
	$y$	-	0.51(6)
	$z$	-	0.96(5)
O (III)	$x$	-	0.26(4)
	$y$	-	0.01(3)
	$z$	-	0.06(5)

**Table 4.7.** Lattice parameters, atomic positions, thermal displacement parameters, and refinement details for heat-treated hydrothermal KNBT30, taken at room temperature.

These refinements are of similar quality, and so the use of the lower symmetry ( $Cc$ ) model to describe the structure cannot be justified on the basis of these data.

KNBT30 structure as a function of temperature was investigated using XRD between room-temperature and 500 °C. Scans of the 31 - 39° 2 $\theta$  range were collected at temperatures up to 500 °C, as well as a 20 – 100 ° 2 $\theta$  scan at 500 °C.

The intensity of the  $\frac{1}{2}\{311\}_{pc}$  peak relative to that of the  $\{110\}_{pc}$  was measured as a function of temperature (Figure 4.31). This is seen to decrease with temperature increase up to 230 °C, beyond which no data are available until 500 °C, by which temperature the  $\frac{1}{2}\{311\}_{pc}$  peak is gone. Extrapolation of a linear fit to the data suggests a phase transition at ~ 300 °C.

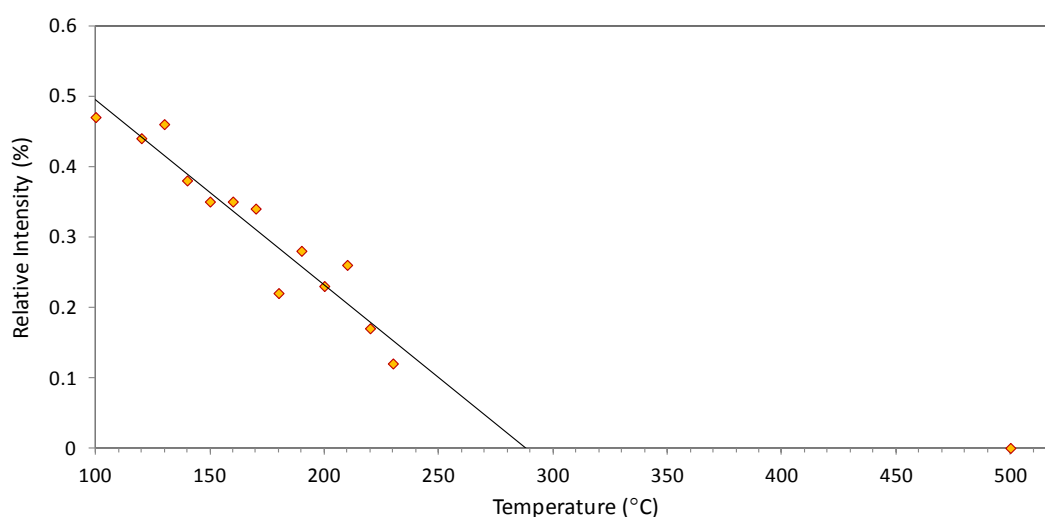


**Figure 4.31.** Intensity of the  $\frac{1}{2}\{311\}_{pc}$  XRD peak relative to the intensity of the  $\{110\}_{pc}$  XRD peak in KNBT30 when heated from 100 °C to 500 °C. The solid line is a linear fit to the data between 100 °C – 230 °C.

The  $\{110\}_{pc}$  and  $\{111\}_{pc}$  peaks were fitted using a pseudo-Voigt peak function in OriginPro 8.5<sup>10</sup>; Figure 4.32 shows the FWHM. Linear fits to the data < 500 °C are shown, and the temperatures at which these intercept with the FWHM of the high-temperature phase are indicated. These suggest a phase transition at ~ 300 °C

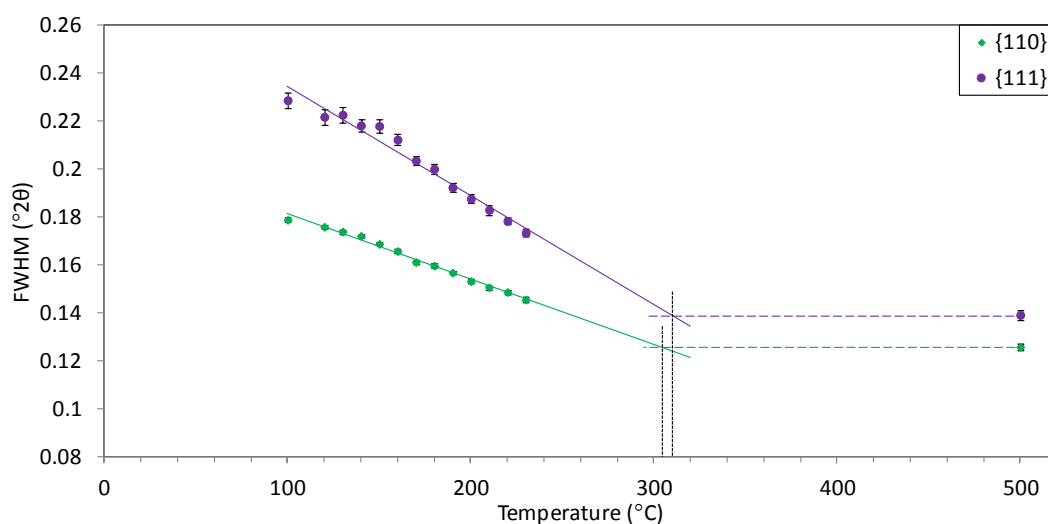


**Figure 4.32.** FWHM of the  $\{110\}_{pc}$  and  $\{111\}_{pc}$  peaks in KNBT30 on heating from 500 °C to 500 °C. Solid lines show linear fits to the data < 500 °C; dashed lines are drawn at the FWHM values of the 500 °C data. The dotted lines indicate the temperatures at which these intercept.

To investigate the structure at a temperature above the possible phase transition, analysis was made of the data collected at 500 °C. The majority of the XRD peaks show no splitting and indicate a cubic symmetry (Figure 4.33). However, the  $\{321\}_{pc}$  peak does show evidence of splitting (Figure 4.34).

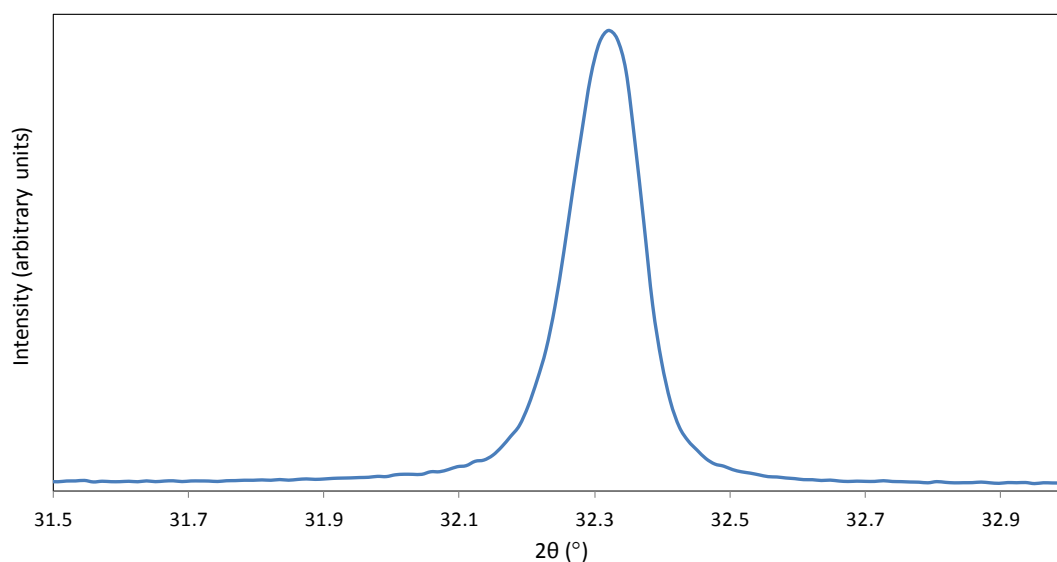


**Figure 4.33.**  $\{110\}_{pc}$  XRD peak of hydrothermal KNBT30 at 500 °C, showing no peak splitting.

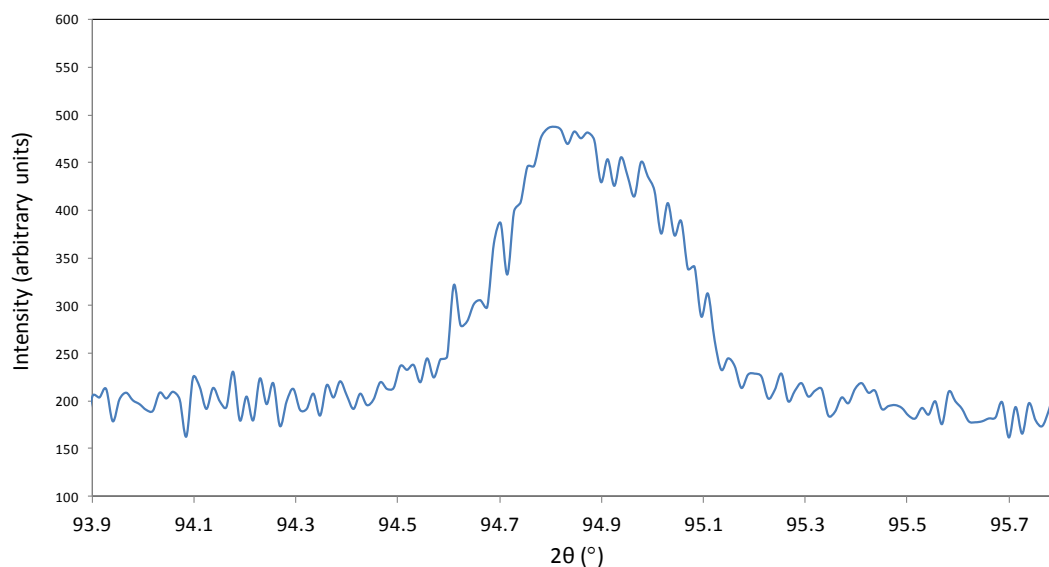


**Figure 4.34.**  $\{321\}_{pc}$  XRD peak of hydrothermal KNBT30 at 500 °C, showing asymmetric peak shape indicative of peak splitting.

A Williamson-Hall<sup>12</sup> plot was used to investigate the possibility of a strained, non-cubic structure. The Williamson-Hall method describes peak broadening ( $B$ ) as the sum of broadening due to particle size ( $B_p$ ) and broadening due to strain ( $B_s$ ). Whilst  $B_s$  is independent of the Bragg angle,  $B_p$  increases at higher  $2\theta$ . A plot of  $B\cos\theta$  against  $\sin\theta$  has a gradient related to the strain in the crystallites, and the intercept related to crystallite size. Figure 4.35 shows this plot for hydrothermal KNBT30, compared with data collected from hydrothermal and solid state cubic NBT, collected at 700 °C and 600 °C respectively. Lines fitted to all three data sets show the same y-axis intercept, indicating equal particle size. However, the gradient of the hydrothermal KNBT30 trend line is steeper, indicating a strained structure. When considered alongside Figure 4.34, this suggests a non-cubic structure.



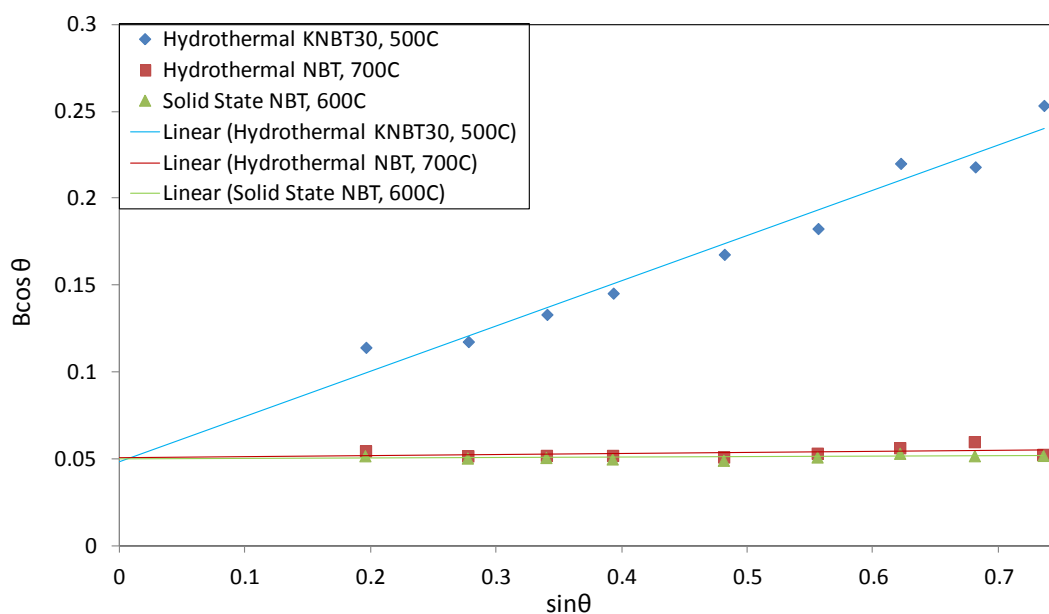


**Figure 4.35.** Williamson-Hall plot of hydrothermal KNBT30 at 500 °C, and cubic hydrothermal and solid state NBT at 700 °C and 600 °C respectively.

Table 4.8 shows the results of Rietveld refinements carried out using a cubic model, and un-tilted rhombohedral ( $R3m$ ) and tetragonal ( $P4mm$ ) models. The quality of the fit is close for all three models, although slightly poorer for the cubic refinement. The  $R$ -factors appear slightly better for the  $R3m$  than  $P4mm$  model, although the difference is minimal and does not favour one space group conclusively.

Crystal system		Rhombohedral	Tetragonal	Cubic
Space group		$R\bar{3}m$	$P4mm$	$Pm\bar{3}m$
Tilt system		$a^0a^0a^0$	$a^0a^0a^0$	$a^0a^0a^0$
$a$ (Å)	5.5345(3)	3.9150(1)	3.9128(2)	3.91300(5)
$b$ (Å)				
$c$ (Å)				
$\alpha, \beta, \gamma$ (°)	90, 90, 90	90, 90, 90	90, 90, 90	90, 90, 90
Pseudo-cubic unit cell volume (Å <sup>3</sup> )		59.970(8)	59.972(3)	59.914(1)
No. Refined parameters		28	27	25
$R_{exp}$		5.049	5.050	5.050
$R_p$ (%)		5.216	5.049	5.859
$R_{wp}$ (%)		6.826	6.854	7.408
$R_{bragg}$ (%)		0.930	1.136	1.257
$\chi^2$		1.352	1.357	1.467
Na/Bi	$x$	0	0	0
	$y$	0	0	0
	$z$	0.012(1)	0	0
	U11 (Å <sup>2</sup> )	0.096(5)	0.102(4)	0.0840(6)
	U22 (Å <sup>2</sup> )			
	U33 (Å <sup>2</sup> )	0.087(9)	0.069(5)	
	U12 (Å <sup>2</sup> )	0.048(3)	0	0
	U13, U23 (Å <sup>2</sup> )	0		
Ti	$x$	0	0.5	0.5
	$y$	0	0.5	0.5
	$z$	0.5	0.498(3)	0.5
	$b$ (Å <sup>2</sup> )	1.19(5)	1.40(4)	1.58(4)
O (I)	$x$	0.1846(7)	0.5	0.5
	$y$	0.8155(7)	0	0.5
	$z$	0.363(2)	0.569(2)	2.80(7)
O (II)	$x$	-	0.5	-
	$y$	-	0.5	-
	$z$	-	0.039(5)	-

**Table 4.8.** Lattice parameters, atomic positions, thermal displacement parameters, and refinement details for heat-treated hydrothermal KNBT30, taken at 500 °C.

From the investigation into the temperature-dependent behaviour of hydrothermal KNBT30, it can be concluded that there is a likely phase transition at ~ 300 °C. The room-temperature structure appears to be  $R3c$ , although  $Cc$  cannot be ruled out. The structure at 500 °C is non-cubic, probably  $R3m$  or  $P4mm$ ; further work remains to determine which. This is different from solid state KNBT30, which contains  $R3m$  and  $P4mm$  structures at room-temperature and is predicted to undergo the Curie transition at  $T_c \sim 220$  °C (Figure

3.61). The un-tilted, non-cubic structure at 500 °C is not predicted by the solid state KNBT phase diagram. Further work analysing more compositions in the solid state KNBT range is warranted, to check for the presence of this phase. A possible explanation for the differing room-temperature structure is that the material contains a lower level of potassium than expected. Support for this theory is provided by the pseudo-cubic unit cell volume (Table 4.7); when compared with those of the solid state KNBT series (Figure 3.22),  $58.9 \text{ \AA}^3$  is close to the expected value for KNBT05.

## References

- <sup>1</sup> G. O. Jones and P. A. Thomas, *Acta Cryst. B* **58**, 168 (2002).
- <sup>2</sup> S. Gorfman, A. M. Glazer, Y. Noguchi, M. Miyayama, H. Luo, and P. A. Thomas, *J. Appl. Cryst.* **45**, 444 (2012).
- <sup>3</sup> A. M. Glazer, *Acta Cryst. A* **31**, 756 (1975).
- <sup>4</sup> C. J. Howard and H. T Stokes, *Acta Cryst. B* **54**, 782 (1998).
- <sup>5</sup> N. Kumada, Y. Morozumi, Y. Yonesaki, T. Takei, N. Kinomura, and T. Hayashi, *J. Ceram. Soc. Jap.* **116**, 1238 (2008).
- <sup>6</sup> O. Subohi, G. S. Kumar, M. M. Malik, and R. Kurchania, *Physica B* **407**, 3813 (2012).
- <sup>7</sup> A. A. Coelho, TOPAS-Academic (<http://www.topas-academic.net/>, Brisbane, 2007).
- <sup>8</sup> P. Jarupoom, T. Tunkasiri, K. Pengpat, S. Eitssayeam, and G. Rujijanagu, *Ferroelectrics* **415**, 88 (2011).
- <sup>9</sup> D Tobaldi, M., A. Tucci, A. Sever Skapin, and L. Esposito, *J. Eur. Ceram. Soc.* **30**, 2481 (2010)
- <sup>10</sup> OriginLab Corporation, OriginPro (Northampton, MA USA, 2010).
- <sup>11</sup> R. D. Shannon and C. T. Prewitt, *Acta. Cryst. B* **25**, 925 (1969).
- <sup>12</sup> G. K. Williamson and W. H. Hall, *Acta. Metal.* **1**, 22 (1953).

## Chapter 5

### Conclusions and Further Work

#### 5.1 NBT

##### 5.1.1 NBT Room-Temperature Structure

The room-temperature structures of solid state and hydrothermal NBT have been investigated in light of both the historically accepted rhombohedral structure<sup>1</sup>, and recent reports of monoclinic structure<sup>2,3,4,5</sup>. The *R3c* and *Cc* models gave refinements with similar visual fits and *R*-factors. Use of the lower symmetry model could not be justified on the basis of this NBT study alone. The *Cc* fits to KNBT05-20 gave better  $\chi^2$ ,  $R_{wp}$ , and  $R_p$  factors than the *R3c* fits. The *Cc* phase region has therefore been extrapolated to include NBT. One possible explanation for the ambiguity is that a monoclinic distortion exists but is very slight, giving a “pseudo-rhombohedral” structure. Another explanation is that local symmetry is reduced to monoclinic by atomic displacements, whilst the long-range order remains rhombohedral<sup>6</sup>. Techniques that study short-range order could further advance this investigation by providing data on the immediate environment of the A-site cations. Such techniques might include NMR or pair distribution function<sup>7</sup>.

##### 5.1.2 Hydrothermal Synthesis of NBT

In agreement with published research<sup>8,9</sup>, hydrothermal synthesis has been found to be a viable low-temperature method of producing NBT. The XRD patterns of as-prepared material resembled those of solid state NBT with three notable differences:

1. the hydrothermal material produces a pattern with broader Bragg peaks, indicative of a smaller crystallite size;

2. the hydrothermal pattern has a more undulating background, indicating greater diffuse scattering from a more disordered material;
3. the  $\frac{1}{2}\{311\}_{pc}$  peak shows a greater relative intensity in hydrothermal NBT, indicative of a more strongly tilted structure.

After heat-treatment at 950 °C for 6 hours, the background becomes smoother and the Bragg peaks sharper, more closely matching the pattern from solid state NBT. This indicates that, when annealed, the structure of the hydrothermal material becomes more similar to that of solid state material. Growth of crystallites during annealing is likely, as a Williamson-Hall plot of the annealed cubic phase of hydrothermal and solid state NBT shows similar particle sizes in both materials (Figure 4.32). The hydrothermal preparation route may not allow thorough mixing of the A-site ions, leading to inhomogeneity that is reduced when these are allowed to mix by heating the sample. OH<sup>-</sup> groups, which have been shown to exist in materials following hydrothermal synthesis<sup>10</sup>, may distort the local environment<sup>11</sup> causing diffuse scattering. The removal of these groups via heating may be responsible for the reduction in background fluctuations. Better mixing of the A-site cations to give a more homogeneous sample may also have improved the background. The relative intensity of the  $\frac{1}{2}\{311\}_{pc}$  peak increases after annealing, indicating a greater degree of octahedral rotation in hydrothermal than solid state NBT. This is borne out in a calculation of tilting angle:  $\omega_{hydrothermal} = 8.5^\circ$ ;  $\omega_{solid\ state} = 6.4^\circ$ . As well as a greater tilting angle, hydrothermal NBT shows a unit cell volume 0.1% smaller than solid state NBT, and polarisation values smaller by approximately half. A possible explanation for all three observations is Bi<sup>3+</sup> deficiency in the hydrothermal sample. The lower average A-site ionic radius resulting from this deficiency<sup>12</sup> would cause greater tilting by a decrease in the tolerance factor, as well as a smaller unit cell. Bi<sup>3+</sup> has been found to be more strongly polarised (i.e. off-centre)<sup>7</sup> than Na<sup>1+</sup>, and so Bi<sup>3+</sup> deficiency may lead to lower polarisation values. Further work remains to measure precisely the cation population, to determine whether Bi<sup>3+</sup> deficiency is

responsible for differences in polarisation and tilting between hydrothermal and solid state NBT. This could be achieved using scanning electron microscopy (SEM) for compositional analysis.

### 5.1.3 Temperature-Dependent Behaviour of NBT

The sequence of phase transitions between room-temperature and the high-temperature cubic phase has been examined in both solid state and hydrothermal NBT. Both were found to undergo two transitions on heating: first, from pseudo-rhombohedral to tetragonal  $P4bm$ ; second, from tetragonal to cubic  $Pm\bar{3}m$ . The pseudo-rhombohedral to tetragonal transition was investigated via analysis of Bragg peak widths, superstructure reflection intensities, and Rietveld refinement. Simultaneous observation of  $\frac{1}{2}\{311\}_{pc}$  and  $\frac{1}{2}\{310\}_{pc}$  peaks indicates the coexistence of pseudo-rhombohedral and tetragonal phases in the region of the first phase transition, whilst the minima in Bragg peak widths and superstructure peak intensities points to a pseudo-cubic structure. Rietveld refinement has been used to verify the viability of a phase coexistence model in the case of hydrothermal NBT. This was not possible for solid state NBT as the tilt peaks could not be distinguished in a refinement-quality scan, although their existence was confirmed in a shorter scan. The coexistence of superstructure peaks suggests that the phase transition takes place at different rates or temperatures in different domains, leading to an overlap in pseudo-rhombohedral/tetragonal symmetry. The transition between pseudo-rhombohedral and tetragonal structures proceeds via a reduction of the distortion to reach a pseudo-cubic structure, increasing in distortion above/below the transition temperature. The phase transition on heating occurs at 300 °C in solid state NBT and 305 °C in hydrothermal NBT. Hysteresis in the transition temperature of 30 °C is observed in solid state NBT, and 20 °C in hydrothermal NBT. Rough estimates of  $T_c$  have been made: 490 °C for solid state NBT and 580 °C for hydrothermal NBT.  $T_c$  is found to occur at a higher temperature in hydrothermal

than solid state NBT; however, the possible ranges for both  $T_c$  values are large (450 °C – 530 °C for solid state NBT; 530 °C – 700 °C for hydrothermal NBT), and so the difference may not be as great as it appears from the estimates.

#### 5.1.4 Mn-doped NBT

The addition of 1 at. % Mn to solid state NBT was not found to have a marked effect on the room temperature structure, or the transition to tetragonal symmetry, which occurred at 300 °C. The tetragonal-to-cubic transition is estimated to occur at  $T_c = 550$  °C, but may be as low as 525 °C, which is within the range of possible  $T_c$  values for solid state NBT.

### 5.2 Solid State KNBT Series

#### 5.2.1 Room-Temperature

XRD data from samples in the range KNBT05 – KNBT20 were found to show better agreement with monoclinic  $Cc$  than rhombohedral  $R3c$  models. Data from samples in the range KNBT25 – KNBT65 were best modelled using a combination of rhombohedral  $R3m$  and tetragonal  $P4mm$  phases. A phase boundary between the  $Cc$  and  $R3m/P4bm$  phases was found to lie between KNBT20 and KNBT25, coincident with a reported peak in electromechanical properties<sup>13</sup>. The region KNBT20-60 has been reported to be bi-phasic<sup>14</sup>, in agreement with this study. Other studies have reported intermediate phase regions at KNBT50-80<sup>15</sup> and KNBT18-40<sup>16</sup>, and morphotropic regions at KNBT16-20<sup>17</sup> and KNBT17-25<sup>13</sup>. The wide variety of reported phase models suggests the structure of the material is sensitive to the preparation conditions<sup>13</sup>. This study has found no evidence of an intermediate phase, but instead found bi-phasic  $R3m/P4mm$  compositions extending as far as KNBT65. It is considered that the equilibrium phase in KNBT25 – KBT is tetragonal  $P4mm$ , and that the presence of rhombohedral  $R3m$  material appears as a result of grinding of the



sample. The fraction of rhombohedral material decreases inconsistently with potassium substitution. Different lengths of time spent grinding different samples may have caused the fluctuations in the amount of rhombohedral material seen in the samples. For compositions KNBT20-65, greater tetragonal XRD peak splitting was found to correlate with a smaller proportion of rhombohedral phase present. Stress-induced structural alterations may explain this link. Stress may reduce tetragonality, leading to rhombohedral distortion. This would explain why a smaller  $c/a$  ratio coincides with a lower proportion tetragonal phase.

Tilting angle of the oxygen octahedra decreases across the range NBT – KNBT20 with increasing potassium content. Using published values for ionic radii<sup>18, 19</sup>, the tolerance factor has been calculated to increase from 0.98 to 0.99 across this range. According to Reaney *et al.*<sup>20</sup>, the change from anti-phase tilted to untilted structure is expected for these tolerance factor values.

The main contribution to the overall polarisation in KNBT was found to come from the Ti-O polarisation, particularly in the rhombohedral and pseudo-rhombohedral phases. Higher polarisation is calculated in the tetragonal than rhombohedral phases, by a factor of  $\sim 2$ . Enhanced polarisation of the pseudo-rhombohedral phase was observed in KNBT20, as might be expected for a composition close to a phase boundary<sup>21</sup>. This agrees with published reports of enhanced physical properties in this region<sup>17,13</sup>. Between KNBT25-65, no clear trend in polarisation is observed with potassium substitution. This is in agreement with the lack of clear trends in physical properties seen by Sasaki *et al.*<sup>17</sup>. However, the polarisation data are highly scattered, owing to the difficulty in observing oxygen positions using x-rays. Further studies, using neutrons, would be required to provide better quality data and more reliable refinements of oxygen positions. This would enable calculation of polarisation data with greater confidence.

## 5.2.2 KNBT10 & KNBT40, High-Temperature

The temperature-dependent phase transitions in KNBT10 and KNBT40 were investigated by analysis of the peak widths and (in the case of KNBT10) superstructure peak intensity. KNBT10 was found to show a phase transition at  $\sim 225$  °C, as determined by convergence of the  $\{110\}_{pc}$  and  $\{111\}_{pc}$  peak widths and the disappearance of the  $\frac{1}{2}\{311\}_{pc}$  peak. The  $\frac{1}{2}\{310\}_{pc}$  peak does not emerge, suggesting either  $Pm\bar{3}m$  or  $P4mm$  symmetry above 225 °C. As the structure is found to be cubic at 335 °C, it is expected that this phase transition is the Curie transition. The decrease in peak widths and tilt peak intensity suggests this follows on from a reduction in rhombohedral strain as observed in NBT. Analysis of peak widths in KNBT40 indicates a phase transition at  $\sim 280$  °C. Analysis of the peak profiles at this temperature indicates a non-cubic structure, and Rietveld refinement favours a combined  $R3m/P4mm$  model over a single-phase model. The structure was found to be cubic at 450 °C, with peak widths very close to those at 280 °C. It is therefore suggested  $T_c \sim 300$  °C for this composition.

## 5.2.3 Solid State KNBT Phase Diagram

Series room-temperature data, as well as high-temperature studies on NBT, KNBT10 and KNBT40, have been used in combination with published high-temperature data<sup>14</sup> to produce a KNBT phase diagram (Figure 3.46).

## 5.3 Hydrothermal KNBT Series

### 5.3.1 Room-Temperature

As-prepared hydrothermal material shows three phase fields: rhombohedral  $R3c$  from NBT – KNBT10; multiphase rhombohedral and tetragonal from KNBT40-60; tetragonal  $P4mm$  from KNBT85 – KBT. The Bragg peaks were very wide, leading to greater difficulty in

performing structural refinements. It was therefore not possible to distinguish between rhombohedral and monoclinic symmetry in the as-prepared materials. Pseudocubic lattice parameters show an increase with increasing potassium content, as a result of the larger average radius of the A-site ion<sup>12</sup>. The pseudocubic  $a$  parameters from both rhombohedral and tetragonal models are close to those expected based on solid state KNBT analysis and published data<sup>15,22,23</sup>. However, the pseudocubic  $c$  parameters from tetragonal models are larger for hydrothermal than solid state KNBT. In KNBT40-60,  $c$  varies between 4.02 – 4.07 Å in hydrothermal material, compared with 3.96 – 3.98 Å in solid state KNBT. This can be seen in the marked splitting of the XRD peaks from hydrothermal material. A larger  $c$  parameter is also seen in KBT, with  $c = 4.09$  Å in hydrothermal KBT, in agreement with a study by Lencka *et al.*<sup>8</sup>, who reported a hydrothermal KBT value of  $c = 4.10$  Å<sup>8</sup>; reported values for solid state KBT vary between 3.99 Å<sup>15,22</sup> and 4.01 Å<sup>23</sup>. The hydrothermal samples may contain OH<sup>-</sup> groups, H<sub>2</sub>O, and oxygen vacancies, as well as inhomogeneous clustering of the A-site ions. These defects may cause the difference between hydrothermal and solid state lattice parameters. Lencka *et al.* found that calcination reduced  $c$  to 4.00 Å<sup>8</sup>, a value within range reported for solid state KBT, and TGA measurements (this study) show continual mass loss from 20 °C – 900 °C, consistent with the continual loss of materials that does not form part of the expected crystal structure.

### 5.3.2. Hydrothermal KNBT30, High-Temperature

Annealed hydrothermal KNBT30 shows  $R3c$  symmetry at room temperature, as evidenced by Rietveld refinement. Analysis of the XRD peak widths and  $\frac{1}{2}\{311\}_{pc}$  peak intensity suggests a phase transition at ~ 300 °C. At 500 °C the structure is not completely cubic, as inferred from the  $\{321\}_{pc}$  peak profile and the gradient of a Williamson-Hall plot. Likely candidates for the symmetry at this temperature are  $R3m$  and  $P4mm$  because of the absence of tilt peaks, although Rietveld refinement does not favour one above the other.

The room-temperature structure is different from that of solid state KNBT30, which shows a clear mixture of  $R3m$  &  $P4mm$  symmetry. A possible explanation for the differing room-temperature structure is that the material contains a lower level of potassium than expected. As NaOH and KOH were used in stoichiometric quantities in the preparation of the sample, this suggests that Na is more readily taken into the structure than K. This theory is supported by results of a study by Lencka *et al.*<sup>8</sup>, in which synthesis of the KNBT end-members required a higher concentration of KOH than NaOH solution. The un-tilted, non-cubic structure at 500 °C is not predicted by the solid state KNBT phase diagram (Figure 3.46). If the sample contained low levels of potassium, the in-phase tilted  $P4bm$  structure might be expected, but the corresponding superstructure peaks are not seen. However, data have not been collected between 230 °C and 500 °C. If the sample went through the  $P4bm$  phase found in the solid state phase diagram, the  $\frac{1}{2}\{310\}_{pc}$  peak would be most intense within this temperature region, and would be expected to diminish as  $T_c$  is approached. The possibility remains, therefore, that the non-cubic and apparently un-tilted structure at 500 °C is, in fact,  $P4bm$ . Compositional analysis, as well as further XRD from 25 °C – 700 °C, could be utilised to elucidate the structure of this material. Based on the suggestion of a phase transition at ~ 300 °C, the weakly distorted structure seen at 500 °C, and pseudo-cubic unit cell volume calculations, it is thought that the composition of this sample may, in fact, be closer to KNBT05.

## 5.4 Hydrothermal KBT

The tetragonal symmetry of as-prepared hydrothermal KBT is clear from the visibly split XRD peaks. After annealing, these peaks are no longer split, showing a significant change in the structure. This may be due to the release of  $OH^-$  groups, which has been found to change the structure of hydrothermal NBT<sup>10</sup>. The possible release of  $OH^-$  groups is supported by the mass loss observed between 25 °C – 900 °C. Another possible explanation

is mixing of the A-site species when heated. During heating, the  $(001)_T$  and  $\{010\}_T$  XRD peaks move closer together, forming first a single, asymmetric peak. At 800 °C the peak becomes symmetric, showing that the structure is cubic and interpreted as the completion of annealing. This does not necessarily mean 800 °C is the optimum annealing temperature, as annealing occurs as a function of time also<sup>24</sup>. Analysis of the asymmetry of the  $(001)_T$  peak indicates anisotropic strain in the material. This increases with temperature up to 600 °C, and decreases above 600 °C, suggesting that annealing begins at this temperature. Further work remains to establish an optimum temperature and duration to anneal hydrothermal KBT. A series of experiments, similar to those performed but with varied heating rates and temperature holding times, could serve this purpose. Further work remains to understand why there is such a large tetragonal distortion in the as-prepared sample. This could include: NMR of samples prepared with deuterated water to establish the presence of H<sub>2</sub>O within the unit cell from the hydrothermal process; IR spectroscopy to establish the presence of OH<sup>-</sup> groups; SEM or TEM with elemental mapping to investigate A-site clustering; and high-resolution TEM to find oxygen vacancies.

## References

- <sup>1</sup> S. B. Vakhrushev, B. G. Ivanitskii, B. E. Kvyatkovskii, A. N. Maistrenko, N. M. Malysheva, and N. N. Parfenova, *Sov. Phys. Solid State* **25**, 1504 (1983).
- <sup>2</sup> S. Gorfman and P. A. Thomas, *J. App. Cryst.* **43**, 1409 (2010).
- <sup>3</sup> E. Aksel, J. S. Forrester, J. L. Jones, P. A. Thomas, K. Page, and M. R. Suchomel, *Appl. Phys. Lett.* **98** (2011)
- <sup>4</sup> S. Gorfman, A. M. Glazer, Y. Noguchi, M. Miyayama, H. Luo, and P. A. Thomas, *J. Appl. Cryst.* **45**, 444 (2012).
- <sup>5</sup> B. N. Rao and R. Ranjan, *Phys. Rev. B* **86**, 4103 (2012).
- <sup>6</sup> J. Kreisel, P. Bouvier, B. Dkhil, P. A. Thomas, A. M. Glazer, T. R. Welberry, B. Chaabane, and M. Mezouar, *Phys. Rev. B* **68**, 14113 (2003).
- <sup>7</sup> D. S. Keeble, E. R. Barney, D. A. Keen, M. G. Tucker, J. Kreisel, and P. A. Thomas, *Adv. Funct. Mat.* **23**, 185 (2012).
- <sup>8</sup> M. M. Lencka, M. Oledzka, and R. E. Riman, *Chem. Mater.* **12**, 1323 (2000).
- <sup>9</sup> Y. J. Ma, J. H. Cho, Y. H. Lee, and B. I. Kim, *Mat. Chem. & Phys.* **98**, 5 (2006).
- <sup>10</sup> N. Kumada, Y. Morozumi, Y. Yonesaki, T. Takei, N. Kinomura, and T. Hayashi, *J. Ceram. Soc. Jap.* **116**, 1238 (2008).
- <sup>11</sup> R. S. Islam, R. A. Davies, and J. D. Gale, *Chem. Mater.* **13**, 2049 (2001).
- <sup>12</sup> R. D. Shannon and C. T. Prewitt, *Acta. Cryst. B* **25**, 925 (1969).
- <sup>13</sup> M. Otonicar, S. D. Skapin, M. Spreitzer, and D. Suvorov, *J. Am. Ceram. Soc.* **30**, 971 (2010).
- <sup>14</sup> O. Elkechai, M. Manier, and J. P. Mercurio, *Phys. Stat. Solidi .A.* **157**, 499 (1996).
- <sup>15</sup> J. Kreisel, A. M. Glazer, G. Jones, P. A. Thomas, L. Abello, and G. Lucazeau, *J. Phys. Condens. Matt.* **12**, 3267 (2000).
- <sup>16</sup> G. O. Jones, J. Kreisel, and P. A. Thomas, *Powder Diffr.* **17**, 301 (2002).
- <sup>17</sup> A. Sasaki, T. Chiba, Y. Mamiya, and E. Otsuki, *Jpn. J. Appl. Phys.* **38**, 5564 (1999).

- <sup>18</sup> R. D. Shannon, *Acta Cryst. A* **32**, 751 (1976).
- <sup>19</sup> R. E. Eitel, C. A. Randall, T. R. Shrout, P. W. Rehrig, W. Hackenberger, and Seung-Eek Park, *Jpn. J. Appl. Phys.* **40**, 5999 (2001).
- <sup>20</sup> I. M. Reaney, E. L. Colla, and N. Setter, *Jpn. J. Appl. Phys* **33**, 3984 (1994).
- <sup>21</sup> D. A. Berlincourt, C. Cmolik, and H. Jaffe, *Proc. IRE* **48**, 220 (1960).
- <sup>22</sup> V. A. Isupov, *Ferroelectrics* **315**, 123 (2005).
- <sup>23</sup> S. M. Emel'yanov, I. P. Raevskii, and F. I. Savenko, *Fiz. Tverd. Tela.* **29**, 2511 (1987).
- <sup>24</sup> P. Jarupoom, T. Tunkasiri, K. Pengpat, S. Eitssayeam, and G. Rujijanagu, *Ferroelectrics* **415**, 88 (2011).